Synthesis and characterization of activated carbon and manganese-based oxide/layered double hydroxide materials for supercapacitor application

By

Ochai-Ejeh Faith

Student number: 15305458

A thesis submitted in partial fulfillment of the requirements for the degree of

DOCTOR OF PHILOSOPHY (Ph.D.) IN PHYSICS

Faculty of Natural and Agricultural Sciences

University of Pretoria

Hatfield, Pretoria

July 2018

Supervisor/Promoter: **Prof. N.I. Manyala**

Declaration of originality

I, **Faith Ochai-Ejeh** hereby declare that this thesis, which I submit for the degree of **Doctor of Philosophy (Ph.D.)** at the University of Pretoria, is my own work and has not been previously submitted by me for a degree at this or any other tertiary institution.

Signature: ………………… Date: ……………………..

Dedication

To the Memory of my beloved mother Mrs. Comfort Ugbo

To my beloved husband and friend, Pastor Ernest Ochai Ejeh

And ultimately

To the Almighty God for seeing me through my Ph.D. programme

Acknowledgment

I would like to, first of all, express my profound gratitude to God Almighty for helping me and seeing me through the course of this Ph.D. programme - Thank you, Lord! I sincerely appreciate my Supervisor Prof. N. I. Manyala for his fatherly care, support, advice and constructive criticisms which helped me to complete this program successfully.

I want to say big thanks to Dr. M.J. Madito, Dr. J.K. Dangbegnon, Dr. A. Bello, Dr. D.Y. Momodu, and Dr. F. Bazegar for their invaluable assistance both in the laboratory and helping to make my study a success. I will like to appreciate Mr. Eudri Venter, Ms. Anthonette Buys and Mr. Andre Botha of the Microscopy unit of the University of Pretoria, Mr. J. Lekitima, of Chemistry department, Mrs. Isbe Van der Westhuizen of the Institute of Applied Physics and Mrs. Wiebke Grote for their help in the sample characterizations.

My sincere thanks go to Prof C.C. Theron, Head of the Department of Physics for part-time jobs to supplement my finances. Special thanks to the University of Pretoria and the NRF through the SARChI for their financial support and to the University of Nigeria, Nsukka for granting me leave to come to the University of Pretoria, South Africa for this programme and the TETFund Academic Staff Training & Development University of Nigeria, Nsukka for their financial support.

I want to also say thank you to my colleagues: Dr. A.A Khaleed, O. Olaniyan, K. Oyedotun, F. Oladepo, Dr. T. M. Masikwa, A. A. Mirgini, Mrs. N.M Ndiaye Fall, and Ms. Fatou Sylla for their meaningful discussions and friendly support.

I would also like to appreciate Mrs. Elfrieda Meybugh the able secretary to the head of the department of physics and Mrs. Suzzette Seymore of the Institute of Applied Materials, South campus for their ever ready assistance.

I am very grateful to God for my siblings for their support, prayers, and encouragement: Mr. Sylvester Ugbo, Mr. God's will Ugbo, Mr. Anthony Ugbo, Mr. Victor Ugbo, Ms. Franca Ugbo and Mr. Edwin Ugbo. Also special thanks to my siblings-in-love: Mrs. Alexander Victoria, Mrs. Shok, Mr. Monies Ejeh, Mr. George Ejeh, Mr. Aboh Ejeh, Mr. Silas Ejeh and Mr. Igwe Ejeh and my father- and mother-in-love Apostle Dr. and Pst. (Mrs.) E. O. Ochai for their unending love and Prayers.

And finally, very special thanks goes to my darling and loving husband, friend, brother and confidant Pastor Ernest Ochai Ejeh, for his prayers, support, and commitment that enabled me to finish successfully.

Abstract

The aim of this study is to synthesize and characterize cheap, efficient and high-performance 3D activated carbon (AC) from cork (Quercus Suber) by KOH and $KHCO_3$ activation respectively, Co-Mn LDH and MnO_2-CNT nanocomposite materials with meso/microporous structures for energy storage application. The AC derived from cork (Q.suber) was synthesized with KOH in order to investigate the electrochemical performance of the AC in relation to KOH activation concentration and the AC synthesized by $KHCO_3$ device because both materials performed well in 1 M KOH alkaline electrolyte, while ACKOH was chosen as the negative electrode in the MnO_2-CNT//ACKOH device because both materials showed good performance in 1 M Li_2SO_4 neutral electrolyte. The aim of the hybrid devices was to take advantage of the individual working potentials of the electrode materials for enhanced electrochemical performance. All devices tested displayed energy densities ranging from ~14 - ~25 Wh kg^{-1} with corresponding power densities ranging from ~450 – ~500 W kg^{-1} at a specific current of 0.5 Ag^{-1} in the operating voltage window of between 1.6 V and 2.0 V in aqueous electrolyte media. All the materials tested displayed 99.7% - ~100 % long-term cycling stability, showcasing the potential use of these materials as electrode materials for electrochemical capacitors.

Table of content

List of figures

CHAPTER ONE

1.0 INTRODUCTION

1.1 Background and motivation

The ever-increasing world population and the consequent over-dependence on the supply of energy from limited fossil fuel has led to the world energy crisis due to the rising demand for energy to power the ever-evolving technology driven society and the global industrial revolution. This has also resulted in environmental pollution and degradation problems due to air and water contaminants in addition to greenhouse gas emissions which has deteriorating impact on the environment and are grossly harmful to human life and existence [1–3].

A major route to tackling this present day energy issue is to focus on renewable forms of energy that are clean, green, and sustainable for both present and future needs. Some of the renewable sources of energy include solar, wind, geothermal and plant biomass wastes [3,4]. In order to adequately harness the energy from these renewable sources, efficient, reliable, high performance, cheap and easy to maintain energy storage devices are therefore urgently needed. Presently, batteries are the conventional energy storage devices that are commonly utilized but they suffer from low power density, poor cycle life, sluggish charge/discharge and are beset with safety challenges due to the toxicity of the materials employed in its fabrication [5,6].

Electrochemical capacitors (ECs) also known as supercapacitors (SCs) which were first described by Becker in 1957 [7] have attracted the interest of numerous researchers in the past two decades and quite recently [1,8] because of their potential capacity to replace/compliment batteries as an energy storage devices. This is because in addition to being low cost, they utilize materials that are cheap, abundant, renewable and environmentally safe. They also offer the merits of delivering power at pulsed rate with good reversibility, superior cycling stability (> 10,000 cycles) with rapid charge and discharge rate (in seconds) and high power density (> 10 kW kg^{-1}).

Electrochemical capacitors can be categorized into three main groups based on their charge storage mechanism namely: Electric double layer capacitors (EDLCs), Pseudocapacitors and Faradaic (Redox) capacitors. EDLCs are electrochemical storage devices which store energy by means of electrostatic reversible ion adsorption/desorption at the electrode/electrolyte interface. EDLC behavior are basically observed in carbon-based materials with different forms of carbon discovered over the years by scientists [9–13]. Pseudocapacitors are capacitors whose storage mechanism mimic the double layer behavior but store energy via electron transfers leading to change in oxidation state [3,14,15]. Common pseudocapacitive materials studied over the years include Manganese oxide and Ruthenium dioxide [16–20], while Faradaic capacitors are capacitors which store energy by rapid reversible Faradaic (redox) reactions which involve ion intercalation at the material active surface. Common examples of materials exhibiting faradaic behavior include NiO, FeO, MoO_2, Fe_3O_4, $Ni(OH)_2$, $MnCo_2O_4$, CoMn LDH, CoAL LDH, NiAl LDH, PANI, PPY [21–28].

A combination of the storage mechanism from different materials could also be explored in order to tap in from the various merits of each of the individual storage mechanisms. Hybrid capacitors are storage devices which combine the charge storage mechanism of both the EDLCs and the faradaic capacitors by synergizing the respective properties of the double-layer and the faradaic-type ECs [15,29,30].

Electrochemical capacitors are however, limited in their use for energy supply for prolonged time duration due to their low energy densities (about 5 and 10 Wh kg^{-1} for commercially available SCs), except when used in combination with batteries (with energy densities $>$ 180 Wh kg^{-1}) [5,8,31,32]. This has necessitated the broad interest by research experts in the field to boost the energy density of supercapacitors to be comparable to that of batteries while keeping their high power density.

In principle, since energy density (E_d) is proportional to specific capacitance and square of electrode material's operating voltage window ($E_d \propto C_{sp} V^2$), the electrochemical performance of the electrode material and the electrolyte utilized is fundamentally important. Therefore, the ongoing research focus is based on improving the material performance in order to increase the voltage window as well as the specific capacitance of the electrode material [3,33–35]. The electrolyte employed for the device fabrication is also important. This is because aqueous alkaline and acidic electrolytes are quite highly conductive, which makes them to attain high specific capacitance values, but their narrow operating voltage makes them achieve very low energy densities due to the thermodynamic decomposition of water at 1.23 V. Organic electrolytes on the other hand, operate with large voltage windows but suffer from low conductivity, high toxicity and high cost. Alternatively, aqueous neutral electrolytes can achieve relatively large voltage windows because of the their pH , strong ion solvation and high over potential for di-hydrogen evolution [2,3,36].

A variety of carbon materials have been investigated as electrode materials for SC application. These includes graphene, carbon nanotubes (CNTs), zeolite-templated carbons, carbide derived carbons (CDCs), onion-like carbons (OLCs) and activated carbons (ACs) [37–41].

Activated carbon is the most commonly utilized material for SC device fabrication because of its excellent properties which include good electrical conductivity, high and controllable porosity, large specific surface area (SSA), lightweight, low cost and ease of production [42]. Activated carbon can be derived from carbon containing precursors but some of the precursors are quite expensive and non-renewable. Biomass wastes have recently been explored for the synthesis of ACs because they are a cheap, abundant and readily available as source of carbon [33,43]. Since a good synergy between the pore size and large SSA is vital for excellent device performance, controlling the pore structure is therefore necessary for proper device application [44][45].

To accomplish this, important physical and chemical processes are needed to produce high quality porous carbons. In the physical process, carbon precursors are carbonized in an inert atmosphere and then gasified with carbon dioxide, oxygen or steam at temperatures ranging from 600-1200 ˚C. The chemical process involves activation of the carbon precursor using H_2SO_4, K_2CO_3, $KHCO_3$,H_3PO_4, $ZnCl_2$ and KOH and carbonized at temperatures ranging from 400 – 900 °C [45]. KOH is the most commonly utilized activating agent because it results in the production of carbons that are highly porous with well-defined meso/micropore structures. However, it’s quite corrosive and environmentally unfriendly nature has led to it limited industrial use.

Ideal morphological and textural characteristics are also needed for the biomass derived carbon for efficient device application. The pretreatment of the biomass carbon precursor to obtain hydrochar has recently been seen as a better procedure to obtain high quality carbons because of the presence of oxygenated functional groups [46]. In addition to hydrothermal pre-treatment of biomass precursors, activation with milder activating agents like K_2CO_3 and $KHCO_3$ have been shown to retain hydrochar morphology when compared to KOH, hence leading to the production of carbons with structures that are closely packed having less diffusion distances and thus exhibiting better electrochemical performance [44,46–48].

Several other materials have also been examined as potential electrode materials for ECs namely; Transition Metal oxides (TMOs), Transition Metal Layered double hydroxides (TM-LDHs), bi-metallic hydroxides and conducting polymers due to their relatively low cost, ease of production, excellent redox activity and environmentally friendly nature [49–51]. Amongst these TMOs, MnO_2 have been reported to possess a large theoretical SSA, but have poor electrical conductivity. In order to curb this problem, they are synthesized with electrically conductive carbon materials like AC, graphene or CNTs [52–55]. Graphene which is a two dimensional (2D) allotrope of carbon can roll up to produce a uni-dimensional (1D) cylindrical nanotube structure called CNTs, which have good mechanical and electronic properties making them ideal for use as composite materials to boost the conductivity of the metal oxide/hydroxide materials [56].

Layered double hydroxides (LDH) also referred to as hydrotalcite-like compounds or anionic clays are a type of natural and synthetic materials which have the general formula: $\mathrm{M^{II}_{1-x}M^{III}_{x}(OH)_2(A^{n-})_{x/n}.mH_2O}$ where $\mathrm{M^{II}}$ are bivalent cations such as Mg^{2+}, Co^{2+}, Ni^{2+}, Cu^{2+},

Zn^{2+}, etc, $\mathrm{M^{III}}$ are trivalent metal cations such as $Al^{3+,}$ Cr^{3+}, Co^{3+}, Ga^{3+} and $A^{n-}$is an n-valent anion such as Cl^-, CO_3^{2-}[57][58][59]. LDHs have been reported to possess higher electrical conductivity, better ion transfer and carrier for reaction species which are vital for high performance hybrid device fabrication[60,61] Several LDH materials which have been investigated as positive electrode material for device fabrication include Co-AL, Ni-Mn, Ni-Co, Co-Mn etc. Co-Mn LDH in particular have been investigated because of its exclusive redox mix of Co^{2+}/Mn^{2+}. A number of studies have been carried out on the structure and morphology of the material but with limited studies on the electrochemical characterization of the material as positive electrode and AC as negative electrode in a hybrid device for EC application.This research study therefore aims to synthesize cheap, environmentally friendly, meso/microporous, high performance activated carbon (AC) from cork (Quercus Suber) biomass, Co-Mn LDH nanoflake and MnO_2-CNT nanocomposite materials with good pore size distribution for energy storage application.

1.2 Aims and objective:

The aims of this study is to synthesize and characterize activated carbon (AC) from cork (Quercus Suber) biomass, Co-Mn LDH nanoflake and MnO_2-CNT nanocomposite and investigate their respective properties for potential energy storage application.

The objectives of this study are to:

1 Synthesize AC from cork (Quercus suber) biomass for high performance energy storage application via direct activation with potassium hydroxide (KOH) and carbonization in

chemical vapor deposition (CVD) system and via hydrothermal pre-treatment, activation with potassium hydrogen carbonate ($KHCO_3$) and carbonization in CVD system.

2 Synthesize Co-Mn LDH via facile solvothermal synthesis technique.

3 Synthesize MnO_2-CNT nanocomposites through facile hydrothermal reflux technique.

4 Characterize the morphology, structure, surface area and porosity of the as-synthesized materials using X-ray diffraction (XRD), scanning electron microscopy (SEM), transmission electron microscopy (TEM), energy dispersive X-ray (EDX), Raman spectroscopy, Fourier transform infra-red (FT-IR) spectroscopy, x-ray photoelectron spectroscopy (XPS) Brunauer-Emmett-Teller(BET) and Barrette-Joyner-Halenda (BJH) techniques.

5 Fabricate and electrochemically evaluate symmetric devices based on AC derived from activation with KOH (ACKOH) and $KHCO_3$($ACKHCO_3$) respectively.

6 Fabricate and electrochemically evaluatehybrid device based on Co-Mn LDH as positive electrode and $ACKHCO_3$as negative electrode and hybrid device based on MnO_2-CNT as positive electrode and ACKOH as negative electrode materials using a multichannel Biologic VMP300 potentiostat/galvanostat workstation.

1.3 Thesis outline

This thesis is presented in five chapters as follows:

Chapter one presents the introduction, aim and objectives of the study and the thesis outline.

Chapter two presents a literature review on electrochemical capacitors.

Chapter Three presents the experimental details which involves the materials’ synthesis and characterization techniques adopted in the study.

Chapter Four presents results and detailed discussion of the results obtained in this work.

Chapter Five presents summary of the research and recommendations for future work.

CHAPTER TWO

2.0 LITERATURE REVIEW

In this chapter, an overview of electrochemical capacitors (ECs), principles of charge storage mechanism in ECs, materials for EC electrodes, electrolytes for ECs, electrochemical measurement of ECs electrodes, carbon based nanocomposite and electrochemical device fabrication were reviewed.

2.1 Electrochemical capacitors

Electrochemical capacitors (ECs) also known as supercapacitors (SCs) or ultracapacitors owing to their very high capacitance are energy storage devices which store energy much the same way like conventional capacitors. But unlike conventional capacitors whose storage mechanism is by accumulation of charges at the two electrodes, ECs store energy based on surface phenomenon through electric double layer or dielectric polarization by forming a charge separation in the range of a few nanometers (0.3 – 0.8 nm) at the electrode/electrolyte interface [62–67]. ECs operate by allowing a voltage to be applied across the two electrodes (cell) separated with an ion permeable separator inserted between the electrodes to avoid electrical contact between them but allows the permeation of electrolyte ions between the electrode and electrolyte solution while the in conventional capacitor, the electrodes are separated by an insulating dielectric material such that when a voltage is applied, the charges are kept separate by the dielectric [63,68]. ECs employ materials with high surface areas (SSA) such as carbonaceous materials with high porosity and shorter distances between the electrodes as compared to conventional capacitors [63,65,69,70]. This allows a large amount of charge to be stored leading to very high capacitances which are higher than that of conventional capacitors by several orders of magnitude [62,68]. The schematics of a conventional capacitor and EC are shown in figures 2.1 and 2.2 respectively.

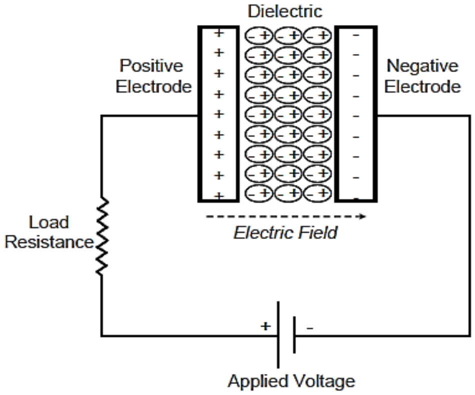

Figure 2.1: Schematic of a conventional capacitor [68]

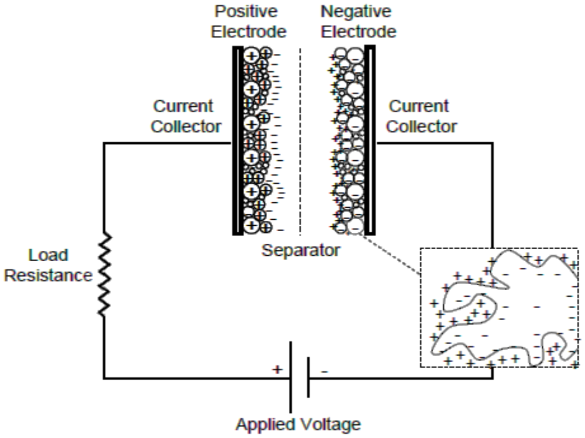

Figure2.2: Schematic of an electrochemical capacitor [68]

ECs as compared to batteries are able to undergo constant full charge-discharge cycles within few seconds with excellent cycle life in the order of 10^5 to 10^6 cycles [8,65]. ECs are able to maintain stability with excellent reversibility within a wide range of temperatures [8,62], whereas batteries which are commonly utilized because of their high energy densities (>180 Wh kg^{-1}) [5,8], are faced with the problem of irreversible phase changes in the electrode materials during the charge-discharge process which greatly reduces their life cycle. This makes the EC a choice energy storage device when high power density device coupled with fast charging and discharging within a short time duration is required [8,62,63,65]. The energy density of ECs are still however smaller than that of batteries but very high when compared to that of electrostatic and electrolytic capacitors. The outstanding power density of ECs (> 1 kW kg^{-1}) makes them superior to conventional capacitors and very complimentary to batteries and fuel cells [62]. Therefore a combination of batteries or other sources of power is still required for the supply of energy for extended period of time [15,62]. A Ragone plot which relates the power density to the energy density that is characteristic of the different energy storage or conversion system is presented in figure 2.3. The unique properties of ECs have made them useful for various applications such as in hybrid electric vehicles and trams with evidence of ability to enhance braking efficiency and battery life, adsorbents, drug delivery systems, hydrogen storage, electrochemical energy storage [2,5,42,45,47,48,71].

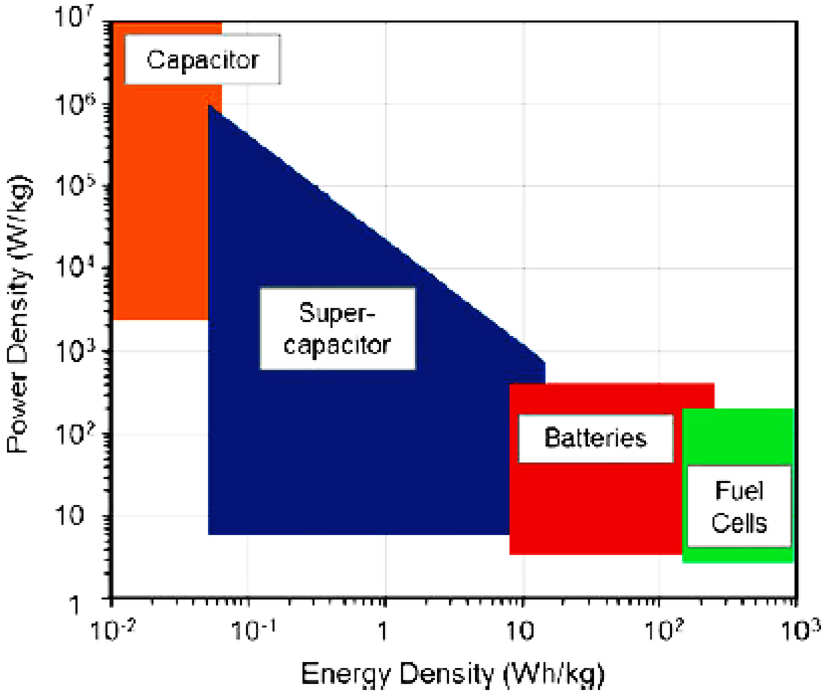

Figure 2.3 Illustration of Ragone plot relating power density to energy density of the respective energy storage or conversion system[72].

2.2 Principle of charge storage mechanisms in ECs

ECs can be grouped into three categories based on charge storage mechanism and depending on the type of material, the electrolyte or cell construction [69] namely: Electric double layer capacitors (EDLCs), faradaic capacitors and pseusocapacitors [73]. Hybrid capacitors are capacitors which combine the individual characteristic of both the EDLC and faradaic/pseudocapacitive type of electrode material in its cell design thereby optimizing their individual characteristic to boost energy density whilst retaining their power density [15,29,74]. An illustration of the different categories of ECs is presented in figure 2.4 below:

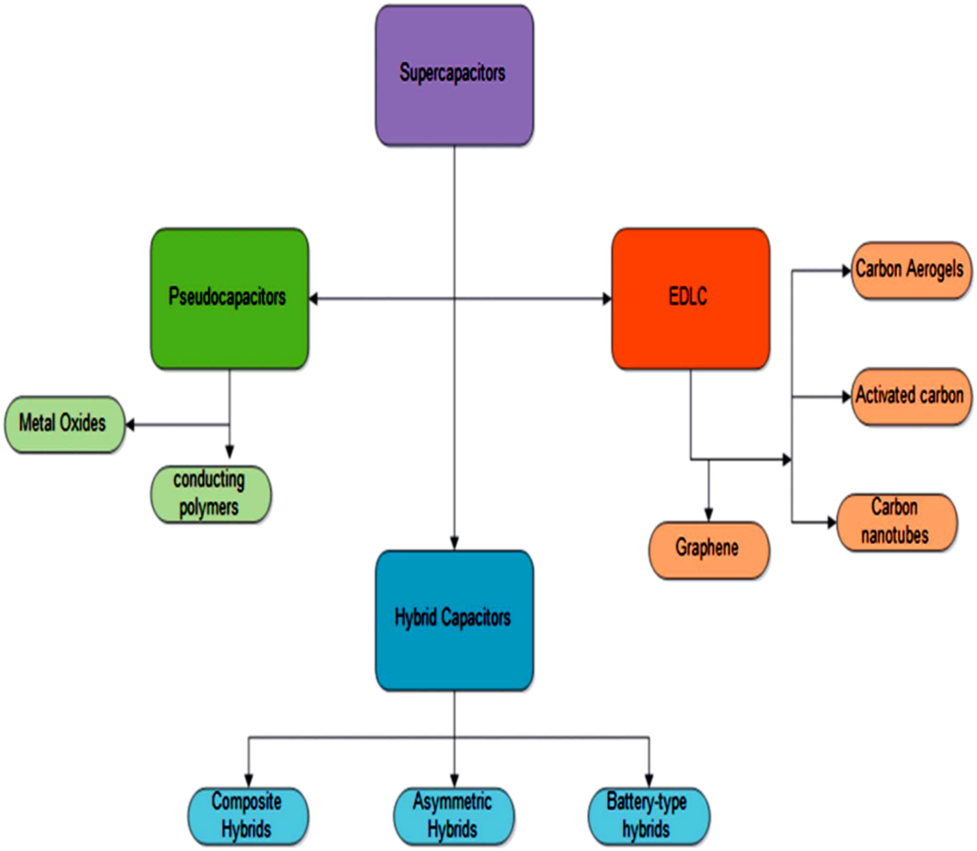

Figure 2.4 Categories of electrochemical capacitors [75]

2.2.1 Charge storage mechanism in Electric double layer capacitors (EDLCs)

EDLCs store electrical energy electrostatically at the carbon electrode/electrolyte interface forming an electrochemical double layer (Helmholtz layer) via a reversible ion adsorption on the surface of the electrode active material [69,76]. The Helmholtz model is analogous to two-plate conventional capacitors (see figure 2.1) and it states that two layers of opposite charge form at the electrode/electrolyte interface and are separated by an atomic distance [69,77] as shown in figure 2.5 (a). The capacitance C (Farad, F) which is the value of the energy stored in the capacitor can be evaluated using the double layer model by Helmholtz [63,76] which is expressed as:

$$C = \varepsilon_0 \varepsilon_r \frac{A}{d} \tag{2.1}$$

where ε_0 is the permittivity of free space, ε_r is the electrolyte dielectric constant, *A* (m^2) is the specific surface area of the electrodes, *d* (m) is the thickness of the electric double layer.

The large specific surface area (SSA) and the short charge separation distances allows for more energy to be stored. Gouy and Chapman later amended the Helmholtz model by suggesting the existence of a diffuse layer and the presence of interaction between the dipole moment of the solvent and the electrode which is a continuous distribution of ions in the electrolyte controlled by thermal motion [76,78] as seen in figure 2.5 (b). The Gouy and chapman model was also later merged with the Helmholtz model by Stern as shown in figure 2.5 (c) due to the overestimation of EDL capacitance by Gouy and chapman model.

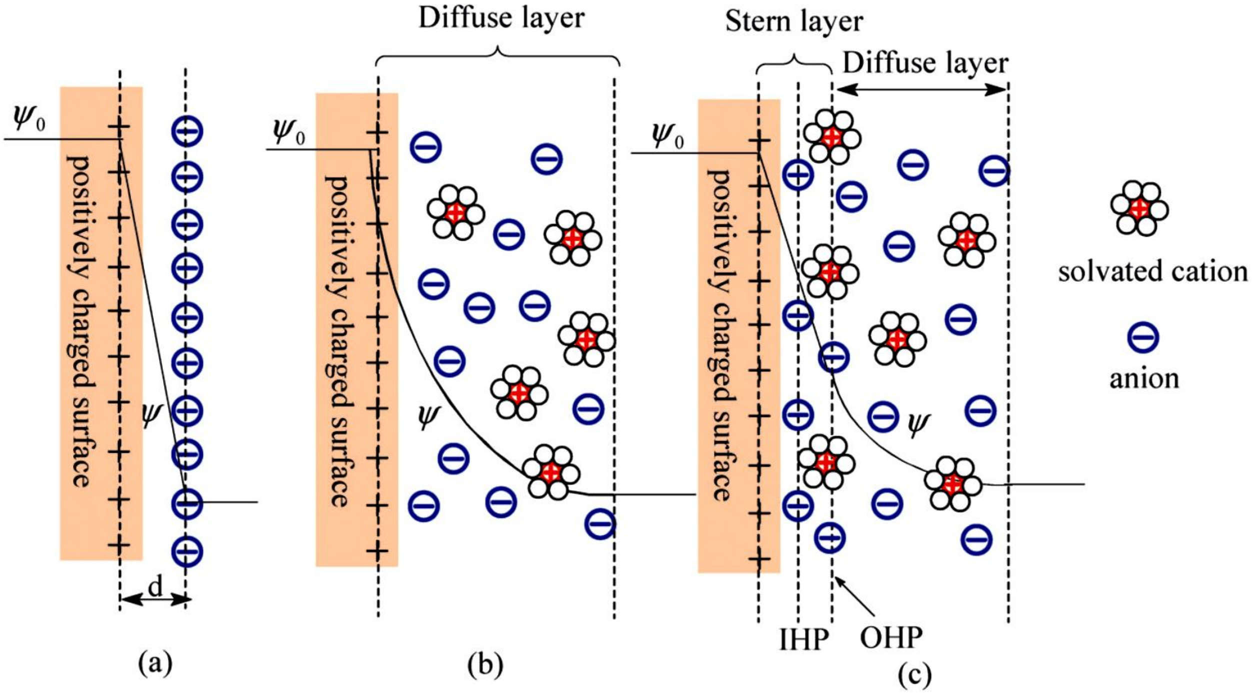

Figure 2.5 (a) Helmholtz model, (b) Gouy–Chapman model, and (c) Stern model, displaying the inner Helmholtz plane (IHP) and outer Helmholtz plane (OHP) of EDLC at a positively charged surface: [78]**.**

The Stern model, from the combination of the above two models, revealed two regions of ion distribution called the inner region (Stern or compact layer) and the diffuse layer. The compact layer is made up of adsorbed ions. These adsorbed ions are categorized into two types – the inner Helmholtz plane (IHP) and outer Helmholtz plane (OHP) [78]. Therefore, the two layers correspond to two capacitors in series with capacitance (C_H) and diffusion layer capacitance (C_D).

The EDL capacitance (C_{DL}) can be defined as the sum of the capacitances from the Helmholtz layer (C_H) and the diffusion layer capacitance (C_D) [76,78] expressed as:

$$\frac{1}{C_{DL}} = \frac{1}{C_H} + \frac{1}{C_D} \qquad 2.2$$

EDLC behavior at the plane electrode surface is determined by the type of electrolyte ion, electric fields across the electrode, solvent used for dissolving the electrolyte ions and the chemical attraction between the surface of the electrode material and the adsorbed ions. However, since the EDLC electrode is usually a porous material, the EDLC behaviour at the porous surface is more intricate than that at the plane surface. The EDLC behavior at the porous surface is determined by the ion convoluted mass transfer path, space constrain with the pores, electrolyte ohmic resistance, and the wettability of the pore surface by the electrolyte. EDLCs are often constructed using porous conductive materials such as activated carbons (ACs) such that the active material electrode is coated on the current collector separated by a thin layer separator soaked in an electrolyte. When voltage is applied, the charges at the electrodes are polarized with equal numbers of anions/cations at the electrode/electrolyte interface (see figure 2.6) [66,76].

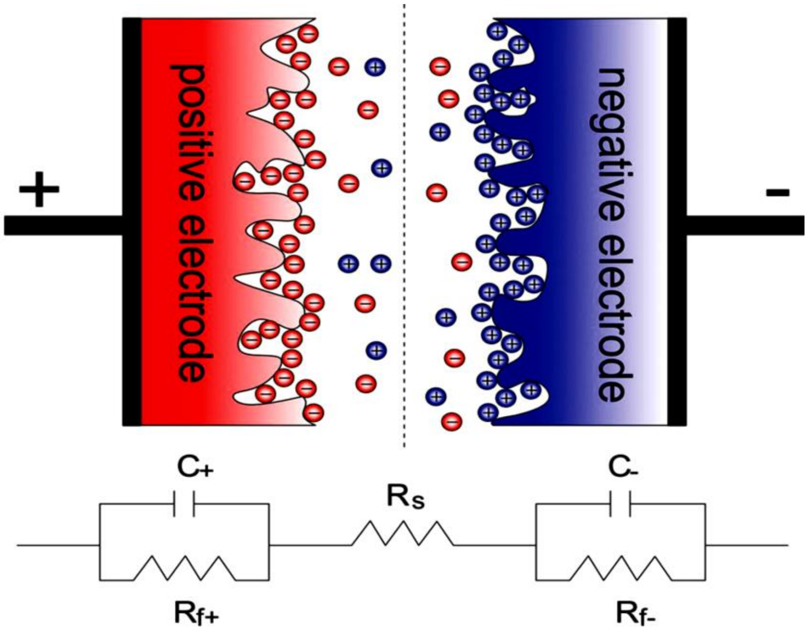

Figure 2.6 EDLC with porous electrodes in a charged state with equivalent circuit [76]

The circuit is equivalent to two capacitors $C_+$and C_-in series with total capacitance, C and can be expressed as:

$$\frac{1}{C} = \frac{1}{C_+} + \frac{1}{C_-} \qquad 2.3$$

The maximum stored energy, E and Power (P) of the single cell is expressed by the equation (2.4 and 2.5) [78,79][76]

$$E = \frac{1}{2} C \Delta V^2 \qquad 2.4$$

$$\mathrm{P} = \frac{\Delta \mathrm{V}^2}{4R_S} \qquad 2.5$$

Where C (F)is the total capacitance of the cell and R_s (Ω) is the equivalent series resistance (ESR) or solution resistance of the circuit. All the elements in the equivalent circuit are important for the overall performance of the EC. The ESR emanates from the different resistances linked with the electrode material, current collector, separator and the electrolyte solution, and the resistance at the interface between the electrode material and the electrolyte solution[15,78] . The electrolyte and the electrode material are essentially important for the performance of ECs. The cell working voltage is limited by the thermodynamic stability of the electrolyte solution.

2.2.2 Charge storage mechanism in pseudocapacitors

As compared to EDLCs, pseudocapacitors store charges through an electron transfer mechanism rather than by just the accumulation of ions at the electrochemical double layer [15,80,81]. Pseudocapacitance occurs due to charge (Δq)acceptance and change in potential (ΔV) and the derivative of *C*, corresponds to the capacitance *C*.

Pseudo-capacitance also results thermodynamic relationships that exhibits itself through absorption, oxidation/reduction and/or intercalation of ionic species [8,76,78]. The pseudocapacitance is faradaic in origin and it involves rapid and reversible redox reactions between the electrolyte and the electrode surface.

The most common pseudocapacitive electrode materials include transition metal oxides e.g MnO_2[82], transition metal nitrides e.g VN [83], conducting polymers e.g PANI [84] and carbon materials with oxygen and nitrogen containing surface functional groups [76,85]. Pseudocapacitance undergoes faradaic charge in contrast to the EDLC, and can attain higher capacitance than EDLCs, it however suffers from low power density as a result of its poor electrical conductivity and poor cycling stability [78]. The most extensively studied pseudocapacitive materials are MnO_2 and RuO_2[19]. The amorphous and crystalline forms of RuO_2 has been vastly studied in aqueous acidic electrolyte due to its high electrical conductivity, intrinsic reversibility for a variety of surface redox couples [86,87], where the amorphous ruthenium oxide ($RuO_2.xH_2O$) have displayed higher specific capacitance of 720 F g^{-1}due to the mixed proton – electron conductivity with the materials owing to the fact that superficial redox transitions of RuO_2 involve proton and the electron double injection/expulsion according to the equation 2.7 below.

Positive electrode:

$HRuO_2 \leftrightarrow H_{1-\delta} RuO_2 + \delta H^+ + \delta e^-$ 2.6

Negative electrode:

$HRuO_2 + \delta H^+ + \delta e^- \leftrightarrow H_{1-\delta} RuO_2$ 2.7

Total reaction:

$HRuO_2 + HRuO_2 \leftrightarrow H_{1-\delta} RuO_2 + H_{1-\delta} RuO_2$ 2.8

Where $0<\delta<1$, $RuO_2$and $HRuO_2$ represents the positive and negative electrodes at the fully charged states respectively. In the process, there is no net ion exchange between the electrode and the electrolyte, the electrolyte concentration may vary as a result of some polarization, EDL formation and the availability of redox reaction during the entire charge and discharge process. In a proton abundant environment (i.e. H_2SO_4) the faradaic charges can be reversibly stored and delivered through the redox transitions of the oxyruthenium groups i.e. Ru(IV)/Ru(III) and Ru(III)/Ru(II).

The theoretical capacitance of $RuO_2.xH_2O$ is in the range of ~1300 – 2200 F g^{-1}[78]. The superior and excellent electrochemical performance is as a result of its tube-like network of porous nanostructure, metallic conductivity and hydrous nature, which provides an excellent route electrolyte ion and charge transport. The hydrous nature also ensures an excellent proton exchange because of the surface of the hydrous oxide which is considered to be a hydrous liquid. However, the high cost of RuO_2 and the challenge of large scale production limits its industrial application. An inexpensive alternative that have been investigated for its pseudocapacitive characteristics is the MnO_2[8] (this metal oxide will be further discussed in section 2.4). A number of other metal oxides include iron oxide, vanadium oxide and so on. [25,88–90].

2.2.3 Hybrid electrochemical capacitors (HECs)

Hybrid electrochemical capacitors are capacitors that combine the EDLC and faradaic type capacitors. As previously described in section 2.2.1, a typical EDLC consists of two similar porous carbon electrodes (see figure 2.6). Most of the available commercial EDLCs are constructed with these symmetric porous carbon materials. The energy storage is governed by the device voltage and the ability of the electrodes to store high amounts of ion per unit electrode mass or volume repeatedly [42]. In EDLCs, the charges are stored on the surface which leads to low volumetric capacity in contrast to battery type electrodes in which the capacity results from intercalation of the ions into the bulk of the electrode. The low volumetric charge storage leads to low EDLC energy density. Furthermore, in order to improve the energy density, effort is focused on improving operating voltage, thus, emphasis is often on the use of organic electrolytes because of their ability to operate within a larger voltage window. But due to their poor conductivity as compared to aqueous electrolytes, their environmental unfriendliness and the need for purification procedures limits their use. The use of aqueous electrotrolytes becomes an obvious alternative nevertheless their limited voltage window (1 V) as a result of the thermodynamic decomposition of water leads to lower energy and power densities. Hybrid capacitors therefore, becomes a promising pathway to overcome the limiting voltage of the aqueous electrolytes by increasing the working voltage, taking advantage of the individual positive and negative electrode materials in order to improve the capacitance, energy density of the capacitor without compromising their high power density [8,42,91].

Hybrid supercapacitor designs often make use of AC and either a conducting polymer or a transition metal oxide/hydroxide or carbon nanocomposite as positive and negative electrode respectively [8]. The advantage of the hybrid design is due to the hydrogen sorption reversibility in porous carbons to provide an increase in the working voltage above the 1.23 V thermodynamic limit [8]. Carbon nanocomposites that include carbon nanotubes (CNTs) or graphene have also been utilized in hybrid asymmetric designs to enhance the energy/power density by decreasing the intrinsic resistances that add to equivalent series resistance [8].

2.3 Materials for EC electrodes

A variety materials have been widely researched on as electrode materials for ECs, which include (i) carbon materials with high SSA such as graphene, ACs, CNTs, onion-like carbons (OLCs), carbide derived carbons (CDCs), Zeolite templated carbons (ZTC), (ii) conducting polymers such as polyaniline (PANI) and polypyrrole (PPy), (iii) transition metal oxides/hydroxides such as MnO_2,RuO_2, NiO, Fe_3O_4, $Co(OH)_2$, $Ni(OH)_2$e.t.c. [27,32,40,41,81,92–95]. There are quite a number of characteristics that are desired in materials for EC application such as [8,62]:

- good conductivity,
- long cycle life ($> 10^5$),
- large SSA ($\sim$1000 to >2000m^2 g^{-1}),
- good corrosion resistance,
- mechanical resilience,
- high temperature stability,
- thermodynamic stability,
- controllable pore structure,

- good pore size distribution
- surface wettability,
- relatively low cost.

2.3.1 Carbon electrode materials

2.3.1.1 Activated carbon

Activated carbon (AC) is a type of disordered carbon with porous structure and large SSA. ACs are mainly amorphous and their network structure consists majorly of sp^2 and some sp^3 bonded atoms [5,42,79]. An example of a scanning electron microscopy image of AC is shown in figure 2.7. ACs are the most commonly used electrode material for ECs application due to their high SSA, low cost, easy production from abundant and renewable sources, good electronic conductivity and excellent cycling stability [42,78]. ACs are produced by thermal (physical) decomposition and/or chemical activation of a wide range of natural and synthetic carbonaceous precursors. Example of the natural precursors include tree barks, nutshells, seeds, coal, fruit pits, starch, leaves and grain [5,6,42,96–99]. The synthetic precursors for the production of ACs with well-developed pores with consistent properties and homogeneous microstructures include polyaniline (PANI), polyvinyl chloride (PVC), polypyrrole (PPy), expandable graphite and so on. [42,100–102]. The thermal decomposition process for the activation of AC involves the carbonization of precursors at temperatures ranging from 700-1200 °C in air, CO_2 or steam. The chemical activation process is usually performed making use of activating agents such as zinc chloride, potassium hydroxide, potassium hydrogen carbonate, potassium carbonate, sulfuric acid, Phosphoric acid and sodium hydroxide and carbonized at temperatures ranging from 400 to 900 °C [44,45,103–107].

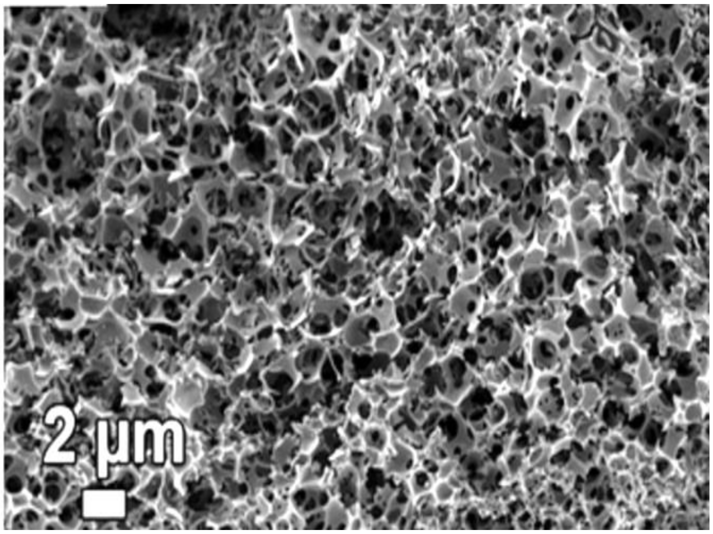

Figure 2.7 SEM image of activated carbon [3]

Most of the available commercial ECs utilize high surface area ACs with SSA ranging from 700 – 2200 m^2 g^{-1}. However low cost carbons with tunable porosities can be derived from innovative techniques offering a better control over their chemistry and pore size distribution with SSA reaching up to between 2100 - 3430 m2 g^{-1}[5,42]. However, despite extensive research on the activation of ACs, controlling the pore structure has been quite challenging with most of the pores ranging from 0.4 – 4 nm and having pore size distribution that is relatively varied that may hinder their performance in some applications [42,78]. As defined by the International Union of Pure and Applied Chemistry (IUPAC), pores can be classified as macropores when their sizes are >50 nm, mesopores when their sizes are between 2 and 50 nm and micropores when their sizes are < 2 nm [76]. An illustration of the different pore sizes in AC is presented in figure 2.8. It has been reported that high SSA plays a role in achieving high capacitance values

[76,108]but for a number of research on ACs as have been observed in literature, the trend is not quite so [78,108]. In a study on ACs having SSA as much as 3000 m^2,a specific capacitance of only about 10 $\mu F\ cm^{-2}$was recorded which is much less than the theoretical value of 15 - 25 $\mu F\ cm^{-2}$ meaning that not all the pores were accessible to the electrolyte ions hence not all pores contributed to the charge storage [10,65]. Also, this is as a result of the fact that narrow micropores may not enhance the total double layer capacitance owing to sieving effect whose magnitude depends on the size of the electrolyte ions [76,109–111]. Although micropores essentially contribute to the adsorption of ions leading to the formation of double layer, they should be electrochemically accessible to the electrolyte ions and hence the presence of mesopores is needed for the efficient ion transport to the entire electrode material permitting the extraction of energy at higher frequencies to be achieved [66]. Thus the wettability and accessibility of the porous structure with sizes fitted to the size of the electrolyte ions for effective ion transport is essential for high performance EC [66].

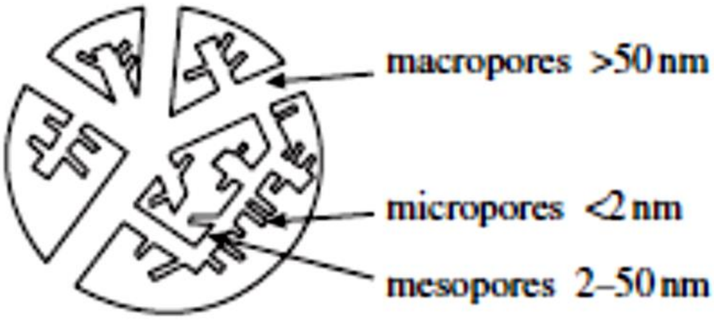

Figure 2.8 Diagramatic representation of different pore sizes in activated carbon

A relationship between the pore sizes in ACs and the electrolyte ions can be confirmed from their performance in various electrolytes. Typically, the specific capacitance values of ACs in aqueous electrolyte is between 100 to 300 F g^{-1} and $\leq$ 150 F g^{-1} in organic electrolytes [78,108]. The higher capacitance values in the aqueous medium might be as a result of the smaller size of the solvated ions and greater dielectric constant as compared to the organic medium. In a study by Raymundo-Pinero et al., it was concluded that suitable pore size is more fundamental than large SSA in AC for high electrochemical performance in various electrolytes where the optimum pore size for good capacitance is 0.7 nm and 0.8 nm for aqueous and organic electrolyte respectively [9]. Commercially available ECs however make use of organic electrolytes because of their higher operating voltages which yield higher energy densities [62]. Other important parameters for enhanced AC performance apart from large SSA include pore shape and structure, electrical conductivity, pore size distribution and surface functional groups which increase the wettability of the ions of the electrolyte on the surface of the carbon thus enhancing the pseudocapacitance [62,78,85].

2.3.1.2 Carbon nanotubes (CNTs)

Carbon nanotubes (CNTs) are allotropes of carbon with cylindrical 1-D carbon structure and a diameter in the order of a few nanometers (approximately 1/50,000th of the width of a human hair) and a length of up to several millimeters. CNTs are categorized into single-walled CNTs (SWCNTs) seamlessly rolled up into one graphitic sheet with a diameter between 0.4 and 2.5 nm and multi-walled CNTs (MWCNTs) consisting of several rolled up coaxial graphitic sheets of up to 100 nm[42,112,113]. The SEM image of CNTs and the molecular structure of SWCNTs and MWCNT are shown in figures 2.9 (a) & (b) and 2.10 respectively. CNTs are synthesized via catalyst-assisted chemical vapour deposition (CVD) techniques making use of hydrocarbon gaseous precursors such as acetylene, methane, propylene among others. As compared to ACs, zeolilte-templated carbons (ZTCs), carbide derived carbons (CDCs), CNTs possess low SSA (< 500 $m^2\ g^{-1}$) and are difficult to fabricate into thick electrodes by conventional electrode preparation techniques and maintaining the intrinsic properties on a microscopic scale is quite challenging with electrolyte-dependent capacitance performance [42][78]. However innovative preparation techniques permit the formation of vertically or horizontally aligned CNT material relative to the current collector which do not require polymeric binder [42].

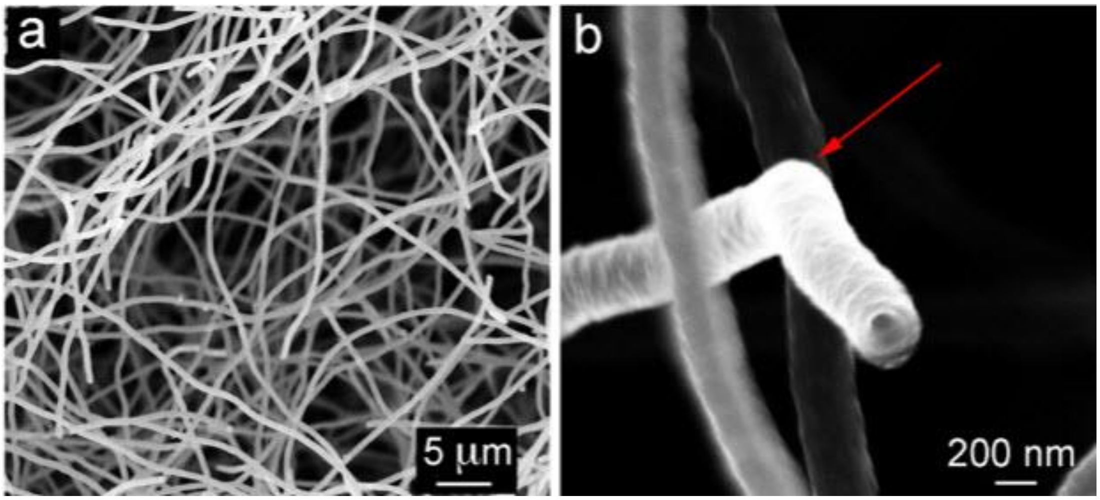

Figure 2.9 Carbon-nanotube (a) SEM micrograph spongy CNT network; (b) High magnification SEM image of a CNT highlighted by the red arrow [114]**.**

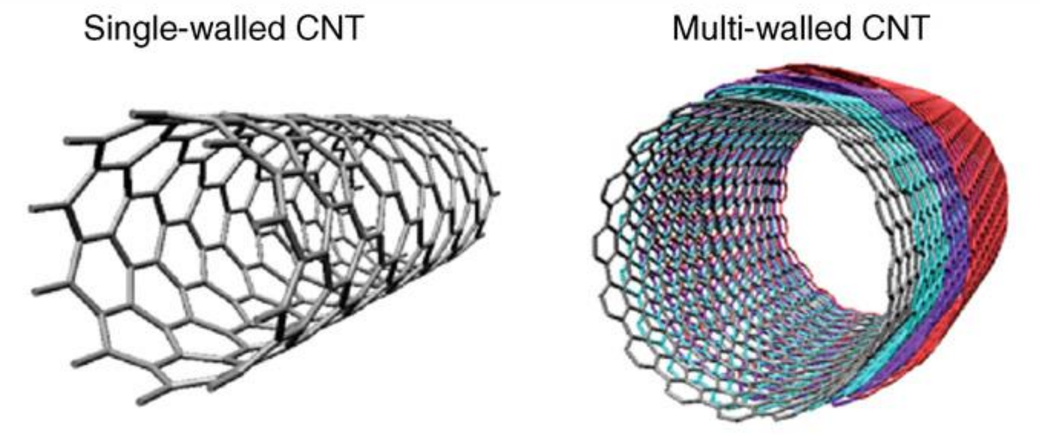

Figure 2.10 molecular structure of single-walled band multi-walled carbon nanotubes

The good electrical conductivity, high mechanical strength, open tubular network which allow for rapid and easy ion transport make them a good choice for high performance ECs and 3D carbon support for the synthesis of carbon nanocomposite materials [42,78]. The open tubular network also contributes to the lowering of the equivalent series resistance (ESR) which invariably enhances the power of the electrode. Furthermore, since the tubular structure possess excellent resiliency, their nanocomposites can easily adjust to the volumetric changes during charging and discharging cycle thus improving the cycling stability of the electrode material [108].

2.3.1.3 Graphene

Graphene is a 2-D allotrope and one-atom thick layer of graphite corresponding to the (002) basal plane of sp^2-bonded carbon atoms in a honeycomb lattice structure[42,115,116]. Its unique and outstanding properties such as good electron transport, high theoretical SSA of ~2630 m^2 g^{-1}), good thermal conductivity (~3000 W mK^{-1}), variable band gap as well as exceptional optical and mechanical characteristics have made it attractive for various application [117,118].

Graphene (2D) can be seen essentially as the basic building block of other carbon materials since it can be wrapped, rolled up or stacked to produce 0-D fullerene (Bucky ball), 1-D CNT, and 3-D graphite respectively[116,119] as illustrated in figure 2.11 . Graphene possesses qualities that are superior to other forms of carbon as shown in Table 1 [117,120–122]. A number of preparation techniques have been employed for the synthesis of graphene and graphene derivatives, such as chemical vapor deposition (CVD), microwave, Hummer's method and dispersion techniques [123–125].

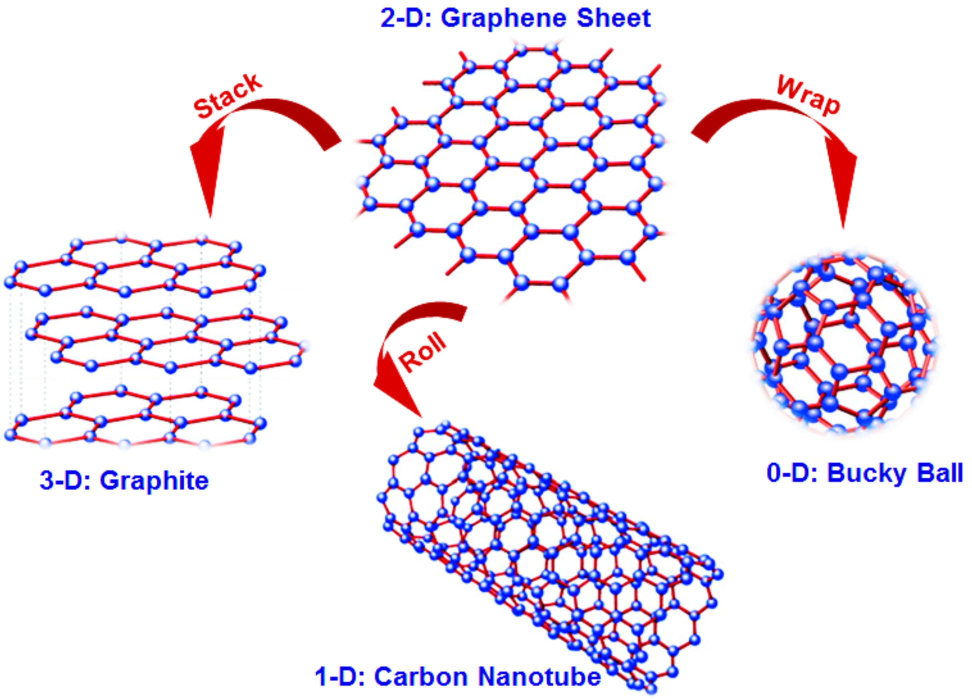

Figure 2.11Graphene the building block for 0-D fullerene, 1-D CNT, and 3-D graphite[119].

Graphene has attracted research interest as a result of its high SSA. Nevertheless, only a specific capacitance of 262 F g^{-1} has been recorded for graphene in aqueous electrolytes [126–

128] , owing to the restacking of graphene as a result of the π-π interactions between the graphene sheets leading to the inaccessibility of the available surface area. The restacking of graphene can be overcome by embedding the sheets with pseudocapacitive materials or by functionalizing it with chemical components such as hydroxyl or carbonyl groups [13,28,129–132].

Table 1 Comparison of graphene with other allotropes of carbon [150]

Allotropes of carbon	**Graphite**	**Diamond**	**Fullerene**	**Carbon nanotubes**	**Graphene**
Dimensionality	Three	Three	Zero	One	Two
Hybridization	Sp^2	Sp^3	mainly Sp^2	mainly Sp^2	Sp^2
Crystal system	Hexagonal	Octahedral	Tetragonal	Icosahedral	Hexagonal
Experimental specific surface area (m^2g^{-1})	~10-20	~20-160	~80-90	~1300	~2675
Density (gcm^{-3})	2.09-2.23	3.5-3.53	1.72	>1	>1
Electrical conductivity ($S\ cm^{-1}$)	Anisotropic $2,3\times104^{a}$, 2.3×106^{b}		10^{-10}	Depends on the particular structure	2000
Electronic properties	Conductor	Insulator, semiconductor	Insulator	Depends on structure. Can be metallic or semiconducting	Semimetal, zero gap semiconductor
Thermal conductivity ($W\ m^{-1}\ K^{-1}$)	1500-2000[a] 5-10[c]	900-2320	0.4	3500	4848-5300
Hardness tenacity	High	Ultrahigh	Highly elastic	High flexible elastic	Highest flexible elastic (single layer)
Optical properties	Uniaxial	Isotropic	Non-linear optical response	Structural dependent	97.7% optical transmittance
[a]a-direction **[b]c-direction**					

2.4 Faradaic materials

2.4.1 Transition metal oxides (TMOs)

Transition metals are d-block elements and are in the group 3 to group 12 of the periodic table. They are all metals and the valence shell electrons are located in the d-orbital and are loosely bound. The transition metals have low ionization potentials and show varied oxidation states and can form various types of compounds because of their varied oxidation states. The transition metal oxidation states at particular voltages give rise to a local or constant charge depending on the number of redox couples within the defined operating potential [8]. The electrochemical performance of TMOs depends on their electrical conductivity which can vary not only among the various metals but also among the polymorphs of each metals that can be synthesized by a variety of methods with some being more conductive than the others [8].

Different TMOs have been investigated including RuO_2, V_2O_5, SnO_2, Fe_3O_4, NiO, Co_3O_4 and MnO_2. As stated earlier, RuO_2 has been studied for its high theoretical capacitance of ~2000 F g^{-1}, excellent stability, high electrical conductivity, high rate capability and excellent reversibility. However, as earlier stated in section 2.2.2, research towards a cheaper, more environmentally friendly alternative makes MnO_2 and other metal oxides a better choice [8,133,134]. MnO_2 have different polymorphs with unique crystallographic structures (α, β, γ, δ andλ). The Birnessite-type manganese dioxide, δ -MnO_2, displays crystalline layered structures with layers of edge-sharing MnO_6 octahedral to contain water molecules or cations of other elements at the interlayer spacing. This layered structure of δ-MnO_2 allows ion intercalation within the interlayer channel while the 2D morphology encourages surface-dependent electrochemical reactions appropriate for energy storage applications, particularly in ECs [133]. Other types of MnO_2 also show good electrochemical performance even though they do not possess layered structures. Charge storage in Mn oxides is generally through the reaction equations 2.10 and 2.11 [133,134].equation 2.10 involves the insertion of electrolyte cations into the bulk of the MnO_2 electrode while equation 2.11 involves surface adsorption of electrolyte cations on the MnO_2electrode[133]:

$$MnO_2 + C^+ + e^- \leftrightarrow MnOOC \qquad 2.9$$

$$(MnO_2)_{surface} + C^+ + e^- \leftrightarrow (MnOOC)_{surface} \qquad 2.10$$

Where C^+ represents (H^+, Li^+, Na^+, and K^+) electrolyte cations (from acid or neutral electrolyte) and both mechanisms involve a redox reaction between the Mn^{3+} and Mn^{4+} oxidation states [133].

With respect to the intercalation mechanism, the variations in valencestate of $MnO_2$are due to the intercalation of electrolyte cations into the crystalline lattice of the layered structure, leading to lattice expansion which induces the reduction of Mn^{4+} to Mn^{3+}. On the other hand, the interfacial reaction causes a change in the oxidation states of manganese (Mn^{4+} to Mn^{3+}) while the electrolyte cations play a role in maintaining the charge balance of manganese oxides. In spite of the relatively high capacitance of MnO_2, the practical application of MnO_2 is limited by its specific capacitance which is lower than 350 F g^{-1}as compared to RuO_2.This poor specific capacitance and rate capability of MnO_2 electrode are due to its poor electric conductivity and electrochemical dissolution during cycling. In order to enhance the electrical conductivity and charge storage ability, the hybridization of$MnO_2$with other materials like carbonaceous or conducting polymers to form compounds which can introduce more defects and charge carriers to improve the conductivity of MnO_2 nanostructured composites are both practicable methods[133,134]. Examples of such composites include MnO_2/graphene [135], MnO_2/CNT [136], MnO_2/PANI [137], MnO_2/carbon nanofibers[138].

2.4.2 Layered double hydroxides (LDHs)

Layered double hydroxides (LDH) also referred to as hydrotalcite-like compounds or anionic clays are a type of lamellar compounds which have the general formula $M^{2+}{}_{1-x}M^{3+}{}_{x}(OH)_2.(A^{n-})_{x/n}.mH_2O$, where $M^{2+}$are bivalent cations such as Mg^{2+},Co^{2+}, Ni^{2+}, Cu^{2+}, Zn^{2+}, etc, M^{3+} are trivalent metal cations such as Al^{3+}, Cr^{3+}, Co^{3+}, Ga^{3+} and A^{n-} is an n-valent anion such as Cl^-, $CO_3{}^{2-}$. [57,139]. Structurally, adjacent layers of positively charged octahedral burcite-like layers, $M(OH)_2$, are held by negatively charged anions located at interlayer positions[134].LDHs have drawn the interest of researchers because they also offer the advantage of low cost, minimal toxicity, flexile structure and morphology and have excellent anion-exchange capability which have potential for high performance EC application[134].

2.5 Carbon based nanocomposites

Pseudocapacitive materials play an important role in the fabrication of ECs with increased voltage and energy storage capacity. The peudocapacitance majorly comes from redox reactions at the surface thus only a very thin surface layer is involved actively in the faradaic process [78]. Also, the poor electrical conductivity and cycling stability of TMOs, e.g. MnO_2 limits their application as electrode materials. Thus, the synthesis of nanocomposites using carbon supports helps to increase the electrical conductivity and mechanical strength of the nanocomposite. Composite materials are a means of obtaining materials with enhanced performance, by combining the varied properties of the individual materials in order to exploit the advantages and overcome the limitations of the non-faradaic (EDLC) and faradaic material respectively. A number of studies have reported the enhanced electrochemical properties of composite materials using different carbon materials as support such as zeolite templated carbon (ZTC) [39], onion-like carbon [18][41], and CNT [140]. For example, CNTs have been reported to be an effective support for TMOs and CPs due to their open tube-like mesoporous structure and excellent electrical/mechanical properties [78]. In a study conducted by Zhang et al, CNT array were employed as carbon support to synthesize PANI-CNT composite and manganese oxide–CNT hierarchical porous nanocomposites. From the studies a high specific capacitance of ~1000 F g^{-1} was recorded for the PANI-CNT composite with good cycling stability and 95 % capacity retention at 118 A g^{-1} and a specific capacitance of 101 F g^{-1} at specific current of 77 A g^{-1} with good cycling stability was recorded for manganese oxide–CNT hierarchical porous nanocomposites [78]. Apart from manganese oxides, the merits of using CNTs as supports for the synthesis of composite materials have been reported for other metal oxides such as iron, cobalt, vanadium and nickel oxides [76].

2.6 Electrolytes for ECs

Electrolytes utilized in ECs are aqueous, organic, or ionic liquids. The two main parameters for the choice of an electrolyte are the electrochemical stability potential window and the ionic conductivity. This is important to maximize the specific energy values and to enhance power values respectively. The choice of electrolytes also influences ionic concentration, solvated ionic radius, toxicity, resistivity and cost of the ECs[76,141].

2.6.1 Aqueous electrolytes

Aqueous electrolytes such as acidic, alkali and neutral electrolytes e.g. H_2SO_4, KOH and Li_2SO_4 respectively, are often utilized in ECs because of their high conductivity as compared to organic electrolytes leading to better power performance. Acidic and alkali aqueous electrolytes have conductivity as high as $\sim$1 S cm^{-1}. However, due to the thermodynamic stability window of water which is 1.23 V, the operating potential is relatively low ($\sim$1 V), consequently, the energy storage capability is reduced. However, the operating potential window of carbon based hybrid ECs in acidic and alkaline aqueous electrolytes can be increased to 1.6 V by using different optimized carbons as positive and negative electrodes (or metal oxides/hydroxides). Also, aqueous neutral electrolytes have been reported to reach voltage values up to 2 V in symmetric AC capacitors and in asymmetric capacitors with an AC negative electrode and a positive electrode from transition metal oxide, for e.g. MnO_2, with good charge-discharge stability[76].

2.6.2 Organic electrolytes

Organic electrolytes are mostly utilized in commercial supercapacitor because of the wide operating potential window in the range of 2.7 – 2.8 V compared to aqueous solutions. However, their ionic conductivity and the specific capacitance (100 –150 F g^{-1}) are lower than those of aqueous electrolytes. The high operating voltage lets ECs using organic electrolytes to deliver a higher specific energy than aqueous systems. The most commonly used solvents in ECs are Propylene carbonate (PC) and acetonitrile (AN). However, due to the high viscosity of PC, the electrochemical performance of ECs prepared with PC is more sensitive to temperature variations compared to AN[76]. Salts generally utilized in organic electrolytes are quaternary ammonium salts. Among these salts, tetraethylammonium tetrafluoroborate (TEA-BF_4) is the most commonly used salt for commercial ECs. Selecting the appropriate salt is important in optimizing the conductivity of the electrolytes. However, due to high costs, EMIM-BF_4 (1-ethyl-3-methylimidazolium tetrafluoroborate) or MEPY-BF_4(1-ethyl-1-methylpyrrolidinium tetrafluoroborate) are presently not appropriate for industrial applications.As an alternative, it is promising to use TEMA-BF_4 (triethylmethylammonium tetrafluoroborate) at higher concentrations (2 M) thereby producing higher ionic conductivities and circumventing ion diminution during charging of large cells at high power. A different salt, TMPY-BF_4 (tetramethylene-pyrrolidinium tetrafluoroborate), shows higher solubility in propylene carbonate which translates to a higher ionic conductivity, and it is presently used commercially [76].

2.6.3 Ionic Liquids (ILs)

Ionic liquids (ILs) are molten salts at room temperature. ILs require no solvent and have quite a number of good properties which include low vapour pressure, stability at increased temperatures surpassing the ∼80 °C limit of organic electrolytes, wide thermodynamic stability window which seems larger to that of organic solvents. However, the ionic conductivity of ILs, especially at room temperature, is generally lower than that of organic electrolytes, therefore limiting the power performance of IL-based supercapacitors [76]. Examples of the ionic liquids are pyrrolidinium, imidazolium, aliphatic ammonium salts such as tetrafluoroborate, trifluoromethanesulfonate, bis(trifluoromethanesulfonyl)imide, bis(fluorosulonyl)mide, or hexafluorophosphate, cyclic amines such as aromatic pyridinium and saturated hexafluorophosphate or hexafluorophosphate and saturated piperidinium, pyrrolidinium[142–145] .

2.7 Electrochemical measurement

2.7.1 Electrode Fabrication

To prepare electrode for testing, the active EC material (which may be any EDLCs, faradaic or pseudocapacitive material) is thoroughly mixed with a conductive agent (carbon or acetylene black) to enhance the conductivity of the electrode materials, a binder (polytetrafluoroethylene (PTFE) or polyvinylidene fluoride (PVDF) and N-methyl-2-pyrolidone (NMP) solvent is added dropwise to form a slurry. The paste is then coated on a current collector made from materials of good electronic conductivity and excellent corrosion resistance such as gold, nickel foam, carbon cloth or paper [38,146]. The thickness of the electrode is determined by the type of the electrode material and application, which is usually tens of micrometers and sub-millimeters. The fabricated electrode is referred to as a working electrode (WE).

2.7.2 Electrode material testing

Electrochemical testing of electrode materials can be carried out in a three-electrode or two-electrode configurations for the single or half-cell and full cell electrode respectively. Three-electrode configuration is mainly used for material investigation. It is largely used to determine the electrochemical performance characteristics of an active material such as specific capacitance or capacity, working potential, material resistance and so on. The three-electrode configuration (as shown in figure 2.12) is made up of the working electrode (WE), counter electrode (CE) and reference electrode (RE). The WE is made up of the active material being investigated and is usually pasted on current collectors and is the point where the electrochemical reaction takes place. The CE permits the generation of the needed amount of current at the WE by changing its potential within the electrolyte solution. The CE is typically made from chemically inert materials with good conductivity such as platinum, glassy or vitreous carbon. The RE functions as the point where the WE potential is measured and regulated by restricting the flow of much current through it.The measurement is usually made with an appropriate electrolyte. The electrolyte medium used often determines the choice of the RE. The choice of the RE is critical to the realization of the objective of the electrode material testing. For example, mercury/mercury oxide (Hg/HgO) or silver/silver chloride (Ag/AgCl) are utilized in aqueous alkaline and neutral electrolytes respectively while saturated calomel electrode (SCE) or Ag/AgCl are utilized in many non-aqueous media such as acetic acid [147–149].

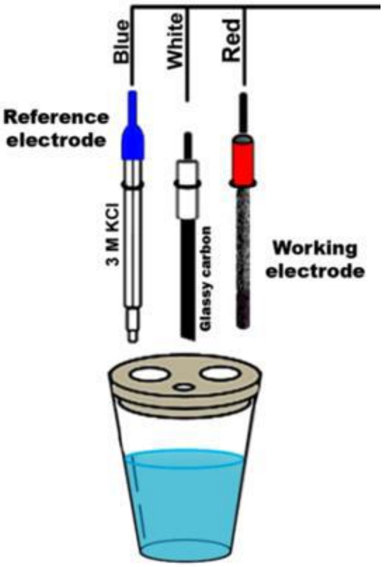

Figure 2.12. Diagram showing three electrode configuration [150]

The two-electrode configuration is mainly used for the measurement ofthe electrochemical performance of a full cell device. In the two electrode configuration, the WE is connected on the positive while the RE and CE are connected together as a second electrode on the negative as shown in figure 2.13. In the testing of symmetric or asymmetric working electrodes, the electrodes are soaked in an electrolyte and separated by a separator. The working potential of the two electrodes is controlled and parameters such as energy density, power density, and cycle life can be evaluated [151].

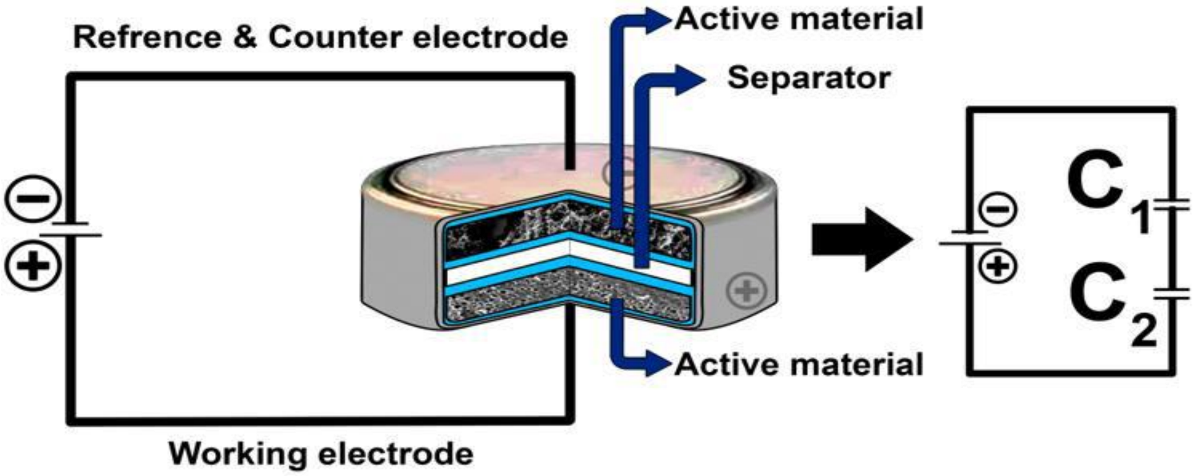

Figure 2.13. Diagram showing two-electrode configuration [150]

2.7.3 Electrochemical evaluation of electrode materials

2.7.3.1 Cyclic Voltammetry (CV)

Cyclic voltammetry (CV) is an electrochemical measurement technique generally employed for the assessment of thermodynamic and electron transference dynamics of the EC at the interface of the active material electrode and the electrolyte. A typical representation CV curves is as shown in figure 2.14. It is a very important means of studying the surface reactions of the active material. Different types of materials generate CV curves typical of the electrochemical behavior of such material. In a reversible electrochemical process, EDLCs material is typically rectangular in shape, while, faradaic capacitors have a shape that is characterized by anodic and cathodic peaks. Ideally, a peak voltage difference between the anodic and current cathodic peaks of ~ 59 mV are observed. The peak positions do not vary with respect to increase in scan rate, and the ratio of the peak currents should also be unity for a reversible electrochemical process. CV is useful for both half-cell and full-cell electrode testing in three-and two-electrode configurations respectively.

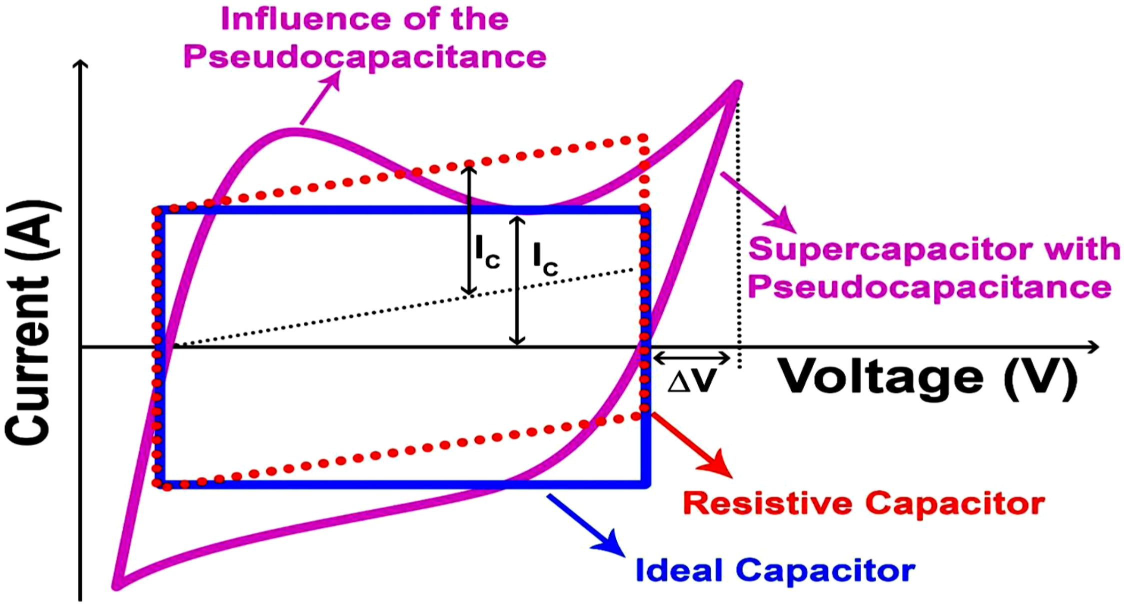

Figure 2.14.Cyclic voltammetry diagram showing the differences between the EDLCs (rectangular shape) and Faradaic (Curved shape with cathodic and anodic peaks)[152]

In CV measurement, the electrochemical cell testing is determined in a specific operating potential, where the potential is applied to the working electrode and measured at various scan rates.The cathodic and anodic current responses at the various scan rates is beneficial in determining the electrochemical characteristics of the electrode. The following equation (2.12) is employed for the evaluation of the specific capacitance (C_s) from the CV curve for both faradic and non-faradic materials [153].

$$C_s = \frac{1}{mv\,(V_a - V_b)} \int_{V_a}^{V_b} I\,(V)dV \qquad 2.11$$

Where m (g) is the mass of the electrode, v is the scan rate, $V_a - V_b$ is the cell potential window and $\int I\ (V) dV$ is the integrated area under the curve[153]

2.7.3.2 Galvanostatic charge – discharge (GCD)

Galvanostatic charge-discharge (GCD) is a technique for the study of electrochemical performance of an electrode material. Typically, an upper and lower voltage limits are set, and a constant current *I* (positive in charge or negative in discharge), and voltage as a function of time is recorded between the minimum and maximum voltage [154]. The next GCD cycle commences once a fixed lower voltage is reached. A reverse in current subsequently follows and leads to the decrease of the voltage to its lower limit. A diagrammatic representation of a typical GCD curve is as shown in Figure 2.15, indicating (1) the cell performance during charging, (2) the cell performance during discharging, (3) the initial process, and (4) Ohmic potential drop, associated with the negative resistive ohmic loss due to cell resistance. However, different materials present a CV shape characteristic of the electrochemical behaviour of that material. For example, EDLC materials e.g activated carbon (AC) present a linear GCD curve ensuing from equal charge distributions during the charge and discharge processes. While faradaic material display non-linear GCD curve (See Figure 2.16, Curve B) originating from the redox GCD process. Specific capacitance (C_s) of electrode material (non-EDLC material) can be evaluated from the GCD curve using the following equation [58,155,156]:

$$C_s = \frac{2I_d}{V^2} \int V(t) dt \qquad 2.12$$

Where I_d (A g^{-1}) is the current density, Δt (s) is the discharge time, V (V) is maximum cell voltage.

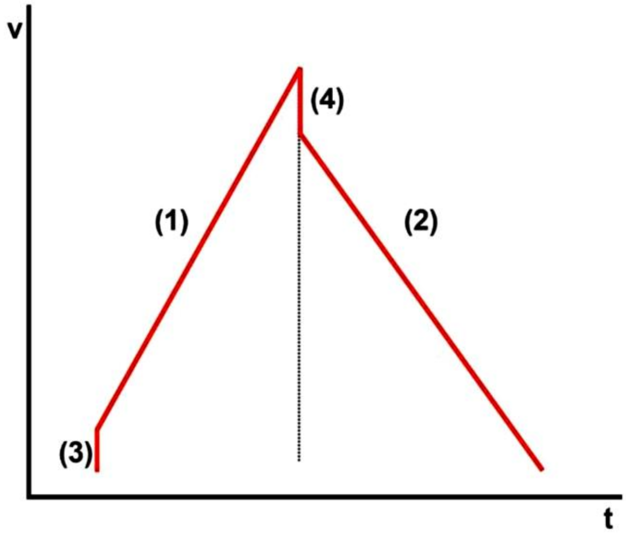

Figure 2.15 Diagrammatic representation of galvanostatic charge-discharge (GCD) process[152]**.**

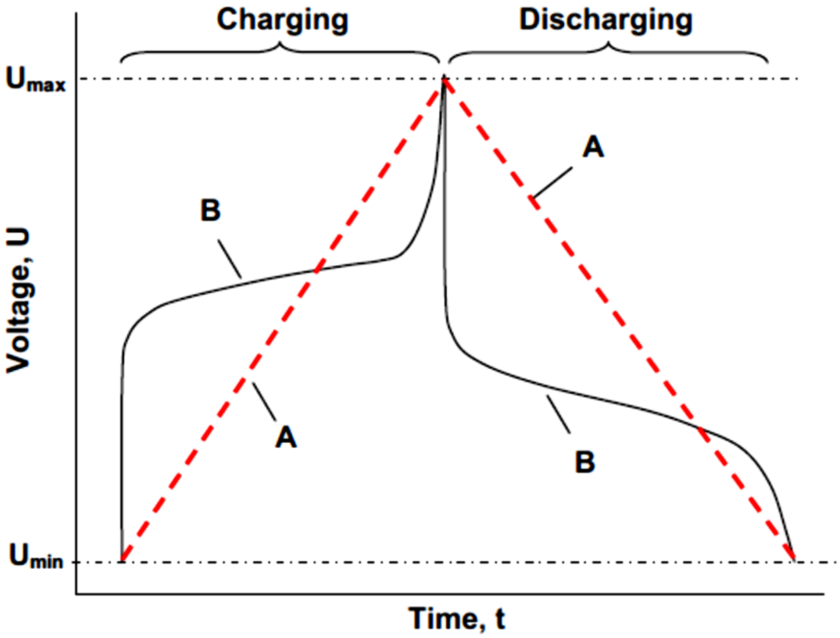

Figure2.16 Diagrammatic representation of EDLC galvanostatic charge-discharge (GCD) process (curve A) and faradaic charge-discharge process (curve B) [157]

But in EDLC materials, the C_s is calculated from the slope of the linear GCD curve using the equation [79]:

$$C_s = \frac{I_d \Delta t}{\Delta V} \tag{2.13}$$

For an electrode exhibiting battery-like or faradaic GCD curve, the specific discharge capacity, $Q_D$can be evaluated from the following equation[79]:

$$Q_D = \frac{It}{m \times 3.6} \tag{2.14}$$

where Q_D is the specific discharge capacity (mA h g^{-1}), t(s) is the discharge duration, I(A) is the current (mA), and m(g) is the mass of the electrode.

2.7.3.3 Electrochemical impedance spectroscopy (EIS) analysis

The electrochemical impedance spectroscopy (EIS) is an important technique for the evaluation of electron and ion transport in an electrochemical cell. It is studied in an open circuit potential at different frequencies, for example from 10 millihertz (mHz) to 100 kilohertz (KHz). EIS can be used to study various parameters such as resistance, capacitance, and inductance. Typically, the impedance of an electrochemical cell over a frequency range is studied by applying a low amplitude voltage (e.g 5 mV) on a steady potential. The Nyquist and the Bode plot is often used to represent the EIS data. The Bode plot is a plot of the phase angle as a function of the applied frequency while the Nyquist plot describes the real ($z'(\omega)$) and the imaginary ($z''(\omega)$) parts of the impedance on the complex plane. An illustration of a Nyquist impedance plot is shown in figure 2.17. The Nyquist plot is divided into high, medium and low frequency regions [158]. The high frequency region indicates the resistive components (R_s) at the intersection of the curve with the real $(z'(\omega))$ axis. At the high to middle frequency region, the diameter of the semicircular arc indicates the presence of charge transfer resistance (R_{ct}) related to a resistive element existing in the electrode. While at the low frequency region, a nearly vertical line parallel to the y-axis show ideal capacitive behaviors, however, the line somewhat deviates from the vertical at angles in-between 45°- 90° as a result of the diffusion process of ions. The intersection of each semi-circular arc with the real Z'-axis shows the solution resistance (Rs) or the equivalent series resistance (ESR) which is a summation of overall interface resistance of electrolyte/electrode material intrinsic resistance and electrode material/e current collector[158,159].

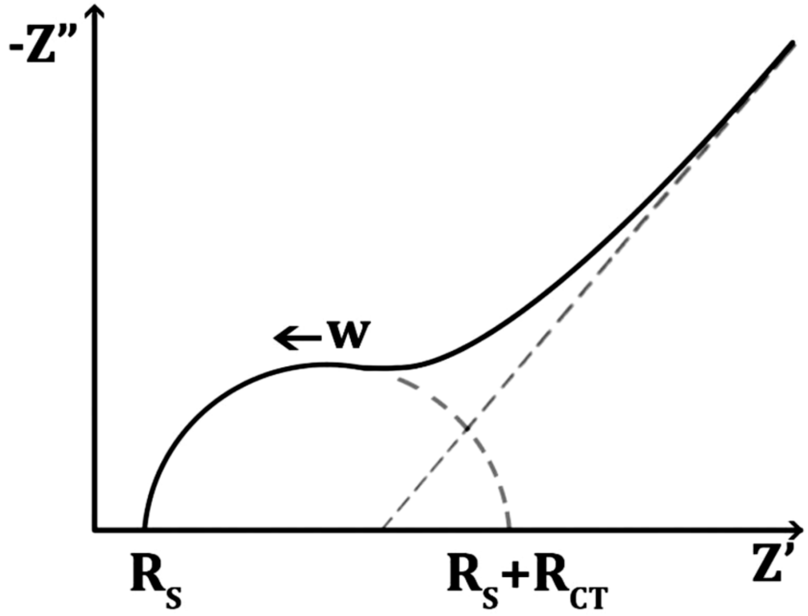

Figure 2.17 Nyquist impedance plot

In the low frequency region, the capacitance (C (ω)) can be described as sum of the real $(C'(\omega))$ and imaginary $(C''(\omega))$ parts of the capacitance as a function of frequency. That is [158]:

$$C(\omega) = C'(\omega) + jC''(\omega) \qquad 2.15$$

$$C'(\omega) = \frac{-Z'(\omega)}{\omega|Z(\omega)|^2} \qquad 2.16$$

$$C'^{\prime(\omega)} = \frac{-Z''(\omega)}{\omega|Z(\omega)|^2} \qquad 2.17$$

Where the low frequency value $C'(\omega)$ corresponds to the capacitance of the cell obtained during the constant current discharge. $C''(\omega)$ corresponds to an energy dissipation by an irreversible process that can lead to hysteresis, $Z|(\omega)|$ is the impedance modulus, ω is the angular frequency [158]. A relaxation time τcan be evaluated from the knee frequency in the real and imaginary of the capacitance plot by applying the equation: τ = 1/f**,** where f is the frequency of the electrochemical cell, corresponding to the maximum on the C'' (ω) curve as a function of frequency plot and τ is the time needed for the stored energy to be delivered. This represents the boundary between a pure capacitive and resistive behavior of the ECs electrode.

The Bode plot highlights the relationship between the frequency and the imaginary parts of the impedance($z''(\omega)$), and the capacitance of the material can be deduced from the linear portion of a graph of log *Z''* against log *f* by applying the equation:

$$C = \frac{1}{2\pi f|Z''|} \qquad 2.18$$

Where C is the capacitance (F), f is the frequency and *Z''* is the imaginary impedance.

2.7.3.4 Stability test

The cycling performance or stability of an electrode material can be tested by charging and discharging for an infinite number of cycles. The stability of an electrochemical cell is dependent on the particular conditions under which cycling is performed for example voltage limits, temperature, current applied, all play a role during cycling[160]. Typically, cyclic stability is performed from GCD cycles. The coulombic efficiency η, can be determined from the following equation[79]:

$$\eta = \frac{t_D}{t_C} \times 100\% \tag{2.19}$$

Where t_D (s) is the discharge time, t_C (s) is the charge time.

2.7.3.5 Voltage holding

Voltage holding (or floating) test is another reliable method for testing the stability of EC electrodes. Voltage holding test is done at a constant load by holding the electrode at maximum voltage and determining the capacitance over an entire time period which is based on a potentiostaic mode and gavanostatic charge discharge which is reiterated over the period.

Voltage holding is very useful technique for stability testing because it provides a direct understanding into the probable degradation that occurs during electrochemical process in EDLCs at high cell voltages as compared to long-duration cycling test which at times displays no degradation. A true resistance effect is also observed after exposing the electrode to maximum voltage which is as close as possible to real or practical application [38,161,162].

2.7.3.6 Self discharge

ECs as energy storage devices store energy for durations ranging from few seconds to several days. The factor responsible for the energy storage duration of ECs is its self-discharge rate. Self-discharge of ECs is the slow reduction in the voltage across the capacitor that take place when the capacitor is left unconnected to an electrical load. In order to measure the self-discharge currents, the capacitors are charged for several hours, and then left without an electrical load to discharge. The objective of the self-discharge test is to estimate the energy loss over the test duration and to determine the drop in the voltage of the capacitor[163].

2.8 Electrochemical device Fabrication

2.8.1 Symmetrical cell design

A Symmetrical EC cell is a cell in which both the positive and negative electrode are the same material, have equal mass, thickness and size. In symmetric capacitors, the total capacitance is equivalent to half the value of a single electrode, that is if $C_1 = C_2$ then, $C_{Total} = C/2$ [76,164]. The Specific capacitance of the cell forEDLC material can be evaluated from the GCD curve as discussed in section 2.6.3.2 using the equation:

$$C_s = 4.\frac{I\Delta t}{m\Delta V} \qquad 2.20$$

The factor 4 is normalization to the mass of a single electrode for the two similar capacitors in series.

The specific energy (or energy density), E (Wh kg^{-1}) of the EC is given by:

$$E = C\frac{1}{2}\Delta V^2 = \frac{1000\times C_s \times \Delta V^2}{2\times 4\times 3600} = \frac{C_s \Delta V^2}{28.8} \quad 2.21$$

And the power density P_d(W kg^{-1}) can be evaluated using:

$$P_d = \frac{3600\times\Delta E}{\Delta t\times 1000} = \frac{3.6\times\Delta E}{\Delta t} \quad 2.22$$

For faradic material the energy density is evaluated using the equation 2.24 [165]:

$$E = \frac{I_d}{3.6}\int V(t)dt \quad 2.23$$

Where I_d (A g^{-1}) is the specific current, Δt (s) is the discharge time, V (V) is maximum cell voltage, $\int V(t)dt$ is area under the discharge curve.

While power density is evaluated same as for EDLC material using equation 2.22 above.

2.8.2 Asymmetrical (Hybrid) cell design

Asymmetric (Hybrid) capacitors in which the positive electrode and negative electrode are made of two distinct materials. The electrodes are of different capacitance values such that one capacitance is larger than the other. In the fabrication of an asymmetric cell, charges on both electrodes are taken into consideration and the charges on the electrodes are balanced using the equation

$$Q_+ = Q_- \quad 2.24$$

where Q_+ and Q_- are the charges stored in the positive and negative electrodes respectively for EDLC materials and Q is expressed by the following equation:

$$Q = C_s m\Delta V \quad 2.25$$

where C_s is the specific capacitance of the electrode, m(g) is the mass of the electrode and ΔV is the cell maximum voltage. The mass balancing is therefore achieved by applying the following equation:

$$\frac{m_+}{m_-} = \frac{C_{s-}\Delta V_-}{C_{s+}\Delta V_+} \tag{2.26}$$

The mass balancing helps to ensure that equal charge exists on both electrodes, thus the cell have similar behavior of a symmetric cell. The specific capacitance, energy, and power densities of the cell can therefore be estimated by applying equations 2.16 -2.18 without normalization with the factor of 4.

For purely faradic or materials with battery-like behavior and where both electrodes are purely faradic,the mass balancing is achieved using the following equation:

$$\frac{m_+}{m_-} = \frac{(I.t_d)_-}{(I.t_d)_+} \tag{2.27}$$

Where m+ and m- are the mass of the positive and negative electrodes, $\frac{(I.t_d)_-}{3.6}$and $\frac{(I.t_d)_+}{3.6}$are the specific capacity of the electrodes.

While for an asymmetric device where the positive electrodes is a faradic material and the negative electrode is an EDLC material, the mass balancing is achieved by using the equation below:

$$\frac{m_+}{m_-} = \frac{C_{s-}\Delta V_-}{Q_{D+}\Delta V_+} \tag{2.28}$$

Where m+ and m- are the mass of the positive and negative electrodes,$C_{s-}$is the specific capacitance of the EDLC material, $Q_{D+}$is the specific capacity of the faradic material**,** $\Delta V_-$and $\Delta V_+$are maximum voltage of the EDLC and faradic electrodes respectively.

CHAPTER THREE

3.0 EXPERIMENTAL DETAILS AND CHARACTERIZATION TECHNIQUES

In this chapter, the material synthesis techniques, the experimental procedures/details of each material synthesized and characterization techniques used for the analysis of samples will be discussed.

3.1 Material Synthesis techniques

3.1.1 Hydro/solvothermal synthesis technique

The term hydrothermal originated from the field of geology. The term was first used by the British geologist Sir Roderick Murchuson to explain the action of water at elevated temperatures and pressure in bringing about changes in the earth's crust and leading to the formation of various rocks and minerals [166]. The first hydrothermal synthesis reported in literature was by Schafhault in 1845. The commercial value of the hydrothermal technique for the synthesis of inorganic compounds was realized when large scale quartz crystal was synthesized by Nacken (1946) and Zeolites by Barrer (1948) [166].

Hydrothermal synthesis generally involves the growth or synthesis of crystals from any heterogeneous reaction in the presence of aqueous solvents in a closed-system under high temperature and pressure conditions to dissolve and recrystallize materials that are relatively insoluble under ordinary conditions. The temperatures and pressure is usually greater than room temperatures and 1 atm. respectively [166,167].The Hydrothermal synthesis route is a cheap, effective and straight forward process for the synthesis of single crystals, bulk powders and nanocomposite materials with varied nanoarchitectures with physical and chemical properties suitable for energy storage applications [168–170]. Water is the reaction medium utilized in hydrothermal conditions in an autoclave system. Autoclaves are sealed steel cylinders that are able to withstand high temperature conditions for a prolonged time duration. The use of water as a reaction medium has several advantages which include non-toxicity, non-flammability and thermodynamic stability. It also assists in the tuning of the temperature and pressure conditions for material formation.

The solvothermal synthesis technique is similar to the hydrothermal technique. The solvothermal synthesis process involves a chemical reaction in a closed system in the presence of solvent (aqueous and non-aqueous) at a temperature higher than the boiling point of the solvent [171].The key factor that determines the growth and nanostructure of the synthesized material is dependent on the solvent utilized, reaction temperature, reaction duration, pH of the reaction medium and pressure of the closed system [171–173]. The morphology of the crystals formed can be tuned by controlling the solvent supersaturation, chemical reagent concentration and process kinetics [173]. Solvothermal method can be used to synthesize thermodynamically stable and metastable states including novel materials that cannot be synthesized from other synthesis techniques [171,173].

In this study, solvothermal synthesis technique was used for the synthesis of Co-Mn LDH and hydrothermal method was use for the pretreatment of raw cork by before carbonization in a tube furnace as described in section 3.2.4 below.

3.1.2 Chemical vapour deposition (CVD) technique

CVD is a very useful and efficient method suitable for the production of metals and non-metals such as carbon and silicon and a variety of materials such as carbides, nitrides, oxides etc coatings, powders, fibers and monolithic components [174]. CVD involves flowing a precursor gas or gases into a reaction chamber containing one or two substrates to be deposited upon. Chemical reactions take place at or close to the hot surfaces, leading to the deposition of the material on the substrate, followed by the production of chemical by-products that are flown out of the chamber together with the unreacted precursor gases [174,175]. A CVD reaction is guided by thermodynamics which is the driving force that indicates the direction the reaction is to proceed and by kinetics, which determines the flow process and rate-control mechanism[174]

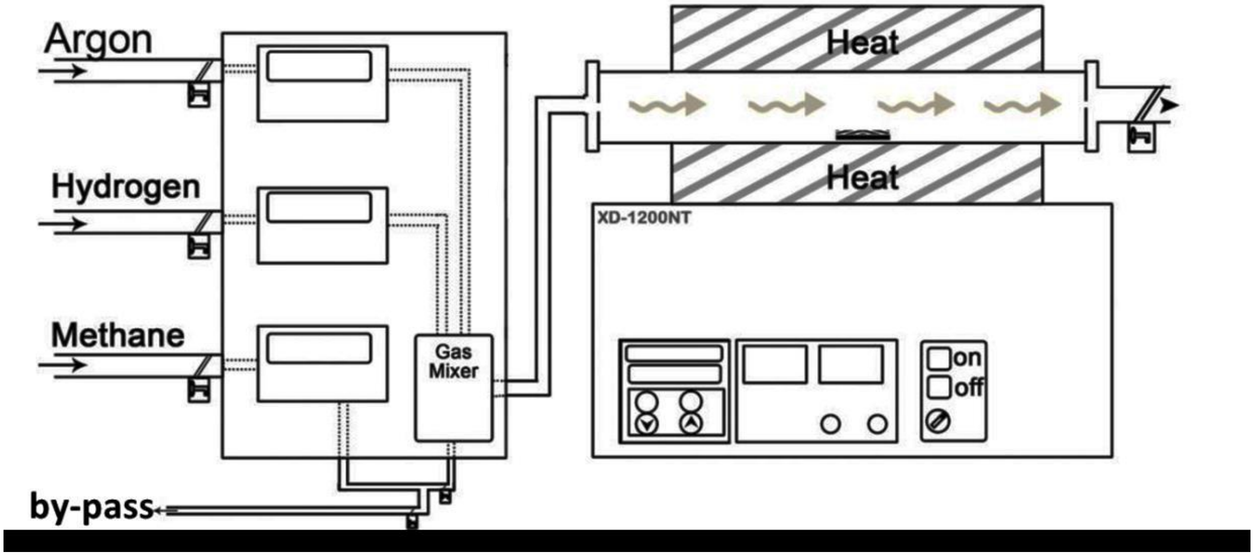

Figure 3.1 Diagram of the chemical vapour deposition system

The CVD system for the purpose of this study was used for the production of activated carbon. As depicted in the diagram in figure 3.1, the CVD system consists of a 2-inch diameter quartz tube which is the reaction chamber, connected to gas flow meters that are in turn connected to the various precursor gases used for the material synthesis.

3.2 Material synthesis

3.2.1 Synthesis of Co-Mn LDH

Co-Mn LDH nanoflakes were synthesized by a facile solvothermal method. Briefly, 0.05 M $Co(NO_3)_2.6\ H_2O$, 0.10 M $MnSO_4$ and 0.60 M CH_4N_2O was put into 60 ml of methanol (CH_3OH) and sonicated for 10 minutes. Then the solution was transferred into a 100 ml teflon lined autoclave and placed in the oven at 120 °C for 6 hours. The resulting product was filtered and washed several times with deionized water. Figure 3.2 shows schematic of the complete synthesis route of the Co-Mn LDH nanoflakes.

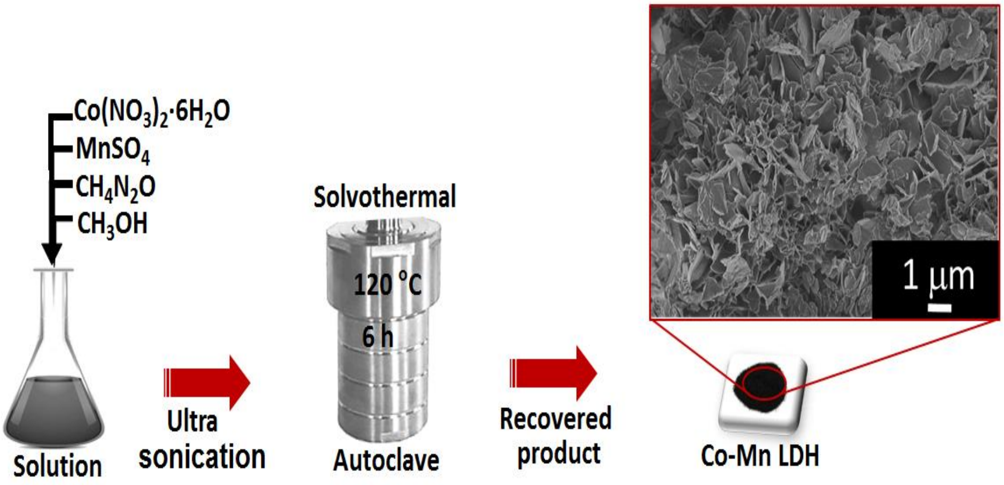

Figure 3.2 Schematic of the synthesis route of the Co-Mn LDH nanoflakes

3.2.2 Synthesis of MnO_2-CNT

The $KMnO_4$ (Merck, Purity $\geq$ 98%), H_2SO_4 (purity 95 -97 %), H_2O_2 (purity 30 %), HNO_3 (Purity 65 %) reagents were of analytical grade and used without further purification. Deionized water was used throughout for the washing of the synthesized sediments until the final product was obtained. Multi-walled carbon nanotubes (CNTs) (Nanolab, purity: > 94%, length: 5-20 µm and diameter: 10-20 nm), were converted to short and uncapped nanotubes bearing acidic functional groups (mainly: -COOH) prior to their use in the synthesis of the nanocomposite. Briefly, 0.5 g of pristine CNTs was refluxed for 48 h in 2.6 M HNO_3. The washed deposits of CNTs were sonicated in a mixture of conc. H_2SO_4/HNO_3 (3:1 ratio, 95-97%, and 65% purity, respectively), followed by washing and stirred at 70 ° C for 15 min. in a mixture of H_2SO_4/H_2O_2 (4:1 ratio, 95-97% and 30% purity, respectively). The black powder of CNTs was finally dried at 60 °C overnight after washing. The CNT-MnO_2 nanocomposite was synthesized via the conventional hydrothermal reflux technique. Typically, 40 mg of CNTs was dispersed by sonication in 0.02 M $KMnO_4$. Subsequently, the mixture (pH = 7.05) was refluxed for 24 h with continuous magnetic stirring. The resultant dispersion was then centrifuged and washed several times and finally dried at 60 °C overnight in a vacuum oven. The schematic illustration of the synthesis process of MnO_2-CNT is shown in figure 3.3 below.

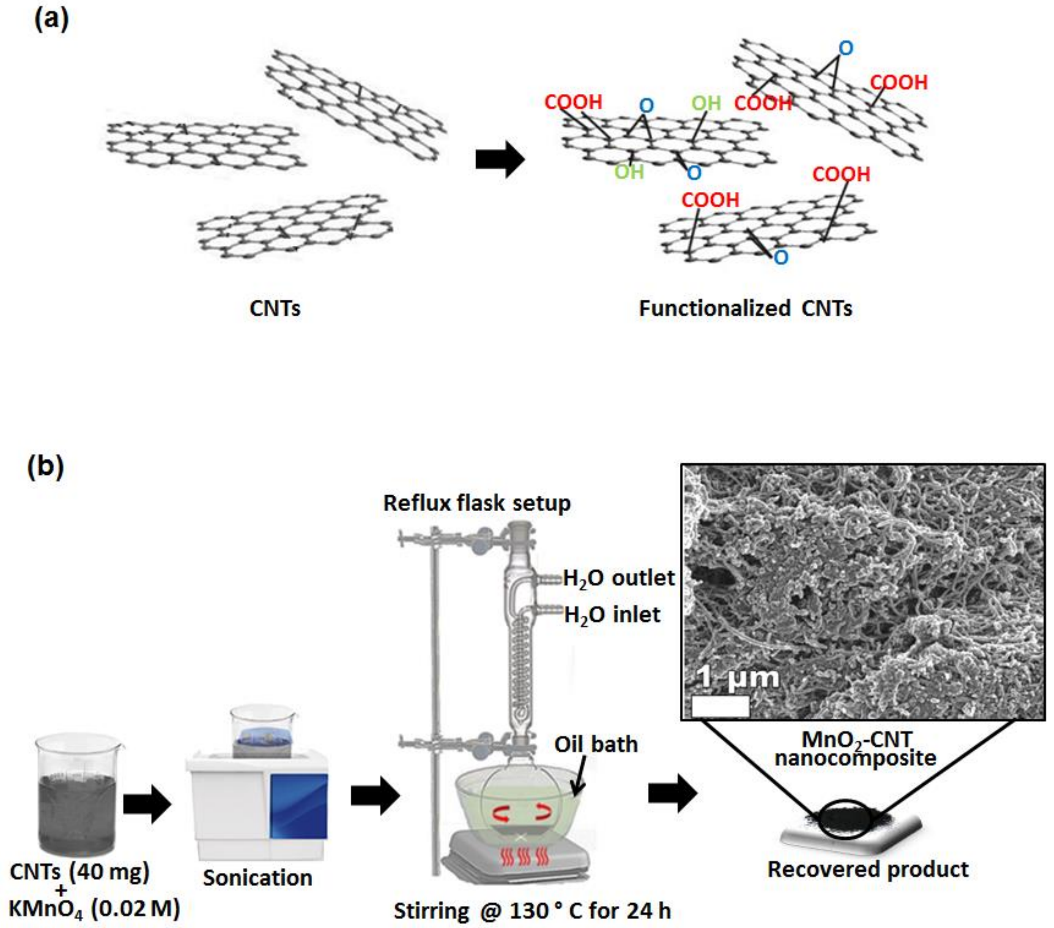

Figure 3.3 Schematic illustration of (a) the chemical structure route from CNTs to functionalized CNTs. (b) Synthesis method for MnO_2-CNT nanocomposite using functionalized CNTs.

3.2.3 Synthesis of AC derived from raw cork (Quercus suber) by activation with KOH

The raw cork material used for this study was collected from Algeria and used for the making of activated carbon. Typically, 5 g of the material was impregnated with KOH in the ratio of 1:1, 1:2 and 1:3 and left for 72 h for the material to properly absorb the KOH before drying it in the oven at 60 ^oC for several hours. The samples were then carbonized in a quartz furnace under 300 sccm argon flow at 800 ^oC with a ramp rate of 5 ^oC/minutes for 2 h. The black material obtained after carbonization was washed in 3 M HCl (to get rid of excess unreacted activating agent present and also to wash off any impurities present in the sample) and then washed repeatedly with deionized water until the filtrate became neutral to a pH indicator. The obtained activated carbon (AC) was denoted as AC 1:1, AC 1:2 and AC 1:3. For material: KOH ratios of 1:1, 1:2 and 1:3 respectively. The schematic showing the synthesis route of the AC is presented in figure 3.4.

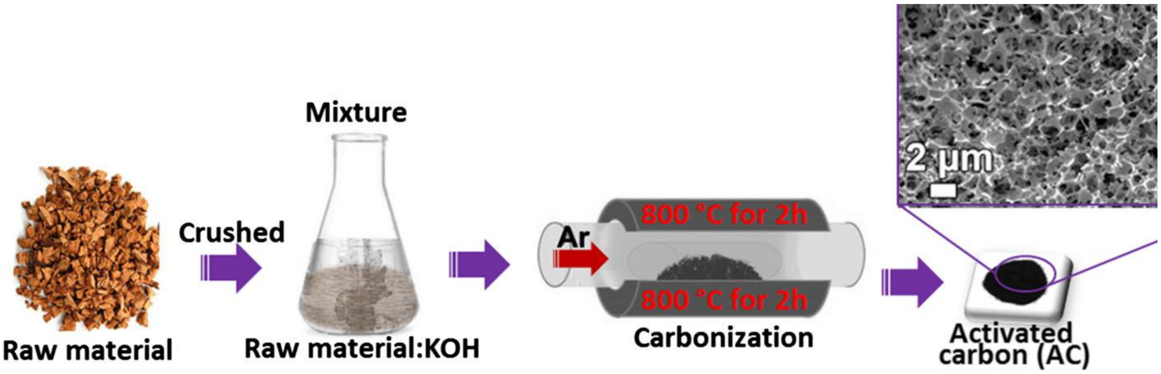

Figure 3.4 Schematic of the synthesis route of the AC produced by KOH activation

3.2.4 Synthesis of AC derived from cork (Quercus suber) by activation with $KHCO_3$

Mesoporous AC was synthesized via a two-step eco-friendly synthesis route by hydrothermal pretreatment to produce hydrochar before activation and carbonization in a chemical vapour deposition system. Briefly, 10 g of raw cork (Quercus Suber) was properly washed using acetone and deionized water and dried in an oven. Then, the raw cork was put into a 100 ml teflon lined autoclave which contains 80 ml deionized water and 0.8 ml of 0.5 M sulphoric acid and treated hydrothermally at 160°C for 12 hours. The hydrochar produced was then washed severally with distilled water and dried in an oven at 60°C for several hours. Next, the hydrochar was activated with $KHCO_3$ in a ratio of 1:1 and carbonized in a CVD system under argon flow at a ramp rate of 5°C /min from room temperature to 850°C for two hours. The black product obtained was washed with 3 M HCL and severally with deionized water until filtrate became clear and was kept to dry in an oven at 60°C for 12 hours. The material was denoted as $ACKHCO_3$ 1:1. A diagrammatic representation showing the synthesis route of the AC is presented in figure 3.5.

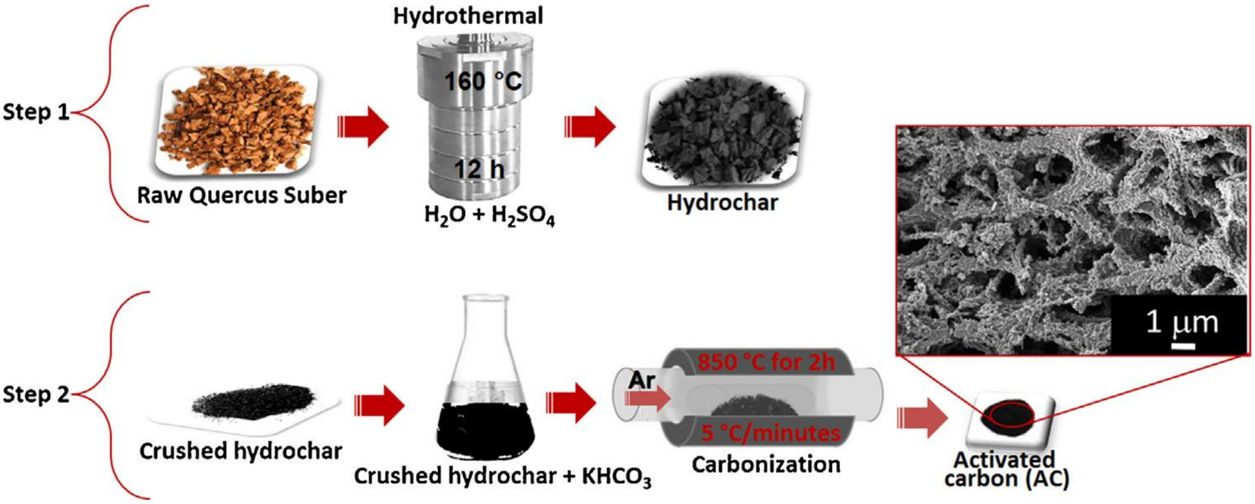

Figure 3.5 Schematic of the Synthesis of activated carbon derived from cork by activation with $KHCO_3$

3.3 Material characterization techniques

3.3.1 Scanning electron microscopy (SEM) and Energy dispersive X-ray spectrometry (EDS)

Scanning electron microscopy is one of the most widely used methods for the examination and analysis of the microstructure, morphology and chemical composition of materials. The chemical characterization aspect is possible when the instrument is used in conjunction with the energy dispersive X-ray spectrometer (EDS). The SEM makes use of a focused electron beam to thoroughly scan the surface of the specimen producing a multitude of signals. Image formation on the SEM is dependent on the acquisition of signals produced from the electron beam and specimen interactions. These interactions are divided into two major categories: elastic and inelastic interactions [176–178]. A diagrammatic representation of the interaction between a specimen and an electron beam is as shown in figure 3.6 below.

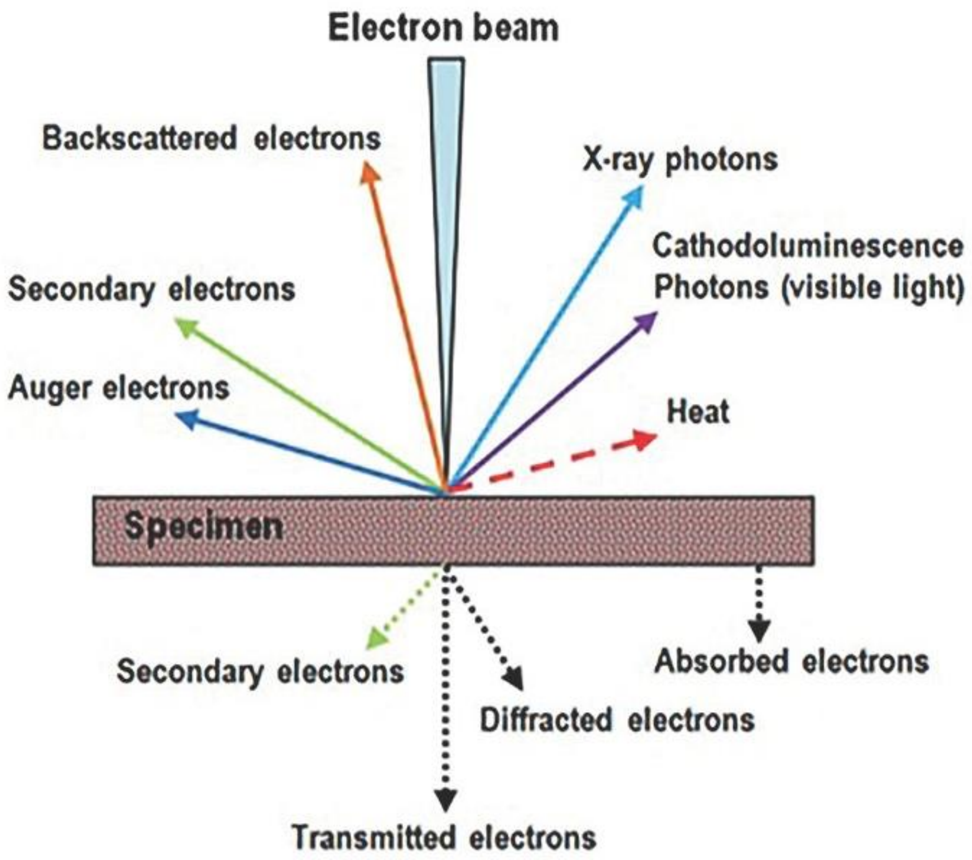

Figure 3.6 Diagram of the interaction between a specimen and the electron beam in a SEM [179]

Elastic scattering results from the deflection of the incident electron by the specimen atomic nucleus or by an outer shell electron of similar energy. Incident electrons elastically scattered through the angle of more than 90˚ are called back scattered electrons (BSE) and can generate a useful signal for scanning a sample with an energy greater than 50 eV. Inelastic scattering takes place through a number of interactions between the incident electrons and atoms of the sample which culminates to the transfer of considerable amount of energy to that atom. The excitation of the sample electrons during the ionization of the sample results to the production of secondary electrons (SEs) which possess energies less than 50 eV and can be used for the sample analysis [176,177].

The other signals that are emitted during the interaction of the electron beam with the sample are characteristic X-rays, Auger electrons and cathodoluminescence. Characteristic X-rays generated by the interaction of primary X-rays with the sample are unique to the sample from which it originates and is useful for elemental composition analysis. Auger electrons are produced when an incident electron beam ionizes an atom in a sample and an electron with a higher energy fills in the vacant electron position. Cathodoluminescence is formed when certain samples release energy in the form of photons with infrared, visible or ultraviolet wavelengths when electrons recombine to fill holes made by incident beam with specimen. The best possible image resolution using this approach is about 50 nm. Transmitted electron are generated when electron beam transmit through the sample with loss of energy if the sample is thin [176,177].

As stated earlier, EDS is usually performed in conjunction with a SEM. EDS makes use of X-ray emitted by a specimen bombarded with incident beam of electrons. All elements from atomic number 4 (Be) to 92 (U) can be detected. Qualitative analysis involves the identification of the lines in the spectrum. Quantitative analysis which is the determination of the concentration of the elements present involves measuring the intensities of each element in the sample and for same elements in calibration standards of known composition[180].

Scanning electron microscopy (SEM) of all samples and energy dispersive X-ray spectroscopy (EDS) analysis were carried out using Zeiss Ultra plus 55 field emission scanning electron microscope (FE-SEM) at an accelerating voltage of 2.0 kV and JEOL 2100 (from Tokyo Japan) operated at 200 kV respectively.

3.2.3 Transmission electron microscopy (TEM)

Transmission electron microscopy (TEM) is a technique in which a beam of electrons is transmitted through a very thin sample, interacting with the sample as it passes through. An image is formed from the interaction of the electrons transmitted through the sample; the image is magnified and focused onto an imaging device, such as a fluorescent screen, on a layer of photographic film, or to be detected by a sensor like charge-coupled device (CCD) camera. The electron beams have very short wavelengths and are emitted from a tungsten filament [178,181,182]. High resolution transmission electron microscopy (HR-TEM), selected area diffraction (SAED) analysis of the samples in this work were performed using JEOL 2100 (from Tokyo Japan) operated at 200 kV.

3.3.3 X-ray powder diffraction (XRD)

X-ray powder diffraction is a very important technique for the identification of the phase of the sample of a material ranging from fluids to powders and crystals. X-ray diffraction pattern of a sample is like the fingerprint unique to the substance. The powder diffraction pattern method is ideally suited for characterizing and identifying polycrystalline phases where every crystalline orientation is represented equally. In powder or polycrystalline diffraction it is important to have a sample with a smooth plane surface. Where necessary, the sample is normally ground to particles of about 0.002 mm to 0.005 mm cross section. The ideal sample is homogeneous and the crystallites are randomly distributed [183–185].

XRD uses the principle of constructive interference of monochromatic X-rays of the sample to be identified. XRD system is made up of three compartments: X-ray tube, X-ray detector and sample holder, which lie in the circumference of a circle known as focusing circle. In the XRD system, electrons generated from a cathode by a heated filament is accelerated toward a target anode (usually copper or cobalt) by an applied voltage. The bombardment of the electrons on the target produces the X-rays. The angle θ (Bragg angle) is the angle between the plane of the sample material and the source of the X-ray. The angle 2θ is the angle between the detector and projection source [183,185]. The rotation of the sample material and the detector produces the X-rays. When the X-ray is incident on the sample material, a constructive interference occurs which satisfies Bragg's law: $n\lambda = 2dSin\theta$ where n is an interger, λ is the wavelength of incident wave, d is the spacing between the atomic lattice planes and θ is the angle between the incident ray and the scattering planes. The X-ray signals are processed and recorded by a detector and then the signals are further converted to count rates transmitted to a mirror [186]. The XRD measurements carried out in this study was performed XPERT-PRO diffractometer (PANalytical BV the Netherlands).

3.3.4 Raman Spectroscopy

Raman spectroscopy is a non-invasive and non-destructive technique used to measure the vibrational, rotational and low frequency modes of a material [187,188]. The technique involves irradiating a sample with a laser which is scattered with a finite probability depending on the sample type. Typically, the laser beam interacts with the vibrational modes of the molecules of the sample and most of the incident laser is transmitted in all directions at the same frequency with the incident radiation with a small fraction elastically scattered (Rayleigh scattering) and a smaller fraction is inelastically scattered (Raman stokes). The Raman scattered radiation is collected and dispersed and the outcome is displayed as Raman spectrum. The Raman spectrum is a graph of the intensity of the inelastically scattered radiation versus the shift in the radiation wavenumber. As the laser interacts with the molecular vibrations or other excitation modes of the sample lattice it leads to the extraction of the chemical and structural information of the vibrational modes of the sample. For example, for the sp^2 carbons, the spectrum displays Raman features which include the G-band which arises from the stretching of the C-C bond in the graphitic material and occurs at ~1580 cm^{-1}, the 2D or G′-band which occurs at ~2500 – 2800 cm^{-1},is a second-order two-phonon process and the D-band indicates the presence of disorder in the sp^2-hybridized carbon [187,189]. In this study, the Raman spectroscopy was performed using a Jobin Yvon Horiba X6400 micro-Raman spectrometer equipped with LabSpecv (Version 5.78.24) analytical software with a 514 nm argon laser and a WiTec alpha 300R+ confocal Raman system (WiTec Gmbh) with a 532-nm excitation laser.

3.3.5 Fourier Transform Infrared Spectroscopy (FT-IR)

FT-IR is a qualitative analysis technique used for the measurement and identification of an unknown sample, quality or consistency of samples or amount of components in a mixture [190] . In a typical procedure, the sample is irradiated with infra-red radiation such that some of the infrared radiation is absorbed and some of it is transmitted. The transmitted radiation measures the transmittance while the absorbed radiation measures the absorbance. The resulting spectrum represents the molecular absorption and transmission, creating a molecular pattern characteristic to that material. Like a fingerprint no two unique molecular structures generate similar infrared spectrum [190]. In this study, FT-IR spectroscopy measurements was performed using Perkin Elmer Spectrum RX I FT-IR system in the 4000 – 500 cm^{-1} range with a resolution of 2 cm^{-1} to determine the sample surface functional groups. The samples were blended homogenously with KBr in a ratio of 1:100 and making them into transparent pellets before measurements

3.3.6 Gas adsorption and desorption technique

Gas adsorption/desorption is a technique used for the measurement of the specific surface area (SSA), pore size distribution (PSD) of a wide range of porous materials [191,192]. In this study, the SSA and PSD measurements were performed using a Micrometrics TriStar II 3020 analyzer employing the Brunauer-Emmett-Teller (BET) and Barrett-Joyner-Halenda (BJH) techniques. The SSA was obtained from the N_2-adsorption/desorption isotherm with nitrogen gas at −196 °C while the PSD data was obtained from the desorption branch of the BJH isotherm in the relative pressure range (*P/P0*) of 0.01 – 1.0. In a typical measurement procedure for obtaining the isotherms, the samples where first weighed and then degassed at 150 ˚C for 12 hours under vacuum to remove any moisture content. Thereafter, the degassed samples were transferred to the analysis compartment in liquid nitrogen at ultra-low pressure and at −196 °C. Next, the samples were allowed to absorb gas which was then evacuated. The amount of the evacuated gas was then measured to obtain the amount of gas absorbed by the samples within a relative pressure P/P_0 range. An adsorption isotherm is usually recorded as volume of gas adsorbed versus relative pressure. The type of isotherm obtained from the analysis gives an indication of the particle and pore size of the sample. Five types of isotherms were first reported in 1940 by Brunauer *et al.* [193]. Six types of the adsorption isotherms were later reported by the International Union of Pure and Applied Chemistry (IUPAC) in 1985 [191] with explanation of the differences between them with accompanying adsorption and desorption hysteresis given by Gregg and Sing [194]. The IUPAC categorization of isotherms is as shown in Figure 3.67(a). Type 1 is referred to as the Langmuir type and is related to adsorption of microporous structure.

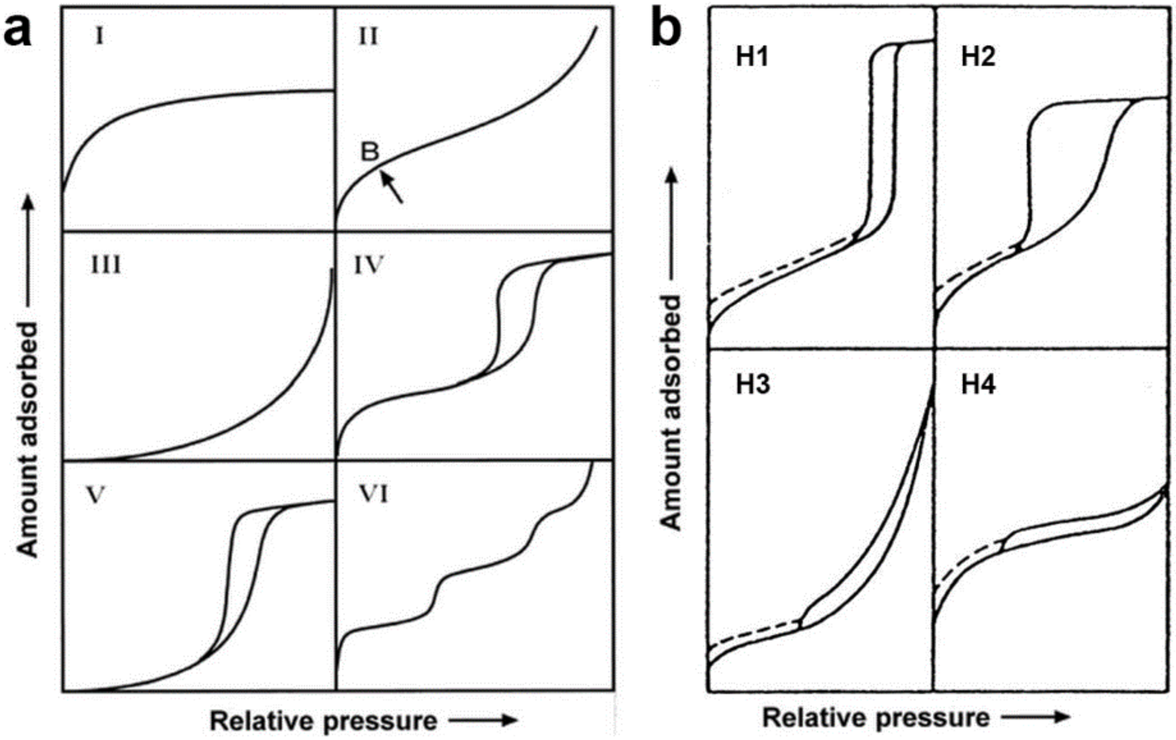

Figure 3.7 (a) The IUPAC categorization of isotherms (b) adsorption-desorption hysteresis loop[193,194]

Type II and III describes non-porous or macroporous samples and weak interactions respectively. Type IV and V are linked with mesoporous structure and weak interactions respectively while Type VI is characterized by stepwise (layer by layer) adsorption on a macroporous surface [193]. The adsorption-desorption hysteresis loop is categorized into H1, H2, H3, and H4 and presented in Figure 3.7 (b). H1 describes narrow distribution of relatively cylindrical –like pores, H2 shows a complex pore structure, H3 is an indication of non-rigid aggregates of plate-like particles or agglomeration of slit-shaped pores, and H4 describes to the complex materials including both micropore and mesopore structure [194].

3.3.7 X-ray photoelectron spectroscopy (XPS)

XPS is a versatile technique used for the study of atoms, molecules, solids and surfaces [195]. XPS is employed for the measurement of the chemical composition, chemical state and electronic state of the elements that exist within a material at parts per thousand range. XPS spectra is obtained by exposing a material to a beam of X-rays (Al-Kα or Mg-Kα) while measuring the kinetic energy and number of elastically scattered photoelectrons that exude from the top 0 to 10 nm of atomic layers from the sample. An XPS spectrum is a plot of the number of electrons identified versus the binding energy of the identified electrons. The XPS peaks is generated by each element at characteristic binding energy values that precisely identifying each element that occurs in or on the surface of the sample analyzed. These distinctive spectral peaks match the electron configuration of the electrons within the atoms, i.e., 1s, 2s, 2p, 3s, etc. The number of electrons identified in each of the characteristic peaks is directly related to the amount of element present in the analyzed material. A Physical Electronics VersaProbe 5000 spectrometer was used for the measurement of the samples in this study

3.3.8 Electrochemical Analysis

The electrochemical analysis of all samples were performed in a three electrode and two electrode configuration with a multi-channel Bio-logic VMP300 potentiostat/gavanostat workstation operated using EC-lab v10.4 software at ambient temperature. The potentiostat/galvanostat workstation measures the potentiqal difference between the working electrode (WE) with current flow and the reference electrode (RE) with no current flow and the potential difference via the counter electrode (CE) and records the current as an iR drop

[196,197]. Cyclic voltammetry (CV), galvanostatic charge discharge (GCD) and electrochemical impedance spectroscopy (EIS) techniques were used for the sample analysis. The EIS study was done in an open circuit potential in the frequency range of 10 mHz to 100 kHz. In the three electrode configuration used for the single electrode or half-cell measurements the active materials served as the WE, Ag/AgCl (3 M KCl) as RE and glassy carbon as CE. 1 M Na_2SO_4, 1 M $NaNO_3$, 1 M Li_2SO_4, 3 M KNO_3, 1 M H_2SO_4, 6 M KOH and 1 M KOH were utilized as electrolytes for analysis of the various single electrodes. A diagrammatic representation of the three electrode set up is as shown in figure 3.8.

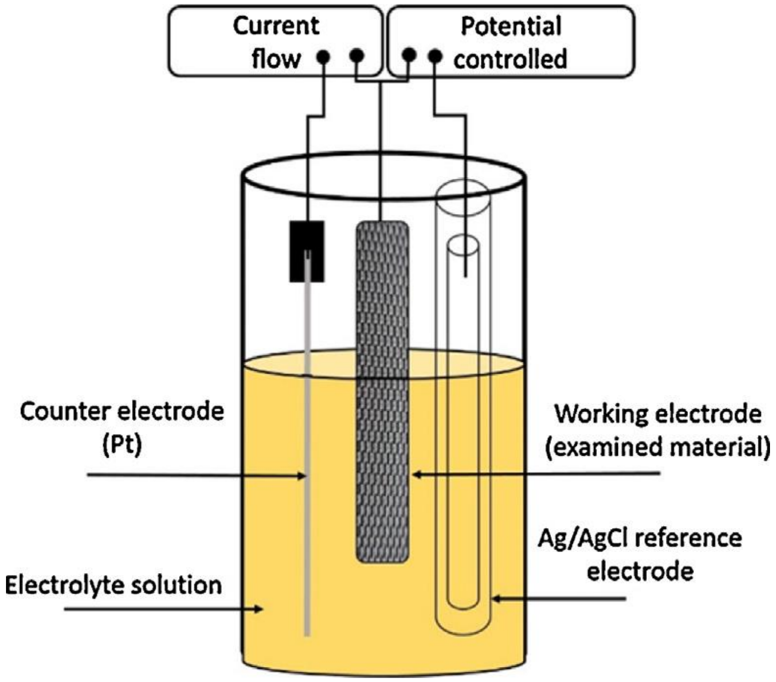

Figure 3.8 Diagrammatic representation of a three-electrode set-up [198]

The materials for the two-electrode testing was assembled using a coin-type cell and Swagelok with microfiber glass filter paper as separator. The electrolytes utilized in the fabrication of the two-electrode cells are 1 M Na_2SO_4, 1 M KOH and 1 M Li_2SO_4 based on their best performances with the active materials in the three-electrode testing. A diagrammatic representation of the coin cell and Swagelok two-electrode configuration is as shown in figure 3.9 below.

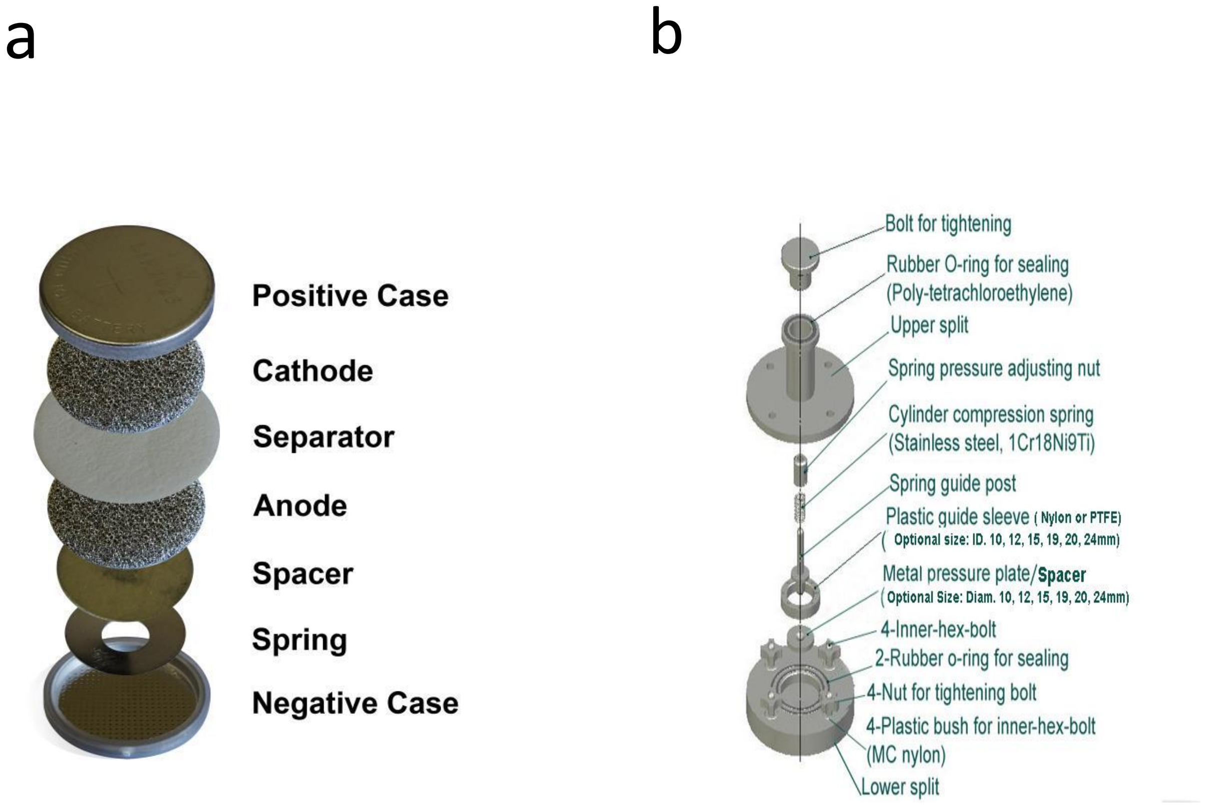

Figure 3.9 diagrammatic representation of (a) coin cell and (b) Swagelok two-electrode configuration[199,200]

The electrodes for the three-electrode measurement were fabricated by preparing a homogeneous mixture of the active material (80 wt. %), carbon black (15 wt. %) (to enhance the conductivity of the material) and polyvinylidene difluoride (PVdF) (5 wt. %) as a binder in an agate mortar. A slurry was made from the above mixture by adding 1-methyl-2-pyrrolidinone (NMP) drop-wise to the mixture and then coated on 2 cm × 2 cm nickel foam (NF) current collectors. The coated samples were then dried in an oven at 60 ^{o}C overnight. The device for the two-electrode measurements was similarly prepared but was coated and pressed on 16 mm diameter NFs and dried at 60 ^{o}C for 8 hours and then assembled in a coin cell or Swagelok with a microfiber glass filter paper as a separator.

CHAPTER FOUR

4.0 RESULTS AND DISCUSSION

The results from the experiments conducted in this research will be presented in this chapter. Publications from each research study will also be presented.

4.1 Electrochemical performance of hierarchical porous activated carbon (AC) derived from cork (Quercus suber) synthesized by KOH activation

4.1.1 Introduction

A number of supercapacitor materials have been explored as potential materials for supercapacitor application. The electrochemical performance of the supercapacitor device depends on the nature of the electrode material and the electrolyte used for the device fabrication [33,34,36]. Carbon materials such as graphene, onion-like carbon (OLC), carbide derived carbon (CDC), carbon nanotubes (CNTs) and activated carbon (AC) [38,137,201,202] are utilized as potential electrode materials for electric double layer capacitors (EDLCs) because of their excellent conductivity, large specific surface areas (SSAs), good cycling stability and good pore size distribution. Among the EDLC materials AC is the most commonly utilized because of its relatively low cost, easy production, light weight and pseudocapacitive charge transfer mechanism which enhances the specific capacitance due to the presence of functional groups [29,32,42,203].

The production of AC from renewable and abundant biomass wastes have received significant attention recently because they are environmentally friendly, cost effective, sustainable with efficiently tunable porosity. Some of these natural and organic biomass wastes include pistachio nutshells, sun flower seed shell, rice husk, wood saw dusts, coconut leaves, coco nut shell and hemp blasts [96,97,204–208]].

As a potential source of carbon, raw cork (Quercus suber) are biomass wastes, which are natural, organic, abundant, light weight, sustainable and renewable. The cork raw material is derived from the bark of the cork tree (Quercus suber). Quercus suber which is widely known as cork oak, is a medium sized, evergreen oak tree in the genus *Fagaceae* family. It grows up to 20 m by 15 m and is native to south Europe to North Africa, Portugal being the world largest cork producer with more than half of the world's wine and bottle corks produced from Portuguese cork [209,210]. A few studies have been carried out on cork by KOH activation and physical activation using CO_2 for application in the control of environmental pollutants and absorbents [210,211]. But from available literature as at the time of this research study no study has been carried out on the activation of cork (Quercus suber) for energy storage applications.

Different activating agents exist for the conversion of biomass wastes into activated carbon. The choice of KOH as an activating agent in this study is because it can be used to synthesize ACs with well-defined micro pores with tunable pore structures. The study was systematically carried out considering the corrosive nature of KOH and the environmental benignity of material produced [212].

Herein, we present and discuss the results of nanostructured activated carbon synthesized by KOH activation of the cork raw material in the ratio of 1:1, 1:2 and 1:3 (denoted as AC 1:1, AC 1:2 and AC 1:3 respectively) and carbonized using chemical vapour deposition system in argon atmosphere with flow rate of 300 sccm at 800 ^{o}C at a ramp rate of 10^{o}C/minute for 2 h. The black product obtained after carbonization was washed in 3 M HCl and then washed severally with deionized water until the filtrate became neutral to a pH indicator. The black product was then dried in an oven at 60^{o}C for several hours.

4.1.2 Result and discussion

The details of the obtained results is presented in the following publication.

J Mater Sci (2017) 52:10600–10613

Polymers

High electrochemical performance of hierarchical porous activated carbon derived from lightweight cork (*Quercus suber*)

Faith O. Ochai-Ejeh[1], Abdulhakeem Bello[1], Julien Dangbegnon[1],
Abubakar Abubakar Khaleed[1], Moshawe Jack Madito[1], Farshad Bazegar[1], and Ncholu Manyala[1,*]

[1] *Department of Physics, Institute of Applied Materials, SARChi Chair in Carbon Technology and Materials, University of Pretoria, Pretoria 0028, South Africa*

Received: 21 February 2017
Accepted: 12 May 2017

ABSTRACT

Activated carbon (AC) derived from biomass lightweight cork (*Quercus suber*) material was synthesized by KOH activation with different mass ratios of *Q. suber*: KOH in order to investigate the electrochemical properties of the AC in relation to KOH concentration. A well-defined porous activated carbon was obtained with a high surface area of 1081 $m^2\ g^{-1}$ and a high pore volume of 0.66 $cm^3\ g^{-1}$ when the *Q. suber*: KOH mass ratio was fixed at 1:2. A specific capacitance of 166 F g^{-1} was obtained for the symmetric device at 0.5 A g^{-1} in 1 M Na_2SO_4 with energy and power densities of 18.6 and 449.4 W Kg^{-1}, respectively. The device displays good cycling stability after floating test for 200 h at 1.8 V and also displays 99.8% capacitance retention after cycling for 5000 cycles. The excellent electrochemical performance of the device makes it a potential material for supercapacitor application.

Introduction

Dealing with the present day energy crisis such as providing sustainable and renewable energy for present and future needs is a major challenge globally. This is as a result of the diminution in the supply of fossil fuel and the deteriorating environmental impact of conventional energy storage technologies, such as batteries which make use of very toxic chemicals like lead and lithium ions which are flammable. Therefore, there is an urgent need for environment-friendly energy storage devices from renewable and sustainable sources to address this need [1–7].

Supercapacitors (SCs) also known as electrochemical capacitors have become desirable as energy storage devices because they offer numerous prospects of being low cost and make use of cheap, abundant and renewable raw materials with promising advantages of operating at high power density with excellent reversibility, oscillatory power supply, long cycle life with fast charging and high-powered charge production [8–10]. The categories of SCs are electric double-layer capacitors (EDLCs),

---

Address correspondence to E-mail: ncholu.manyala@up.ac.za

Springer

DOI 10.1007/s10853-017-1205-4

pseudocapacitors and faradaic SCs. EDLCs are a class of SCs which store charges electrostatically by reversible absorption/desorption of ions at the electrode–electrolyte interface of the active material, which is largely dependent on the structure and morphology of the material [1, 5, 7, 11]. Pseudocapacitors are capacitors that have electrochemical behavior similar to that of EDLC electrodes but in which the charge transfer originates from the electron transfer mechanism rather than on the accumulation of ions in the electrochemical double layer, while faradaic capacitors store charges by rapid redox reactions at the surface of active material [11]. Several SC materials have been explored as potential materials for SC application such as carbonaceous materials, conducting polymers and transition metals. Carbonaceous materials such as graphene, carbon nanotubes and activated carbon (AC) are usually used for EDLCs because of their excellent electronic conductivity, good pore size distribution and large specific surface areas. However, most of the available SCs still suffer from low energy densities when compared to that of batteries. Therefore, research to improve the energy density of SCs is paramount. The electrode material and the electrolyte are the key components that determine the electrochemical performance of SCs [1, 2, 12]. Since energy density (E_d) is proportional to specific capacitance (C_{sp}) and the square of potential window (E_d–C_{sp} V^2) of the electrode material, the research focus is on enhancing the property of the materials by researching on ways to improve on the potential window and/or the specific capacitance of the materials [13–15].

The efforts have been made in the previous studies along this line to improve the working potential and specific capacitance of SCs. For instance, a symmetric carbon/carbon SC with a C_{sp} of 115 F g^{-1} operating at 1.6 V in Na_2SO_4 was reported [15]. Similarly, a report on SWNT electrodes with a C_{sp} of 180 F g^{-1} was obtained at 1.0 V in KOH electrolyte [16]. In another study on $Ni(OH)_2$/graphene and RuO_2/graphene, a C_{sp} of ~153 F g^{-1} was obtained at a potential window of 1.6 V in KOH aqueous electrolyte [17], and an asymmetric SC based on graphene/MnO_2 and AC nanofiber was also reported with a C_{sp} of 113.5 F g^{-1} at 1.8 V in Na_2SO_4 [18]. A study on the unequalization of the electrode capacitance indicated a considerable increase in the working potential of a symmetric SC (up to 1.9 V) in aqueous K_2SO_4 with a C_{sp} of 80 F g^{-1} [1, 13, 15]. There have been reports on several studies on the fabrication of electrode materials from AC with good pore size distribution, large specific surface area, good conductivities and high specific capacitances. However, their industrial and large-scale productions have been limited by high cost and degree of the corrosiveness of the materials utilized in the fabrication [15, 19].

The use of abundant and renewable, cost-effective, lightweight materials with tunable porosity that are efficient, sustainable and environmentally safe is still imperative due to the high cost involved in the production of some materials listed above. Also, the utilization of the same material for both the positive and negative electrodes is essentially important both in terms of cost and large-scale production [3, 13, 19–23]. Biomass trials for the production of AC have become attractive because they are low-cost source of carbon material with tunable properties and hence have been recently explored for SCs. Another important factor to consider is the electrolytes used in the device fabrication. Alkaline, acidic/ionic electrolytes usually have high conductivity which makes them achieve high C_{sp}, but they suffer from low E_d because of inability to operate at large potential windows. This is because thermodynamically, the decomposition of water is at 1.23 V. Neutral electrolytes can attain moderate potential windows leading to better electrochemical performance. Organic electrolytes, however, have large operating potential windows but are toxic, have poor electrical conductivity and are quite expensive. Hence, neutral electrolytes are preferred due to their advantage of enhancing SC performance [24, 25].

In a report on SC from sunflower seed shell, a C_{sp} of 311 F g^{-1} was obtained in a potential window of 0.9 V in 3 M KOH electrolyte [26]. In a study of mesoporous carbon from coconut shell, a C_{sp} of 246 F g^{-1} was obtained within a voltage window of 0.7 V in 0.5 M H_2SO_4 [27] and in another report on SC electrode derived from coconut leaves, a C_{sp} of 133 F g^{-1} was obtained in a potential window of 1.0 V in 6 M KOH [28]. Also, in a study on Pistachio nutshells derived carbon, a C_{sp} of 261 F g^{-1} was obtained in a potential window of 1.1 V in 6 M KOH [29]. These devices have been reported with high capacitance values, but the nature of the electrolytes used and the working potential of the device results to low E_d and therefore limits their industrial application [15, 30].

In this study, we present a carbon–carbon symmetric supercapacitor with good electrical conductivity and specific capacitance with a working voltage of 1.8 V in 1 M Na_2SO_4. The device is produced from cheap and lightweight material cork (*Q. suber*), a spongy material which comes from the bark of an evergreen oak tree. The renewability and sustainability of this material make it a choice material for this study. 1 M Na_2SO_4 was chosen for this study because it has been demonstrated that a stable potential window of up to 2 V can be achieved in a carbon–carbon SC in the neutral electrolyte. Another factor considered was that it is less toxic and corrosive when compared to the acidic electrolytes [1, 13, 15]. The choice of KOH as the activation agent is as a result of the fact that it can be used to produce ACs with well-defined micropores and mesopores with tunable porosity; however, a systematic study was astutely carried out because of the corrosive nature of KOH considering the economic and environmental impact of materials produced [19, 23].

Experimental

Material synthesis

The cork raw material used for this study was collected from Algeria and used for the production of activated carbon. Scheme 1 shows the complete synthesis route of the activated carbon. 5 g of the raw material was impregnated with KOH in the ratio of 1:1, 1:2 and 1:3, left for 72 h for the material to properly absorb the KOH before drying it in the oven at 60 °C for several hours. The samples were then carbonized at 800 °C under argon flow (300 sccm) for 2 h. The black material obtained after carbonization was washed with 3 M HCl and deionized water until the filtrate became neutral to a pH indicator. The obtained activated carbon with porous structure (see micrograph image in Scheme 1) was denoted as AC KOH 1, AC KOH 2 and AC KOH 3 for raw material: KOH mass ratios of 1:1, 1:2 and 1:3, respectively.

Structural, morphological and composition characterization

X-ray diffraction (XRD) studies were carried out using XPERT–PRO diffractometer (PANalytical BV the Netherlands) while Raman analysis was carried out using a Jobin-Yvon Horiba TX 64000 micro-spectrometer. Scanning electron microscopy (SEM) and energy-dispersive X-ray spectroscopy (EDS) analysis were carried out using Zeiss Ultra plus 55 field emission scanning electron microscope (FE-SEM) at an accelerating voltage of 2.0 kV. High-resolution transmission electron microscopy (HRTEM) analysis was carried out using a Jeol-2100F field emission electron microscope operated at 200 kV with a probe size of <0.5 nm. The N_2 adsorption/desorption isotherm measurements were taken with a Micromeritics TriStar II 3020.

Electrochemical measurements

The AC samples were tested in three- and two-electrode configurations in a multichannel VMP300 potentiostat/galvanostat (Biologic, France) workstation at ambient temperature. The electrodes for the three-electrode measurement were fabricated by preparing a homogeneous mixture of the activated carbon material (80 wt%), carbon black (15 wt%) to enhance the conductivity of the material and polyvinylidene difluoride (PVdF) (5 wt%) as a binder in an agate mortar. A paste was made from the above mixture by adding 1-methyl-2-pyrrolidinone (NMP) drop-wise to the mixture and then coated on 2 cm × 2 cm nickel foam current collectors. The

Scheme 1 Schematic of the synthesis route of the activated carbon which is denoted as AC KOH 1, AC KOH 2 and AC KOH 3.

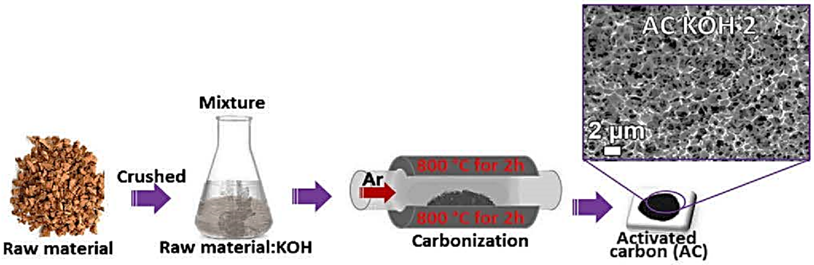

coated samples were then dried in an oven at 60 °C overnight. The symmetric device for the two-electrode measurements was similarly fabricated but was coated and pressed on 16-mm-diameter nickel foams dried at 60 °C overnight and then assembled in a coin cell with a microfiber glass filter paper as a separator. The preliminary test was performed in 1 M Na_2SO_4, 1 M $NaNO_3$ and 1 M Li_2SO_4 aqueous electrolytes with glassy carbon and Ag/AgCl as counter and reference electrodes, respectively. The specific capacitance for the single electrode was calculated from the charge discharge using Eq. 1 [31]

$$C_{sp}\left(\mathrm{Fg}^{-1}\right) = 4I\Delta t/m\Delta U \tag{1}$$

where I (A) is the current, Δt(s) is the discharge time, ΔU(V) is the change in cell voltage and m (g) is the total mass of the electrodes. The energy density E_d and power density P_d of the electrodes were evaluated using Eqs. 2 [31] and 3 [1]

$$E_d\left(\mathrm{W\ h\ kg}^{-1}\right) = C_{sp} \times \Delta U^2/28.8 \tag{2}$$

$$P\left(\mathrm{W\ kg}^{-1}\right) = E_d/\Delta t \tag{3}$$

Results and discussion

Structural, morphological and composition characterization

The structures of the as-synthesized materials were investigated by XRD and Raman spectroscopy. The XRD patterns (Fig. 1a) show peaks at 51° (100) and 76° (110) with an increased intensity identified at the (100) diffraction plane for the AC KOH 2 sample. The peaks represent graphitic diffraction planes, showing that the AC KOH 1 and AC KOH 2 materials belong to the class of graphitized carbon. This indicates that the material is comprised of crystals that are crystal phases of the graphitized carbon; thus, they can be referred to graphitic materials fixed with crystalline carbon owing to the sharp (100) peak while the AC KOH 3 sample contains small crystals that are not well-formed crystal phases and can be referred to as amorphous carbon [32]. The Raman spectra of the activated carbon samples are shown in Fig. 1b. The spectra show the D-band at 1341 cm^{-1} and the G-band at 1589 cm^{-1} of the activated carbon which are typical of the disordered amorphous carbons in the sp^2 carbon network and the characteristic of the tangential vibrations of the graphitic carbons, respectively [5, 33]. The presence of the D and G band present in the Raman spectra indicates the presence of the graphitic carbon in the synthesized materials. The ratio of the intensity of the D and G band (I_D/I_G) is used to determine the degree of graphitization of the materials. In the observed spectra, the ratio of the two bands for AC KOH 1, AC KOH 2 and AC KOH 3 is 0.90, 0.93 and 1.16, respectively, indicating a low degree of graphitic crystalline structure of AC KOH 1 and AC KOH 2 and amorphous structure of AC KOH 3 [5, 8, 9, 34]. The Raman spectra for AC KOH 2 were deconvoluted using the Lorentzian curve fitting (Lorentzians) of different combinations of the Raman peaks as presented in Fig. 1c. In Fig. 1c, the G1 and the D1 bands which are common to all sp^2 carbon materials arise from the stretching of the C–C bond and the edge of graphene sheet carbon atoms of bulk graphitic materials, respectively [35, 36]. The D2 peak is due to lattice vibration corresponding to that of the G band [37] and the D3 peak arises from the amorphous carbon in interstitial sites of the disturbed lattice of a bulk graphitic material [38] and the D4 peak is due to lattice vibrations corresponding to sp^2–sp^3 bonds [39, 40]. A relatively lower intensity of the D3 peak gives information on the amorphous nature of the material.

The SEM micrographs of the as-synthesized samples at low and high magnifications are presented in Fig. 2a–f. The micrographs show good 3D interconnected framework structure consisting mainly of porous structure and the characteristic evolution of the pores and structures of the materials studied at the same carbonization temperature of 800 °C. The structural transformation is as a result of the systematic increase of the KOH activation concentration. Adjustment of the activation agent concentration (KOH) is necessary because it is an important factor in improving the pore size and structure of the carbon thereby achieving a good nanostructured material which ultimately affects the electrochemical performance of the as-synthesized material [22, 23, 27]. The high magnifications of the micrographs show an uneven porous surface of the material activated with a mass ratio of 1:1 (AC KOH 1) (Fig. 2b). Figure 2d shows an uneven well-defined and clear porous surface of the material synthesized with a mass ratio of 1:2 (AC KOH 2), and Fig. 2f shows an uneven porous and perforated surface of the material synthesized with a mass ratio of 1:3 (AC KOH 3). The structure of the latter might be due to

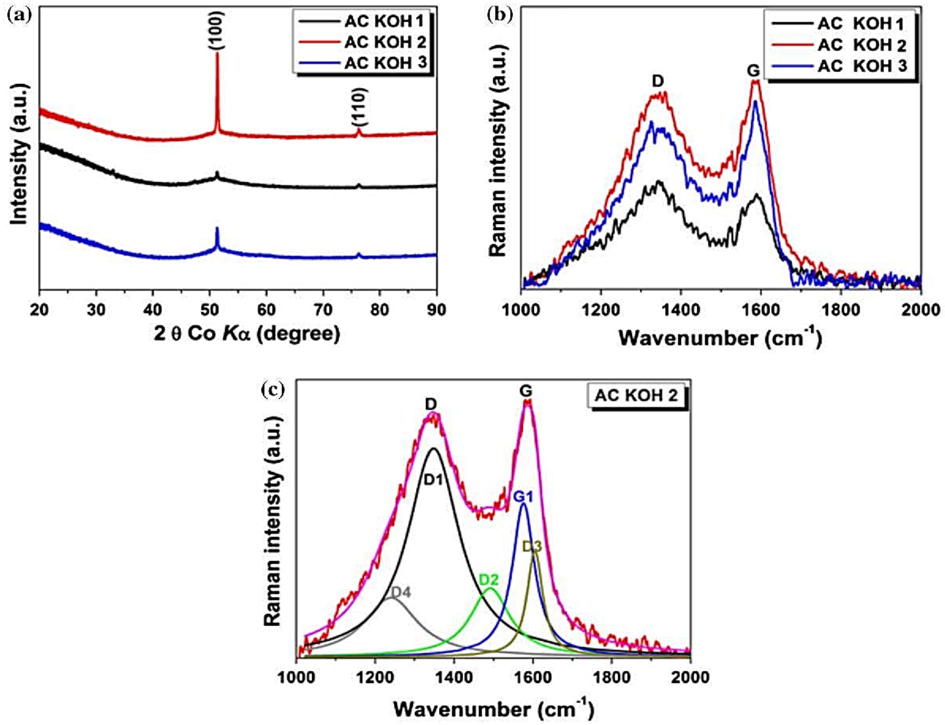

Figure 1 **a** XRD spectra and **b** Raman spectra ($\lambda_0 = 514$ nm) of the AC KOH 1, AC KOH 2 and AC KOH 3, respectively, and **c** the corresponding curve fitting (Lorentzians) of different combinations of the Raman peaks for AC KOH 2.

the etching effect of KOH [19]. The activation mostly commences with the reaction shown in Eq. 4 below. The K_2CO_3 can decompose into CO_2 and K_2O and can proceed through a reduction reaction by carbon to produce K at temperatures exceeding 700 °C, and waning completely at approximately 800 °C generating more porous carbon network [22, 32, 34].

$$6KOH + 2C \rightarrow 2K + 3H_2 + 2K_2CO_3 \quad (4)$$

$$K_2CO_3 \rightarrow K_2O + CO_2 \quad (5)$$

$$C + K_2O \rightarrow 2K + CO \quad (6)$$

The structure of the AC KOH 2 material was further investigated using high-resolution transmission electron microscopy (HRTEM). It is worth noting that under electrochemical measurements the AC KOH 2 material showed high electrochemical performance compared to AC KOH 1 and AC KOH 3 materials; hence, it was further investigated using HRTEM. Figure 3a, b shows low- and high-resolution HRTEM micrographs of AC KOH 2 material, respectively. The HRTEM micrograph in Fig. 3a shows a porous microstructure of the material consisting mainly of tightly curled disordered carbon layers (sheet-like morphology). In high-resolution HRTEM micrograph (Fig. 3b), lattice fringes are not observable suggesting that the material is mostly amorphous which is in agreement with the observed selected-area electron diffraction (SAED) pattern (Fig. 3c), which exhibits halo ring with few detectable diffraction spots indicating poor crystallinity of the material.

The EDS spectra for the as-synthesized ACs are presented in Fig. 4. The elemental compositions of the samples are summarized in Table 1. The AC materials show a high percentage of carbon followed by oxygen which could originate from the surface functional group present in the sample. The small percentage of chlorine present in the samples might be a contribution from the Embed 812 epoxy resin used in the sample preparation prior to EDS analysis.

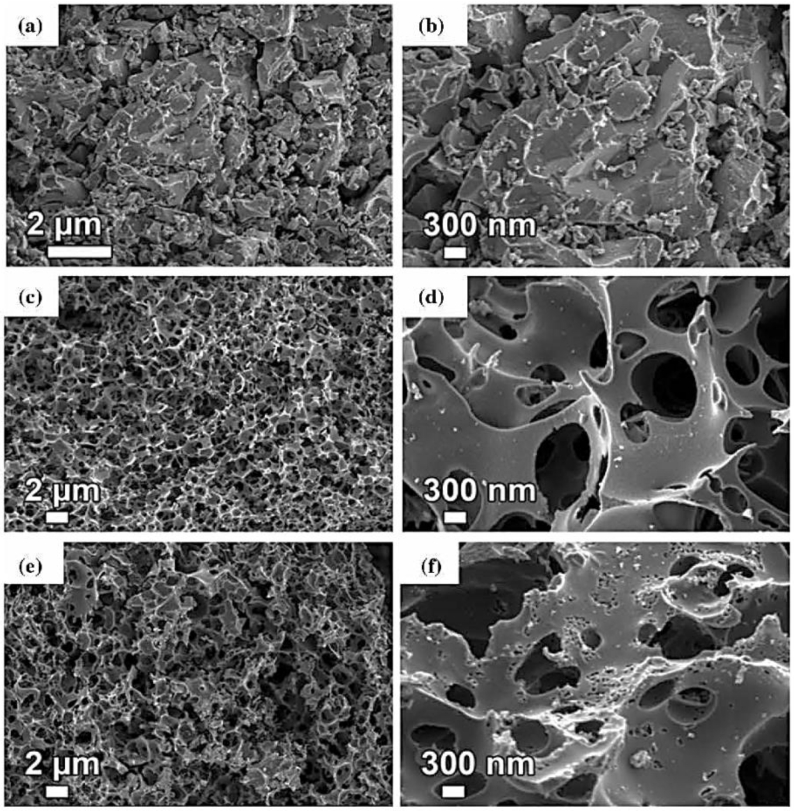

Figure 2 SEM micrographs showing low and high magnifications of **a**, **b** AC KOH 1, **c**, **d** AC KOH 2 and **e**, **f** AC KOH 3.

The porosity of the samples was investigated using the N_2 isotherms studied at −196 °C. Figure 5a, b shows typical type IV with H4 hysteresis loops signifying complex materials comprising micropores and mesopores with relative pressure (P/P_o) range of 0.01–1.0. A summary of the structural and textural properties is presented in Table 2. AC KOH 2 sample showed the highest specific surface area (SSA) and the smallest particle size. Figure 4c shows that increasing the KOH concentration enhanced the surface area of the carbon. However, a decrease in the BET SSA and an increase in the particle size can be observed for the AC KOH 3 sample when the KOH concentration was increased further, indicating a correlation between pore microstructures and activation parameters including KOH mass ratio [19, 23]. The pore size distribution (PSD) was analyzed with Barrett–Joyner–Halenda (BJH) method from the desorption branch showing PSD of the samples ranging from 2.0 to 4.2 nm.

Electrochemical measurements

The CV curves of the electrode materials (AC KOH 1, AC KOH 2 and AC KOH 3) tested in the typical three-electrode system in 1 M Na_2SO_4 neutral electrolyte at a scan rate of 50 mV s^{-1} are presented in Fig. 6a. The CV curves show rectangular shapes both in the positive and negative potential windows which are characteristic of the double-layer capacitive behavior of the material. The CV curves show different current responses within the positive and negative voltage windows of −0.8 to 0 and 0–0.8 V versus Ag/AgCl for the samples, and the CV curve

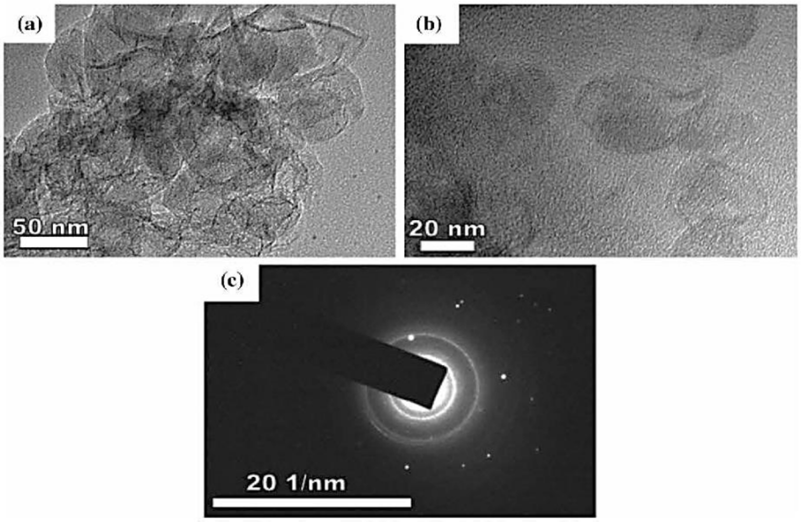

Figure 3 **a**, **b** Low- and high-resolution HRTEM micrographs of AC KOH 2 material, respectively, and **c** the corresponding selected-area electron diffraction (SAED) pattern.

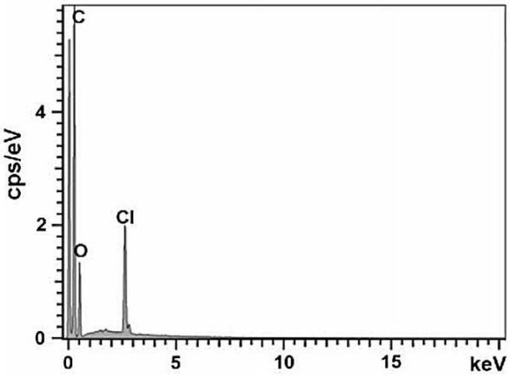

Figure 4 EDS spectra for as-synthesized AC KOH 2 sample.

Table 1 Summary of the elemental compositions of as-synthesized samples

Samples	C (wt%)	O (wt%)	Cl (wt%)
AC KOH 1	69.47	25.16	5.37
AC KOH 2	72.69	21.57	5.73
AC KOH 3	70.75	23.26	5.99

for AC KOH 2 displays better current response compared to AC KOH 1 and AC KOH 3. The C_{sp} for AC KOH 2 sample is 90.6 F g^{-1} in the positive and 100.6 F g^{-1} in the negative potential, respectively. The unequal capacitances might be because the voltage where the electrode material and/or electrolyte starts to discharge relative to the equipotential, which is the potential of the positive and negative electrodes of the device at zero voltage, are not always symmetrical for the positive and negative electrodes [13, 15]. The AC KOH 2 material was further tested in the three-electrode system in working potential windows of 0 to −0.9 V and 0–0.9 V at 50 mV s^{-1} in 1 M Na_2SO_4 and two other electrolytes, 1 M $NaNO_3$ and 1 M Li_2SO_4, as shown in Fig. 6b. The CV curves show similar rectangular curves in all three electrolytes, indicating a typical reversible EDLC behavior of the material in the different electrolytes. However, a better current response is observed in the CV curve for the electrode material tested in 1 M Na_2SO_4. It is clear from both Fig. 6a, b that sample denoted as AC KOH 2 in the 1 M Na_2SO_4 electrolyte shows the best electrochemical performance and hence from now on will concentrate on these two parameters for the two-electrode device.

The CV curves for the two-electrode measurements for the symmetric device assembled from AC KOH 2 investigated at different working potentials ranging from 1.4 to 2.0 V in 1 M Na_2SO_4 to determine the stable potential window of the cell are presented in

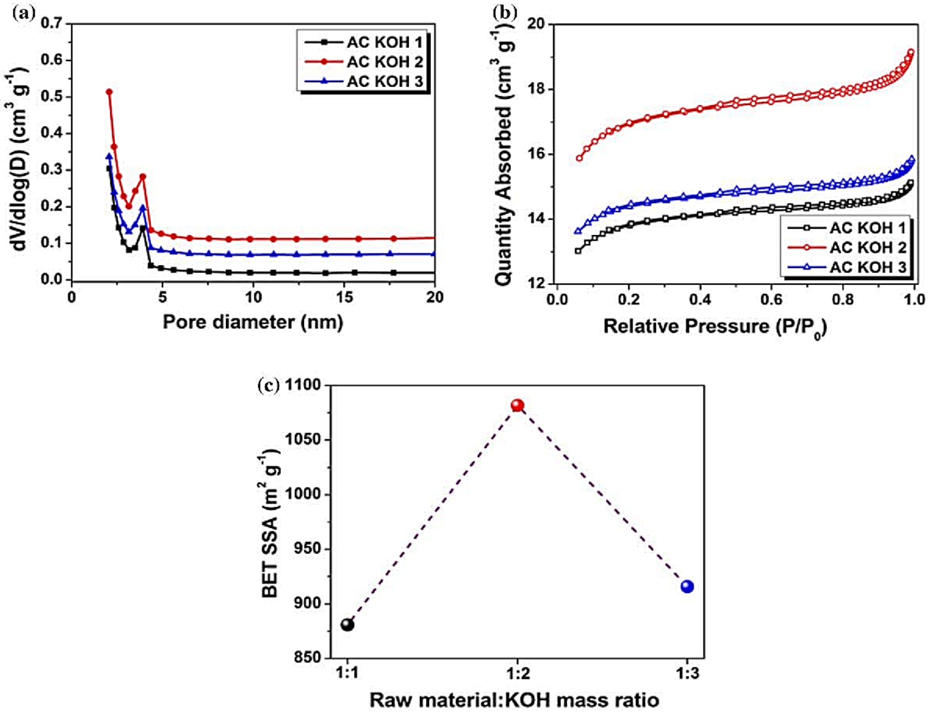

Figure 5 **a** A plot of pore size distribution of AC KOH 1, AC KOH 2 and AC KOH 3. **b** N_2 adsorption desorption isotherms of AC KOH 1, AC KOH 2 and AC KOH 3. **c** A plot of BET SSA as a function of raw material:KOH activation mass ratio.

Table 2 Textural and porosity properties of porous AC samples

Samples	Surface area (m^2 g^{-1})	Micropore volume[a] (cm^3 g^{-1})	Cumulative volume[b] (cm^3 g^{-1})	Pore diameter[c] (nm)
AC KOH 1	881	0.40	0.52	3.8
AC KOH 2	1082	0.47	0.66	4.1
AC KOH 3	916	0.42	0.54	4.0

[a] *t*-plot micropore volume

[b] BJH desorption cumulative pores between 100 and 300000 nm diameter

[c] BJH desorption average pore diameter (4 V/A)

Fig. 7a. The CV curves exhibit rectangular shape within these potential windows which is typical of electric double-layer supercapacitors indicating very quick charge/ion transport. The CVs show good stability within this operating voltage. However, above 1.8 V, the anodic current leap is observed indicating gas or oxygen evolutions as the potential tends to 2 V [13]. However, the functional groups can enhance the ion adsorption and hydrophilicity resulting in quick charge transport within the porous network of the carbon material. Thus, 1.8 V is a more stable voltage for the electrode material because no current leap is observed for this potential. Neutral electrolyte could operate up to 2.0 V because of the presence of H^+ and OH^- in low amounts relative to those of acidic and alkaline electrolytes [1, 15]. Also,

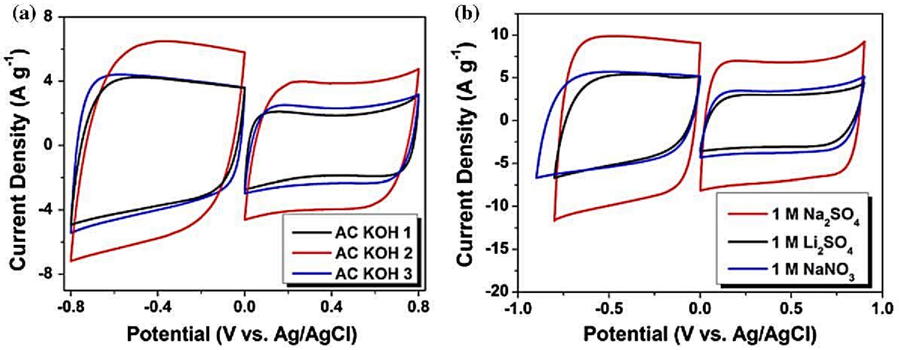

Figure 6 Three electrode measurements: **a** CV curves for AC KOH 1, AC KOH 2 and AC KOH 3 in −0.8 to 0 and 0 0.8 V potential windows at 50 mV s^{-1} and **b** CV curves of AC KOH 2 at potential windows of 0 to−0.9 and 0 0.9 V at 50 mV s^{-1} in three different electrolytes.

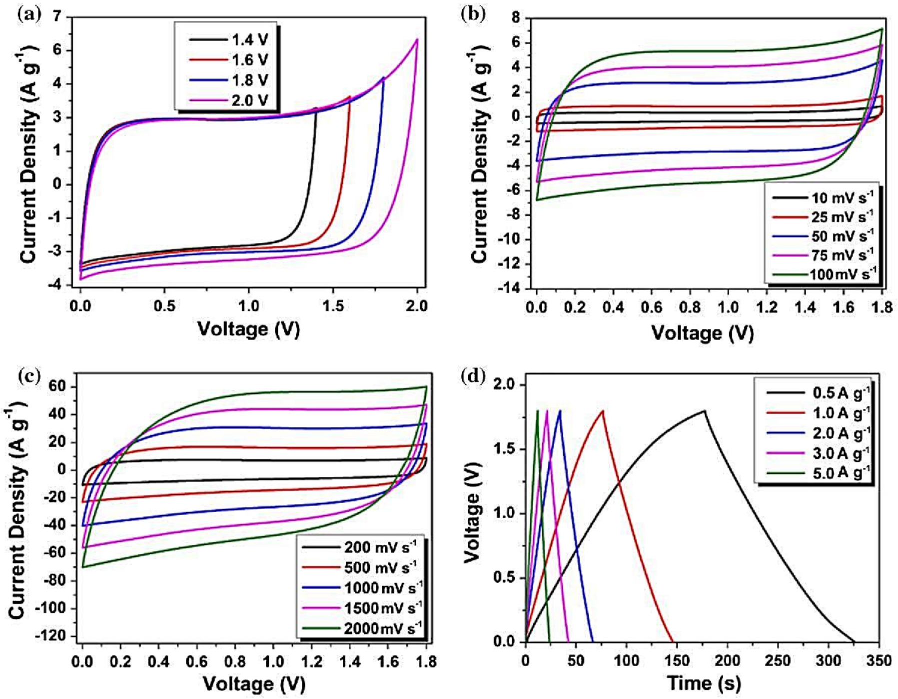

Figure 7 **a** CV curves of AC KOH 2 device at 50 mV s^{-1} at different potential windows in 1 M Na_2SO_4, **b** CV curves of AC KOH 2 at scan rates ranging from 10 to 100 mV s^{-1}, **c** CV curves of AC KOH 2 at high scan rates ranging from 200 to 2000 mV s^{-1}, **d** CD curves of AC KOH 2 symmetric device at 0.5 5 A g^{-1} in 1 M Na_2SO_4.

neutral electrolytes are able to achieve higher or extended voltage window of up to 2.0 V than acid and alkaline electrolytes because of their pH, strong ion solvation and high over-potential for di-hydrogen evolution at the negative electrode [15]. Figure 7b, c shows the CV curves of the two-electrode cell within

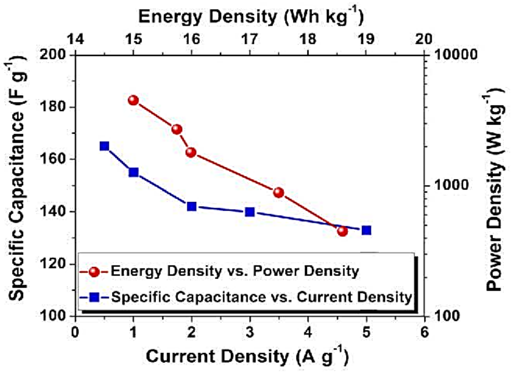

Figure 8 Specific capacitance as a function of current density and the energy density as a function of power density (Ragone plot) for the symmetric device.

the potential window of 0.0–1.8 V at scan rates of 10–100 mV s^{-1} and at high scan rates of 200–2000 mV s^{-1}, respectively. The CV curves maintain rectangular shapes with symmetric cathodic and anodic current responses even at very high scan rates indicating quick charge transport which is as a result of the low equivalent series resistance (R_{es}) of the electrodes and is characteristic of highly capacitive and reversible electrochemical performance of the as-synthesized material [13, 41]. The galvanostatic charge/discharge (GCD) measurements performed at 0.5–5 A g^{-1} are presented in Fig. 7d. A linear charge/discharge curve is observed which is typical of an ideal EDLC with reversible anodic and cathodic ionic transport. A good rate capability is indicated by the cell as only a slight decrease in capacitance is observed at the different current densities. A C_{SP} of 166 F g^{-1} is observed for the symmetric cell at 0.5 A g^{-1} and is maintained at 133 F g^{-1} as the current density is increased to 5 A g^{-1}, displaying 80% capacitance retention of the symmetric device with increasing current density.

The energy and power densities of the symmetric device were calculated from Eqs. 2, 3. The C_{SP} as a function of current density was calculated using Eq. 2. The Ragone plot which relates the energy and power densities of the symmetric device is presented in Fig. 8. The symmetric device displays a high energy density of 18.6 W h kg^{-1} and power density of 449.4 W kg^{-1} at a current density of 0.5 A g^{-1}. This work shows superior electrochemical performance as compared to other biomass-derived activated carbon [1, 15, 26–30, 34, 42, 43]. A comparison of this work with other previous reports is presented in Table 3. The excellent performance of this device can be attributed to the high specific surface area, high pore volume and large mesopore volume and well-defined pore size distribution which boost proper ion transfer within the electrolyte at higher current densities which are necessary for EDLCs to achieve high power delivery rate and high storage capacity and also on the ability of the material to work within the positive and negative potential windows thereby enhancing the potential range of the material in the symmetric device [22, 27, 30].

The stability of the symmetric device was investigated over 5000 charge/discharge cycles, and the device displays ~100% capacitance retention at the end of the charge/discharge cycle (Fig. 9a). Also, stability test based on voltage holding was used to

Table 3 Electrochemical performance comparison of activated carbon derived from different precursors

Precursor	Activation agent	S_{BET} (m^2 g^{-1})	Voltage (V)	Specific capacitance (F g^{-1})	Current density (A g^{-1})	Electrolyte	Energy density (W h Kg^{-1})	References
Pine cone	KOH	1515	2.0	137	0.1	1 M Na_2SO_4	19	[1]
Pine cone	KOH	1515	1.0	90	0.1	1 M Na_2SO_4		[34]
Coconut shell	$ZnCl_2$	2440	0.7	246	0.25	0.5 H_2SO_4	7.6	[27]
Tree bark biomass	KOH	1018	0.6	114	0.3	−1 M Na_2SO_4		[43]
Coconut leaves		492.9	1.0	133	0.2	6 M KOH		[28]
Rubber wood saw dust		913	1.0	138		H_2SO_4	2.63	[44]
Pistachio nutshells	KOH	1069	1.1	261	0.2	6 M KOH	10	[29]
Sunflower seed shell	KOH	2584	0.9	311	0.25	3 M KOH	4.8	[26]
Cork (*Q. Suber*)	KOH	1081	1.8	166	0.5	1 M Na_2SO_4	18.6	This work

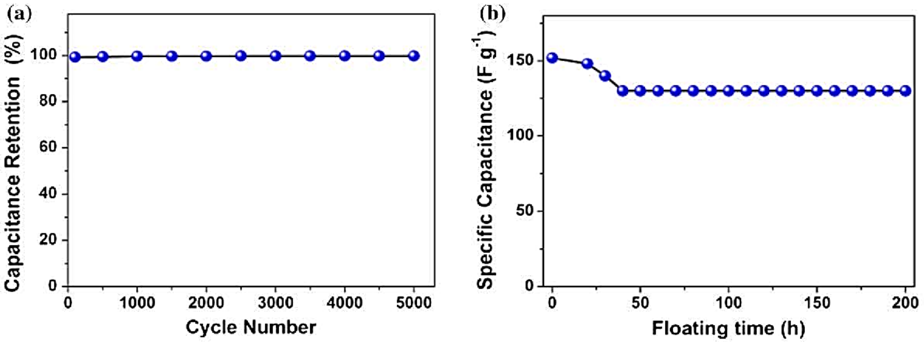

Figure 9 Stability test of AC KOH 2 sample: **a** capacitance retention as a function of a number of cycles and **b** specific capacitance as a function of floating time.

study the long-term stability of the symmetric device. Figure 9b shows the curve of voltage holding over a time duration of 200 h. The floating time is based on periodic potentiostatic mode and sequential GCD at 1 A g^{-1}. The floating and galvanostatic processes are reiterated for a total of 200 h. The floating shows a

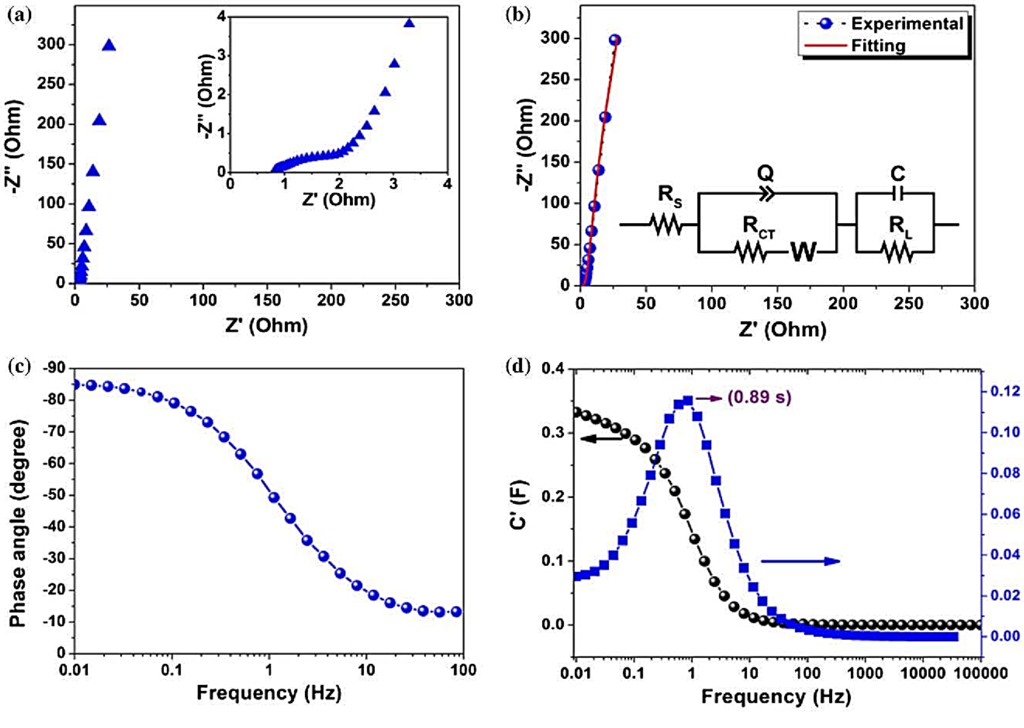

Figure 10 **a** EIS plot, **b** EIS fitting and equivalent series circuit (*inset*), **c** phase angle as a function of frequency and **d** real and imaginary plot of capacitance as a function of frequency.

significant effect on the capacitive behavior of the devices which decreases in the first 40 h of floating before stabilizing at $\sim 130 \text{ F g}^{-1}$ for the rest of the floating time, with capacitance retention of 85% over 200 h. The decrease in capacitance could be as a result of the wearing of the surface functional group which could facilitate ion transport within the electrode material [44].

Electrochemical impedance spectroscopy (EIS) measurements were also taken. Figure 10a shows the Nyquist impedance plot for the EIS measurements analyzed in the frequency range of 100 kHz–0.01 Hz. The diameter of the arc within the high- and middle-frequency region shows the charge transfer resistance (R_{ct}) of 1.3 Ω. The solution resistance (R_s) of 0.77 Ω (intercept to the x-axis, see inset of Fig. 10a) was observed from the Nyquist impedance plot with the real Z' axis which sums up the resistive components within the device [44, 45]. The fitting of the Nyquist plot is presented in Fig. 10b with the equivalent circuit (insert to Fig. 10b). The constant phase element Q and the charge transfer resistance (R_{ct}) are connected in series with R_s. The diffusion element (W) which is in series with the R_{ct} corresponds to the diffusion from the high- to the low-frequency region. Normally, an ideal electrode with mass capacitance (C) at very low frequencies should lead to a vertical line parallel to the $-Z''$ axis [44]. However, from Fig. 10a, a slight deviation from the ideal behavior is observed which can be as a result of the resistive element linked with C. This resistive element termed leakage current is connected in parallel with the mass capacitance. The real and imaginary part of the capacitances as a function of frequency [$C'(\omega)$ and $C''(\omega)$] was evaluated using a complex capacitance model and is presented in Fig. 10d. For the electrodes, the value of C' at 0.01 Hz is 0.33 F which corresponds to the real reachable capacitance of the cell at this frequency. C'' represents the energy utilized and it also shows the frequency evolution between an ideal capacitive and resistive behavior [46]. The relaxation time (τ) evaluated from $\tau = 1/\omega_{\max} = 1/(2\pi f_{\max})$ is ~ 0.89 s corresponding to a frequency of ~ 1.0 Hz. This relaxation time shows that the energy stored in the cell can be released within 0.89 s. The phase angle as a function of frequency is presented in Fig. 10c. It shows that the phase angle of the cell is $\sim -85°$, which is very near to $-90°$ indicating a complete capacitive behavior of the electrodes.

Conclusions

Activated carbon from lightweight material cork (*Q. Suber*) has been successfully synthesized using a systematic approach which is environmentally-friendly and cost effective. The material shows well-defined and clear porous surface with large surface area and good micropore and mesopore volume. A high specific capacitance of 166 F g^{-1} was obtained at a current density of 0.5 A g^{-1} and was maintained at 133 F g^{-1} as the current density increased to 5.0 A g^{-1} with energy and power densities of 18.6 and 449.4 W kg^{-1}, respectively, for the symmetric device. This device displays good rate capability in the neutral electrolyte. The device also shows excellent stability and without significant degradation after 200 h of floating time. The results suggest that the material is a potentially excellent material for supercapacitor applications.

Acknowledgements

This work is based on research supported by the South African Research Chairs Initiative (SARChI) of the Department of Science and Technology and the National Research Foundation (NRF) of South Africa (Grant No. 61056). Any opinion, finding and conclusion or recommendation expressed in this material is that of the author(s) and the NRF does not accept any liability in this regard. Faith O. Ochai-Ejeh acknowledges NRF through SARChI in Carbon Technology and Materials, and the Department of Physics at the University of Pretoria for financial support.

Compliance with ethical standards

Conflict of interest The authors declare no competing financial interest.

References

[1] Bello A, Manyala N, Barzegar F et al (2016) Renewable pine cone biomass derived carbon materials for supercapacitor application. RSC Adv 6:1800 1809. doi:10.1039/C5RA21708C

[2] Yu G, Hu L, Vosgueritchian M et al (2011) Solution-processed graphene/MnO_2 nanostructured textiles for high-

performance electrochemical capacitors. Nano Lett 11:2905 2911. doi:10.1021/nl2013828

[3] Biswal M, Banerjee A, Deo M, Ogale S (2013) From dead leaves to high energy density supercapacitors. Energy Environ Sci 6:1249. doi:10.1039/c3ee22325f

[4] Shaikjee A, Coville NJ (2012) The role of the hydrocarbon source on the growth of carbon materials. Carbon NY 50:3376 3398. doi:10.1016/j.carbon.2012.03.024

[5] Gan JK, Lim YS, Pandikumar A et al (2015) Graphene/polypyrrole-coated carbon nanofiber core shell architecture electrode for electrochemical capacitors. RSC Adv 5:12692 12699. doi:10.1039/C4RA14922J

[6] Majeau-Bettez G, Hawkins TR, Strømman AH (2011) Life cycle environmental assessment of lithium-ion and nickel metal hydride batteries for plug-in hybrid and battery electric vehicles. Environ Sci Technol 45:4548 4554. doi:10.1021/es103607c

[7] Zhang LL, Zhao XS (2009) Carbon-based materials as supercapacitor electrodes. Chem Soc Rev 38:2520. doi:10.1039/b813846j

[8] Stoller MD, Ruoff RS (2010) Best practice methods for determining an electrode material's performance for ultracapacitors. Energy Environ Sci 3:1294. doi:10.1039/c0ee00074d

[9] Patil DS, Shaikh JS, Dalavi DS et al (2011) Chemical synthesis of highly stable PVA/PANI films for supercapacitor application. Mater Chem Phys 128:449 455. doi:10.1016/j.matchemphys.2011.03.029

[10] Miller JR, Simon P (2008) Materials science. Electrochemical capacitors for energy management. Science 321:651 652. doi:10.1126/science.1158736

[11] Jain A, Balasubramanian R, Srinivasan MP (2016) Hydrothermal conversion of biomass waste to activated carbon with high porosity: a review. Chem Eng J 283:789 805. doi:10.1016/j.cej.2015.08.014

[12] Chen H, Hu L, Chen M et al (2014) Nickel cobalt layered double hydroxide nanosheets for high-performance supercapacitor electrode materials. Adv Funct Mater 24:934 942. doi:10.1002/adfm.201301747

[13] Chae JH, Chen GZ (2012) 1.9 V aqueous carbon carbon supercapacitors with unequal electrode capacitances. Electrochim Acta 86:248 254. doi:10.1016/j.electacta.2012.07.033

[14] Peng C, Zhang S, Zhou X, Chen GZ (2010) Unequalisation of electrode capacitances for enhanced energy capacity in asymmetrical supercapacitors. Energy Environ Sci 3:1499. doi:10.1039/c0ee00228c

[15] Demarconnay L, Raymundo-Piñero E, Béguin F (2010) A symmetric carbon/carbon supercapacitor operating at 1.6 V by using a neutral aqueous solution. Electrochem Commun. doi:10.1016/j.elecom.2010.06.036

[16] An K, Kim W, Park Y, Moon J (2001) Electrochemical properties of high-power supercapacitors using single-walled carbon nanotube electrodes. Adv Funct Mater 11:387 392

[17] Wang H, Liang Y, Mirfakhrai T et al (2011) Advanced asymmetrical supercapacitors based on graphene hybrid materials. Nano Res 4:729 736

[18] Fan Z, Yan J, Wei T et al (2011) Asymmetric supercapacitors based on graphene/MnO_2 and activated carbon nanofiber electrodes with high power and energy density. Adv Funct Mater 21:2366 2375. doi:10.1002/adfm.201100058

[19] Sevilla M, Fuertes AB (2016) A green approach to high-performance supercapacitor electrodes: the chemical activation of hydrochar with potassium bicarbonate. Chemsuschem 9:1880 1888. doi:10.1002/cssc.201600426

[20] Wei L, Yushin G (2012) Nanostructured activated carbons from natural precursors for electrical double layer capacitors. Nano Energy 1:552 565. doi:10.1016/j.nanoen.2012.05.002

[21] Wang H, Xu Z, Kohandehghan A et al (2013) Interconnected carbon nanosheets derived from hemp for ultrafast supercapacitors with high energy. ACS Nano 7:5131 5141. doi:10.1021/nn400731g

[22] Wang J, Kaskel S (2012) KOH activation of carbon-based materials for energy storage. J Mater Chem 22:23710. doi:10.1039/c2jm34066f

[23] Lv Y, Zhang F, Dou Y et al (2012) A comprehensive study on KOH activation of ordered mesoporous carbons and their supercapacitor application. J Mater Chem 22:93. doi:10.1039/c1jm12742j

[24] Béguin F, Presser V, Balducci A, Frackowiak E (2014) Carbons and electrolytes for advanced supercapacitors. Adv Mater 26:2219 2251. doi:10.1002/adma.201304137

[25] Bello A, Barzegar F, Madito MJ et al (2016) Stability studies of polypyrole- derived carbon based symmetric supercapacitor via potentiostatic floating test. Electrochim Acta 213:107 114. doi:10.1016/j.electacta.2016.06.151

[26] Li X, Xing W, Zhuo S et al (2011) Preparation of capacitor's electrode from sunflower seed shell. Bioresour Technol 102:1118 1123. doi:10.1016/j.biortech.2010.08.110

[27] Jain A, Xu C, Jayaraman S et al (2015) Mesoporous activated carbons with enhanced porosity by optimal hydrothermal pre-treatment of biomass for supercapacitor applications. Microporous Mesoporous Mater 218:55 61. doi:10.1016/j.micromeso.2015.06.041

[28] Sulaiman KS, Mat A, Arof AK (2016) Activated carbon from coconut leaves for electrical double-layer capacitor. Ionics 22:911 918. doi:10.1007/s11581-015-1594-9

[29] Xu J, Gao Q, Zhang Y et al (2014) Preparing two-dimensional microporous carbon from Pistachio nutshell with high areal capacitance as supercapacitor materials. Sci Rep 4:845 854. doi:10.1038/srep05545

[30] Barzegar F, Bello A, Fashedemi OO et al (2015) Synthesis of 3D porous carbon based on cheap polymers and graphene foam for high-performance electrochemical capacitors. Electrochim Acta 180:442 450. doi:10.1016/j.electacta.2015.08.148

[31] Laheäär A, Przygocki P, Abbas Q, Béguin F (2015) Appropriate methods for evaluating the efficiency and capacitive behavior of different types of supercapacitors. Electrochem Commun. doi:10.1016/j.elecom.2015.07.022

[32] Zheng X, Lv W, Tao Y et al (2014) Oriented and interlinked porous carbon nanosheets with an extraordinary capacitive performance. Chem Mater 26:6896 6903. doi:10.1021/cm503845q

[33] Lee JW, Hall AS, Kim J-D, Mallouk TE (2012) A facile and template-free hydrothermal synthesis of Mn_3O_4 nanorods on graphene sheets for supercapacitor electrodes with long cycle stability. Chem Mater 24:1158 1164. doi:10.1021/cm203697w

[34] Manyala N, Bello A, Barzegar F et al (2015) Coniferous pine biomass: a novel insight into sustainable carbon materials for supercapacitors electrode. Mater Chem Phys 182:139 147. doi:10.1016/j.matchemphys.2016.07.015

[35] Wang Y, Alsmeyer DC, McCreery RL (1990) Raman spectroscopy of carbon materials: structural basis of observed spectra. Chem Mater 2:557 563. doi:10.1021/cm00011a018

[36] Malard LM, Pimenta MA, Dresselhaus G, Dresselhaus MS (2009) Raman spectroscopy in graphene. Phys Rep 473:51 87. doi:10.1016/j.physrep.2009.02.003

[37] Sadezky A, Muckenhuber H, Grothe H et al (2005) Raman microspectroscopy of soot and related carbonaceous materials: spectral analysis and structural information. Carbon NY 43:1731 1742. doi:10.1016/j.carbon.2005.02.018

[38] Jawhari T, Roid A, Casado J (1995) Raman spectroscopic characterization of some commercially available carbon black materials. Carbon NY 33:1561 1565. doi:10.1016/0008-6223(95)00117-V

[39] Sze S (2001) Raman spectroscopic characterization of carbonaceous aerosols. Atmos Environ 35:561 568. doi:10.1016/S1352-2310(00)00325-3

[40] Dippel B, Jander H, Heintzenberg J (1999) NIR FT Raman spectroscopic study of flame soot. Phys Chem Chem Phys 1:4707 4712. doi:10.1039/a904529e

[41] Jang Y, Jo J, Choi Y-M et al (2013) Activated carbon nanocomposite electrodes for high performance supercapacitors. Electrochim Acta 102:240 245. doi:10.1016/j.electacta.2013.04.020

[42] Momodu DY, Madito MJ, Barzegar F et al (2017) Activated carbon derived from tree bark biomass for high performance electrochemical capacitors. J Solid State Electrochem 21:859 872. doi:10.1007/s10008-016-3432-z

[43] Taer E, Deraman M, Talib IA et al (2011) Preparation of a highly porous binderless activated carbon monolith from rubber wood sawdust by a multi-step activation process for application in supercapacitors. Int J Electrochem Sci 6:3301 3315

[44] Barzegar F, Bello A, Momodu D et al (2016) Preparation and characterization of porous carbon from expanded graphite for high energy density supercapacitor in aqueous electrolyte. J Power Sources 309:245 253. doi:10.1016/j.jpowsour.2016.01.097

[45] Luo J, Jang HD, Huang J (2013) Effect of sheet morphology on the scalability of graphene-based ultracapacitors. ACS Nano 7:1464 1471. doi:10.1021/nn3052378

[46] Taberna PL, Simon P, Fauvarque JF (2003) Electrochemical characteristics and impedance spectroscopy studies of carbon carbon supercapacitors. J Electrochem Soc 150:A292. doi:10.1149/1.1543948

4.1.4 Concluding remark

Activated carbon (AC) was successfully synthesized using KOH as an activating agent in different mass ratios denoted as AC 1:1, AC 1:2 and AC 1:3 respectively. The study of the morphology, structure and porosity of the samples showed a correlation between the sample microstructures and KOH activation concentration. The samples were tested in three electrode system in 1 M Na_2SO_4, 1 M $NaNO_3$ and 1 M Li_2SO_4 neutral electrolytes. The AC 1:2 material displayed best performance among the materials synthesized at different mass ratios and also in 1 M Na_2SO_4. A symmetric device was successfully fabricated using AC 1:2 and 1 M Na_2SO_4 which displayed a specific capacitance of 166 F g^{-1} at 0.5 A g^{-1} and maintained a capacitance value of 133 F g^{-1} as the current density is increased to 5 A g^{-1}, displaying 99.8 % capacitance retention of the symmetric device and excellent stability after potentioatic floating for 200 h at 1.8 V maximum voltage.

4.2 Investigation of electrochemical performance of hybrid supercapacitor based on Co-Mn LDH as positive electrode and AC derived from cork (quercus suber) as negative electrode.

4.2.1 Introduction

The fabrication of high-performance energy storage devices is essential for meeting the increasingly high demands for high power, high energy density and low cost energy storage devices[213]. Supercapacitors based on EDLC electrode materials can deliver high power densities due to their non-faradaic surface reactions but their energy density is considerably limited. On the other hand, Faradaic capacitors which store charges by rapid redox reaction involving intercalation/de-intercalation and diffusion of ions, results in low power density production of the device. Therefore, for future energy needs involving large-scale energy storage systems bridging the gap by overcoming the limitation of both low power density and low energy density is a fundamental issue[15,81,213].

Hybrid supercapacitors often combine the advantages of the EDLC and faradaic capacitors in order to increase the energy density without compromising the power density [29,213]. However, for optimal performance of the hybrid device, the choice/production of highly functional material for the device fabrication is essential.

Among the materials often considered for use as positive electrode materials for hybrid supercapacitors, metal layered double hydroxides (LDH) have shown to possess good redox activity, high conductivity, large inter-layer spacing and good ion transport for reaction species which are vital for high performance hybrid devices [1,50]. Co-Mn LDH has drawn research interest because it is easily synthesized, environmentally friendly and has a distinctive redox combination of the Co^{2+} and Mn^{2+} ions.

EDLC materials considered for use as negative electrode materials are quite exhaustive but activated carbon is the top choice material because of its unique properties which include large SSA, good pore size distribution, and high concentration of oxygenated functional groups[47,214].

In this section, we discuss the electrochemical performance of the hybrid device based on Co-Mn LDH with flake-like morphology as positive electrode. The Co-Mn LDH was synthesized using a facile solvothermal method by dissolving $Co(NO_3)_2.H_2O$, $MnSO_4.H_2O$ and CH_4N_2O in methanol in a ratio of 1:2:12, as detailed in section 3. Activated carbon derived from cork (Quercus suber) by $KHCO_3$activation after hydrothermal pretreatment of the raw cork material was used as negative electrode. The device displayed good electrochemical performance with an excellent cycling stability over a prolonged period of time.

4.2.2 Result and discussion

Details of the results from this work is in the following publication.

Electrochimica Acta 252 (2017) 41–54

Contents lists available at ScienceDirect

Electrochimica Acta

journal homepage: www.elsevier.com/locate/electacta

Research Paper

High performance hybrid supercapacitor device based on cobalt manganese layered double hydroxide and activated carbon derived from cork (Quercus Suber)

F.O. Ochai-Ejeh, M.J. Madito, D.Y. Momodu, A.A Khaleed, O. Olaniyan, N. Manyala*

Department of Physics, Institute of Applied Materials, SARChI Chair in Carbon Technology and Materials, University of Pretoria, 0028, South Africa

ARTICLE INFO

Article history:
Received 22 June 2017
Received in revised form 18 August 2017
Accepted 27 August 2017
Available online 31 August 2017

Keywords:
Supercapacitor
Hybrid device
Activated Carbon
Solvothermal
Cobalt manganese LDH

ABSTRACT

Thin Co-Mn layered double hydroxide (LDH) nanoflakes and Activated carbon (AC) from cork raw material (Quercus Suber) with highly porous structure and good textural properties was synthesized by a facile solvothermal and two-step eco-friendly hydrothermal syntheses routes respectively. A hybrid device was successfully fabricated using Co-Mn LDH as the positive electrode and AC as negative electrode. The device exhibited a high energy density of 20.3 W h kg^{-1} and corresponding power density of up to 435 W kg^{-1} at 0.5 A g^{-1} current density in 1 M KOH aqueous electrolyte. The device also displayed a very high stability with 99.7% capacitance retention after 10,000 continuous charge-discharge cycles and negligible degradation after subsequently subjecting it to voltage holding test at its maximum operating voltage for 70 hours. These results showcase the potential use of this hybrid device as possible electrodes for high energy density supercapacitor application.

1. INTRODUCTION

Supercapacitors (SCs) are highly desirable as energy storage devices because they have the merit of being low cost, with high power density, excellent reversibility, good stability and fast charge – discharge propagation [1–3]. As compared to electrolytic and electrostatic capacitors, SCs have higher energy density but they are still reasonably lower than batteries and fuel cells. This limits their use to supply energy for extended periods of time except when they are combined with lithium-ion batteries or some other power sources [2,4]. This has stimulated the research interest on the energy density of SCs to be comparable to that of batteries. Based on the mechanism of charge, SCs can be grouped into three categories namely, electric double layer capacitors (EDLCs), faradaic capacitors or pseudocapacitors. EDLCs store energy by a non-faradaic process which involves electrostatic reversible absorption or desorption of ions at the interface of the electrode/electrolyte. Faradaic capacitors store charges through rapid redox reaction involving intercalation of ions at the active material surface. While pseudocapacitors, store charges through an electron transfer mechanism rather than by just the accumulation of ions on the electrochemical double layer [4–7]. Hybrid supercapacitors often make use of both EDLC and faradaic type storage mechanism by combining the individual characteristics of the faradaic and non-faradaic capacitors so as to optimize their energy without losing the power density [4,8,9].

Several types of EDLC materials have been utilized as SCs material electrodes. These includes carbide-derived carbons, graphene, carbon-nanofibers, zeolite-templated carbon, carbon nanotubes (CNTs) and activated carbon [10–22]. Amongst these materials, the most commonly used in hybrid devices is activated carbon due to its high specific surface area (SSA), ease of production, light weight, relatively low cost, good porosity and presence of pseudocapacitive charge transfer mechanism which can contribute to increased specific capacitance due to the presence of functional groups [3,8,23–25]. However, controlling the pore structure has not been that easy to achieve despite extensive research and improvement on the activation process and this greatly limits their performance in some applications [13,24,26]. This is because supercapacitors require a good combination of a hierarchical pore size distribution with large SSA for optimal performance [27,28]. In the production of porous carbons, KOH has been the most common chemical activating agent, but its corrosiveness and environmental unfriendliness limits its industrial utilization [27,28].The poor textural and morphological properties recorded from many carbon-containing precursors including some biomass materials, have also hampered

---

* Corresponding author.
E-mail addresses: ncholu.manyala@up.ac.za, manyalancholu@gmail.com (N. Manyala).

http://dx.doi.org/10.1016/j.electacta.2017.08.163
0013-4686/

on the efficient device application of activated carbon [24,27,29]. Recently, hydrochar has been considered a better precursor for the synthesis of high performance carbons since they have a high concentration of oxygenated functional groups[27,29–31]. In addition to pre-treatment of the carbon containing sources, some studies have also adopted other types of activating agents for the synthesis of porous carbons with good porosity and high surface areas [23,27–29]. Amongst these, potassium bi-carbonate (K_2CO_3) and potassium hydrogen carbonate ($KHCO_3$), have been recently shown to preserve the hydrochar morphology due to its mild nature as compared to KOH, leading to production of activated carbons with closely packed porous structures with lesser ion diffusion distances resulting in better electrochemical performance [23]. Potassium-based activating agents easily operate independent of the ordering of the material structure which makes the K-intercalation easily attainable [30]. Various materials have also been used as positive electrode materials for hybrid SC devices. These includes conducting polymers, metal oxides, metal hydroxides and bi-metallic hydroxides [31–33] because they offer good redox activity, are relatively cheap, easily produced with facile synthesis techniques, have low toxicity and are environmentally friendly [33,34].

Metal layered double hydroxides (LDH) have been reported to have higher conductivity, large inter-layer spacing, better ion exchange and transport for the reaction species which are neccessary for the production of hybrid devices with superior electrochemical performance [35–37]. Some of the LDH materials that have been investigated as positive electrode materials for hybrid supercapacitors include Ni-Co, Co-Al, Ni-Al, Ni-Mn, Co-Mn etc [41–44]. More specifically, Co-Mn has recently attracted research interest due to the unique redox combination of both Co^{2+}/Mn^{2+} and many researchers have reported on optimizing the structure and morphology of the as-synthesized Co-Mn LDH and its composites with other materials using various interesting techniques. Nonetheless, they are still quite limited studies which have been actively carried out on the electrochemical evaluation of the Co-Mn LDH material using it as a positive electrode material with activated carbon from cheap biomass sources as the negative electrode for high energy density hybrid supercapacitors. Furthermore, only a few studies actually exist on studying the device stability of this particular hybrid combination with respect to actual testing conditions suitable for practical use.

The present report, embarks on a detailed evaluation of the electrochemical performance of a hybrid electrochemical capacitor consisting of nanostructured Co-Mn LDH as positive electrode and activated carbon as negative electrode. The full device after being subjected to the routine electrochemical tests was also exposed to lengthy floating and self-discharge tests to fully elucidate the processes taking place at the electrode/electrolyte level. The results obtained from this study would aid in the further understanding of the processes which occur after a maximum voltage has been applied over a long period of time and this would lead to developing novel blueprints for designing stable and efficient hybrid energy storage devices.

2. EXPERIMENTAL

2.1. Material synthesis

2.1.1. Synthesis of Co-Mn LDH (Positive electrode material)

CH_4N_2O (Merck, Purity ≥98%), $Co(NO_3)2.6H_2O$ (Sigma Aldrich ≥98%), $MnSO_4.H_2O$ (Merck, Purity ≥98%) and CH_3OH (Sigma Aldrich ≥99.9%) were used without further purification. Co-Mn LDH nanoflakes was synthesized by a facile solvothermal method. In a typical synthesis procedure, 0.05 M $Co(NO_3)_2.6H_2O$, 0.10 M $MnSO_4.H_2O$ and 0.60 M CH_4N_2O was put into 60 ml of methanol (CH_3OH) and sonicated for 10 minutes. The solution was then poured into a 100 ml Teflon lined autoclave and placed in the oven at 120 °C for 6 hours. The resulting product was then filtered and washed several times with deionized water. Scheme 1 shows the complete synthesis route of the Co-Mn LDH nanoflakes (see micrograph image).

2.1.2. Synthesis of AC (Negative electrode material)

Low-cost mesoporous activated carbon was synthesized via a two-step eco-friendly synthesis route (See Scheme 2). Firstly, 10 g of raw cork (Quercus Suber) was properly washed using acetone and deionized water and dried in an oven. Then, the raw cork was put into a 100 ml Teflon lined autoclave which contains 80 ml deionized water and 0.8 ml of 0.5 M sulfuric acid and treated hydrothermally at 160 °C for 12 hours. The addition of sulfuric acid is adopted to reduce the lignin and cellulose content present in the raw cork material and improve the quality of the hydrochar obtained. The hydrochar produced was then washed severally with distilled water and dried in an oven. The hydrochar was crushed and weighed again followed by activation with potassium hydrogen carbonate ($KHCO_3$) in a 1:1 ratio. Then, the activated hydrochar was put into a quartz tube and carbonized at a ramping temperature of 5 °C/min from ambient temperature to 850 °C for 2 hours in argon flow. The obtained activated carbon was washed with 3 M HCl (to remove excess unreacted activating agent present and also to wash off any impurities present in the sample) and deionized water and left to dry in the oven at 60 °C for 12 hours.

2.2. Morphological, Structural, Composition and Electrochemical Characterization

Scanning electron microscopy (SEM) analysis was performed using a Zeiss Ultra plus 55 field emission scanning electron microscope (FE-SEM) working at an accelerating voltage of 2.0 kV

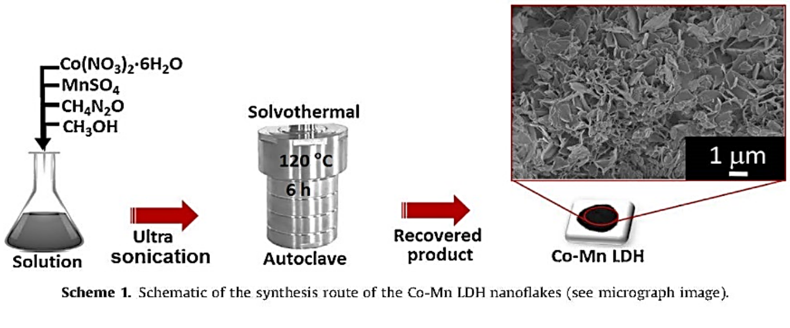

Scheme 1. Schematic of the synthesis route of the Co-Mn LDH nanoflakes (see micrograph image).

Scheme 2. Schematic of the synthesis route of the activated carbon.

to determine the morphology of the materials. High resolution transmission electron microscopy (HR-TEM), selected area diffraction (SAED) and the energy-dispersive X-ray (EDX) analysis of the samples were performed using JEOL 2100 (from Tokyo Japan) operated at 200 kV. X-ray Diffraction (XRD) studies was performed using an XPERT-PRO diffractometer (PANalytical BV the Netherlands) to determine the structural properties of the samples. A Micrometrics TriStar II 3020 analyzer was used to measure the specific surface area (SSA) and pore size distribution (PSD) using the Brunauer-Emmett-Teller (BET) and Barrett-Joyner-Halenda (BJH) techniques. The SSA was obtained from the N_2-adsorption/desorption isotherm while the PSD data was obtained from the desorption part of the BJH isotherm. Fourier transform infrared (FT-IR) spectroscopy was performed in the range of 4000–500 cm^{-1} at 2 cm^{-1} resolution using Perkin Elmer Spectrum RX I FT-IR system. Prior to taking the FT-IR measurements, the pellets used were prepared by properly mixing the samples with KBr in a ratio of 100:1. X-ray photoelectron spectroscopy (XPS) measurements of the samples were carried out using a Physical Electronics VersaProbe 5000 spectrometer.

The Co-Mn LDH and AC samples were tested in three- and two-electrode configurations with a multichannel channel Bio-Logic VMP300 potentiostat/galvanostat workstation at room temperature. The AC electrode for the three-electrode measurements was produced by making a homogenous paste of 80 wt % AC material, 15 wt % carbon black (to increase the material conductivity) and 5 wt % polyvinyl difluoride (PVdF) binder with dropwise addition of 1- methyl-2-pyrrolidinone in an agate mortar. The paste was coated on nickel foam current collector and kept in an oven to dry at 60 °C for 8 hours. The Co-Mn LDH electrode was likewise prepared by making a homogenous paste of 80 wt % Co-Mn LDH material, 10 wt % carbon black, 10 wt % polyvinyl difluoride (PVdF) binder with dropwise addition of 1- methyl-2-pyrrolidinone in an agate mortar and then coated on nickel foam current collector and kept in an oven to dry at 60 °C for 8 hours. The positive and negative electrodes for the two-electrode measurements were similarly prepared but coated on 16 mm diameter nickel foams and dried in an oven at 60 °C for 8 hours and was thereafter assembled with a microfiber glass filter paper as separator in a swagelok and 1 M KOH aqueous electrolyte was added to soak the electrodes. The mass loading of the material was 2.88 mg for the negative electrode and 1.92 mg for the positive electrode and total mass of both electrodes was 4.80 mg/cm^2 for the complete cell. In line with the consideration for appropriate mass loading in order to

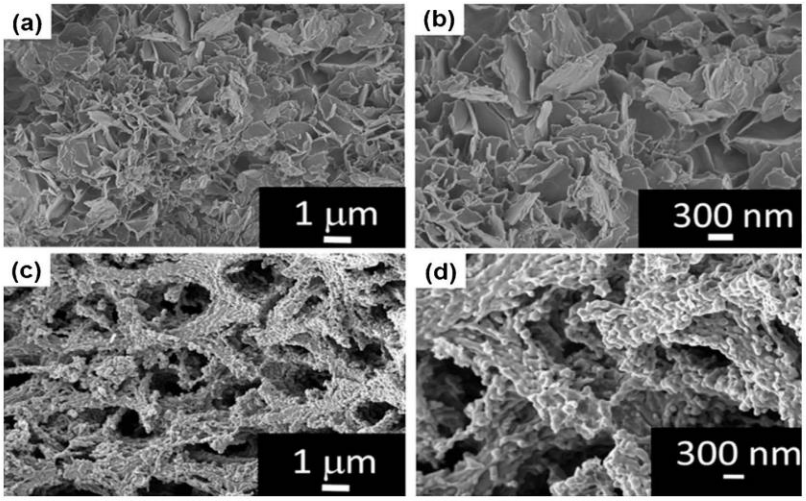

Fig. 1. SEM micrographs of Co-Mn LDH nanosheets at (a) low and (b) high magnifications respectively; SEM micrographs of AC porous network at (c) low and (d) high magnifications respectively.

obtain a significant amount of stored energy [45]. The three-electrode measurements were performed in 1 M KOH with glassy carbon as counter electrode and Ag/AgCl as reference electrode. The specific capacitances (C_s) of the Co-Mn-LDH, AC and the Co-Mn LDH//AC hybrid cell electrode which show pseudo-capacitor behavior were evaluated from the integral of discharge curves using Eq. (1) [42,43]

$$C_s(Fg^{-1}) = \frac{2I}{V^2 m}\int V dt \tag{1}$$

where I (A) is the current, Δt(s)is the discharge time, V (V) is maximum voltage and m (g) is the total mass of the electrodes. The energy density, E_d and power density, P_d of the electrodes were calculated using Eqs. (2) [43] and (3) [48] respectively;

$$E_d(\mathrm{Whkg^{-1}}) = C_s \times V^2/7.2 \tag{2}$$

$$P_d(\mathrm{Wkg^{-1}}) = E_d/\Delta t \tag{3}$$

In order to fabricate the hybrid cell, the C_s of the individual electrodes was taken into consideration. This is to ensure a mass balance on the electrode materials such that equal charges exist on the parallel electrodes such that $Q_+ = Q_-$; where Q_+ and Q_- is the charge stored on the positive electrode and negative electrodes. The charge Q is expressed as:

$$Q = C_s mV \tag{4}$$

The mass balance is therefore obtained by using the equation:

$$m_+/m_- = C_{S-}V_-/C_{s+}V_+ \tag{5}$$

where C_s is the specific capacitance of the electrode material, m is the mass of the electrodes, and V is the maximum potential.

The EIS measurements were carried out in open circuit potential in 100 kHz – 10 mHz frequency range to obtain the device behavior at varying frequencies. The device stability tests involved continuously cycling the full device for a large number of cycles and subsequently subjecting it to voltage holding tests and finally a self-discharge test to obtain the device response in practical testing conditions.

3. RESULTS AND DISCUSSION

3.1. Morphological, Structural and Composition Characterization

The SEM micrographs of the Co-Mn LDH and AC samples at low and high magnifications are presented in Fig. 1. Fig. 1(a) and (b) shows the Co-Mn LDH micrographs with a highly interconnected thin flake-like morphology necessary for interface reactions during electrochemical processes. The Co-Mn LDH nanoflake formation process involves nucleation and growth of the material crystals and is affected by the solvent polarity and solubility [49], hence, the morphology of the material is tuned by the solvent used in the synthesis [49–51].The formation mechanism for the unique flake-like structure of the Co-Mn LDH material is briefly elucidated as follows: The methanol molecules from the solvothermal reaction environment aggregates with an adequate supporting surface for nanoflake growth [38,50,51]. The presence of a mixture of the Co^{2+} and Mn^{2+} ions from the precursor salts with the Urea also leads to the formation of an initial seed-layer growth template for the self-assembly of the individual crystals necessary for nanoflake growth. The entire process involves a rapid nucleation of individual crystallites, followed by the actual growth and final self-aggregation of the crystallites to form nanosheets [49,52,53]. In the presence of a continuous supply of reacting solvent (methanol) and urea necessary for methanolysis [54] an equilibrium condition is attained between the solid-liquid interfaces. The forces which contribute to the self-aggregation leading to the flake-like morphology includes Van der waal forces, crystal phase interactions, electrostatic and dipolar fields linked with the aggregates [55]. Other newly formed crystallites also align themselves forming initial points of growth for other semi-stable crystallites forming the LDH nanosheets with flake-like morphology [55]. The AC morphology shown in Fig. 1(c) and (d) displays a good interconnected spherical framework consisting mainly of a 3D porous structure. The material framework and morphology shows

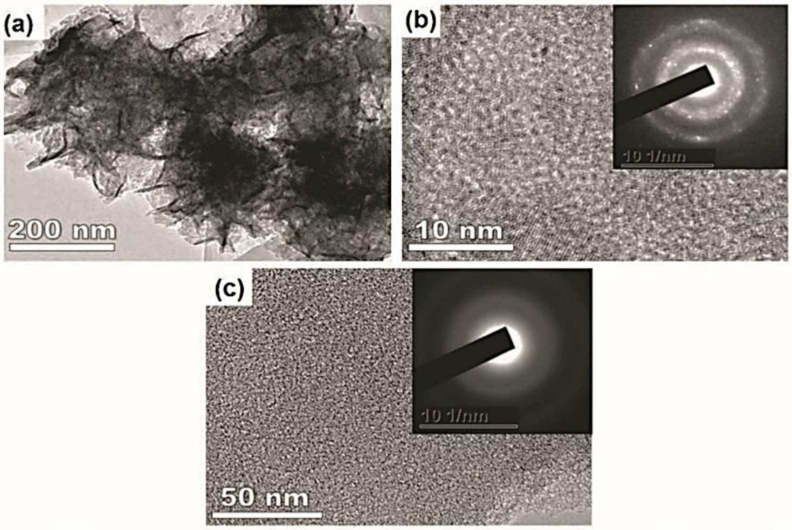

Fig. 2. HRTEM micrographs of Co-Mn LDH at (a) low and (b) high magnifications respectively (Inset to (b) is SAED pattern of Co-Mn LDH); (c) HRTEM micrograph of activated carbon and the corresponding SAED pattern (Inset).

that the $KHCO_3$ activating agent leads to the production of an activated carbon sample with microspheres suitable for easy and fast diffusion of ions within the material ideal for charge storage consistent with the research findings previously reported [23]. The formation of micro and mesopores in the AC material is as a result of the gasification and evolution of CO_2 and the availability of oxygen in the material. Typically, CO_2 is formed from the breakdown of $KHCO_3$ during the process of activation and is increased during the carbonization process at elevated temperatures. The CO_2 thus, reacts with the intermediate hydrochar which leads to pore formation and enlargement of existing ones. Also, $KHCO_3$ can react with carbon to produce metallic K leading to the production and evolution of CO_2 thus leading to pore formation [27,48].

For further information on the morphology, the samples were investigated using HR-TEM. Fig. 2 (a) and (b) shows the HR-TEM micrographs of Co-Mn LDH at low and high magnifications respectively, revealing the nanoflake-like morphology. The inset to Fig. 2 (b) displays a selected area electron diffraction pattern (SAED) of a Co-Mn LDH which shows diffraction rings revealing the polycrystalline nature of the material. In Fig. 2(c), a high magnification HRTEM micrograph of AC is shown which displays no lattice fringes suggesting that AC is not crystalline. Besides, the SAED pattern (inset in Fig. 2(c) does not show diffraction rings revealing that AC is amorphous. EDX analysis was carried out to confirm the elemental composition of the as-prepared Co-Mn LDH and activated carbon materials and is presented in Fig. 3 (a) and (b). The EDS spectrum in Fig. 3 (a) confirms the predominance content of Co and Mn in Co-Mn LDH and the spectrum for activated carbon (Fig. 3 (b)) confirms the predominance content of C in the sample. The observed low-intensity peaks of Si and S could originate from quartz tube or Teflon during sample preparation and the observed Cu (in Fig. 3 (a) are due to the formal-coated copper grid.

The structure of the as-synthesized Co-Mn-LDH and AC materials were further investigated by X-ray diffraction using a Co-K_α (1.7890 Å) source. The XRD spectra are presented in Fig. 4 (a) and (b) for the Co-Mn LDH and AC samples respectively. The XRD pattern for the Co-Mn LDH sample (Fig. 4 (a)), showed peaks observed at 2θ values of about 12°, 26°, 39°, 44°, 52°,68° and 70° and corresponding to (003), (006), (009),(015), (018),(110) and (113) lattice planes respectively for a hydrotalcite-like structure of LDH. This is consistent with earlier reports on similar LDH type structures [35,36]. However, the observed peak shifts in positions may be as a result of the Co-K_α X-ray source used for the analysis which is of a different wavelength as compared to Cu-K_α [45]. Fig. 4 (b) reveals the XRD spectrum of the AC sample showing a broad peak at a 2θ angle of 26° and a weak peak at 51° which is related to the (002) and (100) planes of graphitic carbon. The broad and low intensity of the peaks is an indication that the AC material is mostly non-crystalline and therefore can be referred to as amorphous carbon [46]. FT-IR spectrum for the samples performed in the wavenumber range of 4000–500 cm^{-1} are presented in Fig. 4 (c) and (d). This measurement is important for the determination of surface functional groups in the as-synthesized Co-Mn LDH and AC samples. the FT-IR spectrum for the Co-Mn LDH (Fig. 4 (a)), shows peaks at ~3440 $cm^{-1}$and ~1629 cm^{-1} which are due to O-H bending mode of water and hydrogen bonded to the hydroxyl groups [37,47,48]. The peaks appearing at about ~2945 cm^{-1} and ~2815 cm^{-1} and the bands occurring at ~1056 cm^{-1} is related to C—O and C—H stretching vibrations [60]. Whereas the peak position observed at about ~2207 cm^{-1} is due to O—C—O the stretching vibrations of antisymmetric Carbon di-oxide in air [49]. The peak occurring at 1384 cm^{-1} are assigned to the typical vibration of carbonate ions and the peak occurring at about ~627 cm^{-1} is attributed to the metal bonded to the hydroxyl group Co-OH [37,48]. The FT-IR spectra for AC after carbonization at 850 °C for 2 hours and hydrochar after hydothermal treatment at 160 °C for 12 hours is presented in Fig. 4 (b). A reduction in the intensity of the peaks of the AC as compared to that of the hydrochar can be observed. This may be due to the breaking of the water molecule bond and loss of moisture in the sample due to carbonization at high temperatures. The ~3435 cm^{-1} is due to the O-H stretching vibrations of water due to surface hydroxyl groups. The bands occurring at ~2942 cm^{-1} in the hydrochar and AC samples indicate the C-H bond of the aliphatic group and the peak at ~1608 cm^{-1} indicates the C = O stretching vibrations of the carboxyl groups. The peaks occurring at ~1180 cm^{-1} and ~502 cm^{-1} may be due to the – C- C stretching vibration [44].

The results from the textural analysis of the samples using the BET measurements are presented in Fig. 5 (a) and (b). The N_2 adsorption-desorption isotherm of the Co-Mn LDH (Fig. 5 (a)) shows a type III and a H3 hysteresis loop indicating agglomeration of plate-like particles with slit-shaped pores and the presence of mesopores in the double-layered configuration [50]. While the N_2 adsorption-desorption isotherm of the AC sample (see Fig. 5 (b)) shows a type IV and a H4 hysteresis loop demonstrating a composite material comprising of microporous and mesoporous structures. The SSA of the Co-Mn LDH was recorded as 44.60 $m^2 g^{-1}$ while that of the AC sample was recorded as 1056.52 $m^2 g^{-1}$. The

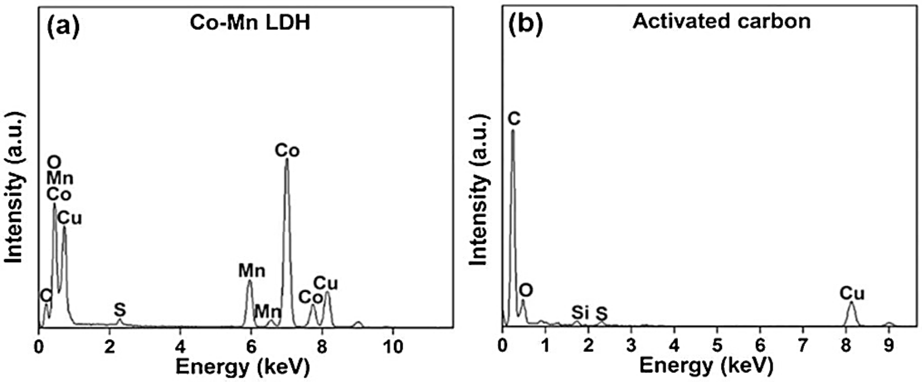

Fig. 3. EDS spectra of (a) Co-Mn LDH and (b) Activated carbon.

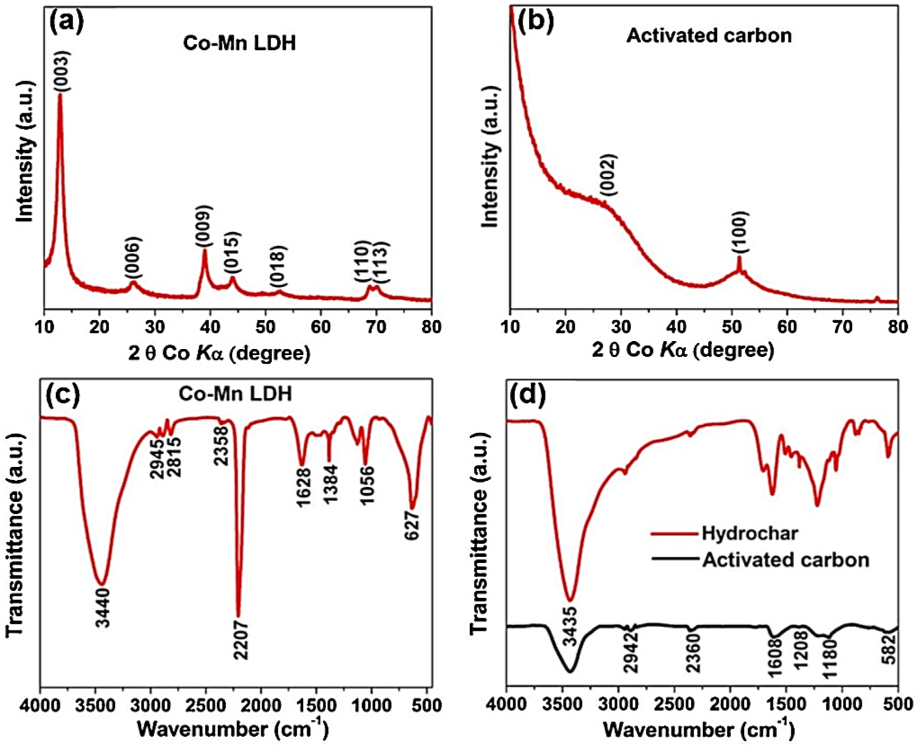

Fig. 4. X-ray diffraction pattern of (a) Co-Mn LDH; and (b) activated carbon; FTIR spectra of (c) Co-Mn LDH and (d) Activated carbon and Hydrochar.

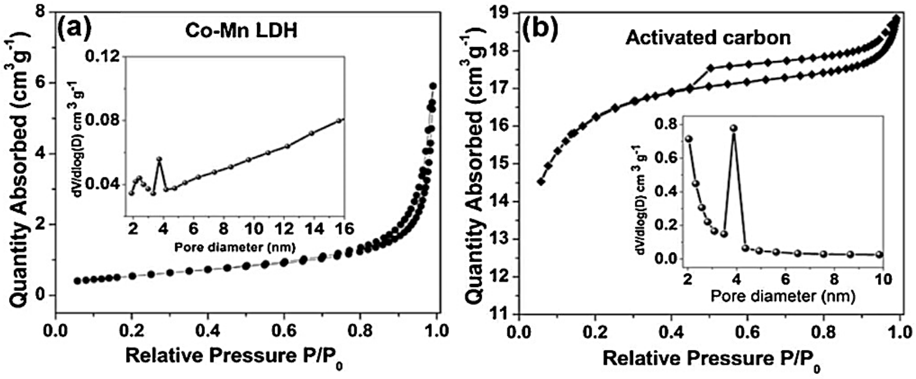

Fig. 5. N_2 Adsorption-desorption isotherm for (a) Co-Mn LDH and (b) Activated carbon (Insets to the figure show pore size distribution plots).

insets to Fig. 5 (a) and (b) show the Pore size distribution (PSD) plots for the Co-Mn LDH and AC samples signifying that the Co-Mn LDH is made up of mainly mesoporous structure with an overall pore volume of 0.15 $cm^3\,g^{-1}$ and average pore diameter of 16.1 nm while the AC is made up of both micropores and mesopores with overall pore volume of 0.64 $cm^3\,g^{-1}$ and average pore diameter of 3.4 nm. The active micropores and mesopores in the samples provide the necessary sites for ion trapping required for efficient energy storage and serve as the channels used for the electrolyte ion transport required for device power delivery [51].

Furthermore, to analyze the oxidation states of the Mn and Co in the Co-Mn LDH, the sample was analyzed by XPS including activated carbon sample. Fig. 6(a) shows the wide scan XPS spectra of the as-received Co-Mn LDH sample (i.e. without sputter

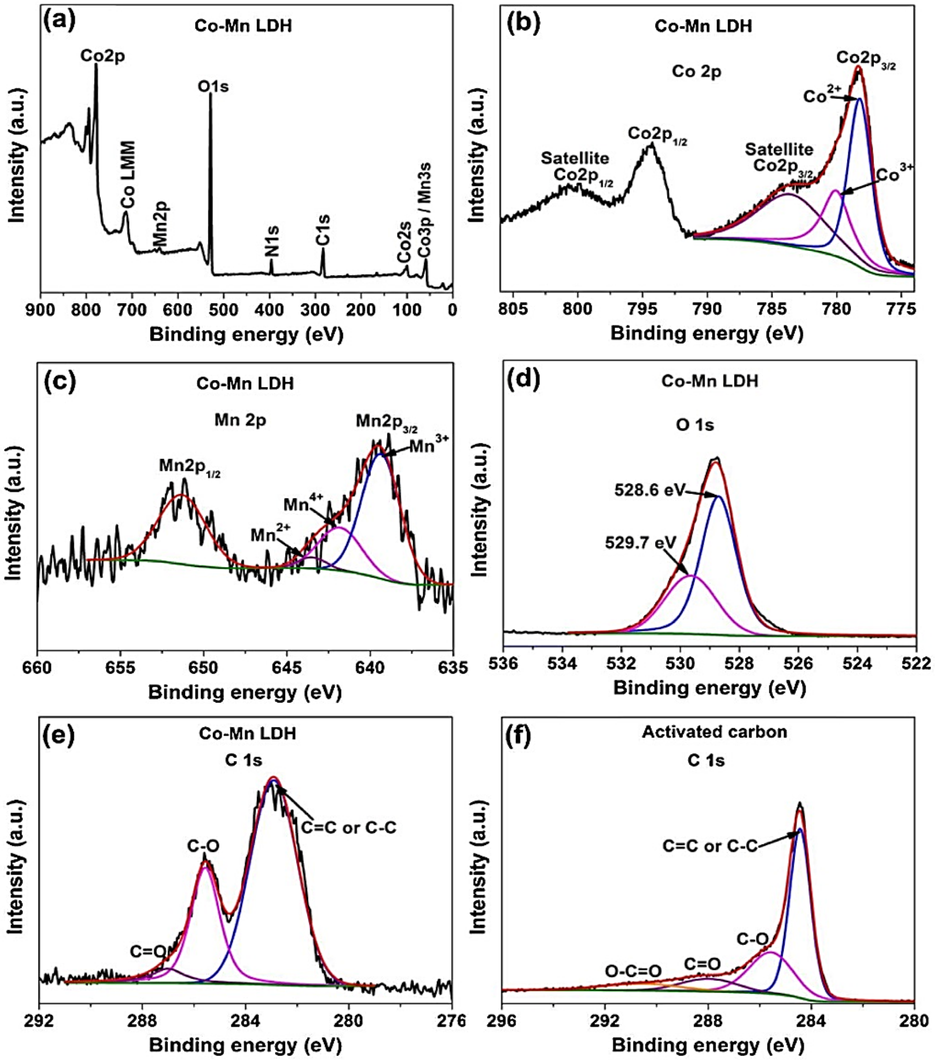

Fig. 6. (a) The wide scan XPS spectra of the as-received Co-Mn LDH nanosheets sample. The core level spectrum of (b) Co 2p, (c) Mn 2p, (d) O 1 s and (e) C 1 s of a Co-Mn LDH nanosheets sample. (f) The core level spectrum of C 1 s of an activated carbon.

cleaning) which displays the main elements (Co, Mn, and O) of the composition of the sample. Fig. 6(b) shows the core level spectrum of Co 2p of the Co-Mn LDH sample which reveals the binding energy peaks at 778.4 eV and 783.5 eV which correspond to Co $2p_{3/2}$ core level, and other binding energy peaks at 794.3 eV and 800.9 eV which correspond to Co $2p_{1/2}$ core level. The fitted Co $2p_{3/2}$ peaks suggest that the Co oxidation state of the Co-Mn LDH sample is mainly Co^{2+}. On the other hand, the core level spectrum of Mn 2p of the Co-Mn LDH sample reveals the binding energy peaks at 639.3 and 651.5 eV corresponding to Mn $2p_{3/2}$ and Mn $2p_{1/2}$ core levels, respectively, as shown in Fig. 6 (c). The fitted Mn $2p_{3/2}$ peaks suggest that the Mn oxidation state of the sample is composed of Mn^{2+}, Mn^{3+} and Mn^{4+} [63]. Fig. 6(d) shows the core level spectrum of O 1s with fitted peaks at 528.6 and 529.7 eV which could be ascribed to O 1 s in Co–O and Mn–O compounds. The core level spectrum of C 1 s (Fig. 6 (e)) shows a high-intensity peak at about 283.5 eV which corresponds to the graphitic carbon, C=C and/or C—C and other fitted peaks related to some of the carbon-oxide components as suggested by FT-IR analysis. Similar to the core level spectrum of C 1 s of a Co-Mn LDH sample, the C 1 s core level spectrum of the activated carbon sample reveals the graphitic carbon peak (C=C and/or C—C) and carbon-oxides peaks. However, for the activated carbon sample the high-intensity peak at about 284.2 eV (C=C and/or C—C) confirms the predominance content of graphitic carbon in the sample.

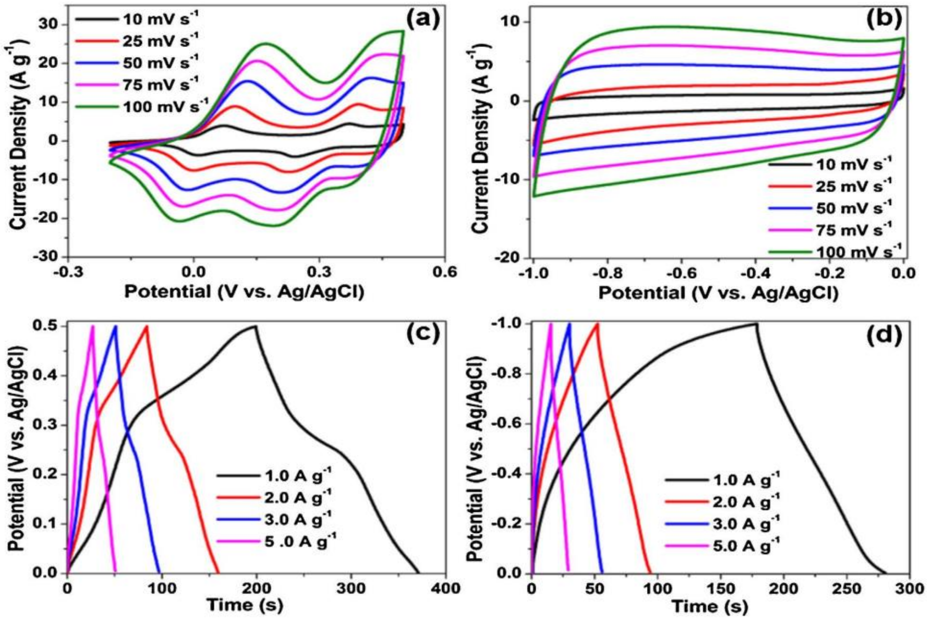

Fig. 7. CV curves of (a () Co-Mn LDH from 10 mV s^{-1} to 100 mV s^{-1} (b) AC from 10 mV s^{-1} to 100 mV s^{-1} in 1 M KOH; CD profiles of (c) Co-Mn-LDH and (d) AC at current density of 1.0 A g^{-1} – 5 A g^{-1} in 1 M KOH.

3.2. Electrochemical analysis

The results from the electrochemical analysis of Co-Mn LDH positive electrode material and the AC negative electrode material performed in a three electrode configuration is presented in Fig. 7. The CV curves for the Co-Mn LDH positive electrode material performed at scan rates of 10 mV s^{-1} to 100 mVs^{-1} (see Fig. 7 (a)), displayed a very good quasi-reversible faradaic behavior. Two redox couples can be observed with peak separation between 60 to 110 mV for each of the redox peaks, within the negative/positive voltage of –0.2 V to 0.5 V, indicating relatively fast surface redox reactions of the Co^{2+} and Mn^{2+} in the Co-Mn LDH material. The first anodic and cathodic current peaks were observed at ~-0.01 V and ~0.1 V respectively and the second was observed at ~0.24 V and 0.39 V respectively. Where the latter is indicative of the quasi-reversible faradaic behavior related to the transition between Co^{2+}/Co^{3+}at the various scan rates related to the reaction [52,53]

$$CoOOH + OH^- \leftrightarrow CoO_2 + H_2O + e \qquad (6)$$

Thus, the first redox couple could be assigned to the reversible faradaic reaction related to transition from Mn^{2+} to Mn^{3+} in the reaction [65].

$$Mn(OH)_2 + OH^- \leftrightarrow MnOOH + H_2O + e \qquad (7)$$

The CV curves of the AC material performed at 10 mV s^{-1} – 100 mV s^{-1} scan rates are presented in Fig. 7 (b). The CV curves exhibited rectangular shapes which are related to electric double layer capacitive (EDLC) features for porous carbon materials coupled with a good current response in the negative potential range of –1.0 V – 0.0 V. The results from the charge-discharge (CD) tests performed in the three electrode configuration at varying current densities of 1.0–5.0 A g^{-1} for the Co-Mn LDH and AC electrodes are presented in Fig. 7 (c) and (d). The CD profiles of the Co-Mn LDH and AC electrodes are directly related to the observed redox and EDLC characteristics for the CV curves of the Co-Mn LDH and AC respectively. A specific capacitance of 318 F g^{-1} and 103 F g^{-1} were calculated for the Co-Mn LDH and AC respectively at 1.0 A g^{-1} using Eq. (1).

The results from testing the assembled hybrid device taking into cognizance the electrochemical performance values obtained from the half-cell analyses of the individual electrodes and adopting the mass balance approach to ensure equal charge concentration is reported in Fig. 8. Fig. 8 (a) shows the individual CV curves superimposed to illustrate the combination of the independent operating potentials of both the EDLC and Faradaic-type materials in order to maximize the final operating voltage of the hybrid device. An optimized voltage window was determined by cycling the full device at a moderate 25 mV s^{-1} scan rate whilst varying the voltage from 1.0 V – 1.7 V as shown in Fig. 8 (b). The CV curves mimic the CV shape of AC within the voltage window of 0.0 V – 0.8 V and above 0.8 V that of the LDH seen earlier in Fig. 8 (a). An anodic current leap can be observed beyond 1.6 V which may be attributed to gas evolution as the potential is increased. Therefore, the ideal operating voltage was chosen as 1.5 V for the hybrid device based on the ideality of the CV plot. The hybrid device is able to work within this potential window of 1.5 V, beyond the thermodynamic decomposition of water (1.23 V) in 1 M KOH because of the synergistic operation of the individual operating potentials of the positive electrode and the negative electrode materials, thus, combining the high overpotential for di-hydrogen and oxygen evolutions at the positive and negative electrodes respectively [32,54]. The CV curves of the hybrid device at 5 mV s^{-1} – 100 mV s^{-1} scan rates are presented in Fig. 8 (c). The current response increases as scan rate is increased with the signatory redox peaks still observed from the typical faradaic behavior.

The associated CD curves of the hybrid cell performed at various current densities are presented in Fig. 8 (d). The calculated specific

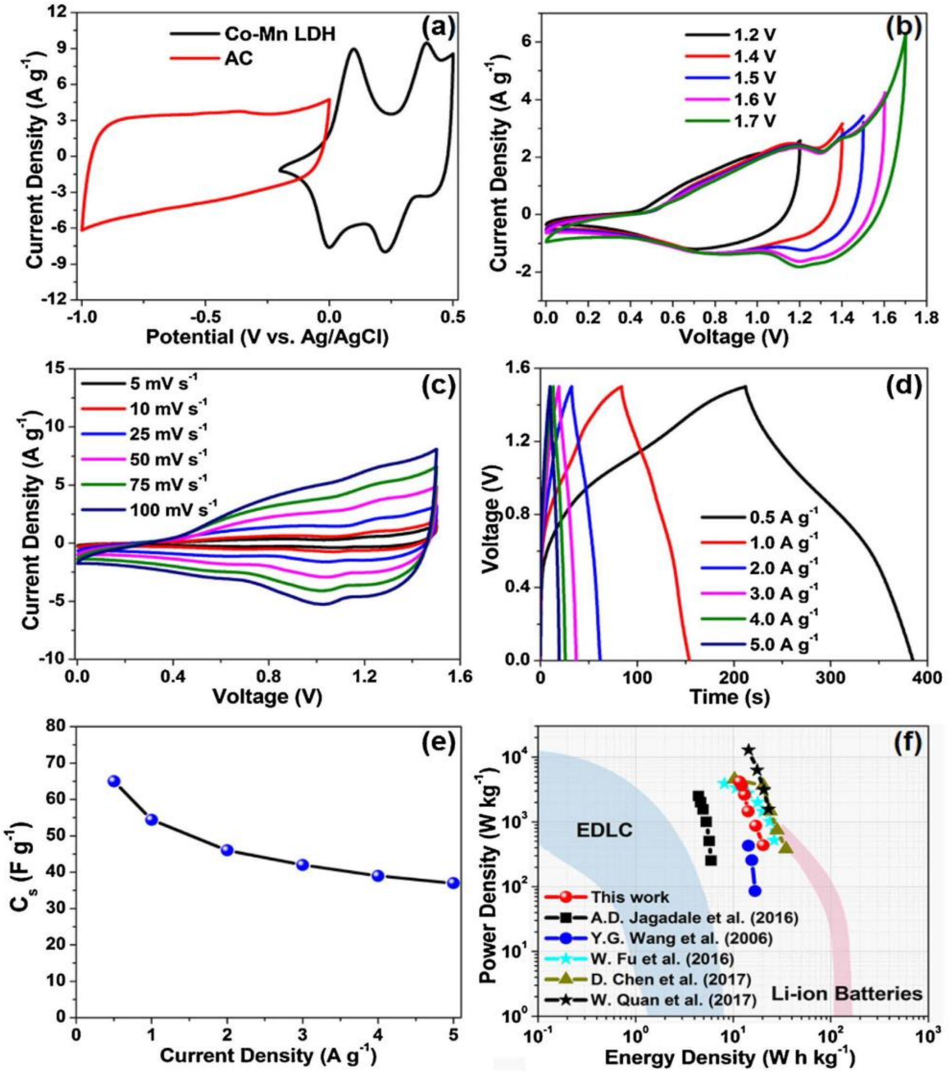

Fig. 8. (a) CV curves of AC and Co-Mn LDH at 25 mV s^{-1}, (b) CV plots of hybrid cell of Co-Mn-LDH//AC at 25 mV s^{-1} for different operating voltages in 1 M KOH, (c) CV plots from 5 mV s^{-1} to 100 mV s^{-1}, (d) the associated GCD plots from 0.5 A g^{-1}–5.0 A g^{-1} in same voltage window, (e) Capacitance variation with current density and (f) Ragone plot.

capacitance value of the Co-Mn LDH//AC hybrid device was recorded as 65 F g^{-1} at 0.5 A g^{-1} current density which decreased to about 37 F g^{-1} (retaining more than 50% of its original value) even when the current density is increased by 10-fold to 5.0 A g^{-1}. This is indicative of good rate capability of the hybrid device as the current is increased. The specific capacitance as a function of current density is presented in Fig. 8 (e). A maximum energy density of 20.3 W h kg^{-1} was recorded for the hybrid device at 0.5 A g^{-1} current density with a corresponding power density of 425 W kg^{-1}. The Ragone plot (Fig. 8 (f)) displays the energy density values as a function of power density, and shows that the energy density values for Co-Mn LDH//AC hybrid device are close to the upper end region of the lithium ion batteries which confirms good EDLC contribution, the dominating faradaic behavior and good electrochemical performance of the of the hybrid device. It is worthy to note that this energy density value is much higher than some earlier reports on similar asymmetric type hybrid devices. For example, CoMn LDH/Ni foam//AC electrodes by A. D. Jagadale et al. [36], CoAl LDH//AC by Y.G. Wang et al. [55], NiMn LDH/MnO$_2$//AC by W. Quan et al. [68] as shown in Fig. 8 (f). The obtained values in this report are also comparable to other similar research studies reported for ZnCo$_2$O$_4$@Ni$_x$Co$_{2x}$(OH)$_{6x}$//AC by W. Fu et al. [56], NiCoS$_4$@Co(OH)$_2$//AC by R. Li [57] and NiMn LDH/rGO//AC by M. Li [37], CoMn LDH/NF//AC by D. Chen et al. [7]. In addition to the high energy density, the material in this work displays good cycling stability.

LDH/rGO//AC (74.1% after 10,000 cycles) [37], CoMn LDH/Ni foam//AC (84.2% after 5000 cycles) [36], NiCoS$_4$@Co(OH)$_2$//AC (70.10% after 5000 cycles) [70], for ZnCo$_2$O$_4$@Ni$_x$Co$_{2x}$(OH)$_{6x}$//AC (81.4% after 2000 cycles) [56], NiMn LDH/MnO$_2$//AC (87% after 5000 cycles) [68] and CoMn LDH/NF//AC (83.7% after 3000 cycles) [7] (as shown in Fig. 9 (b)). The SEM images of the electrode materials after cycling have been included in the supporting information (Fig. S1) to further validate the stability of the material electrodes. The stability of the device was further tested using the voltage holding method at its maximum operating voltage of 1.6 V and 1.0 A g^{-1} current density for 70 hours and the result is presented in Fig. 9 (c). The voltage holding test (also known as floating test) shows a decrease in the device capacitance after the first 20 hours (approx. 1 day) before stabilizing for the rest of the floating time with a capacitance retention of ~80%. The observed floating performance might be linked to the stable network of the porous carbon structure inhibiting the disintegration or collapse of the material after floating at maximum voltage [44].

Lastly, to conclude all stability tests in relation to practical device operation, the device was subjected to a self-discharge test on open circuit potential to observe the routine device behavior after being fully charged to its maximum operating voltage. The initial drop in the voltage (see Fig. 9 (d)) is attributed to decomposition of any moisture in the electrolyte directly in contact with the active material electrode [60]. As observed in Fig. 9 (d), about 0.8 V is still retained after 60 hours of self-discharge test which means that half of the amount of the initial voltage is retained which shows the potential of the device to retain charge on open potential. The mechanism of self-discharge is described based on the established models in literature [61,62]. The self-discharge can be described by relating the leakage current to a resistance by applying the expression:

$$V = V_0 exp^{\left(-\frac{t}{RC}\right)} \quad (8)$$

Where V_0 is the maximum applied voltage, R is the resistance and C is the charge stored in the device. The self –discharge curve in this experiment however deviates from the linear fit of the plot of lnV as a function of time (See Fig. 9 (e)). The self-discharge profile subsequently follows a diffusion-controlled process (See Fig. 9 (f)) in which the accumulated ionic-charge are lost during the process of discharge. The discharge profile is governed by the voltage polynomial expressed as:

$$V = V_o - mt^{0.5} \quad (9)$$

where m is a diffusion parameter and is related to V_o, the initial applied maximum voltage and t is the time duration of the self-discharge process.

The EIS study was done in open circuit potential in 10 mHz to 100 kHz frequency range and is presented in Fig. 10. Electrochemical impedance spectroscopy (EIS) is very important in evaluating the electron and ion transport of an electrochemical capacitor [63]. The Nyquist plots for the Co-Mn LDH//AC device before and after stability is presented in Fig. 10 (a). Semicircles in the high frequency regions for the plots before and after stability (inset to Fig. 10 (a), indicates the presence of charge transfer resistance linked to a resistive element present in the electrode. The nearly vertical lines at the low frequency regions parallel to the y-axis show ideal capacitive behaviors. The intersection of each semicircle with the real Z'-axis shows the solution resistance (R_s) which is a summation of the overall electrolytic resistance, electrode material intrinsic resistance and the resistance between the

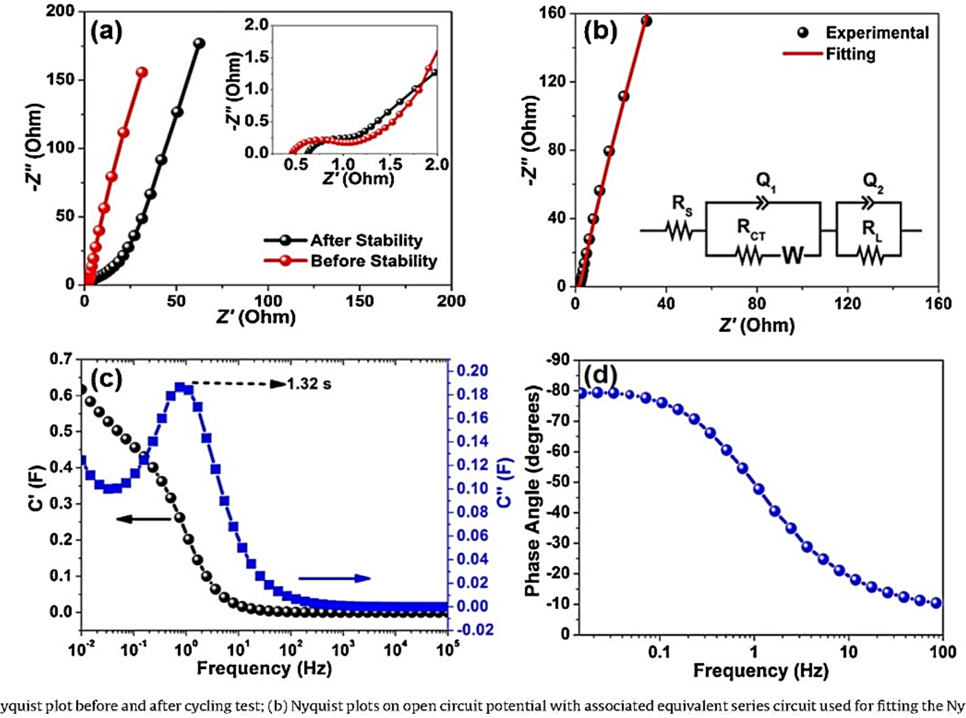

Fig. 10. (a) Nyquist plot before and after cycling test; (b) Nyquist plots on open circuit potential with associated equivalent series circuit used for fitting the Nyquist plot data; (c) Real and imaginary part of cell capacitance as a function of frequency and (d) Phase angle as a function of frequency, for the Co-Mn LDH//AC hybrid device in 1 M KOH.

electrode material and the current collector [46,63]. An R_s-value of 0.46 Ω was recorded for the Nyquist plot before stability, indicating good ion diffusion and conductivity between the electrolyte and the surface of the active material [64]. This might be due to the synergy between the thin nano-flake structure of the Co-Mn LDH and the spherical porous structure of the AC electrodes enabling good electron transport and ion percolation. A value of 0.67 Ω was recorded for the charge transfer resistance (R_{ct}), which is in the Z' – axis intercept from the high to middle frequency region and it is indicative of a good charge transfer and conductivity of the material. The R_s values are smaller than those earlier reported for similar electrode devices such as 0.75 Ω, 0.75 Ω, 0.88 Ω reported for CoMn LDH/Ni foam//AC [36] $ZnCo_2O_4@Ni_xCo_{2x}(OH)_{6x}$//AC [56] and $NiCoS_4@Co(OH)_2$//AC[70] respectively. The R_{ct} value is also smaller than those reported for CoMn LDH/Ni foam//AC (3.4 Ω)[39], $ZnCo_2O_4@Ni_xCo_{2x}(OH)_{6x}$//AC (1.12 Ω) [56] but higher than that reported for $NiCoS_4@Co(OH)_2$//AC(0.01 Ω) [70]. The R_s value recorded after stability is 0.63 Ω which is very close to 0.46 Ω (the Rs value before stability) and the R_{ct} value after stability is 0.68 Ω which is only ~ 1.5% increase from the value before stability. This shows very good ion diffusion and conductivity, and low degradation of the material even after 10,000 continuous CD cycles and further confirms the stability of the hybrid device.

The associated equivalent series circuit fitted for the Nyquist plot data is presented in Fig. 10 (b). In the equivalent series circuit (inset to Fig. 10 (b)), the R_s is in series with Q_1 (constant phase element) which is connected in parallel to the charge transfer resistance R_{ct}. The element, Q_1 is the double layer capacitance attached to the Warburg diffusion element (W) which is in series with R_{ct}. Q_2 (mass capacitance) is an indication of ideal polarizable capacitance connected in parallel to R_L (impedance element), which is responsible for the deviation of the vertical line from the ideal behavior [34,65]. The shift from the typical vertical behavior also suggests that there is a leakage resistance, R_L which is a resistive element associated with Q_2.

The impedance (Z) of Q_1, is expressed as [34,66];

$$Z_{Q_1} = K(j\omega)^{\ b} \tag{10}$$

where ω is angular frequency, k and b are frequency-independent constants. The static or real ($C'(\omega)$) and imaginary($C''(\omega)$) parts of the capacitance as a function of frequency is presented in Fig. 10 (c). From Fig. 10 (d), the capacitance ($C(\omega)$) is the sum of $C'(\omega)$ and $C''(\omega)$ and are expressed by Eqs. ((9)–(11)) [67] below:

$$C'(\omega) = -\frac{Z''(\omega)}{\omega|Z(\omega)^2|} \tag{11}$$

$$C'(\omega) = -\frac{Z'(\omega)}{\omega|Z(\omega)^2|} \tag{12}$$

$$C(\omega) = C'(\omega) + jC''(\omega) \tag{13}$$

where $C'(\omega)$ is the static capacitance, $C''(\omega)$ is related to the energy dissipated by the capacitor and also the frequency transition between an ideal capacitive and resistive characteristics [80], ω is the frequency and $|Z(\omega)^2|$ is impedance modulus. The value of C' at a frequency of 10 mHz is 0.63 F which is the real attainable capacitance of the hybrid cell at this frequency. C'' describes the frequency transition between an ideal capacitive and resistive characteristics of the hybrid device [80] with a relaxation time (τ) which was calculated for the hybrid device as 1.32 s corresponding to a frequency of ~1.0 Hz using the equation:

$$\tau = \frac{1}{f_{max}} = 2\pi\omega_{max}^{1} \tag{14}$$

The direct interpretation of the relaxation time simply means that the energy stored within the Co-Mn LDH//AC hybrid device can be released in a period of 1.32 s. The plot of phase angle of the cell as a function of frequency is presented in Fig. 10(d). The phase angle is recorded at approximately −80° (close to −90°) which is indicative of the capacitive behavior of the hybrid cell similar to the ideal device.

4. CONCLUSIONS

Thin Co-Mn-LDH nanoflakes with exceptional morphological and textural properties and highly porous activated carbon (AC) from cork raw material (Quercus Suber) and was successfully synthesized by a facile solvothermal and a two-step eco-friendly hydrothermal syntheses routes respectively. A hybrid device was successfully fabricated with a specific capacitance value of 65 F g^{-1} obtained at 0.5 A g^{-1} current density. The device displayed a good rate capability in a 1 M KOH aqueous electrolyte with the energy and power densities of 20.3 Wh kg^{-1} and 425 W kg^{-1} respectively. The device had a remarkable stability response with an initial capacitance retention of 97.7% after a few cycles which subsequently improved to a final capacitance retention value of 99.7% for up to 10,000 constant GCD cycles. There was also negligible degradation recorded after 70 hours of floating time at the maximum cell voltage and the cell still retained more than half of its operating voltage after 60 h of self-discharge test. The results recorded in this study on the Co-Mn LDH//AC hybrid device depict the as-synthesized material as potential electrodes for high performance supercapacitor applications.

ACKNOWLEDGEMENTS

This research was supported by the South African Research Chairs Initiative (SARChI) of the Department of Science and Technology and the National Research Foundation (NRF) of South Africa (Grant No. 61056). Any idea, finding, conclusion or recommendation expressed in this material is that of the author (s). The NRF does not accept any liability in this regard. F. O. Ochai-Ejeh acknowledges NRF through SARChI in Carbon Technology and Materials, and the Department of Physics at the University of Pretoria for financial support.

Appendix A. Supplementary data

Supplementary data associated with this article can be found, in the online version, at http://dx.doi.org/10.1016/j.electacta.2017.08.163.

References

[1] J.W. Lee, A.S. Hall, J.-D. Kim, T.E. Mallouk, A Facile and Template-Free Hydrothermal Synthesis of Mn_3O_4 Nanorods on Graphene Sheets for Supercapacitor Electrodes with Long Cycle Stability, Chem. Mater. 24 (2012) 1158–1164, doi:http://dx.doi.org/10.1021/cm203697w.

[2] D.S. Patil, J.S. Shaikh, D.S. Dalavi, S.S. Kalagi, P.S. Patil, Chemical synthesis of highly stable PVA/PANI films for supercapacitor application, Mater. Chem. Phys. 128 (2011) 449–455, doi:http://dx.doi.org/10.1016/j.matchemphys.2011.03.029.

[3] J.K. Gan, Y.S. Lim, A. Pandikumar, N.M. Huang, H.N. Lim, Graphene/polypyrrole-coated carbon nanofiber core–shell architecture electrode for electrochemical capacitors, RSC Adv. 5 (2015) 12692–12699, doi:http://dx.doi.org/10.1039/C4RA14922J.

[4] M.D. Stoller, R.S. Ruoff, Best practice methods for determining an electrode material's performance for ultracapacitors, Energy Environ. Sci. 3 (2010) 1294, doi:http://dx.doi.org/10.1039/c0ee00074d.

[5] T. Brousse, D. Belanger, J.W. Long, templa, J. Electrochem. Soc. 162 (2015) A5185–A5189, doi:http://dx.doi.org/10.1149/2.0201505jes.

[6] X. Zhang, S. Wang, L. Xu, T. He, F. Lu, H. Li, J. Ye, Controllable synthesis of cross-linked CoAl-LDH/NiCo 2 S 4 sheets for high performance asymmetric supercapacitors, Ceram. Int. (2017), doi:http://dx.doi.org/10.1016/j.ceramint.2017.07.159.

[7] D. Chen, H. Chen, X. Chang, P. Liu, Z. Zhao, J. Zhou, G. Xu, H. Lin, S. Han, Hierarchical CoMn-layered double hydroxide nanowires on nickel foam as electrode material for high-capacitance supercapacitor, J. Alloys Compd. (2017), doi:http://dx.doi.org/10.1016/j.jallcom.2017.07.313.

[8] F. Zhang, T. Zhang, X. Yang, L. Zhang, K. Leng, Y. Huang, Y. Chen, A high-performance supercapacitor-battery hybrid energy storage device based on graphene-enhanced electrode materials with ultrahigh energy density, Energy Environ. Sci. 6 (2013) 1623, doi:http://dx.doi.org/10.1039/c3ee40509e.

[9] K. Grupo, Español del Carbo'n, W. Naoi, Boletin del Grupo Español del Carbo'n., Grupo Español del Carbo'n, (2005) https://digital.csic.es/handle/10261/81752?locale=en (Accessed 8 April)..

[10] Z. Fan, J. Yan, T. Wei, L. Zhi, G. Ning, T. Li, F. Wei, Asymmetric Supercapacitors Based on Graphene/MnO2 and Activated Carbon Nanofiber Electrodes with High Power and Energy Density, Adv. Funct. Mater. 21 (2011) 2366–2375, doi:http://dx.doi.org/10.1002/adfm.201100058.

[11] J. Zhao, J. Chen, S. Xu, M. Shao, D. Yan, M. Wei, D.G. Evans, X. Duan, CoMn-layered double hydroxide nanowalls supported on carbon fibers for high-performance flexible energy storage devices, J. Mater. Chem. A. 1 (2013) 8836, doi:http://dx.doi.org/10.1039/c3ta11452j.

[12] C.O. Ania, V. Khomenko, E. Raymundo-Piñero, J.B. Parra, F. Béguin, The Large Electrochemical Capacitance of Microporous Doped Carbon Obtained by Using a Zeolite Template, Adv. Funct. Mater. 17 (2007) 1828–1836, doi:http://dx.doi.org/10.1002/adfm.200600961.

[13] C. Portet, Z. Yang, Y. Korenblit, Y. Gogotsi, R. Mokaya, G. Yushin, Electrical Double-Layer Capacitance of Zeolite-Templated Carbon in Organic Electrolyte, J. Electrochem. Soc. 156 (2009) A1–A6, doi:http://dx.doi.org/10.1149/1.3002375.

[14] Y. Korenblit, M. Rose, E. Kockrick, L. Borchardt, A. Kvit, S. Kaskel, G. Yushin, High-Rate Electrochemical Capacitors Based on Ordered Mesoporous Silicon Carbide-Derived Carbon, ACS Nano. 4 (2010) 1337–1344, doi:http://dx.doi.org/10.1021/nn901825y.

[15] V. Presser, M. Heon, Y. Gogotsi, Carbide-Derived Carbons – From Porous Networks to Nanotubes and Graphene, Adv. Funct. Mater. 21 (2011) 810–833, doi:http://dx.doi.org/10.1002/adfm.201002094.

[16] S. Dörfler, I. Felhösi, T. Marek, S. Thieme, H. Althues, L. Nyikos, S. Kaskel, High power supercap electrodes based on vertical aligned carbon nanotubes on aluminum, J. Power Sources. 227 (2013) 218–228, doi:http://dx.doi.org/10.1016/j.jpowsour.2012.11.068.

[17] S.R. Sivakkumar, J.M. Ko, D.Y. Kim, B.C. Kim, G.G. Wallace, Performance evaluation of CNT/polypyrrole/MnO2 composite electrodes for electrochemical capacitors, Electrochim. Acta. 52 (2007) 7377–7385, doi:http://dx.doi.org/10.1016/j.electacta.2007.06.023.

[18] Q. Gao, L. Demarconnay, E. Raymundo-Piñero, F. Béguin, Exploring the large voltage range of carbon/carbon supercapacitors in aqueous lithium sulfate electrolyte, Energy Environ. Sci. 5 (2012) 9611, doi:http://dx.doi.org/10.1039/c2ee22284a.

[19] A. Bello, F. Barzegar, M.J.J. Madito, D.Y.Y. Momodu, A.A.A. Khaleed, T.M.M. Masikhwa, J.K.K. Dangbegnon, N. Manyala, Stability studies of polypyrole-derived carbon based symmetric supercapacitor via potentiostatic floating test, Electrochim. Acta. 213 (2016) 107–114, doi:http://dx.doi.org/10.1016/j.electacta.2016.06.151.

[20] W. Guo, C. Yu, S. Li, J. Yang, Z. Liu, C. Zhao, H. Huang, M. Zhang, X. Han, Y. Niu, J. Qiu, High-Stacking-Density, Superior-Roughness LDH Bridged with Vertically Aligned Graphene for High-Performance Asymmetric Supercapacitors, Small. (2017) 1701288, doi:http://dx.doi.org/10.1002/smll.201701288.

[21] P. Wang, Y. Li, S. Li, X. Liao, S. Sun, Water-promoted zeolitic imidazolate framework-67 transformation to Ni–Co layered double hydroxide hollow microsphere for supercapacitor electrode material, J. Mater. Sci. Mater. Electron. 28 (2017) 9221–9227, doi:http://dx.doi.org/10.1007/s10854-017-6656-5.

[22] F. Wang, S. Sun, Y. Xu, T. Wang, R. Yu, H. Li, High performance asymmetric supercapacitor based on Cobalt Nickle Iron-layered double hydroxide/carbon nanofibres and activated carbon, Sci. Rep. 7 (2017) 4707, doi:http://dx.doi.org/10.1038/s41598-017-04807-1.

[23] L. Demarconnay, E. Raymundo-Piñero, F. Béguin, Adjustment of electrodes potential window in an asymmetric carbon/MnO2 supercapacitor, J. Power Sources. 196 (2011) 580–586, doi:http://dx.doi.org/10.1016/j.jpowsour.2010.06.013.

[24] W. Gu, G. Yushin, Review of nanostructured carbon materials for electrochemical capacitor applications: advantages and limitations of activated carbon, carbide-derived carbon, aerogels, carbon nanotubes, onion-like carbon, and graphene, WIREs Energy Environ 3 (2014) 424–473, doi:http://dx.doi.org/10.1002/wene.102.

[25] L.L. Zhang, R. Zhou, X.S. Zhao, Graphene-based materials as supercapacitor electrodes, J. Mater. Chem. 20 (2010) 5983, doi:http://dx.doi.org/10.1039/c000417k.

[26] K. Zhang, L.L. Zhang, X.S. Zhao, J. Wu, Graphene/polyaniline nanofiber composites as supercapacitor electrodes, Chem. Mater. 22 (2010) 1392–1401, doi:http://dx.doi.org/10.1021/cm902876u.

[27] M. Sevilla, A.B. Fuertes, A Green Approach to High-Performance Supercapacitor Electrodes: The Chemical Activation of Hydrochar with Potassium Bicarbonate, ChemSusChem. 9 (2016) 1880–1888, doi:http://dx.doi.org/10.1002/cssc.201600426.

[28] J. Hayashi, T. Horikawa, I. Takeda, K. Muroyama, F. Nasir Ani, Preparing activated carbon from various nutshells by chemical activation with K2CO3, Carbon 40 (2002) 2381–2386, doi:http://dx.doi.org/10.1016/S0008-6223(02)00118-5.

[29] A. Jain, C. Xu, S. Jayaraman, R. Balasubramanian, J.Y. Lee, M.P. Srinivasan, Mesoporous activated carbons with enhanced porosity by optimal hydrothermal pre-treatment of biomass for supercapacitor applications, Microporous Mesoporous Mater. 218 (2015) 55–61, doi:http://dx.doi.org/10.1016/j.micromeso.2015.06.041.

[30] A. Jain, R. Balasubramanian, M.P. Srinivasan, Hydrothermal conversion of biomass waste to activated carbon with high porosity: A review, Chem. Eng. J. 283 (2016) 789–805, doi:http://dx.doi.org/10.1016/j.cej.2015.08.014.

[31] A. Jain, C. Xu, S. Jayaraman, R. Balasubramanian, J.Y.Y. Lee, M.P.P. Srinivasan, Mesoporous activated carbons with enhanced porosity by optimal hydrothermal pre-treatment of biomass for supercapacitor applications, Microporous Mesoporous Mater. 218 (2015) 55–61, doi:http://dx.doi.org/10.1016/j.micromeso.2015.06.041.

[32] A. Özhan, Ö. Şahin, M.M. Küçük, C. Saka, Preparation and characterization of activated carbon from pine cone by microwave-induced ZnCl2 activation and its effects on the adsorption of methylene blue, Cellulose. 21 (2014) 2457–2467, doi:http://dx.doi.org/10.1007/s10570-014-0299-y.

[33] E. Raymundo-Pinero, P. Azais, T. Cacciaguerra, D. Cazorla-Amorós, a. Linares-Solano, F. Béguin, E. Raymundo-Piñero, P. Azaïs, T. Cacciaguerra, D. Cazorla-Amorós, a. Linares-Solano, F. Béguin, KOH and NaOH activation mechanisms of multiwalled carbon nanotubes with different structural organisation, Carbon 43 (2005) 786–795, doi:http://dx.doi.org/10.1016/j.carbon.2004.11.005.

[34] X. Liu, R. Ma, Y. Bando, T. Sasaki, A General Strategy to Layered Transition-Metal Hydroxide Nanocones: Tuning the Composition for High Electrochemical Performance, Adv. Mater. 24 (2012) 2148–2153, doi:http://dx.doi.org/10.1002/adma.201104753.

[35] C. Zhong, Y. Deng, W. Hu, J. Qiao, L. Zhang, J. Zhang, A review of electrolyte materials and compositions for electrochemical supercapacitors, Chem. Soc. Rev. 44 (2015) 7484–7539, doi:http://dx.doi.org/10.1039/C5CS00303B.

[36] S.B. Kulkarni, U.M. Patil, I. Shackery, J.S. Sohn, S. Lee, B. Park, S. Jun, High-performance supertcapacitor electrode based on a polyaniline nanofibers/3D graphene framework as an efficient charge transporter, J. Mater. Chem. A. 2 (2014) 4989–4998, doi:http://dx.doi.org/10.1039/c3ta14959e.

[37] F. Barzegar, A. Bello, D.Y. Momodu, J.K. Dangbegnon, F. Taghizadeh, M.J. Madito, T. moureen Masikhwa, N. Manyala, J. Madito, T. moureen Masikhwa, N. Manyala, Asymmetric supercapacitor based on an α-MoO3 cathode and porous activated carbon anode materials, RSC Adv. 5 (2015) 37462–37468, doi:http://dx.doi.org/10.1039/C5RA03579A.

[38] D. Wang, J. Li, D. Zhang, T. Liu, N. Zhang, Layered Co –Mn hydroxide nanoflakes grown on carbon cloth as binder-free flexible electrodes for supercapacitors, J. Mater. Sci. 51 (2016) 3784–3792, doi:http://dx.doi.org/10.1007/s10853-015-9696-3.

[39] A.D. Jagadale, G. Guan, X. Li, X. Du, X. Ma, X. Hao, A. Abudula, Ultrathin nanoflakes of cobalt?manganese layered double hydroxide with high reversibility for asymmetric supercapacitor, J. Power Sources 306 (2016) 526–534, doi:http://dx.doi.org/10.1016/j.jpowsour.2015.12.097.

[41] S. Dong, A.Q. Dao, B. Zheng, Z. Tan, C. Fu, H. Liu, F. Xiao, One-step electrochemical synthesis of three-dimensional graphene foam loaded nickel–cobalt hydroxides nanoflakes and its electrochemical properties, Electrochim. Acta 152 (2015) 195–201, doi:http://dx.doi.org/10.1016/j.electacta.2014.09.061.

[42] H. Chen, L. Hu, M. Chen, Y. Yan, L. Wu, Nickel-Cobalt Layered Double Hydroxide Nanosheets for High-performance Supercapacitor Electrode Materials, Adv. Funct. Mater. 24 (2014) 934–942, doi:http://dx.doi.org/10.1002/adfm.201301747.

[43] L. Zhang, J. Wang, J. Zhu, X. Zhang, K. San Hui, K.N. Hui, 3D porous layered double hydroxides grown on graphene as advanced electrochemical pseudocapacitor materials, J. Mater. Chem. A. 1 (2013) 9046, doi:http://dx.doi.org/10.1039/c3ta11755c.

[44] L.-H.H. Su, X.-G.G. Zhang, Y. Liu, Electrochemical performance of Co-Al layered double hydroxide nanosheets mixed with multiwall carbon nanotubes, J. Solid State Electrochem. 12 (2008) 1129–1134, doi:http://dx.doi.org/10.1007/s10008-007-0455-5.

[45] A. Balducci, D. Belanger, T. Brousse, J.W. Long, W. Sugimoto, Perspective—A Guideline for Reporting Performance Metrics with Electrochemical Capacitors: From Electrode Materials to Full Devices, J. Electrochem. Soc. 164 (2017) A1487–A1488, doi:http://dx.doi.org/10.1149/2.0851707jes.

[46] B. Akinwolemiwa, C. Peng, G.Z. Chen, Redox Electrolytes in Supercapacitors, J. Electrochem. Soc. 162 (2015) A5054–A5059, doi:http://dx.doi.org/10.1149/2.0111505jes.

[47] A. Laheaar, P. Przygocki, Q. Abbas, F. B??guin, A. Laheäär, P. Przygocki, Q. Abbas, F. Béguin, Appropriate methods for evaluating the efficiency and capacitive behavior of different types of supercapacitors, Electrochem. Commun. 60 (2015) 21–25, doi:http://dx.doi.org/10.1016/j.elecom.2015.07.022.

[48] A. Bello, N. Manyala, F. Barzegar, A.A. Khaleed, D.Y. Momodu, J.K. Dangbegnon, Renewable pine cone biomass derived carbon materials for supercapacitor application, RSC Adv. 6 (2016) 1800–1809, doi:http://dx.doi.org/10.1039/C5RA21708C.

[49] Y. Song, J. Wang, Z. Li, D. Guan, T. Mann, Q. Liu, M. Zhang, L. Liu, Self-assembled hierarchical porous layered double hydroxides by solvothermal method and their application for capacitors, Microporous Mesoporous Mater. 148 (2012) 159–165, doi:http://dx.doi.org/10.1016/j.micromeso.2011.08.013.

[50] F. Deng, L. Yu, M. Sun, T. Lin, G. Cheng, B. Lan, F. Ye, Controllable Growth of Hierarchical NiCo2O4 Nanowires and Nanosheets on Carbon Fiber Paper and their Morphology-Dependent Pseudocapacitive Performances, Electrochim. Acta. 133 (2014) 382–390, doi:http://dx.doi.org/10.1016/j.electacta.2014.04.070.

[51] L. Yu, L. Zhang, H. Bin Wu, G. Zhang, X.W. (David) Lou, Controlled synthesis of hierarchical $Co_x Mn_{3-x} O_4$ array micro-/nanostructures with tunable morphology and composition as integrated electrodes for lithium-ion batteries, Energy Environ. Sci. 6 (2013) 2664–2671, doi:http://dx.doi.org/10.1039/C3EE41181H.

[52] S. Liu, S.C. Lee, U. Patil, I. Shackery, S. Kang, K. Zhang, J.H. Park, K.Y. Chung, S. Chan Jun, Hierarchical MnCo-layered double hydroxides@$Ni(OH)_2$ core?shell heterostructures as advanced electrodes for supercapacitors, J. Mater. Chem. A. 5 (2017) 1043–1049, doi:http://dx.doi.org/10.1039/C6TA07842G.

[53] G.H. and, D. O'Hare, Unique Layered Double Hydroxide Morphologies Using Reverse Microemulsion Synthesis, J.AM.Chem.Soc. 127 (2005) 17808–17813, doi:http://dx.doi.org/10.1021/JA0549392.

[54] K. Shukla, V.C. Srivastava, Synthesis of organic carbonates from alcoholysis of urea: A review, Catal. Rev. 59 (2017) 1–43, doi:http://dx.doi.org/10.1080/01614940.2016.1263088.

[55] L. Xu, Y.-S. Ding, C.-H. Chen, L. Zhao, C. Rimkus, R. Joesten, S.L. Suib, 3D Flowerlike α-Nickel Hydroxide with Enhanced Electrochemical Activity Synthesized by Microwave-Assisted Hydrothermal Method, Chem. Mater. 20 (2008) 308–316, doi:http://dx.doi.org/10.1021/cm702207w.

[56] D. Momodu, A. Bello, J. Dangbegnon, F. Barzeger, F. Taghizadeh, M. Fabiane, A.T. C. Johnson, N. Manyala, Solvothermal synthesis of NiAl double hydroxide microspheres on a nickel foam-graphene as an electrode material for pseudo-capacitors, AIP Adv. 4 (2014) 097122, doi:http://dx.doi.org/10.1063/1.4896125.

[57] N. Manyala, A. Bello, F. Barzegar, A.A.A. Khaleed, D.Y.Y. Momodu, J.K.K. Dangbegnon, Coniferous pine biomass: A novel insight into sustainable carbon materials for supercapacitors electrode, Mater. Chem. Phys. 182 (2015) 139–147, doi:http://dx.doi.org/10.1016/j.matchemphys.2016.07.015.

[58] A.N. Naveen, S. Selladurai, A 1-D/2-D hybrid nanostructured manganese cobaltite?graphene nanocomposite for electrochemical energy storage, RSC Adv. 5 (2015) 65139–65152, doi:http://dx.doi.org/10.1039/C5RA09288D.

[59] J.P. Cheng, L. Liu, J. Zhang, F. Liu, X.B. Zhang, Influences of anion exchange and phase transformation on the supercapacitive properties of α-Co(OH)2, J. Electroanal. Chem. 722–723 (2014) 23–31, doi:http://dx.doi.org/10.1016/j.jelechem.2014.03.019.

[60] B.K. Pandey, A.K. Shahi, R. Gopal, Magnetic colloid by PLA: Optical, magnetic and thermal transport properties, Appl. Surf. Sci. 347 (2015) 461–470, doi:http://dx.doi.org/10.1016/j.apsusc.2015.04.045.

[61] W. Yang, Z. Gao, J. Wang, J. Ma, M. Zhang, L. Liu, Solvothermal one-step synthesis of Ni-Al layered double hydroxide/carbon nanotube/reduced graphene oxide sheet ternary nanocomposite with ultrahigh capacitance for supercapacitors, ACS Appl. Mater. Interfaces. 5 (2013) 5443–5454, doi:http://dx.doi.org/10.1021/am4003843.

[62] M. Zhi, C. Xiang, J. Li, M. Li, N. Wu, Nanostructured carbon-metal oxide composite electrodes for supercapacitors: a review, Nanoscale. 5 (2013) 72–88, doi:http://dx.doi.org/10.1039/c2nr32040a.

[63] S. Hu, Y. Li, F. Lai, X. Zhang, Q. Li, Y. Huang, X. Yuan, J. Chen, H. Wang, Enhanced electrochemical performance of $LiMn_2 O_4$ cathode with a $Li_{0.34} La_{0.51} TiO_3$ –coated layer, RSC Adv. 5 (2015) 17592–17600, doi:http://dx.doi.org/10.1039/C4RA15374J.

[64] C. Guan, J. Liu, C. Cheng, H. Li, X. Li, W. Zhou, H. Zhang, H.J. Fan, Hybrid structure of cobalt monoxide nanowire @ nickel hydroxidenitrate nanoflake aligned on nickel foam for high-rate supercapacitor, Energy Environ. Sci. 4 (2011) 4496, doi:http://dx.doi.org/10.1039/c1ee01685g.

[65] S.I. Cordoba, R.E. Carbonio, M.L. Teijelo, V.A. Macagno, The electrochemical response of binary mixtures of hydrous transition metal hydroxides co-precipitated on conducting substrates with reference to the oxygen evolution reaction, Electrochim. Acta. 31 (1986) 1321–1332, doi:http://dx.doi.org/10.1016/0013-4686(86)80155-4.

[66] K. Fic, G. Lota, M. Meller, E. Frackowiak, Novel insight into neutral medium as electrolyte for high-voltage supercapacitors, Energy Environ. Sci. 5 (2012) 5842–5850, doi:http://dx.doi.org/10.1039/C1EE02262H.

[67] Y.-G. Wang, L. Cheng, Y.-Y. Xia, Electrochemical profile of nano-particle CoAl double hydroxide/active carbon supercapacitor using KOH electrolyte solution, J. Power Sources. 153 (2006) 191–196, doi:http://dx.doi.org/10.1016/j.jpowsour.2005.04.009.

[68] W. Quan, C. Jiang, S. Wang, Y. Li, Z. Zhang, Z. Tang, F. Favier, New nanocomposite material as supercapacitor electrode prepared via restacking of Ni-Mn LDH and MnO 2 nanosheets, Electrochim. Acta. 247 (2017) 1072–1079, doi:http://dx.doi.org/10.1016/j.electacta.2017.07.010.

[70] R. Li, S. Wang, Z. Huang, F. Lu, T. He, NiCo2S4@Co(OH)2 core-shell nanotube arrays in situ grown on Ni foam for high performances asymmetric supercapacitors, J. Power Sources. 312 (2016) 156–164, doi:http://dx.doi.org/10.1016/j.jpowsour.2016.02.047.

[80] P.L. Taberna, P. Simon, J.F. Fauvarque, Electrochemical Characteristics and Impedance Spectroscopy Studies of Carbon-Carbon Supercapacitors, J. Electrochem. Soc. 150 (2003) A292, doi:http://dx.doi.org/10.1149/1.1543948.

4.2.4 Concluding remarks

Co-Mn LDH with nanoflake-like morphology was successfully synthesized by facile solvothermal synthesis and AC with good porous structure was successfully synthesized by environmentally friendly hydrothermal/CVD syntheses routes. A hybrid device Co-Mn LDH//AC was successfully fabricated with Co-Mn LDH as positive electrode and AC as negative electrode. The device displayed very good electrochemical performance with a high energy density of 20.3 W h kg^{-1} and corresponding power density of up to 435 W kg^{-1} at 0.5 A g^{-1} current density in 1 M KOH aqueous electrolyte. A very high stability with 99.7% capacitance retention was obtained after 10,000 continuous charge-discharge cycles and negligible degradation after subsequently subjecting it to voltage holding test for 70 hours at 1.6 V maximum voltage. The results indicate the potential use of the hybrid device as possible electrode for energy storage application.

4.3 Electrochemical characterization of activated carbon derived from cork (Quercus suber) synthesized by chemical activation with $KHCO_3$

4.3.1 Introduction

Different chemical activating agents have been employed for the activation of biomass wastes for the production of porous activated carbons which include H_3PO_4, H_2SO_4, $ZnCl_2$, NaOH, KOH e.t.c. But the most commonly utilized is KOH owing to the fact it is useful for the production of carbons with well-defined micro- and meso-pore structures with high yield and adjustable porosity [45,215]. However, the industrial application of KOH is limited by its corrosive nature. This environmental unfriendliness has necessitated the need for milder alternatives for the production of porous activated carbons. It has been reported that mild alkaline salts such as K_2CO_3, $KHCO_3$ can yield good porous carbons with good textural properties [36,44].

The difficulty in controlling the pore structure and morphology of the carbon from some biomass sources activated with corrosive chemical activating agents in spite of extensive research and improvement in activation process greatly hinders their electrochemical performance [42,45]. The pre-treatment of carbon containing precursors have also been considered to be a better option for the production of high quality carbons with good pore structures with high electrochemical performance because of the presence of oxygenated functional groups [45]. Mild alkaline salts have also been shown to preserve the hydrochar morphology leading to the production of carbons with shorter diffusion distances leading to improved electrochemical performance.

In section 4.1, we discussed the electrochemical performance of AC in relation to KOH activation concentration. The effect of KOH activation concentration on the morphology, SSA, porosity and electrochemical performance of AC was succinctly elucidated. In this section we present the results of AC synthesized from hydrothermally pretreated cork (Quercus suber) activated with mild $KHCO_3$ activating agent in a ratio of 1:1, in order to investigate the effect of the use of a milder potassium salt in the electrochemical performance of AC. The electrochemical characterization of the as-synthesized $ACKHCO_3$ material was carried out in the three-electrode set-up in acidic 1 M H_2SO_4, alkaline 6 M KOH and neutral 3 M KNO_3 aqueous electrolytes to find the best working parameters. From this investigation, 3 M KNO_3 neutral electrolyte was used for the design of the full cell symmetric device based on its performance in both positive and negative potentials.

The details of the result from this investigation is presented in the following publication

4.3.3 Result and discussion

AIP ADVANCES **8**, 055208 (2018)

Nanostructured porous carbons with high rate cycling and floating performance for supercapacitor application

F. O. Ochai-Ejeh,[1] D. Y. Momodu,[1] M. J. Madito,[1] A. A. Khaleed,[1]
K. O. Oyedotun,[1] S. C. Ray,[2] and N. Manyala[1,a]
[1] *Department of Physics, Institute of Applied Materials, SARChI Chair in Carbon Technology and Materials, University of Pretoria, 0028, South Africa*
[2] *Department of Physics, University of South Africa, Florida Science Campus, Florida, Johannesburg 1709, South Africa*

(Received 20 January 2018; accepted 22 April 2018; published online 8 May 2018)

Biomass-derived activated carbon from cork (Quercus Suber) (ACQS) was prepared via a two-step environment-friendly route using mild $KHCO_3$ as the activating agent. This synthesis route makes the material produced less toxic for usage as electrode material for energy storage application. The ACQS has well-defined microporous and mesoporous structures and a specific surface area of 1056.52 $m^2\ g^{-1}$ and pore volume of 0.64 $cm^3\ g^{-1}$. Three-electrode tests were performed in 6 M KOH, 1 M H_2SO_4 and 3 M KNO_3 aqueous electrolytes, to analyse the material performance in acidic, basic, and neutral media. Specific capacitance values (C_s) of 133 F g^{-1}/167 F g^{-1} at 1.0 A g^{-1} was obtained in 3 M KNO_3 in the positive/negative potential windows. Due to the observed best performance in neutral 3 M KNO_3, further electrochemical analysis of the symmetric device was carried out using the same electrolyte. The device displayed a C_s value of 122 F g^{-1}, energy and power densities of ~14 W h kg^{-1} and 450 W kg^{-1} respectively; at 0.5 A g^{-1}. The device also displayed an excellent stability after potentiostatic floating at a maximum voltage of 1.8 V for 120 h and ~100% capacitance retention after 10,000 charge-discharge cycles. The excellent stability makes the cork-derived material a potential excellent, cost-effective material for supercapacitor application. https://doi.org/10.1063/1.5023046

I. INTRODUCTION

Dependence on the energy supply from limited fossil fuels has led to increased environmental pollution and degradation through the emission of air pollutants and greenhouse gases.[1–3] A better way to combat this issue is by designing a means by which the amount of energy produced by fossil fuels is drastically reduced via conversion into cleaner and safer energy generation routes. The realistic solution to a clean, renewable, sustainable, efficient and safer energy generation option is in the use of renewable energy from clean sources such as the sun, wind, geothermal, plant biomass waste amongst others.[1,4,5] Biomass waste materials have been referred to as one of the key renewable energy sources which transform raw waste into porous carbons for supercapacitor application.[3,6,7] However, to successfully pilot the as-generated energy for effective use in different applications, there is a need for a reliable and efficient storage model.[2] The most common storage gadgets today are high-performance batteries (hpBs) which are plagued with low power densities and to some safety issues which limits their use in high-power applications.[8,9]

---

[a] Corresponding author's email: ncholu.manyala@up.ac.za; Tel.: + (27)12 420 3549; Fax: + (27)12 420 2516

2158-3226/2018/8(5)/055208/15

Electrochemical capacitors (ECs) on the other hand, which are characterized by reasonably high power density, good cyclic life, relative high safety and low maintenance cost, have been reported as an emerging storage technology with a potential to replace/compliment batteries even though they are plagued with low energy density as well, as compared to batteries.[10–13] The backbone behind the excellent performance of both batteries and supercapacitors lie in the nature of the materials used to make up the devices. Therefore, it is highly important to develop highly functional materials that will be able to store energy efficiently over time. ECs make use of different forms of materials as electrode materials. Among these materials, porous carbons have been widely and commercially utilized successfully due to their long-term cycling stability, easy production, ability to operate in aqueous and non-aqueous electrolytes, large specific surface areas (SSA), good conductivity, low cost, nontoxicity and tunable microstructure etc.[1,4,8,14–17] Owing to these numerous advantages, activated carbon has been employed in different applications such as drug delivery systems, absorbents, hydrogen storage and electrochemical energy storage.[1,3,18–20]

Numerous studies on the conversion of biomass wastes to materials for various applications have been carried out[7,18,21–25] using pre-treatment hydrothermal techniques, simple drying, spray drying, pyrolysis, controlled combustion in an inert gas. Studies have shown that for electrochemical energy storage applications, the appropriate combination of micropore/mesopore volume, surface area, and pore size distribution is ideal for excellent supercapacitor performance which combines good specific capacitance value with good rate capability, high rate power delivery, high energy storage capability without compromising the stability.[1,7,23] To achieve this, strategic physical or chemical processes are required to produce carbons of the desired properties.[1,7] The physical process involves gasifying carbon precursors previously carbonized in an inert atmosphere with CO_2, O_2 or steam within a temperature range of 600 - 1200 °C, while chemical activation involves impregnating the carbon precursor with activating agents like $ZnCl_2$, H_2SO_4, KOH, etc. The latter is the most commonly utilized because it results in a material with high specific surface areas and high micropore volume with good pore size distribution which are necessary for good electrochemical performance.[11,20] Although, KOH has been considered to be corrosive leading to limitation in its industrial utilization,[23,26] interestingly in our earlier studies[9] KOH was utilized as an activating agent, and was optimized with respect to KOH - raw material mass ratio, carbonization temperature and time to obtain activated carbon material activated with mild KOH concentration having good microstructures suitable for better electrochemical performance and an environment friendly energy storage device were established.

In this regard, the present study embarked on the use of mild $KHCO_3$ activating agent (which is even more environmentally friendly as compared to KOH) in a 1:1 ratio with hydrothermally treated active raw cork (Quercus Suber) biomass for the material synthesis. An extensive electrochemical testing of the as-synthesized ACQS material was done in the three-electrode set-up in acidic 1 M H_2SO_4, alkaline 6 M KOH and neutral 3 M KNO_3 aqueous electrolytes to obtain the best working parameters in the half-cell electrodes. From the analysis, 3 M KNO_3 neutral electrolyte was then adopted for the design of the full device based on its outstanding performance in both positive and negative potentials. The results obtained show-cased an excellent stability up to 10,000 charge-discharge cycles, excellent capacitance retention and an exceptional capacitance improvement after the first 10 h of the 120 h floating period depicting a relatively stable symmetric device with a potential for energy storage.

II. EXPERIMENTAL DETAILS

A. Material synthesis

10 g of raw cork (Quercus Suber) was washed using acetone and deionized water and dried in an oven at 60 °C for several hours. Then the raw cork was pre-treated with 0.8 ml of 0.5 M sulfuric acid and 80 ml deionized water in a hydrothermal system at 160 °C for 12 hours. The hydrochar obtained was washed with deionized water several times and dried in an oven. The hydrochar was then ground and re-weighed and activated with potassium hydrogen carbonate ($KHCO_3$) in a ratio of 1:1. The activated hydrochar was carbonized under argon flow in a chemical vapour deposition system at

850 °C for 2 hours. The product obtained was then washed several times using 3 M HCl and deionized water and dried in an oven at 60 °C overnight.

B. Material characterization

Scanning electron microscopy (SEM) measurements were performed using Zeiss Ultra plus 55 field emission scanning electron microscope (FE-SEM) operating at an accelerating voltage of 2.0 kV. Energy-dispersive X-ray (EDX) analysis, high-resolution transmission electron microscopy (HRTEM) and selected area diffraction (SAED) analysis of the sample was measured using JEOL 2100 (Tokyo Japan) operated at 200 kV. X-ray photoelectron spectroscopy (XPS) measurements were performed using a Physical Electronics Versa Probe 5000 spectrometer. X-ray Diffraction (XRD) analysis was performed using XPERT-PRO diffractometer (PANalytical BV the Netherlands). Fourier transform infrared (FT-IR) spectroscopy was carried out using Perkin Elmer Spectrum RX I FT-IR system in the 4000 – 500 cm^{-1} range with a resolution of 2 cm^{-1} to determine the sample surface functional groups. The FT-IR measurements were performed by properly blending the samples with KBr in a ratio of 1:100 and making them into transparent pellets before measurements. The Brunauer-Emmett-Teller (BET) technique was used to obtain the specific surface area and the N_2 adsorption/desorption isotherm measurements was performed at -196 °C with a Micrometrics TriStar II 3020. Raman analysis was performed using a Jobin-Yvon Horiba TX 64000 micro-spectrometer.

C. Electrochemical characterization

Three- and two-electrode measurements of the ACQS sample was performed in a multichannel VMP300 potentiostat/galvanostat (Biologic, France) workstation at room temperature. The electrodes for the three-electrode measurements were made by adding 80 wt.% ACQS material, 15 wt.% carbon black (to boost the conductivity of the material) and 5 wt.% polyvinylidene difluoride (PVdF) as a binder in an agate mortar and then mixed properly by adding 1-methyl-2-pyrrolidinone (NMP) drop-wise to make a paste. This was then pasted on nickel foam (NF)/carbon cloth current collectors and dried in an oven at 60 °C for several hours. The paste for the two-electrode tests was prepared using the same method but was coated on 16 mm diameter Nickel foam (NF) and dried at 60 °C, pressed and then assembled in a coin cell with a microfiber glass filter paper as a separator. The three electrode tests were performed in 3 M KNO_3, 6 M KOH and 1 M H_2SO_4 aqueous electrolytes using Ag/AgCl and glassy carbon as reference and counter electrodes respectively. The two electrode tests were then performed in 3 M KNO_3 neutral electrolyte because of the good reversibility of the material in both positive and negative voltage windows in this electrolyte. The specific capacitance, C_s for the half-cell electrode in a three electrode configuration is given by equation (1):[27]

$$C_s(\text{F g}^{-1}) = \frac{I\Delta t}{m\Delta U} \tag{1}$$

The specific capacitance, C_{sp} per single electrode of the full device was calculated from the charge-discharge profile using equation (2):[3]

$$C_{sp}(\text{F g}^{-1}) = \frac{4I\Delta t}{m\Delta U} \tag{2}$$

Where I is the applied current (A), Δt is the discharge time (s), ΔU is the maximum cell voltage (V), and m is the total mass of the electrodes (g). Four (4) is a normalization factor of the symmetric electrodes to the mass of a single electrode. The energy density, E_d and power density, P_d were calculated from equation (3) and (4)[3,28] (using parameters from equation (2)).

$$E_d(\text{W h kg}^{-1}) = \frac{C_{sp} \times \Delta U^2}{28.8} \tag{3}$$

$$P_d\left(\text{W kg}^{-1}\right) = \frac{E_d}{\Delta t} \tag{4}$$

III. RESULTS AND DISCUSSION

A. Material characterization

The SEM images of the ACQS material are presented in Fig. 1. Figs. 1(a) and (b) display the SEM images of the ACQS sample at low and high magnifications. The micrographs display 3D granular porous network structures of the material. The surface morphology of the material shows that $KHCO_3$ activation leads to the production of porous granular carbons which could improve the fast diffusion of ions along the material surfaces, useful for high-performance supercapacitor application.[23] The carbonization reaction mostly proceeds by the decomposition of $KHCO_3$ between the temperature ranges of 100 – 400 °C in the following reaction[23,29,30]

$$2KHCO_3 \leftrightarrow K_2CO_3 + H_2O + CO_2 \tag{5}$$

K_2CO_3 decomposes into CO_2 and K_2O via a reaction with carbon to yield K at temperatures > 700 °C,

$$K_2CO_3 + 2C \rightarrow 2K + 3CO \tag{6}$$

K_2CO_3, however, does not melt at temperatures < 890 °C thereby allowing the granular morphology of the carbon to be preserved.[23] Any unreacted K_2CO_3 slowly decomposes at 850 °C according to the following equation:[23]

$$K_2CO_3 \rightarrow K_2O + CO_2 \tag{7}$$

At this temperature, the surface area and porosity of the material might be increased or modified because the CO_2 gas interacting with the carbon material to create more pores or modify existing ones.[23,30]

The morphology of the as-synthesized ACQS material was further studied using HRTEM and is presented in Figs. 2(a) and (b). The high and low magnifications HRTEM images of the sample show no lattice fringes which are an indication that ACQS is mostly amorphous carbon. This is supported by the SAED pattern (inset to Fig. 2(b) which shows halo ring with no diffraction spots indicating the amorphicity of ACQS material.

EDX spectrum for the ACQS material is presented in Figure 2(c). The EDX plot confirmed the high carbon content of the as-synthesized ACQS material. The summary of the elemental composition is presented in Table I.

The oxygen content recorded is linked to the functional group present in the sample. The Cu recorded in trace amount was a contribution from the copper grid. The structure of the ACQS sample was studied by XRD technique. The XRD pattern of the ACQS sample (Fig. 3(a)) shows a wide and broad peak at 26° (002) and a weak peak at 51° (012). The diffraction peaks of the ACQS sample can be indexed to a hexagonal crystal structure of graphite having a space group of *P*63*mc* utilizing the most appropriate matching Inorganic Crystal Structure Database (ICSD) card #31170. The peaks represent graphitic diffraction planes, but the broad and low intensity of the peaks is an indication that the ACQS material is mostly non-crystalline and can be referred to as amorphous carbon.[31]

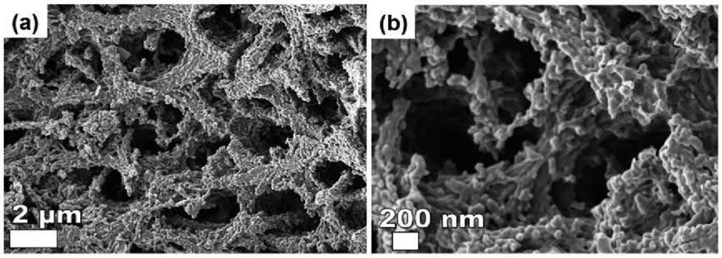

FIG. 1. SEM micrographs of ACQS at (a) low and (b) high magnification.

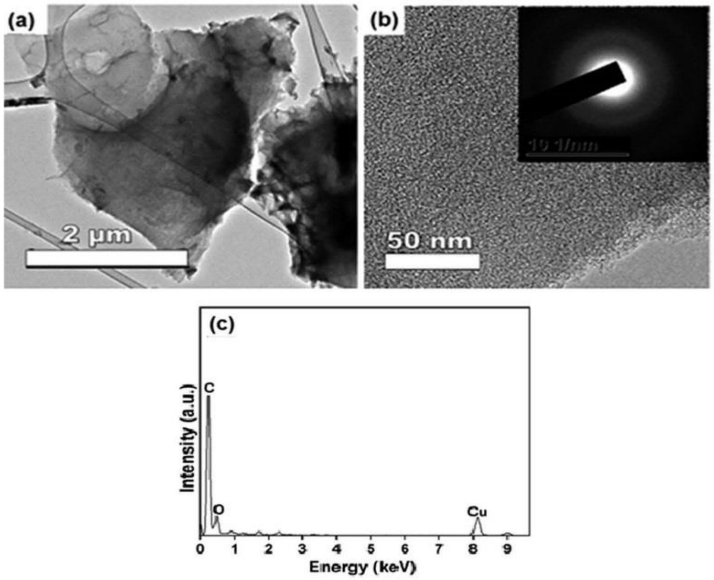

FIG. 2. HRTEM micrographs of ACQS at (a) low and (b) high magnifications; (c) EDX spectrum of ACQS.

FT-IR measurement was carried out to determine the presence of surface functional groups in the as-synthesized ACQS sample in the wavenumber range of 500 to 4000 cm^{-1} (Fig. 3(b)). The bands occurring at ~3435 cm^{-1} is as a result of the O-H stretching vibrations of water molecule due to surface hydroxyl groups. The peaks at ~2942 cm^{-1} indicate the C-H bond of the aliphatic group while the peak at ~1608 cm^{-1} is attributed to the C=O stretching vibrations of the carboxyl groups. The peaks occurring at ~1050 cm^{-1} and ~582 cm^{-1} may be due to the -C-C stretching vibration.[3,32]

The ACQS sample composition was further analyzed with XPS. The high-resolution survey spectrum of the as-received ACQS sample (without sputter cleaning) is presented in Fig. 4(a) and a summary of the sample composition showing high carbon content of the as-synthesized ACQS material is displayed in Table II. Fig. 4(b) shows core level spectrum of C 1s with intensity peaks associated with the graphitic carbon C=C or C-C and other peaks relating to C-O, C-O=C or C=O. Figure 4c shows the spectrum for the O 1s with peaks at binding energies 531.7 eV and 533.2 eV associated with C-O and O-C indicating the presence of functional groups as suggested by FT-IR measurements.

The Raman spectrum of the ACQS sample is presented in Fig. 5(a). The spectrum shows the D band at ~1338 cm^{-1} and the G band at ~1587 cm^{-1} which are characteristic of disordered carbons in the sp^2 carbon network and graphitic carbon tangential vibrations respectively.[33,34] The ratio of the intensity of the D and G peaks (I_D/I_G) expresses the extent of graphitization of the material. This ratio

TABLE I. Summary of the elemental composition of the sample.

Element	Weight %	Atomic %
C K	89.24	91.75
O K	10.72	8.24
Cu K	0.05	0.01

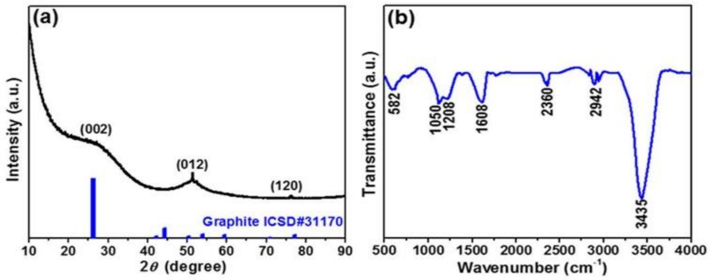

FIG. 3. (a) XRD spectrum (b) FT-IR spectrum of ACQS as-synthesized sample.

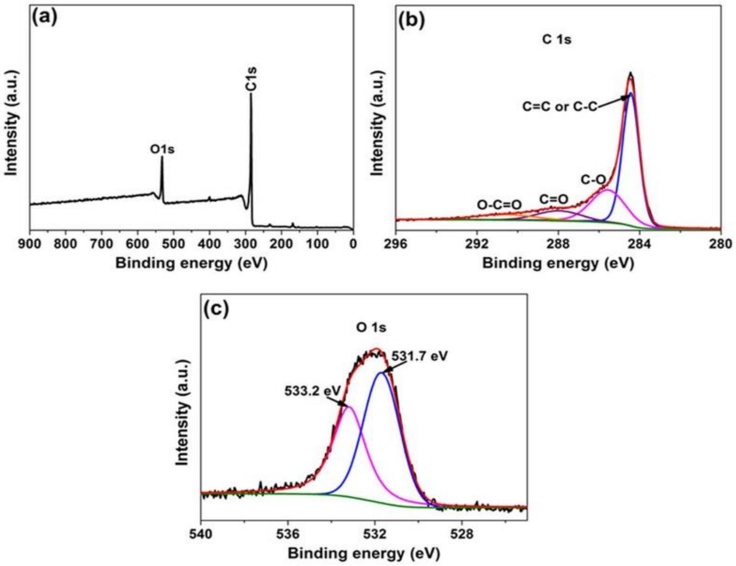

FIG. 4. (a) XPS survey spectrum of the as-received (without sputter cleaning) ACQS; High-resolution core level spectra of (b) C1's and (c) O1's of ACQS.

for the ACQS sample is 0.89 which is an indication of a low amount of graphitic crystallinity[34–37] further confirming the observed XRD result. The broadband in Fig. 5(a) was deconvoluted using Lorentzian distribution for the curve fitting, (see Fig. 5(b)). The peak 1 curve is ascribed to the lattice vibrations linked to sp^2-sp^3 network and peak 2 curve characteristically stems from the dissemination of unstructured carbon in interstitial sites in the disturbed graphitic lattice.[38] In a nutshell, the Raman spectrum indicates that the ACQS material contains a substantial quantity of interstitial unstructured carbon in the lattice framework.

TABLE II. A summary of the sample composition from XPS analysis.

Sample	C at. %	O at. %
ACQS	88.92 ±0.66	11.11 ±0.29

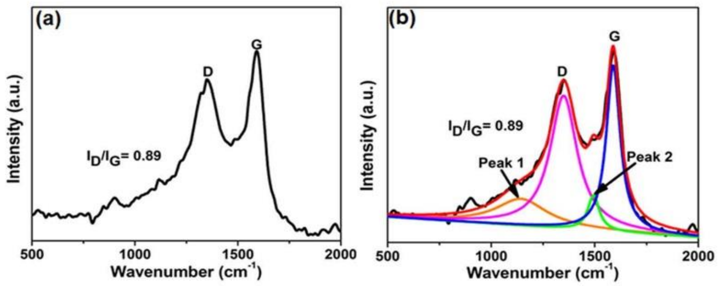

FIG. 5. (a) Raman spectra of ACQS and (b) Lorentzians curve fitting of the Raman spectrum for ACQS showing deferent peaks.

N_2 adsorption-desorption isotherms of the ACQS sample studied at -196 °C is presented in Fig. 6. Fig. 6 shows typical type IV with an H4 hysteresis loop signifying materials consisting of a microporous and mesoporous structure with relative pressure (P/P_o) > 0.2 and SSA of 1056.52 m^2 g^{-1} and pore volume of 0.64 cm^3 g^{-1}. The pore size distribution (PSD) (inset to Fig. 6 is in the range of 2-10 nm. The high SSA of the material and the PSD narrow range coupled with the granular microstructures can provide more active sites that ensure that the ACQS surface is sufficiently exposed for the electrolyte ions to access the micropores of the material.[39,40]

B. Electrochemical analysis

The CV plots of the ACQS electrodes tested in the three-electrode configuration in 6 M KOH, 1 M H_2SO_4 and 3 M KNO_3 aqueous electrolytes at 50 mV s^{-1} scan rate are shown in Fig. 7. Rectangular shaped CV profiles are observed for the ACQS sample in the positive and negative potential windows of 0.0 to 0.9 V and -0.9 to 0.0 V in 3 M KNO_3 aqueous neutral electrolyte, which are typical of electric double layer capacitive (EDLC) performance of the ACQS sample. It can be observed that the material is able to operate reversibly with typical rectangular EDLC curves and is stable within the positive and negative potential windows with di-hydrogen and oxygen evolutions only observed as the potential is increased to -1.0 and 1.0 V (See Fig. S1 in the supplementary material). From Fig. 7, quasi-rectangular curves can be observed for the ACQS sample in 6 M KOH in the negative potential window of -1.0 to 0.0 V and for the material tested in 1 M H_2SO_4 in the positive potential window of 0.0 to 0.9 V. Also for the ACQS sample tested in 6 M KOH, the onset of oxygen evolutions can already be observed beyond 0.2 V in the positive potential window and in 1 M H_2SO_4,

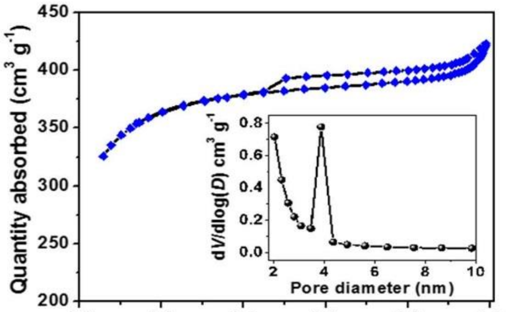

FIG. 6. Nitrogen absorption-desorption isotherm with inset showing the BJH pore size distribution of ACQS.

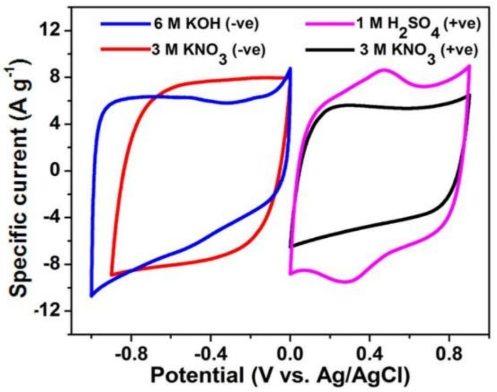

FIG. 7. CV curves at 50 mV s^{-1} scan rate in 3 M KNO_3 at -0.9 to 0.0 V and 0.0 to 0.9 V potential windows, 6 M KOH at -1.0 to 0.0 V potential window and 1 M H_2SO_4 at 0.0 to 0.9 V potential window.

oxygen evolutions can be observed as the potential approaches 1.0 V and di-hydrogen evolutions can be observed to already occur beyond -0.2 V (see Fig. S1 in the supplementary material). This phenomenon might be due to the decomposition of the ions of the electrolytes beyond 1.2 V and -1.2 V in the alkaline and acidic electrolytes respectively due to the thermal decomposition of water at 1.23 V.[9,22,41] Also, from Fig. 7, the CV curves display different current responses within their respective operating potential windows (see the CV curves of the ACQS electrode materials at various scan rates ranging from 10 to 100 mV s^{-1} in 6 M KOH, 1 M H_2SO_4 and 3 M KNO_3 aqueous electrolytes in Fig. S2 of supplementary material). The disparity observed in electrochemical performances of the ACQS material in the various electrolytes could be due to the pH of the different electrolytes and/or pseudo-capacitance contribution from surface functional groups.[26,42,43] For example, in 3 M KNO_3 neutral electrolyte, the H^+ and OH^- ions are fewer as compared to those in the acidic and alkaline electrolytes, and the pH is balanced on the H^+/OH^- ions such that the ions of the electrolyte are not biased to react with the electrode material in any preferred potential.[3,26,44] Whereas the acidic and alkaline electrolytes have an abundance of the OH^- and H^+ ions which can make the material have a biased reaction in a given potential.[44] Other parameters such as the sizes of the ionic radii, ionic conductivities, and radii of the ionic hydration spheres and the mobility of the ions of the electrolytes may play a role as they interact with the electrode material.[2,15,42,44] These electrolyte properties are itemized in Table III. From the Table III, it can be observed that the radius of hydration spheres for the electrolytes in any particular potential, decreases in this order: $H^+ < K^+$ & $OH^- < NO_3^- < SO_4^{2-}$ and the molar and ionic conductivities of the electrolyte ions increases in this order: $H^+ > K^+$ & $OH^- > SO_4^{2-} > NO_3^-$, so the molar and ionic conductivities might be a contributing factor in the difference in electrochemical responses. The high molar conductivities of the OH^- ions and the H^+ and SO_4^{2-} in KOH and H_2SO_4 electrolytes, which are higher than that of NO_3^- in KNO_3 might be the reason

TABLE III. Size, crystal radius, radius of hydration sphere, ionic conductivity, Gibbs energy and mobility of the electrolyte ions (These values were obtained from Refs. 2 and 43).

Ion	Crystal radius (Å)	Hydration sphere radius (Å)	Molar conductivity (S cm^2 mol^{-1})	Ionic mobility (μ10^{-5} cm^2 s^{-1} V^{-1})
K^+	1.33	3.31	73.5	7.6
H^+	1.15	2.80	349.8	36.2
SO_4^{2-}	2.90	3.79	160.0	8.3
NO_3^-	2.64	3.35	71.42	-
OH^-	1.76	3.00	198.0	20.6

for the higher specific capacitance of the material in the H_2SO_4 and KOH electrolytes. However, the ACQS material is only able to operate reversibly in the positive and negative potential windows in the 3 M KNO_3 electrolyte, hence its utilization in the symmetric device fabrication.

The Charge-discharge (CD) curves measured in the positive and negative potential windows of 0.0 to 0.9 V and -0.9 to 0.0 V, respectively in 3 M KNO_3 at 1.0 A g^{-1} to 5.0 A g^{-1} specific current are presented in Figs. 8(a) and (b). The CD profiles show triangular symmetrical shapes corresponding to the characteristic EDLC behavior observed for the CV curves.

The Specific capacitance (C_S) values calculated from the CD profiles in the positive potential window are from 133 to 94.0 F g^{-1} and in the negative potential window, from 167 to 139 F g^{-1}, at 1.0 to 5.0 A g^{-1}, respectively. The CD profiles for the test performed at specific currents of 1.0 to 5.0 A g^{-1} in 6 M KOH in the negative potential window of - 1.0 to 0.0 V and in 1 M H_2SO_4 positive potential window of 0.0 to 0.9 V are presented in Figs. 8(c) and (d). The observed triangular shapes are however slightly distorted due to the presence of hydroxyl functional groups in the sample (as indicated by FT-IR measurement), which could readily react with the abundant H^+ and OH^- ions. The calculated C_S values from the CD profiles for the material in 6 M KOH are from 250 to 130 F g^{-1}

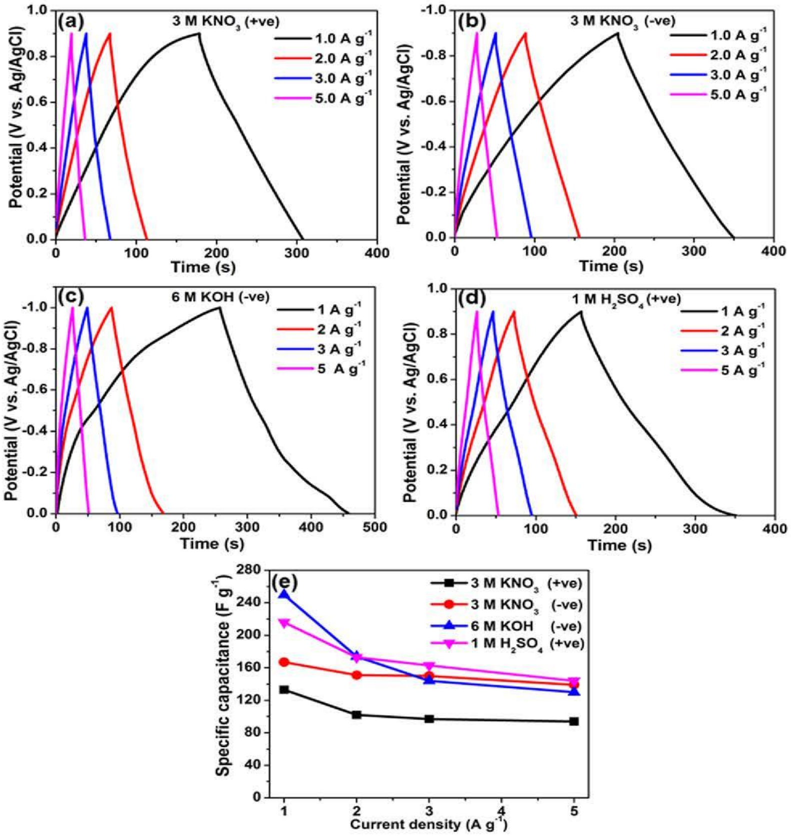

FIG. 8. Charge-discharge profile at 1.0 A g^{-1} to 5.0 A g^{-1} specific currents for the ACQS material in (a) and (b) 3 M KNO_3 in the positive and negative potential windows of 0.0 to 0.9 V and -0.9 to 0.0 V, (c) 6 M KOH in the negative potential window of -1.0 to 0.0 V and (d) 1 M H_2SO_4 in the positive potential window of 0.0 to 1.0 V. (e) Specific capacitance versus specific current in 3 M KNO_3, 6 M KOH and 1 M H_2SO_4 in the positive and negative potential windows.

and the C_S values calculated from the CD profiles for the material in 1 M H_2SO_4 are from 216 to 144 F g^{-1} at 1.0 to 5.0 A g^{-1}, respectively. A plot of the C_S values as a function of specific currents for the material in 3 M KNO_3, 6 M KOH and 1 M H_2SO_4 electrolytes in the positive and negative potential windows are shown in Fig. 8(e).

A symmetric device was assembled based on the performance of the material in the three-electrode configuration. The CV plots of the the ACQS//ACQS symmetric device fabricated from ACQS electrodes in 3 M KNO_3 at various voltage windows ranging from 1.4 to 1.8 V at 25 mV s^{-1} scan rate is presented in Fig. 9(a). The optimization of the working voltage windows is to obtain the most stable voltage window of the symmetric device. It has been shown in previous reports that neutral electrolytes are able to function with large operating potentials as a result of high over potential for di-hydrogen evolutions.[7,9,26,44]

The CV curves displayed rectangular shapes within the operating voltages but a current leap begins to be observed as the voltage is increased to 1.8 V. This anodic current leap towards the more positive voltage might be as a result of oxygen or gas exudation as the voltage reaches 1.8 V.[45] However functional groups present in the sample can enhance the ion diffusion culminating in active electron mobility in the granular porous carbon sample. Hence, the working voltage of 1.8 V is stable for the symmetric device.

Fig. 9(b) shows the CV plots of the symmetric device in the voltage window of 0 - 1.8 V at scan rates of 10 to 100 mV s^{-1}. The CV curves maintain symmetric rectangular shapes as the scan rate increases up to 2.0 V s^{-1} as shown in Fig. 9(c). This is an indication of a highly capacitive electrochemical performance of the ACQS material.[14,45]

The CD profiles recorded within the voltage window of 0.0 – 1.8 V at varying specific currents of 0.5 A g^{-1} to 5.0 A g^{-1} are presented in Fig. 9(d). Linear CD profiles are observed which corresponds to typical EDLC behavior showing high reversibility of anodic and cathodic ionic transport.

The plot of the C_{sp} values calculated from the CD profiles versus specific currents for the ACQS//ACQS symmetric device is shown in Fig. 10(a). A C_{sp} value of 122 F g^{-1} is recorded for the

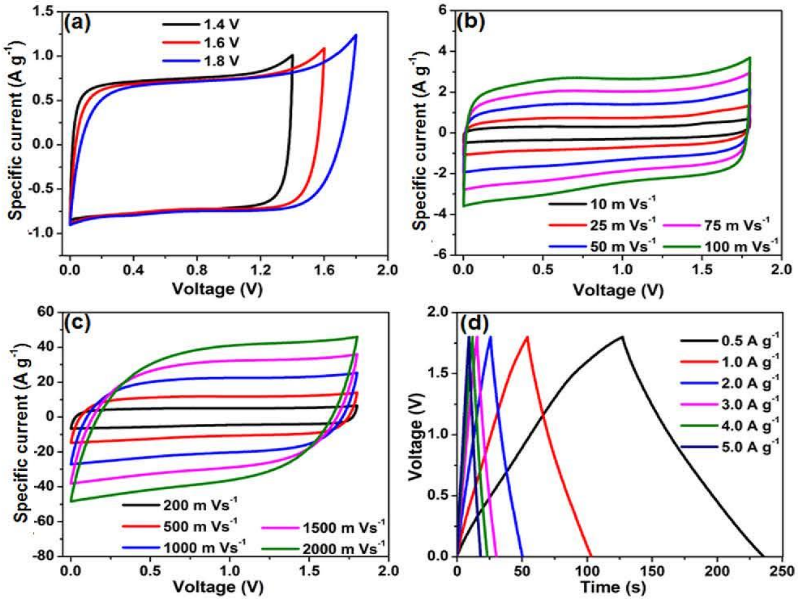

FIG. 9. (a) CV plots at varied operating voltage windows (b) and (c) detailed CV plots at various scan rates (d) associated CD profiles for the of ACQS//ACQS symmetric device in 3 M KNO_3.

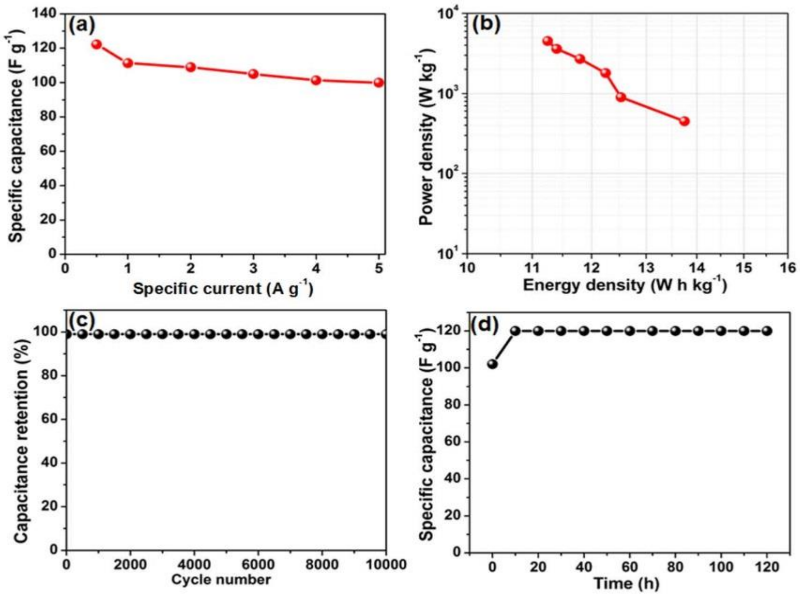

FIG. 10. (a) Specific capacitance versus specific current (b) Ragone Plot (c) Stability plot: capacitance retention versus cycle number at 5.0 A g^{-1} (d) Specific capacitance versus floating time for the ACQS//ACQS symmetric device.

electrode at 0.5 A g^{-1} and 100 F g^{-1} at 5.0 A g^{-1}. A good rate capability is observed for the symmetric device as it displays more than 90% capacitance retention for each increase in specific current. This shows the ability of the material to retain reasonable capacitance even at high specific current. A plot of energy density versus power density (Ragone plot) for the symmetric device is shown in Fig. 10(b). The device displays an energy density of ~14 W h kg^{-1} and power density of ~450 W kg^{-1} at a specific current of 0.5 A g^{-1} (as determined from equation 3 and 4). This work displays remarkable electrochemical performance relative to other biomass-derived activated carbon.[6,18,46–50] A correlation of this results with other earlier reports from biomass-derived activated carbon (AC), which was activated with KOH, $ZnCl_2$ and MgO, is shown in Table IV. The high electrochemical performance of this device might be as result of the high SSA, high pore volume and large mesopore volume which resonate well with the granular porous network and good pore size distribution with good packing properties which enhance proper ion transfer.[1,18,51] The stability of the symmetric

TABLE IV. Comparison of electrochemical performance of different materials with present work.

Precursor	Activation agent	S_{BET} (m^2 g^{-1})	Voltage (V)	Specific capacitance (F g^{-1})	Specific Current (A g^{-1})	Electrolyte	Energy Density (W h Kg^{-1})	Ref
Hazel nutshell	MgO	552	2.0	19.9	0.25	1 M Na_2SO_4	11.1	50
Coconut shell	KOH	1416	1.3	186	0.25	Polymer Gel	11	49
Cork	KOH	1081	1.8	166	0.5	1 M Na_2SO_4	18.6	9
Cotton Fiber	$ZnCl_2$	2549	1.8	239	0.5	1 M Na_2SO_4	13.75	47
Coconut shell	$ZnCl_2$	2440	-	-	-	H_2SO_4	7.6	18
Pistachio nutshells	KOH	1069	1.1	261	0.2	6 M KOH	10	46
Cork (Quercus Suber)	**$KHCO_3$**	**1056**	**1.8**	**122.2**	**0.5**	**3 M KNO_3**	**14.0**	**This work**

device studied at 5.0 A g^{-1} and 1.8 V maximum cell working voltage over 10,000 constant charge-discharge cycles is presented in Fig. 10(c). The device displayed ~100% capacitance retention after the 10,000**th** charge-discharge cycle with no degradation observed in the cell performance. The device was subsequently subjected to a voltage holding test to further investigate the long-term stability of the cell. Voltage holding as compared to the normal charging and discharging over many cycles helps to study the cell stability and shows the real resistance effects and physiochemical deterioration that might be taking place during the electrochemical process[41] after floating at 1.8 V maximum voltage. The voltage holding plot which is a plot of specific capacitance as a function of voltage holding time is presented in Fig. 10(d). The floating process involves periodic potentiostatic mode and subsequent galvanostatic charge-discharge cycle at 1.0 A g^{-1}. The floating and charge-discharge cycles are iterated for a period of 120 h. The voltage holding analysis showed an improvement in the performance of the device which increases after the first 10 h of floating which is an indication that more pore sites where accessed by the electrolyte as a result of prolonged floating, with only slight decay at the end of 120 h. The increase in capacitance might also be due to the expansion of the material granular porous network thereby allowing more adsorption and intercalation of ions into the material active sites thus increasing the cell capacitance.[35,52]

The electrochemical impedance spectroscopy (EIS) measurements were carried out in an open circuit potential and the Nyquist plots for the ACQS//ACQS symmetric device before and after stability is presented in Fig. 11(a). The EIS study is important for understanding the electron and ion transport in the electrolyte and the electrode material.[21] The EIS study was performed in an open circuit potential from 0.01 Hz to 100 kHz frequencies. Nearly vertical lines and small semi-circles (inset to Fig. 11(a)) can be observed at the high and low-frequency regions of the Nyquist plots indicating the presence of charge transfer resistance R_{ct} of 0.2 Ω showing good electron and ion conductivity and typical electric double layer capacitive behavior. R_{ct} of 0.5 Ω was obtained after cycling stability test, this large increase of the R_{ct} value after stability could be attributed to

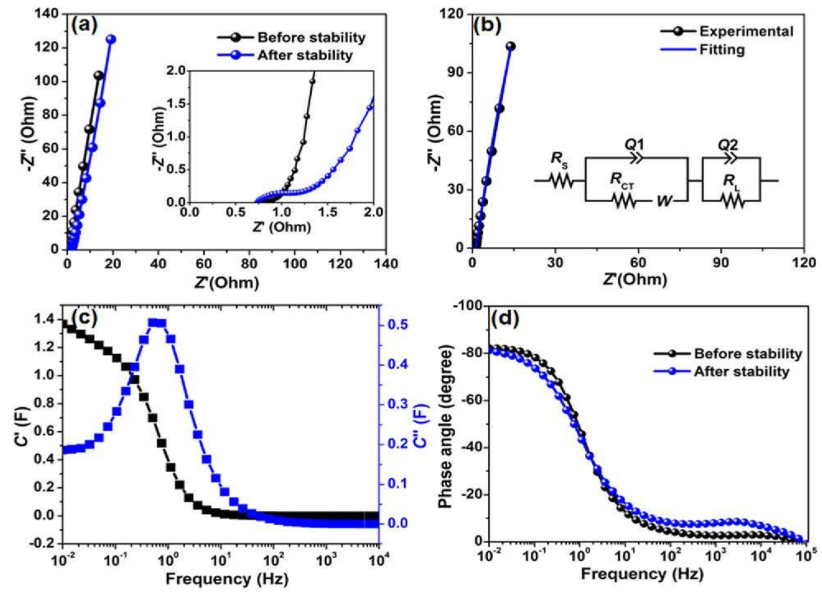

FIG. 11. (a) EIS plot before and after cycling test (b) EIS plots on open circuit potential and equivalent circuit (inset to the figure) (c) Real and imaginary parts of the cell capacitance versus frequency and (d) Phase angle as a function of frequency before and after stability, for the ACQS//ACQS cell in 3 M KNO_3.

the fact that electron transfer and ion diffusion within the electrode material/electrolyte has slowed down as a result of the prolonged cycling of the electrode.[40] The intersection of the semicircle with the *Z'* axis shows the solution resistance (R_s) before and after cycling stability, with values of 0.75 Ω and 0.74 Ω respectively. This R_s element is made up of the electrolytic resistance, intrinsic electrode material resistance and the resistance between the electrode material and the current collector.[35,53]

The equivalent series circuit fitted for the Nyquist plot before stability is as presented in Fig. 11(b). The equivalent series circuit shows a series connection between the solution resistance, Rs and the constant phase element, Q_1 which is connected in parallel with $R_{\mathrm{ct,}}$ the charge transfer resistance. The Q_1 element shows the double layer capacitance associated with the Warburg diffusion element (W) which is connected in series with R_{ct}. Q_2 is the mass capacitance and is associated with the ideal polarizable capacitance connected in parallel to an impedance characteristic element R_{L}, which accounts for the shifting of the vertical line from the typical EDLC characteristic.[54,55] The deviation from the typical vertical behavior connotes that there is a leakage resistance, R_{L} which is a resistive element connected with Q_2.

The impedance (Z) of Q_1, is expressed as;[55,56]

$$Z_{Q_1} = e(j\omega)^{-b} \tag{8}$$

Where e and b are frequency-independent constants and ω is angular frequency. $C'(\omega)$ and $C''(\omega)$ which are the real and imaginary parts of the capacitance versus frequency is presented in Fig. 11(c). A value of 1.38 F was recorded for C' at a frequency of 10 mHz is which is the real attainable capacitance of this symmetric device at this frequency. C'' describes the frequency transition between a typical capacitive and resistive characteristics of the symmetric cell[57] with a relaxation time (τ) of 1.32 s corresponding to a frequency of ~1.0 Hz which was calculated for the symmetric cell using the equation:

$$\tau = \frac{1}{f_{max}} = 2\pi\omega_{max}^{-1} \tag{9}$$

The relaxation time simply means that the stored energy contained in the ACQS//ACQS symmetric cell can be retrieved in a period of 1.32 s. The phase angle of the cell versus frequency is presented in Fig. 11(d). The phase angle of the cell is recorded at approximately -83° (which is close to -90°) and a value of -81° was recorded for the phase angle after cycling stability, which is indicative of the good capacitive performance of the symmetric cell similar to the ideal device.

IV. CONCLUSIONS

Activated carbon derived from cork (Quercus Suber) (ACQS) was successfully produced via a two-step environment-friendly synthesis route. This green synthesis route makes the synthesized material less toxic for utilization as an electrode material for energy storage application. The activated carbon has well-defined microporous and mesoporous structures which provide a good interface for fast rate ion transfer. The granular network structures also provide good packing properties for better ion diffusion and intercalation. The electrochemical study of the symmetric device assembled from the synthesized activated carbon as electrode materials displayed a specific capacitance of 122.2 F g^{-1}, energy density of ~14.0 Wh Kg^{-1} and power density of 450.0 W kg^{-1} at a current density of 0.5 A g^{-1} with an excellent long-term cycling life after 10,000 CD cycles and subsequent floating at maximum voltage for 120 h. The excellent stability after floating test and the ~100% capacitance retention after 10000 CD cycles makes the Cork derived activated carbon material a potential material for energy storage application.

SUPPLEMENTARY MATERIAL

See supplementary material for additional information on the electrochemical characterization of the ACQS material.

ACKNOWLEDGMENTS

The South African Research Chairs Initiative (SARChI) of the Department of Science and Technology, the National Research Foundation (NRF) of South Africa (Grant No. 61056) through SARChi, and the Department of physics, University of Pretoria is acknowledged for their financial support. Any view, result and conclusion or recommendation expressed in this work is that of the author(s) and the NRF does not accept any liability in this regard. Mr. J. Lekitima is acknowledged for the FT-IR measurements.

[1] J. Wang and S. Kaskel, J. Mater. Chem. **22**, 23710 (2012).
[2] C. Zhong, Y. Deng, W. Hu, J. Qiao, L. Zhang, and J. Zhang, Chem. Soc. Rev. **44**, 7484 (2015).
[3] A. Bello, N. Manyala, F. Barzegar, A. A. Khaleed, D. Y. Momodu, and J. K. Dangbegnon, RSC Adv. **6**, 1800 (2016).
[4] R. Li, S. Wang, Z. Huang, F. Lu, and T. He, J. Power Sources **312**, 156 (2016).
[5] H. Sun, L. Cao, and L. Lu, Energy Environ. Sci. **5**, 6206 (2012).
[6] X. Li, W. Xing, S. Zhuo, J. Zhou, F. Li, S.-Z. Qiao, and G.-Q. Lu, Bioresour. Technol. **102**, 1118 (2011).
[7] Z.-Z. Pan, L. Dong, W. Lv, D. Zheng, Z. Li, C. Luo, C. Zheng, Q.-H. Yang, and F. Kang, Chem. An Asian J. **12**, 503 (2017).
[8] P. Simon and Y. Gogotsi, Acc. Chem. Res. **46**, 1094 (2013).
[9] F. O. Ochai-Ejeh, A. Bello, J. Dangbegnon, A. A. Khaleed, M. J. Madito, F. Bazegar, and N. Manyala, J. Mater. Sci. **52**, 10600 (2017).
[10] P. Simon and Y. Gogotsi, Nat. Mater. **7**, 845 (2008).
[11] J. Pu, F. Cui, S. Chu, T. Wang, E. Sheng, and Z. Wang, ACS Sustain. Chem. Eng. **2**, 809 (2014).
[12] H. Jiang, P. S. Lee, and C. Li, Energy Environ. Sci. **6**, 41 (2013).
[13] J. R. Miller and P. Simon, Science **321**, 651 (2008).
[14] Y. Jang, J. Jo, Y.-M. Choi, I. Kim, S.-H. Lee, D. Kim, and S. M. Yoon, Electrochim. Acta **102**, 240 (2013).
[15] R. N. Reddy and R. G. Reddy, J. Power Sources **124**, 330 (2003).
[16] L. Dong, C. Xu, Q. Yang, J. Fang, Y. Li, and F. Kang, J. Mater. Chem. A **3**, 4729 (2015).
[17] L. Dong, C. Xu, Y. Li, Z.-H. Huang, F. Kang, Q.-H. Yang, and X. Zhao, J. Mater. Chem. A **4**, 4659 (2016).
[18] A. Jain, C. Xu, S. Jayaraman, R. Balasubramanian, J. Y. Lee, and M. P. Srinivasan, Microporous Mesoporous Mater. **218**, 55 (2015).
[19] A. Jain, R. Balasubramanian, and M. P. Srinivasan, Chem. Eng. J. **283**, 789 (2016).
[20] W. Gu and G. Yushin (2013).
[21] B. Abdulhakeem, B. Farshad, M. Damilola, T. Fatemeh, F. Mopeli, D. Julien, and M. Ncholu, RSC Adv. **4**, 39066 (2014).
[22] F. Béguin, V. Presser, A. Balducci, and E. Frackowiak, Adv. Mater. **26**, 2219 (2014).
[23] M. Sevilla and A. B. Fuertes, ChemSusChem **9**, 1880 (2016).
[24] R. C. Saxena, D. K. Adhikari, and H. B. Goyal, Renew. Sustain. Energy Rev. **13**, 167 (2009).
[25] H. B. Goyal, D. Seal, and R. C. Saxena, Renew. Sustain. Energy Rev. **12**, 504 (2008).
[26] L. Demarconnay, E. Raymundo-Piñero, and F. Béguin, Electrochem. Commun. **12**, 1275 (2010).
[27] S. Ratha, S. R. Marri, N. A. Lanzillo, S. Moshkalev, S. K. Nayak, J. N. Behera, and C. S. Rout, J. Mater. Chem. A **3**, 18874 (2015).
[28] G. Yu, L. Hu, M. Vosgueritchian, H. Wang, X. Xie, J. R. McDonough, X. Cui, Y. Cui, and Z. Bao, Nano Lett. **11**, 2905 (2011).
[29] J. Przepiorski and A. Oya, J. Mater. Sci. Lett. **17**, 679 (1998).
[30] J. Hayashi, T. Horikawa, I. Takeda, K. Muroyama, and F. Nasir Ani, Carbon **40**, 2381 (2002).
[31] X. Zheng, W. Lv, Y. Tao, J. Shao, C. Zhang, D. Liu, J. Luo, D.-W. Wang, and Q.-H. Yang, Chem. Mater. **26**, 6896 (2014).
[32] A. E. Ofomaja and E. B. Naidoo, Chem. Eng. J. **175**, 260 (2011).
[33] J. W. Lee, A. S. Hall, J.-D. Kim, and T. E. Mallouk, Chem. Mater. **24**, 1158 (2012).
[34] J. K. Gan, Y. S. Lim, A. Pandikumar, N. M. Huang, and H. N. Lim, RSC Adv. **5**, 12692 (2015).
[35] N. Manyala, A. Bello, F. Barzegar, A. A. Khaleed, D. Y. Momodu, and J. K. Dangbegnon, Mater. Chem. Phys. **182**, 139 (2015).
[36] D. S. Patil, J. S. Shaikh, D. S. Dalavi, S. S. Kalagi, and P. S. Patil, Mater. Chem. Phys. **128**, 449 (2011).
[37] M. D. Stoller and R. S. Ruoff, Energy Environ. Sci. **3**, 1294 (2010).
[38] A. Sadezky, H. Muckenhuber, H. Grothe, R. Niessner, and U. Pöschl, Carbon **43**, 1731 (2005).
[39] A. G. Pandolfo and A. F. Hollenkamp, J. Power Sources **157**, 11 (2006).
[40] L. Dong, G. Liang, C. Xu, D. Ren, J. Wang, Z.-Z. Pan, B. Li, F. Kang, and Q.-H. Yang, J. Mater. Chem. A **5**, 19934 (2017).
[41] A. Bello, F. Barzegar, M. J. Madito, D. Y. Momodu, A. A. Khaleed, T. M. Masikhwa, J. K. Dangbegnon, and N. Manyala, Electrochim. Acta **213**, 107 (2016).
[42] X. Zhang, X. Wang, L. Jiang, H. Wu, C. Wu, and J. Su, J. Power Sources **216**, 290 (2012).
[43] L. Qie, W. Chen, H. Xu, X. Xiong, Y. Jiang, F. Zou, X. Hu, Y. Xin, Z. Zhang, and Y. Huang, Energy Environ. Sci. **6**, 2497 (2013).
[44] K. Fic, G. Lota, M. Meller, and E. Frackowiak, Energy Environ. Sci. **5**, 5842 (2012).
[45] J. H. Chae and G. Z. Chen, Electrochim. Acta **86**, 248 (2012).
[46] J. Xu, Q. Gao, Y. Zhang, Y. Tan, W. Tian, L. Zhu, and L. Jiang, Sci. Rep. **4**, 845 (2014).
[47] G. Ma, D. Guo, K. Sun, H. Peng, Q. Yang, X. Zhou, X. Zhao, and Z. Lei, RSC Adv. **5**, 64704 (2015).
[48] D. Momodu, M. Madito, F. Barzegar, A. Bello, A. Khaleed, O. Olaniyan, J. Dangbegnon, and N. Manyala, J. Solid State Electrochem. **21**, 859–872 (2017).
[49] F. Barzegar, A. A. Khaleed, F. U. Ugbo, K. O. Oyeniran, D. Y. Momodu, A. Bello, J. K. Dangbegnon, and N. Manyala, AIP Advances **6**, 115306 (2016).

[50] N. Sinan and E. Unur, J. Energy Chem. **26**, 783 (2017).
[51] F. Barzegar, A. Bello, O. O. Fashedemi, J. K. Dangbegnon, D. Y. Momodu, F. Taghizadeh, and N. Manyala, Electrochim. Acta **180**, 442 (2015).
[52] G. Ren, X. Pan, S. Bayne, and Z. Fan, Carbon **71**, 94 (2014).
[53] J. Luo, H. D. Jang, and J. Huang, ACS Nano **7**, 1464 (2013).
[54] H. Wang, Y. Liang, T. Mirfakhrai, Z. Chen, H. Sanchez Casalongue, and H. Dai, Nano Res. **4**, 729 (2011).
[55] F. Barzegar, A. Bello, D. Y. Momodu, J. K. Dangbegnon, F. Taghizadeh, M. J. Madito, T. M. Masikhwa, and N. Manyala, RSC Adv. **5**, 37462 (2015).
[56] D. Pech, M. Brunet, H. Durou, P. Huang, V. Mochalin, Y. Gogotsi, P.-L. Taberna, and P. Simon, Nat. Nanotechnol. **5**, 651 (2010).
[57] P. L. Taberna, P. Simon, and J. F. Fauvarque, J. Electrochem. Soc. **150**, A292 (2003).

4.3.4 Concluding remarks

Activated carbon synthesized from hydrothermally pretreated cork (Quercus suber) and activated with mild $KHCO_3$ has been successfully studied. The SEM micrograph showed a good porous granular network structure of the as-synthesized $ACKHCO_3$ material. The activated carbon has well-defined microporous and mesoporous structures which provide a good interface for rapid ion transport. A symmetric device $ACKHCO_3//ACKHCO_3$ was fabricated. The device displayed a specific capacitance of 122 F g^{-1} in 3 M KNO_3, energy density of ~14 W h kg^{-1} and corresponding power density of 450 W kg^{-1} respectively at 0.5 A g^{-1} specific current. The device also exhibited an excellent stability after voltage holding test at a maximum voltage of 1.8 V for 120 h and ~100% capacitance retention after 10,000 charge-discharge cycles. The excellent stability makes the cork-derived material a potential excellent, cost-effective material for supercapacitor application.

4.4 Hybrid supercapacitor device based on manganese oxide decorated on functionalized carbon nanotubes and porous activated carbon nanostructures

4.4.1 Introduction

MnO_2 has been extensively studied for ECs application because it is environmentally benign, inexpensive, abundant, and very redox-active, with a high theoretical capacitance of ~1370 F g^{-1} and demonstrates good pseudocapacitive performance in aqueous neutral electrolytes as compared to acidic and alkaline electrolytes. MnO_2 however displays low power density which can be attributed to their poor electric conductivity, which restricts electron transfer. Also, the swelling and contraction of the electrode materials during the charging and discharging processes results in poor cycling stability. Hence, synthesizing MnO_2 with conductive materials such as carbonaceous materials as nanocomposites can help overcome the poor electrical conductivity by speeding up the reaction kinetics and providing more active sites for the charge transfer reactions. The carbon materials also acting as a support for the growth of the metal oxide can make the material electrode more resilient against swelling and damage during the charge-discharge process [140,203,216,217]. Thus, the high pseudo-capacitance of the MnO_2 combined with the electrical conductivity of the carbon material should have improved electrochemical performance.

Another way of harnessing the advantages of both metal oxides and EDLC materials is by hybrid cell fabrication. As mentioned in section 4.2.1, hybrid ECs combine the advantages of the EDLC and faradaic capacitors in order to increase the energy density without conceding the power density [29,213]. In this section, we present and discuss MnO_2 synthesized with functionalized CNT as positive electrode and AC derived from cork (Quercus suber) as negative electrode for energy storage application. The detailed results and discussion is presented in the paper below.

4.4.2 (Manuscript under review)

Electrochemical performance of hybrid supercapacitor device based on birnessite-type manganese oxide decorated on uncapped carbon nanotubes and porous activated carbon nanostructures

F.O. Ochai-Ejeh[a.b], M.J. Madito[a], K. Makgopa[c], M.N. Rantho[a], O. Olaniyan[a], N. Manyala[a]

[a]Department of Physics, Institute of Applied Materials, SARChI Chair in Carbon Technology and Materials, University of Pretoria 0028, South Africa.

[b]Department of Physics and Astronomy, University of Nigeria, Nsukka 410001, Nigeria.

[c]Department of Chemistry, Faculty of Science, Tshwane University of Technology (Acardia Campus), Pretoria 0001, South Africa.

ABSTRACT

Birnessite-type MnO_2 synthesized on the surface of carbon nanotubes (CNTs) via facile hydrothermal reflux technique to produce MnO_2-CNT nanocomposite and 3D microporous nanostructured activated carbon (AC) derived from cork (Quercus Suber) with good microstructural, morphological and electrochemical properties are herein reported. A hybrid supercapacitor device comprising of MnO_2-CNT nanocomposite as positive electrode and AC as negative electrode was successfully fabricated and tested for energy storage application. The device displayed a maximum working potential of up to 2V due to the excellent synergistic contribution from the MnO_2-CNT nanocomposite and AC material derived from cork (Quercus Suber). The fabricated device displayed good electrochemical performance having an energy density of ~25 Wh Kg^{-1} that corresponds to power density of 500 W Kg^{-1} at a current density of 0.5 A g^{-1} in 1M Li_2SO_4 aqueous neutral electrolyte. The device exhibited an excellent stability of ~100% coulombic efficiency after 10,000 charge-discharge cycles and excellent capacitance retention after potentiostatic floating test for 60 hours.

KEYWORDS: Birnessite-type MnO_2; activated carbon; hybrid device; reflux synthesis; nanocomposi

INTRODUCTION

The dependency on limited fossil fuel as source of energy that is unclean and detrimental to the environment and the high demands of energy globally compel for more innovative ideas on alternative energy sources that are efficient and clean. Electrochemical capacitors (ECs) mostly known as supercapacitors, are high power density energy storage systems characterized by numerous advantageous properties such as rapid charging-discharging ability, excellent stability, wide operating temperatures and excellent stability e.t.c. ECs have gained much research interest due to their excellent properties that display potential promise of meeting the present day global energy needs and have found considerably vast application in systems involving high power density such as light weight electronic devices (LWEs), hybrid electric vehicles (HEVs), trams, buses, trains, aircraft and wind turbines[1–7]. Electrochemical capacitors occupy an intermediary position among the energy storage and conversion systems in such a way that their energy density is higher than that of conventional capacitors but lower than that of batteries (which possess lower power density and are also plagued with poor stability, rapid temperature increase in operative conditions and slow charge-discharge rate) [2,8–10]. In order for ECs to find application in systems which require both high power and high energy density, intensive studies focusing on fine-tuning the electrode materials that will result in excellent energy and power densities have to be conducted to meet the requirements of such desired application[9,11]. Energy density (E_d) expressed as$E_d = 1/2\,CV^2$,where C being the cell specific capacitance and V the cell maximum potential [10–13], largely depends on the cell potential window which is directly dependent on the nature of the electrolyte used as well as the electrode materials used in the cell fabrication [7,14]. Also, the combination of different pseudocapacitive or faradaic redox electrode materials and electric double layer (EDL) materials with different operating potentials in aqueous electrolytes synergistically helps to enhance the energy density of ECs [4,8,10,12,15]. Studies have demonstrated that aqueous neutral electrolytes are able to attain large practical potentials owing to their pH values as compared to acidic and alkaline electrolytes [4,13,16–19]. EDL materials such as graphene, carbon nanotubes (CNTs), onion-like carbon (OLC), carbide derived carbon and activated carbon (AC) are mostly utilized as the negative electrode materials in ECs, which is majorly due to their high electrical conductivities, low cost, high surface area, good stability and non-toxicity [1,4,15,20–23]. Due to the above excellent properties of carbon nanomaterials employed as suitable negative electrode materials in device fabrication for ECs applications, much effort has been devoted on the synthesis of carbon nanomaterials from various renewable and abundant carbon sources ([24–29]). Some of these renewable sources include tree barks [30], seeds [24], leaves [25] nuts shells [31,32]. Recently, activated carbon (AC) obtained from cheap and lightweight material cork (Q. suber), a spongy material which comes from the bark of an evergreen oak tree, has been explored for ECs applications ([13,15]). The AC obtained from the cork (Q. suber) exhibited good electrochemical performance, their specific capacitance values was relatively high [33,34] although less than the values resulting from conducting polymers and metal oxides [35,36], their large operating potential window in aqueous neutral electrolyte can be explored for good and synergestic electrochemical cell fabrication. On the other hand, conducting polymers (i.e., poly aniline (PANI), polypyrrole (PPY), etc.) and transition metal oxides/hydroxides (e.g. MnO_2, $Ni(OH)_2$, etc.), including their nanocomposites with EDLC materials, have been employed as positive electrode materials. Among several metal oxides, MnO_2 has been widely researched for ECs application since they are cheap, naturally abundant, environmentally friendly, highly redox-active, possesses a high theoretical capacitance of ~1370 F g^{-1} and displays good performance in aqueous neutral electrolytes than in acidic and alkaline electrolytes [1,4,19,37]. In spite of the good properties displayed by MnO_2, their electrical conductivity is quite low resulting in low cycling stability that compromises their electrochemical performance[1,38]. In order to curb this challenge, carbon nanomaterials with excellent conductivity are used as supports to provide a framework during

MnO_2synthesis[39–42] . Thus, nanocomposites resulting from EDLC materials and manganese oxide-based electrode materials combine electric double layer capacitance of the carbon material and pseudocapacitive charge transfer reactions of the manganese oxide for an improved electrochemical performance [39,40]. Among the EDLC carbon nanomaterials, CNTs are more commonly utilized as support for the growth of metal oxide composite because of its excellent and outstanding intrinsic properties which includes high electrical conductivity (10^4 S cm^{-1}), large surface-to-volume ratio and 1D tubular porous structures which enhance quick ion and electron mobility [1,37,42–44] and functionalizing the CNT material further increases its surface reactivity and wettability thus making the CNT material more electrolyte accessible thereby increasing the charge storage ability [45]. Several studies on MnO_2–CNT nanocomposites with different morphologies such as nanoflake, nanosheets and nanoflower [4,39,46] have been previously reported, however only a limited study exists on the tube-like morphology for the MnO_2–CNT nanocomposite. Reports have shown that the tubular morphology display large surface areas and high surface–to-volume ratio which enhances the flow of electrolyte ions within short diffusion distances [37]. Thus growing MnO_2 on CNT helps to achieve a tubular morphology with the combined advantage of having large surface-to-volume ratio with short electrolyte diffusion distances, rapid ion transport, improved electrical conductivity and enhanced electrode performance[37].

In this report, we present a fabrication of MnO_2-CNT nanocomposite with a tubular morphology that exhibits enhanced electrochemical performance as the positive electrode material with 3D nanostructured AC material obtained from cheap and lightweight material cork (Q. suber)as the negative electrode operating synergistically in 1 M Li_2SO_4 at 2 V in a hybrid (asymmetric) cell device. The EC device displayed excellent stability and improved electrochemical performance after 10 000 charge-discharge cycles.

2. EXPERIMENTAL

2.1 Synthesis of electrode materials

2.1.1 Functionalization of CNTs and Synthesis of MnO_2-CNT

The $KMnO_4$ (Merck, Purity ≥ 98%), H_2SO_4 (purity 95 -97 %), H_2O_2 (purity 30 %), HNO_3 (Purity 65 %) reagents were of analytical grade and used without further purification. Deionized water was used throughout for the washing of the synthesized sediments until the final product was achieved. Multi-walled carbon nanotubes (CNTs) (Nanolab,purity: > 94%, length: 5-20 µm and diameter: 10-20 nm), were converted to short and uncapped nanotubes bearing acidic functional groups (mainly: -COOH) prior to their use in the synthesis of the nanocomposite (Scheme 1(a)). Briefly, 0.5 g of pristine CNTs was refluxed for 48 h in 2.6 M HNO_3. The washed deposits of CNTs were sonicated in a mixture of conc. H_2SO_4/HNO_3(3:1 ratio, 95-97%, and 65% purity, respectively), followed by washing and stirring at 70 ° C for 15 min. in a mixture of H_2SO_4/H_2O_2 (4:1 ratio, 95-97% and 30% purity, respectively). The black powder of CNTs was finally dried at 60 °C overnight after washing. The MnO_2-CNT nanocomposite was synthesized via the conventional hydrothermal reflux technique, as shown in scheme 1(b). Typically, 40 mg of CNTs was dispersed by sonication in 0.02 M $KMnO_4$. Subsequently, the mixture (pH = 7.05) was refluxed at 130 °C in an oil bath for 24 h with continuous magnetic stirring. The resultant dispersion was then centrifuged and washed several times and finally dried at 60 °C overnight in a vacuum oven.

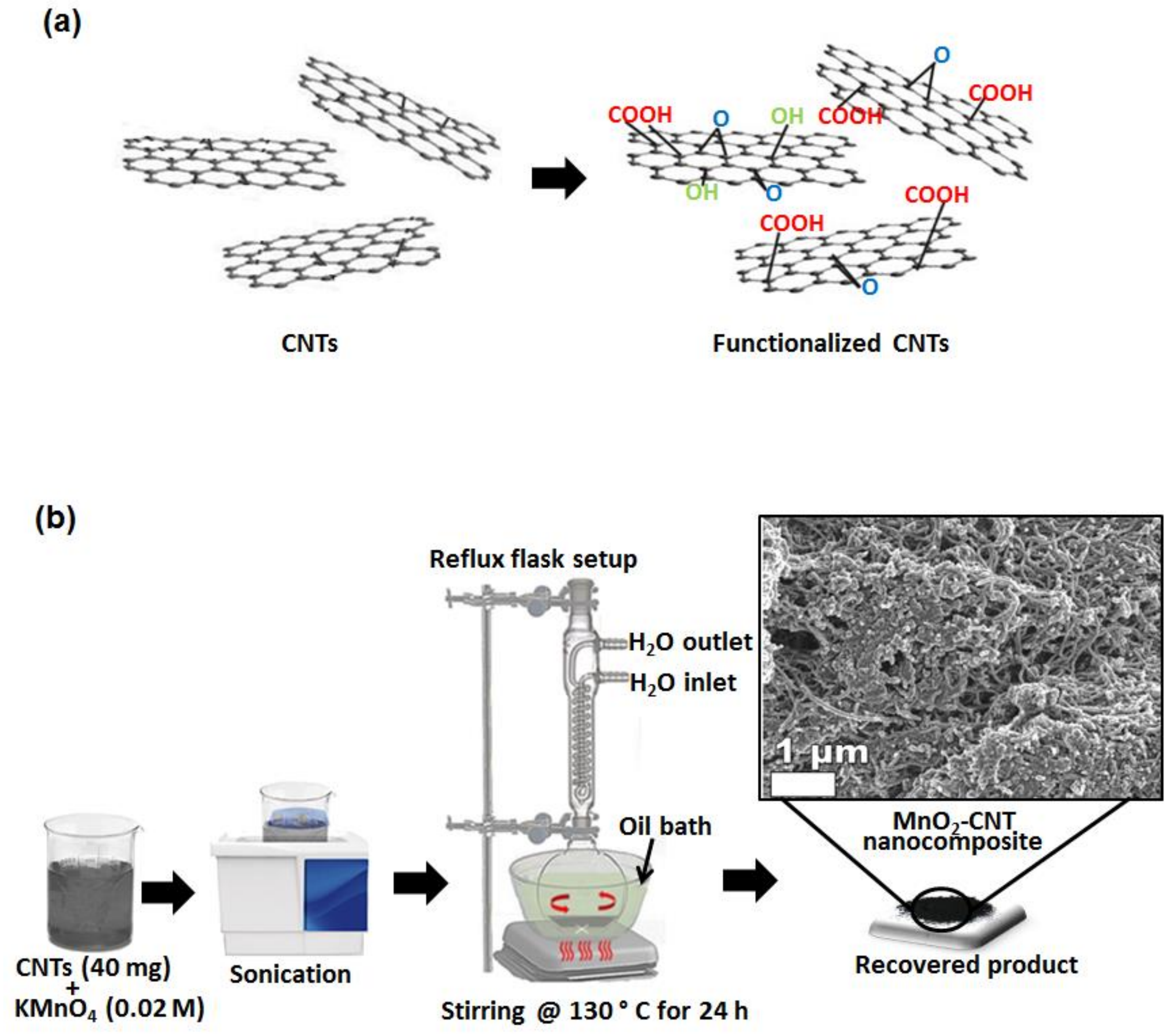

Scheme 1. (a) Schematic view of the chemical structure route from CNTs to functionalized CNTs. (b) Synthesis route for MnO_2-CNT nanocomposite using functionalized CNTs.

2.1.2 Synthesis of AC from Cork (Quercus Suber)

The AC 3D nanostructure material was prepared via a similar procedure in our previous work [13] but with some modification. Briefly, 5 g of cork was crushed and activated with 10 g of KOH and allowed to dry in an oven. The sample was then carbonized in argon flow at 5 ^oC/min from room temperature to

850 °C for 2 hours (Scheme 2). The carbonized products was collected and washed with 3 M HCl and deionized water until filtrate was clear.

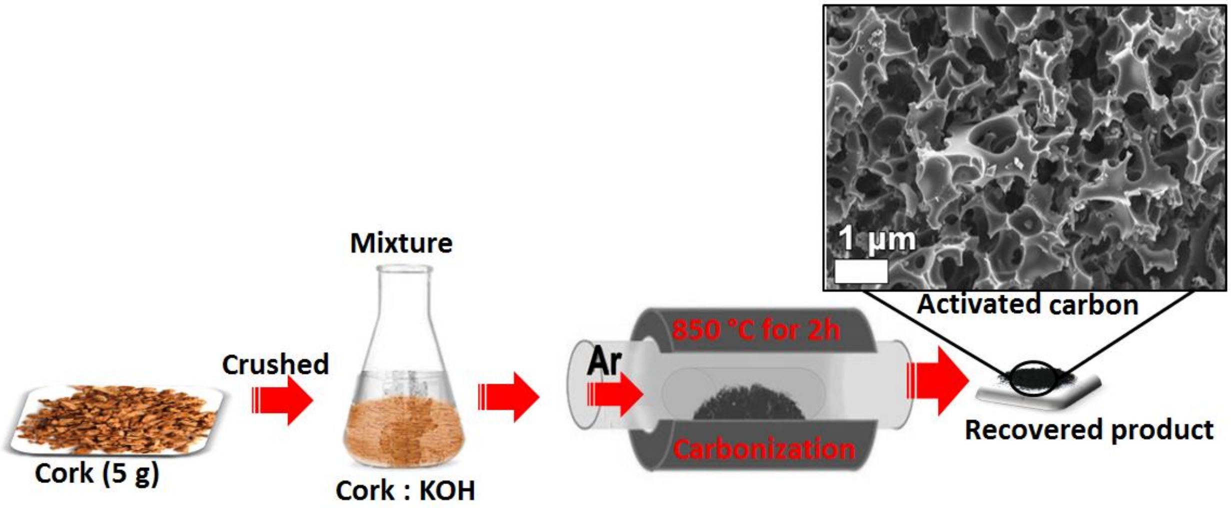

Scheme 2. Synthesis route for 3D nanostructuredactivated carbon (AC).

2.2 Structural, Morphological, Composition and Electrochemical Characterization

The morphology of the materials were studied via scanning electron microscopy (SEM) using Zeiss ultra plus 55 field emission microscope (FE-SEM) at an accelerating voltage of 2.0 kV. The transmission electron microscopy (TEM) analysis of the samples was carried out in a high-resolution transmission electron microscopy (HR-TEM)JEOL 2100 (from Tokyo Japan) equipped with LaB_6 filament, a Gartan U1000 camera of 2028 x 2028 pixels and operated at 200 kV.The X-ray Diffraction studies of the materials was performed using XPERT-PRO diffractometer (PANalytical Netherlands). Raman analysis was performed using a WiTec alpha 300R+ confocal Raman system (WiTecGmbh). X-ray photoelectron spectroscopy (XPS) analysis was performed using Physical Electronics Versaprobe 5000 spectrometer.

The electrochemical characterization of the MnO_2-CNT and AC samples characterization was performed in a three- and two-electrode system using a multi-channel Bio-logic VMP300 potentiostat/galvanostat system at ambient temperature. The MnO_2-CNT electrode for the three-electrode measurement was prepared by thoroughly mixing 80 wt% MnO_2-CNT, 15 wt% carbon black (to enhance the conductivity of the material), and 5 wt% polyvinyl difluoride (PVDF) binder followed by dropwise addition of 1-methylpyrrolydinone (NMP) in an agate mortar until a uniform paste was obtained. The paste was then coated on 2 cm X 2 cm Nickel foam (NF) and dried in an oven at 60°C for several hours. The AC electrode was similarly prepared and pasted on 2 cm X 2 cm NF. The MnO_2-CNT positive electrode and AC negative electrode materials used in the two electrode measurement were also prepared by same method but coated on 8 mm radius NFs and dried in an oven at 60 °C for several hours. The electrodes prepared for the two-electrode measurements were then soaked in 1 M Li_2SO_4aqueous electrolyteand assembled in a Swagelok cell compartment using a microfiber glass filter paper as separator. The three-electrode tests were carried out in the 1 M Li_2SO_4aqueous electrolyte, using Ag/AgCl and glassy carbon as reference and counter electrode respectively. The mass loading for the positive electrode was 1.8 mg and that of the negative electrode was 2.2 mg and total mass of the electrode was 4.0 mg/cm^2. The specific capacitance values of the MnO_2-CNT, AC and MnO_2-CNT//AC hybrid device was determined using equation (1):

$$C_s\,(F\ g^{-1}) = \frac{I\Delta t}{m\Delta U} \tag{1}$$

where *I* (A) is the current, $\Delta t\ (s)$is the discharge time, *m* is the total mass of the electrodes, ΔU is the maximum potential. The energy density, E_d and the power density, P_d of the MnO_2-CNT//AC hybrid device was calculated using equation (2) and (3) respectively:

$$E_d(Wh\ kg^{-1}) = \frac{C_s \Delta U^2}{7.2} \tag{2}$$

$$P_d(WKg^{-1}) = \frac{3.6 \times E_d}{\Delta t} \tag{3}$$

The hybrid device was fabricated taking into consideration the specific capacitance of the MnO_2-CNT and AC electrodes respectively. Since the charge stored in each electrode is:

$$Q = C_s m \Delta U \tag{4}$$

The mass balance equation was adopted to ensure equal charges exists on both electrodes using equation (5):

$$\frac{m_+}{m_-} = \frac{C_{s-}\Delta U_-}{C_{s+}\Delta U_+} \tag{5}$$

The electrochemical impedance spectroscopy measurements were carried out in an open circuit potential in the frequency range of 100 KHz- 10 mHz. Thereafter, the stability tests were performed by continuous charge-discharge for several cycles followed by potentiostatic floating tests at maximum cell potential.

3 RESULTS AND DISCUSSION

3.1 Morphological, structural and compositional characterization

The SEM images of CNT and MnO_2-CNT nanocomposite and AC are presented in figure 1. Figure 1(a) and 1(b) show the SEM images of the tubular morphologies of CNTs at low and high-magnifications and figure 1(c) and 1(d) display the micrographs of MnO_2-CNT nanocomposites at low and high magnifications. The morphologies show the tube-like nanostructure of the CNT uniformly decorated with MnO_2 nanoparticles. The formation of the MnO_2 on the carbon support can be described by the agglomeration of spherical MnO_2 nanoparticles from the thermal decomposition of $KMnO_4$, which self-assemble from spherical aggregates whose rate of evolution is accelerated by the aging temperature. The presence of the ions of $KMnO_4$ in solution leads to the initial formation of the MnO_2 spherical nanostructures at nucleation points where nanoparticles subsequently formed agglomerate into clusters of spherical nanoparticles as a result of increased surface energies. This can be described by the Ostwald ripening process. The gradual transformation of the spherical aggregates to well-defined MnO_2 tube-like nanostructure is dependent on the specific aging temperatures. This one-dimensional growth process could be as a result of their unique anisotropic characteristic buildup of the nanoparticles [37,39,44]. Figure 1(e) and 1(f) display the SEM images of the AC sample at low and high magnification. The micrographs show a 3D interconnected porous network structure. The formation mechanism follows the process of reduction of KOH by carbon leading to the production of metallic K and K_2CO_3 at >700 ^oC. K_2CO_3 which decomposes at temperatures ≥ 800 ^oC, is further reduced by carbon leading to the production of Co_2 and the formation of porous structure.

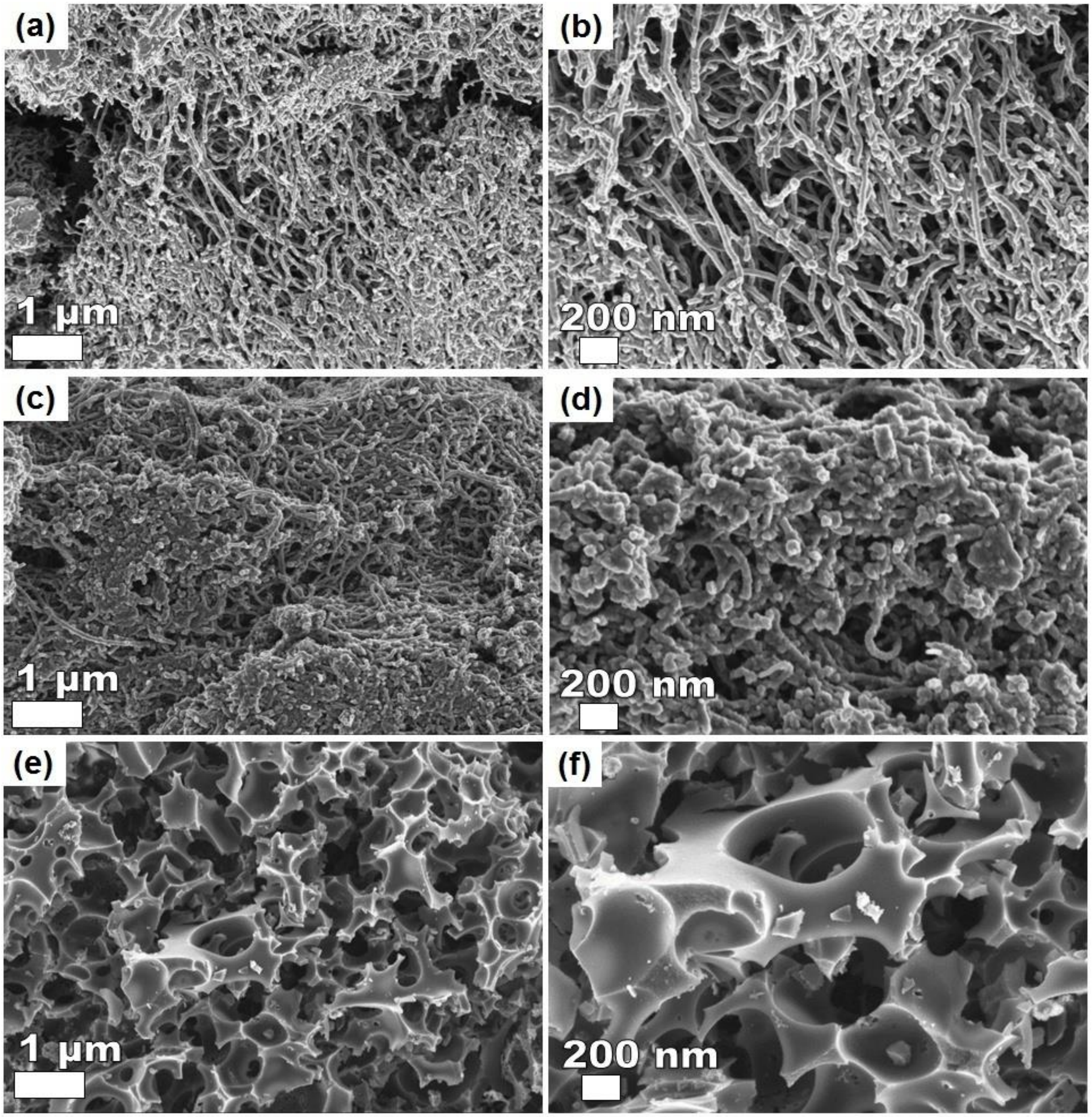

Figure 1. SEM micrographs of (a, b) CNT at low magnification and high magnification, (c, d) MnO_2-CNT at low magnification and high magnification and (e, f) AC at low magnification and high magnification.

Figure 2 compares the TEM images of the CNT and MnO_2-CNT materials which further examine their surface morphology. In Figure 2(b) and 2(c), it can be seen that the CNT are decorated by MnO_2 nanoparticles confirming a successful synthesis of the MnO_2-CNT nanocomposites (nanohybrid) on the surface of the CNTs. These observations corroborate well with the results obtained from the SEM analysis.

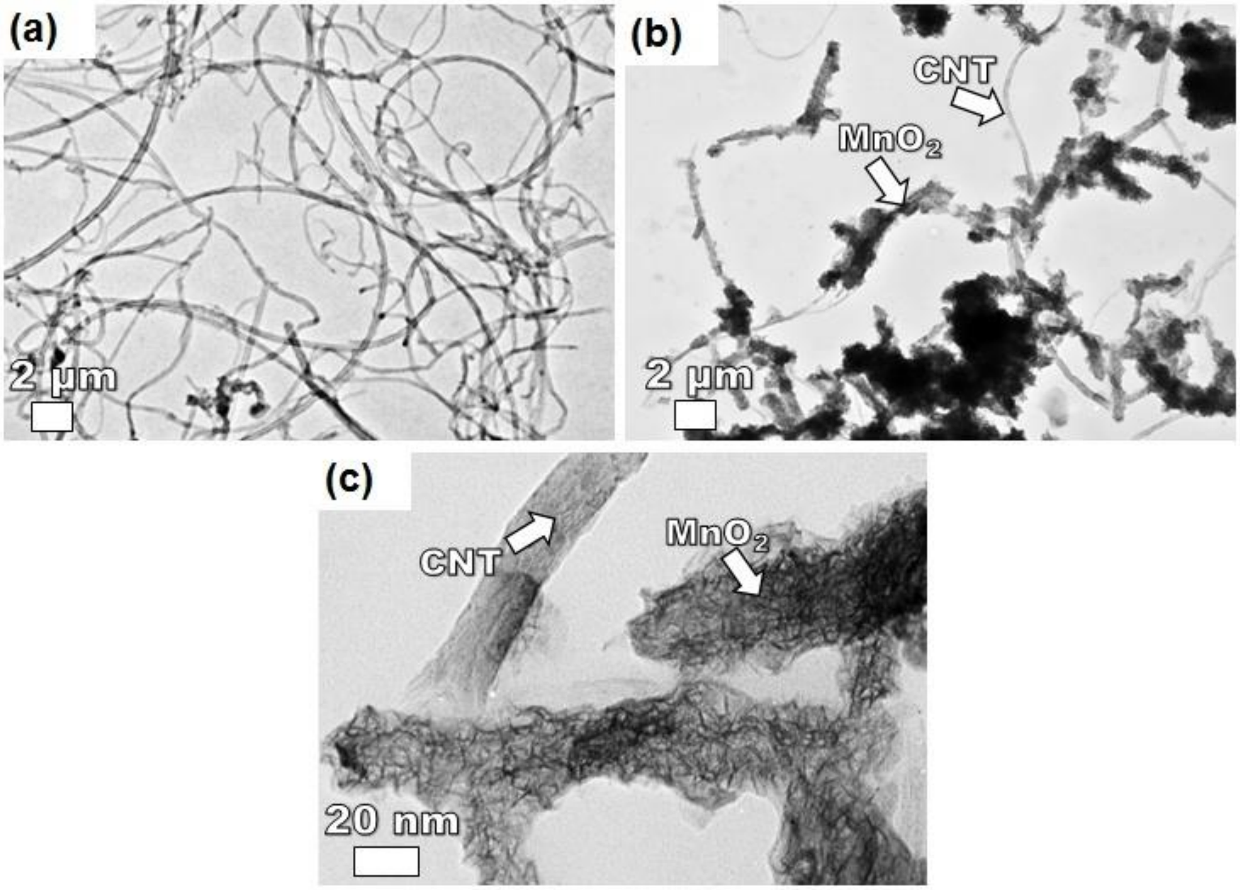

Figure 2. TEM micrographs of (a) CNT and (b) MnO_2-CNT at low magnificationto view the tubular structure of the CNT. (c) High-resolution TEM image of MnO_2-CNT.

The structure of the MnO_2-CNT nanocomposite and AC 3D nanomaterial studied by XRD are presented in figure 3(a) and 3(b). The diffraction peaks occurring at 2 theta (°) values of 12°, 25°, 37° and 66° (Figure 3(a)) corresponds to the lattice planes of (001), (002), (111) and (020) related to the birnessite-type MnO_2 (PDF #42-1317). The peak observed at 26° in the CNT spectrum which was also observed in the MnO_2-CNT nanocomposite can be indexed to the (002) plane (PDF #75-1621). The presence of this peak in the MnO_2-CNT nanocomposite is an indication of the presence of carbon in the nanocomposite. The broadening of the diffraction peaks indicates the low crystallinity and/or confirm the nanostructure of the nanocomposite [8,37,46,47]. The XRD pattern of the 3D AC samples shows peaks occurring at 2 theta (°) values of 51° and 76° which is related to (100) and (110) lattice planes. The low intensity of the peaks shows poor crystallinity of the as-synthesized 3D AC nanostructure. The structure of the MnO_2-CNT nanocomposite and AC samples was further studied via Raman spectroscopy and the Raman spectra are presented in figure 3(c) and 3(d). The Raman spectrum of MnO_2-CNT nanocomposite (Figure 3(c)) shows Raman peaks occurring at 495, 570 and 640 cm^{-1} which are in agreement with the three major vibrational features of the birnessite-type MnO_2 compounds, therefore affirming the presence of MnO_2 [48] in the as-synthesized MnO_2-CNT nanocomposite as observed in the XRD results[48]. The presence of CNT in the nanocomposite is signaled by the D and G Raman peaks occurring at ~1346 cm^{-1} and ~1587 cm^{-1} respectively, which are characteristic of the disordered carbon in the sp^2-hybridized carbon network (D-band) and the tangential vibrations of the graphitic carbons (G-band). The D and G peaks which can also be clearly observed in the MnO_2-CNT nanocomposite is an indication of the presence of CNT in the as-synthesized material also confirming the XRD results. In addition, figure 3(c) shows the deconvoluted Raman spectra (Lorentzian fit) of the nanocomposite and CNT materials. In the deconvoluted Raman spectra, the D1-mode arises from the defects/disorder present in the carbon lattice structure, the D2-mode from the lattice vibration corresponding to that of the G (G1) mode. These bands, observed in nanocomposite and CNT materials at the same peak positions suggest that the structure of the CNT material is maintained in the nanocomposite. Furthermore, an evaluation of the ratio of the D to G peak intensities, I_D/I_G shows only a slight increase in the peak ratio value from 0.95 to 0.98 indicating that the structure of the CNT component is not changed in the nanocomposite material. Similar to figure 3(c), figure 3(d) shows the deconvoluted Raman spectra of AC. The D3-mode arises from the distribution of amorphous carbon in interstitial sites of the disturbed carbon lattice structure while the D4-mode is related to sp^2-sp^3 lattice vibrations. Both of these modes suggest that there exists a level of amorphousness and sp^2-sp^3 bonds within the AC.

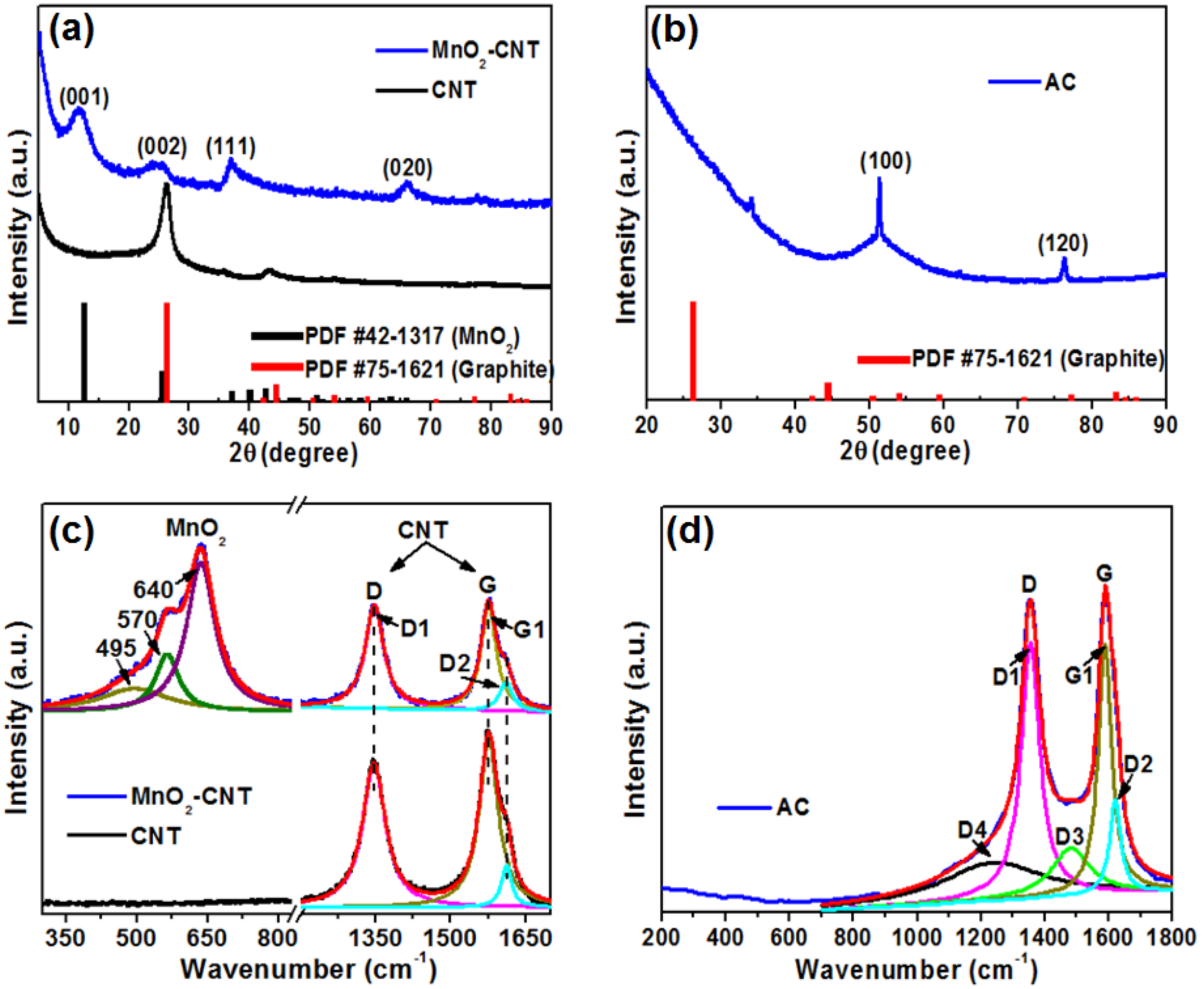

Figure 3. XRD patterns of (a) MnO_2-CNT, CNT, and (b) of AC. The deconvoluted Raman spectra (Lorentzian fit) of (c) MnO_2-CNT, CNT, and (d) of AC.

For further investigation, the samples were analyzed by X-ray photoelectron spectroscopy (XPS) as shown in figure 4. The results from figure 4(a) shows the wide scan XPS spectrum of the as-received MnO_2-CNT nanocomposite, which displays the main elements (26.98 at% Mn 2p, 45.87 at% O 1s and 27.15 at% C 1s) of the composition of the material. Figure 4(b) shows the core level spectrum of Mn 2p of the nanocomposite material which reveals the binding energy peaks at 642.5 and 654.1 eV corresponding to Mn $2p_{3/2}$ and Mn $2p_{1/2}$ core levels, respectively. The fitted Mn $2p_{3/2}$ peaks show different Mn oxidation state of the material. Figure 4(c) shows the core level spectrum of O 1s of the nanocomposite material with fitted peaks at 529.8, 530.9 and 532.6 eV which could be ascribed to Mn−O bonds in the manganese oxide and partly to carbon-oxide components (see figure 4(d)). In addition, the core level spectrum of C 1s of the nanocomposite material (Figure 4(d)) shows the strongest peak at about 284.5 eV attributed to the graphitic carbon, C=C and/or C-C bonds that exist in the CNT, and other peaks at 285.5 and 287.6 eV corresponding to C−O and C=O (carbon-oxide components/functional groups). This is in agreement with the core level spectrum of C 1s of the CNT material which shows the C=C, C−O, C=O and O−C=O components at 284.5, 285.5, 287.6 and 290.3 eV, respectively, as shown in figure 4(e). Moreover, the core level spectrum of C 1s of the AC material (Figure 4(f)) shows similar peaks as the CNT confirming the predominance content of graphitic carbon in the materials.

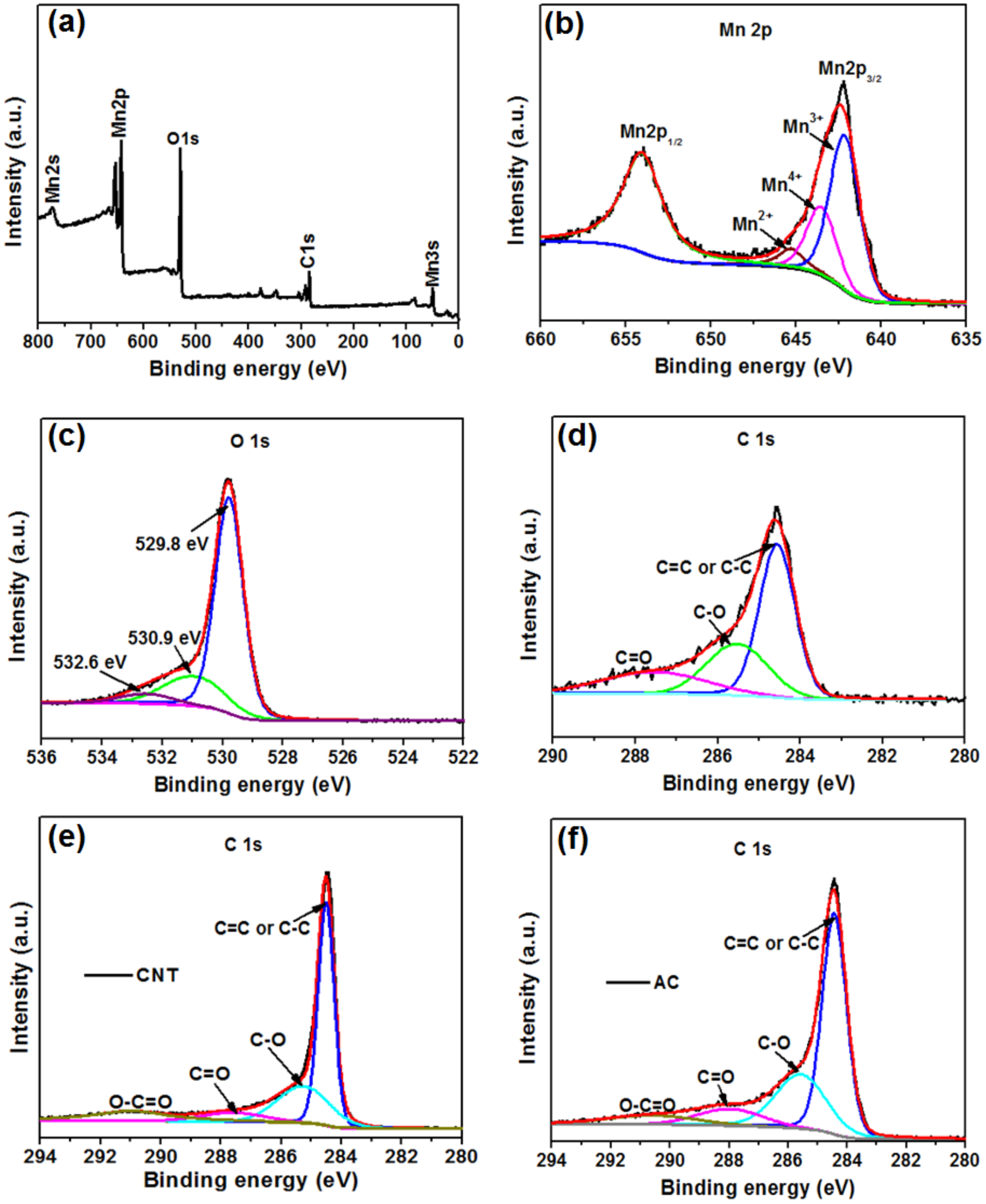

Figure 4. (a) The wide scan XPS spectra of the as-received MnO_2-CNT nanocomposite material. The core level spectrum of (b) Mn 2p, (c) O 1s and (d) C 1s of the MnO_2-CNT nanocomposite material. The core level spectra of C 1s of the (e) CNT and (f) AC materials.

3.2 Electrochemical characterization

The three-electrode measurements of the MnO_2-CNT nanocomposite and the 3D AC nanostructure measured in 1 M Li_2SO_4aqueous electrolyte are presented in figure 5. Figure 5(a) shows the CV curves of the MnO_2-CNT nanomaterial measured in the potential window of 0.0 - 1.0 V vs Ag/AgCl at different scan rates from 10 - 100 mV s^{-1}. Symmetric quasi-rectangular and reversible pseudocapacitive CV curves with no redox peaks can be observed which are related to the combined electrochemical behavior of MnO_2 and CNT component of the MnO_2-CNT nanomaterial. Figure 5(b) displays the CV curves of the AC material performed in the potential window of -1.0 – 0.0 V vs Ag/AgCl measured at different scan rates of 10 – 100 mV s^{-1}. Nearly rectangular, symmetric CV curves with good current response are observed which are characteristic of electric double layer capacitive behavior of carbon material. The charge-discharge (CD) plots of the MnO_2-CNT and AC electrode materials measured at various current densities from 0.5 – 5.0 A g^{-1} are displayed in figure 5(c) and 5(d). The CD curves display almost linear plots. The specific capacitance of the MnO_2-CNT and AC electrode at 0.5 A g^{-1},evaluated from equation (1) are 125.5 F g^{-1} and 105 F g^{-1} respectively. Based on the results from the half-cell measurements of the electrode materials, a hybrid electrochemical device, MnO_2-CNT//AC, was fabricated with MnO_2-CNT as the positive electrode and AC as the negative electrode. The charge balance theory (equation (5)) was used to balance up the charges that exist on both electrodes.

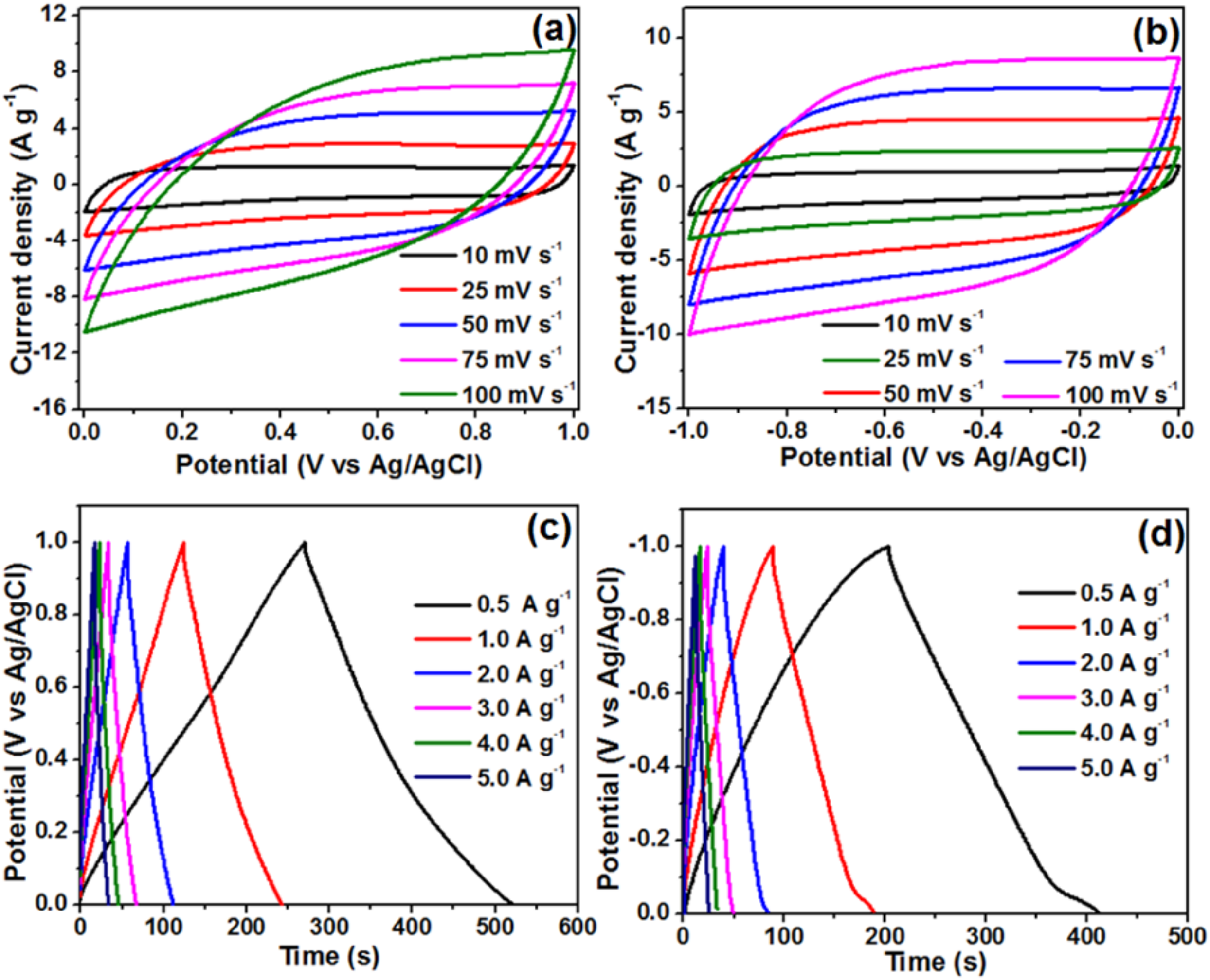

Figure 5. Cyclic voltammetry curves of (a) MnO_2-CNT and (b) AC. The charge-discharge curves of (c) MnO_2-CNT and (d) AC materials.

The two-electrode measurements of the MnO_2-CNT//AC hybrid electrode device are presented in figure 6. Figure 6(a) shows the respective CV curves of the MnO_2-CNT and AC electrodes in 1 M Li_2SO_4 aqueous electrolyte within the potential window of -1.0 – 1.0 V vs Ag/AgCl at a scan rate of 25 mV s^{-1}. The comparative CV plots show that the Pseudocapacitive and electric double layer characteristic of the MnO_2-CNT and AC electrodes, respectively, can be effectively combined for the fabrication of a hybrid cell device. Both electrodes displayed good current response with good stability within their respective operating potential windows. Therefore, from this observation, it is expected that the hybrid cell device should operate excellently within the combined potential windows of both electrode materials leading to the enhanced energy densities [8,15,39]. Figure 6(b) illustrates the CV curves of the hybrid cell at different operating potentials from 1.6 – 2.0 V showing that the hybrid electrode indeed is able to operate within the extended potential window of up to 2.0 V as observed by the behavior of the half-cell (three electrode) analysis. This excellent increase in the operating window of the hybrid (asymmetric) device is also assisted by the use of the neutral electrolytes, that are able to operate with large operating potential windows due to their excellent ion solvation, pH and the over-potential for the hydrogen evolution [13,18]. The CV curves of the MnO_2-CNT//AC hybrid cell device at various scan rates ranging from 10 – 100 mV s^{-1} is presented in figure 6(c). Rectangular CV curve related to an ideal capacitive electrode is observed for the MnO_2-CNT//AC hybrid device in the potential window of 0 - 2.0 V. The rectangular shape of the CV curves are still maintained even as the scan rate is increased to 100 mV s^{-1} which is an indication of good capacitive behavior of the hybrid electrode. Figure 6(d) displays the CD plots of the hybrid cell carried out at various current densities of 0.5 - 5.0 A g^{-1}. The specific capacitance of the hybrid cell ranges from 44.25 – 31.25 F g^{-1} at 0.5 – 5.0A g^{-1} (taking into consideration the total mass of the electrodes). The device displayed the retention of over 70% of the specific capacitance value at the high current density of 5.0 A g^{-1}. The plot of specific capacitance vs current density is presented in figure 6(e). An energy density value of 24.58 Wh kg^{-1} corresponding to a power density of 500 W Kg^{-1} was obtained from the hybrid device. The Ragone plot of the MnO_2-CNT//AC that is a plot of power density vs energy density is as shown in figure 6(f). The energy density value obtained from this device is superior or comparable to similar hybrid device electrodes reported earlier in literature, as shown in the Ragone plot and table 1. Table 1 is a comparison of this work with works earlier reported.

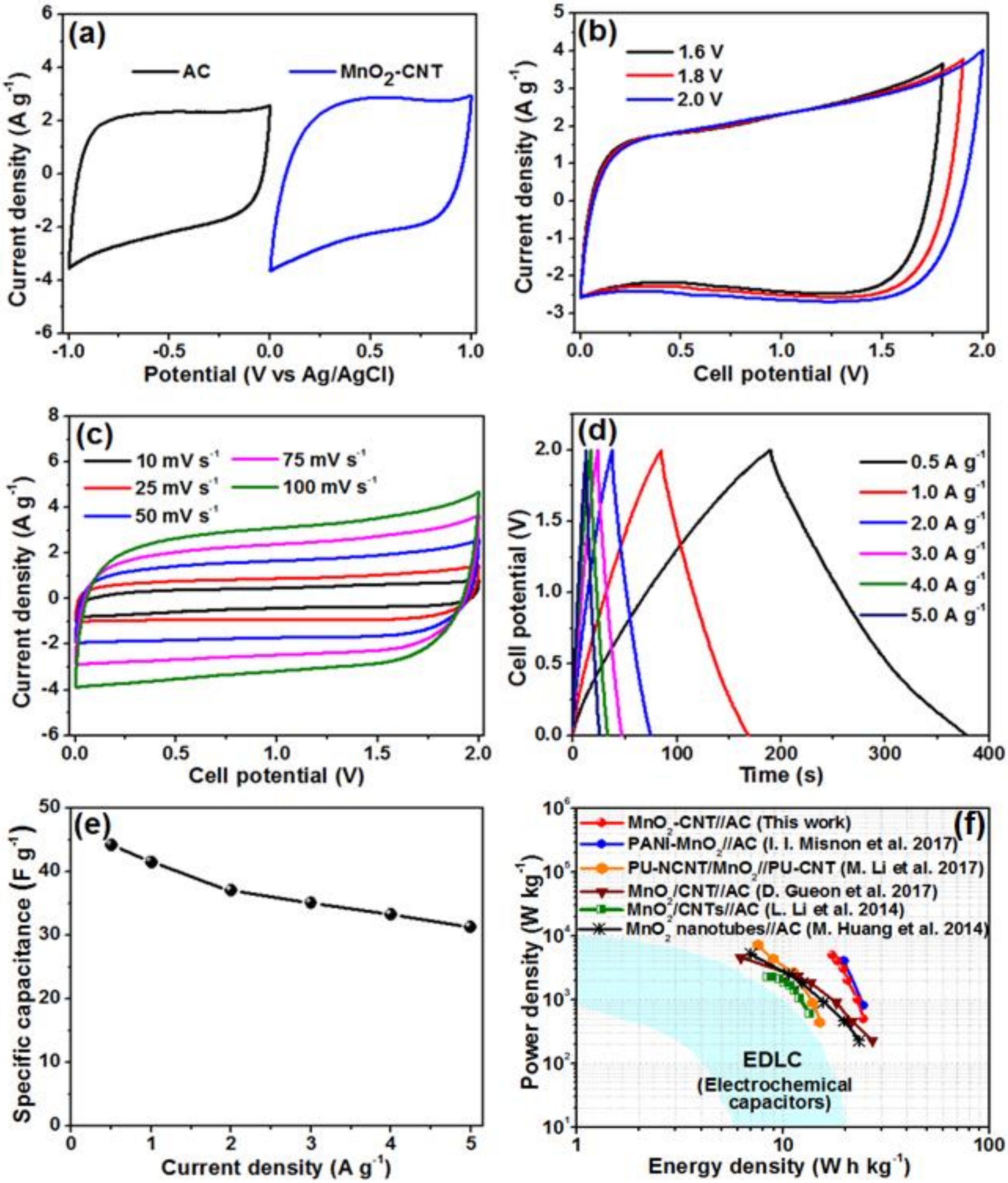

Figure 6. (a) CV curves of MnO$_2$@CNT and AC at 25 mV s^{-1}, (b) CV plots of hybrid Cell of MnO2@CNT//AC at 25 mV s^{-1} at various potential windows in 1 M Li$_2$SO$_4$, (c) CV plots of MnO$_2$@CNT//AC ranging from 10 mV s^{-1}- 100 mV s^{-1},(d) CD plots of MnO$_2$@CNT//AC ranging from 0.5 A g^{-1}, - 5.0 A g^{-1}, (e) Plot of specific capacitance as a function of specific current and (f) Ragone plot of the cell with comparison to similar work in the literature

Table 1. Electrochemical performance comparison of hybrid cell devices of this work and works earlier reported.

Electrode device	Electrolyte	Current density (A g^{-1})	Potential window (V)	Energy density (Wh kg^{-1})	Power density (W Kg^{-1})	Ref.
MnO_2CNT//AC	0.5 M Na_2SO_4	1.0	2.0	13.9	-	[4]
MnO_2//AC	1 M Na_2SO_4	0.1	2.0	17.1	100	[8]
PU-NCNT/MnO_2//PU-CNT	1 M Na_1SO_4	1.0	1.8	14.76	7211	[49]
MnO_2/CNT//AC	2 M KNO_3	0.1	2.0	21.0	123	[50]
MnO_2/CNT//AC	1 M Na_2SO_4	0.25	1.8	27.0	225	[39]
MnO_2 nanotubes//AC	1 M Na_2SO_4	0.25	1.8	22.5	146200	[37]
Pani-MnO_2//AC	6 M KOH	0.5	1.6	20	400	[51]
AC//MnO_2/CNT	1 M Na_2SO4	1.0	1.5	13.3	600	[1]
MnO_2-CNT//AC	**1 M Li_2SO_4**	**0.5**	**2.0**	**24.58**	**500**	**This work**

In addition to the high energy density displayed by the hybrid device, it also exhibited excellent stability of ~100% columbic efficiency at up to 10,000 cycles (see figure 7(a)). The stability test of a device is important because it shows the electrochemical behavior of the device over a prolonged period [15,52,53]. The remarkable stability performance of this device may be attributed presence of the MnO_2-CNT nanocomposite because of their nano tube-like structure possess high resiliency which is able to accommodate large capacity changes throughout the charge/discharge duration with enhanced effect on the life cycle of the device[54]. Also the synergistic contribution from the 3D porous AC which provides more accessible pores sites for the diffusion of electrolyte ions [37,55]. This excellent electrode performance is confirmed by the improvement on the capacitance of the hybrid device after 10 000 charge/discharge cycles as depicted in the CV and CD plots shown in figure 7(b) and 7(c). The stability of the MnO_2-CNT//AC hybrid device was further tested via potentiostatic floating test at 1.0 A g^{-1} and maximum potential of 2.0 V for 60 hours as it is an adopted reliable technique to accurately evaluate the stability performance of the supercapacitor device. A plot of specific capacitance vs floating time for the hybrid device is presented in figure 7(d). A decrease in specific capacitance can be observed during the first 10 hours, which stabilized for the rest of the floating time displaying 90% capacitance retention. The stability performance of this device demonstrates the excellent capacitive performance which indicates that the long term cycling and floating does not significantly affect the stable tube-like/porous structure of the MnO_2-CNT//AC hybrid electrode [15,56].

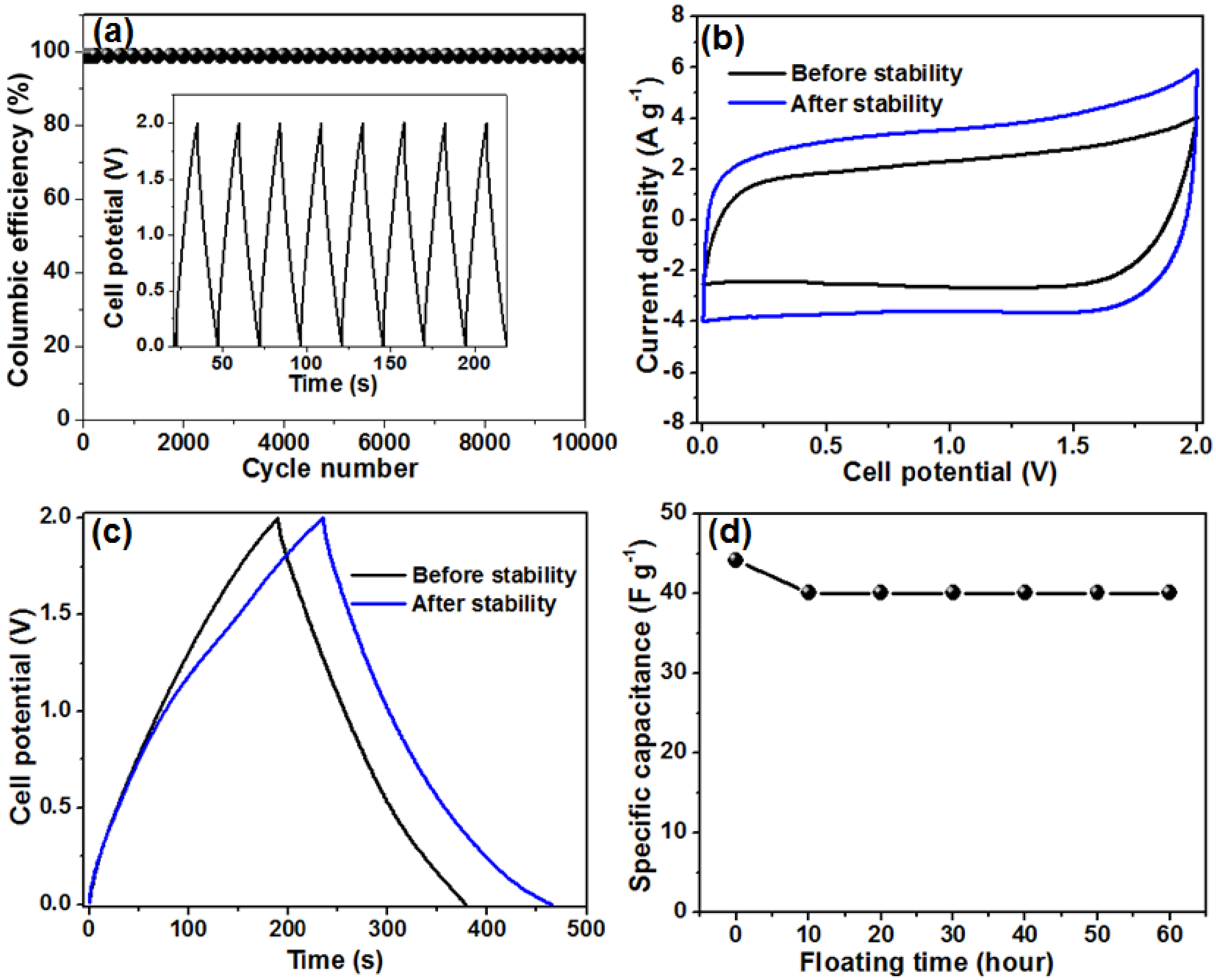

Figure 7. (a) Plot of columbic efficiency as a function of cycle number, (b) CV curves before and after

stability of the MnO_2-CNT//AC hybrid device at 25 mV s^{-1}, (c) CD curves before and after stability of the MnO_2-CNT//AC hybrid device at 0.5 A g^{-1} and (d) Plot of specific capacitance as a function of floating time.

The electrochemical impedance spectroscopy (EIS) analysis was carried out in an open circuit potential in the frequency range of 10 mHz to 100 kHz. EIS is an important tool for investigating the electron and ion mobility in an electrode material. The MnO_2-CNT//AC hybrid device Nyquist plot is presented in figure 8(a). The intersection of the semicircle and the real Z'-axis, indicates the solution resistance (R_S) with the value of 1.2 Ω (see inset to figure 8(a)). In the high to middle frequency region, the diameter of the semicircle (inset to figure 8(a)), shows the charge transfer resistance (R_{ct})with the value of 1.0 Ω. Nearly vertical lines parallel to the *y*-axis close to the low frequency region can be observed indicating ideal capacitive behavior of the hybrid electrode device. The equivalent circuit and fitting for the Nyquist plot is presented in figure 8(b). In the equivalent circuit (inset to Fig. 8(b)), the solution resistance is connected in series with the constant phase element (Q) which is connected in parallel to R_{ct} . The Warburg diffusion element (W) which models the transition from the high to low frequency region is connected in series with the R_{ct}. These are then connected in series with the mass capacitance (C_L). In an ideal capacitive electrode, this mass capacitance should give rise to a straight line parallel to the *y*-axis but a deviation from the ideal behavior was observed as seen in figure 8(a). This deviation is as a result of the resistive element, R_L which is a leakage current connected in parallel to C_L[57,58]. The real (C') and imaginary (C'') parts of the capacitance as a function of frequency are presented in figure 8(c). C' is the real attainable capacitance of the hybrid device with a value of 1.2 F corresponding to a frequency value of 0.01 Hz. C'' which indicates the transition frequency between an ideal capacitive and ideal resistive behavior [59] of the hybrid device is represented by the peak which occurs at a maximum frequency value of ~0.16 Hz corresponding to a relaxation time, τ of ~6.3 s, evaluated from $\tau = {}^{1}/_{\omega_{max}} =$

$^{1}/_{2\pi f_{max}}$. The phase angle of the hybrid device is -78° which is close to the ideal value of -90°indicating good capacitive behavior.

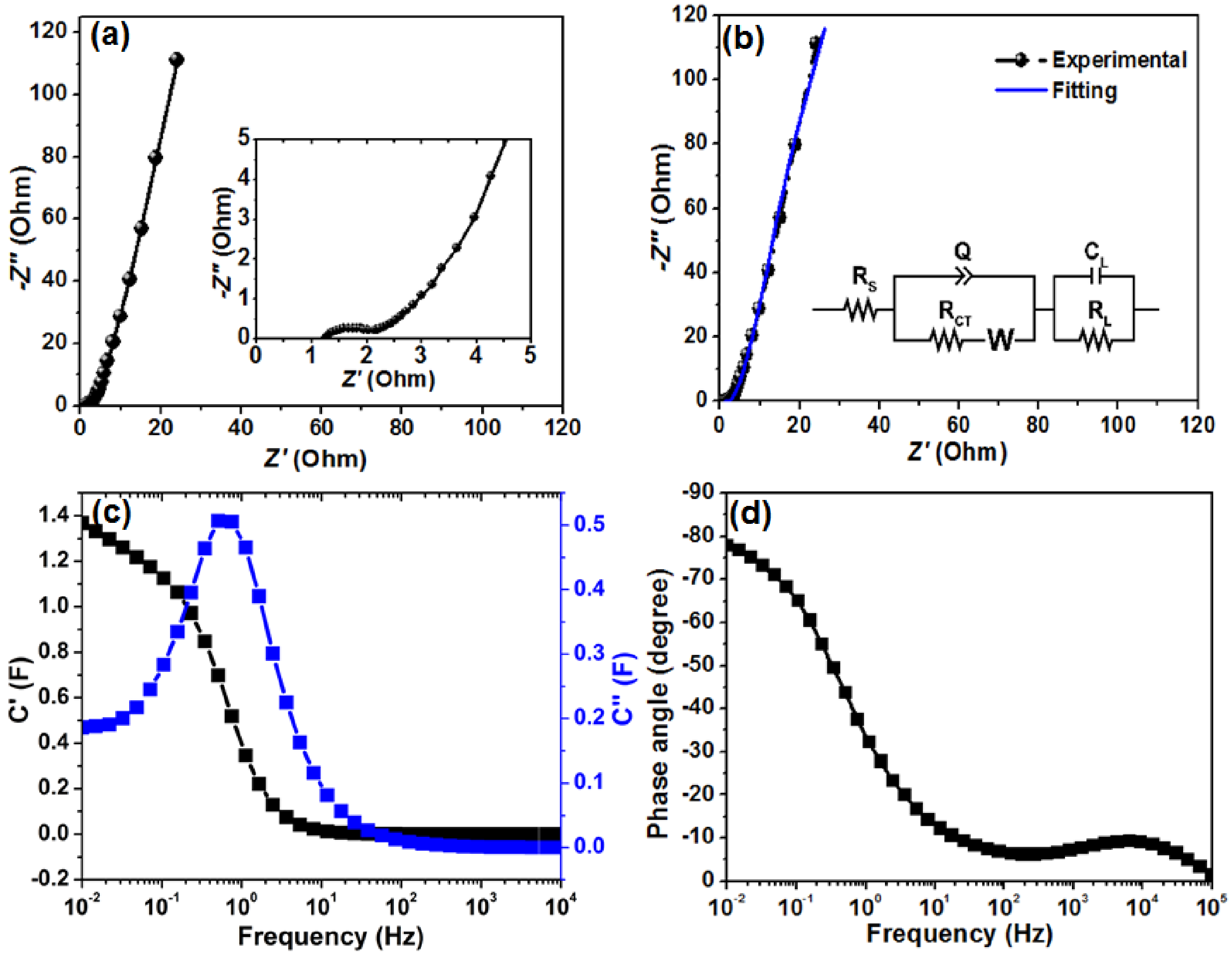

Figure 8. (a) Nyquist plot of MnO$_2$-CNT//AChybrid device, (b) Nyquist plot with fitting by the equivalent circuit inset to the figure, (c) plot of real and imaginary capacitances as a function of frequencyand (d)plot of phase angle as a function of frequency.

CONCLUSION

This work has investigated the electrochemical pseudocapacitive performance of MnO_2-CNT as the positive electrode and AC derived from the cork (Quercus Suber) as the negative electrode in a successfully fabricated MnO_2-CNT//AC device. The MnO_2-CNT nanocomposite and 3D nanostructured activated carbon displayed excellent properties that resulted with good microstructural, morphological and electrochemical properties. The synergistic effects of the MnO_2-CNT and the 3D microporous AC material was maximized to increase the working potential of the hybrid device up to 2 V. The device displayed an energy density of $\sim$25 Wh Kg^{-1} and corresponding power density of 500 W Kg^{-1} at a current density of 0.5 A g^{-1} in 1 m Li_2SO_4 aqueous neutral electrolyte. The device exhibited an excellent stability of $\sim$100% after 10 000 charge-discharge cycles and excellent capacitance retention after potentiostatic floating test for 60 hours. The results obtained suggests that the hybrid device has the potential for high-energy storage device application.

ACKNOWLEDGEMENTS

This research work was supported by the South African Research Chairs Initiative (SARChI) of the Department of Science and Technology and the National Research Foundation (NRF) of South Africa (Grant No. 61056). Any opinion, finding and conclusion or recommendation expressed in this material is that of the author(s) and the NRF does not accept any liability in this regard. Faith O. Ochai-Ejeh acknowledges NRF through SARChI in Carbon Technology and

Materials, the Department of Physics at the University of Pretoria, the TETFund through the University of Nigeria for financial support.

REFERENCES

[1] L. Li, Z.A. Hu, N. An, Y.Y. Yang, Z.M. Li, H.Y. Wu, Facile Synthesis of MnO $_2$ /CNTs Composite for Supercapacitor Electrodes with Long Cycle Stability, J. Phys. Chem. C. 118 (2014) 22865–22872. doi:10.1021/jp505744p.

[2] Electrochemical Capacitor Applications, (2008). https://www.electrochem.org/dl/interface/spr/spr08/spr08_p53-57.pdf (accessed September 7, 2017).

[3] High performance hybrid supercapacitor device based on cobalt manganese layered double hydroxide and activated carbon derived from cork (Quercus Suber), Electrochim. Acta. 252 (2017) 41–54. doi:10.1016/J.ELECTACTA.2017.08.163.

[4] L. Demarconnay, E. Raymundo-Piñero, F. Béguin, Adjustment of electrodes potential window in an asymmetric carbon/MnO2 supercapacitor, J. Power Sources. 196 (2011) 580–586. doi:10.1016/j.jpowsour.2010.06.013.

[5] M. Gidwani, A. Bhagwani, N. Rohra, Supercapacitors: the near Future of Batteries, Int. J. Eng. Invent. 4 (2014) 2278–7461. www.ijeijournal.com (accessed September 7, 2017).

[6] P. Simon, Y. Gogotsi, Capacitive Energy Storage in Nanostructured Carbon–Electrolyte Systems, Acc. Chem. Res. 46 (2013) 1094–1103. doi:10.1021/ar200306b.

[7] A. Brandt, S. Pohlmann, A. Varzi, A. Balducci, S. Passerini, Ionic liquids in supercapacitors,

MRS Bull. 38 (2013) 554–559. doi:10.1557/mrs.2013.151.

[8] Rapid hydrothermal synthesis of hierarchical nanostructures assembled from ultrathin birnessite-type MnO2 nanosheets for supercapacitor applications, Electrochim. Acta. 89 (2013) 523–529. doi:10.1016/J.ELECTACTA.2012.11.089.

[9] J.W. Lee, A.S. Hall, J.-D. Kim, T.E. Mallouk, A Facile and Template-Free Hydrothermal Synthesis of Mn_3O_4 Nanorods on Graphene Sheets for Supercapacitor Electrodes with Long Cycle Stability, Chem. Mater. 24 (2012) 1158–1164. doi:10.1021/cm203697w.

[10] Y. Zhou, H. Xu, N. Lachman, M. Ghaffari, S. Wu, Y. Liu, A. Ugur, K.K. Gleason, B.L. Wardle, Q.M. Zhang, Advanced asymmetric supercapacitor based on conducting polymer and aligned carbon nanotubes with controlled nanomorphology, Nano Energy. 9 (2014) 176–185. doi:10.1016/j.nanoen.2014.07.007.

[11] B.G. Choi, M. Yang, W.H. Hong, J.W. Choi, Y.S. Huh, 3D Macroporous Graphene Frameworks for Supercapacitors with High Energy and Power Densities, ACS Nano. 6 (2012) 4020–4028. doi:10.1021/nn3003345.

[12] W.G. Pell, B.E. Conway, Peculiarities and requirements of asymmetric capacitor devices based on combination of capacitor and battery-type electrodes, J. Power Sources. 136 (2004) 334–345. doi:10.1016/j.jpowsour.2004.03.021.

[13] F.O. Ochai-Ejeh, A. Bello, J. Dangbegnon, A.A. Khaleed, M.J. Madito, F. Bazegar, N. Manyala, High electrochemical performance of hierarchical porous activated carbon derived from lightweight cork (Quercus suber), J. Mater. Sci. 52 (2017) 10600–10613.

doi:10.1007/s10853-017-1205-4.

[14] C. Zhong, Y. Deng, W. Hu, J. Qiao, L. Zhang, J. Zhang, A review of electrolyte materials and compositions for electrochemical supercapacitors, Chem. Soc. Rev. 44 (2015) 7484–7539. doi:10.1039/C5CS00303B.

[15] F.O. Ochai-Ejeh, M.J. Madito, D.Y. Momodu, A.. Khaleed, O. Olaniyan, N. Manyala, High performance hybrid supercapacitor device based on cobalt manganese layered double hydroxide and activated carbon derived from cork (Quercus Suber), Electrochim. Acta. 252 (2017) 41–54. doi:10.1016/j.electacta.2017.08.163.

[16] F. Béguin, V. Presser, A. Balducci, E. Frackowiak, Carbons and Electrolytes for Advanced Supercapacitors, Adv. Mater. 26 (2014) 2219–2251. doi:10.1002/adma.201304137.

[17] A. Bello, F. Barzegar, M.J. Madito, D.Y. Momodu, A.A. Khaleed, T.M. Masikhwa, J.K. Dangbegnon, N. Manyala, Stability studies of polypyrole- derived carbon based symmetric supercapacitor via potentiostatic floating test, Electrochim. Acta. 213 (2016) 107–114. doi:10.1016/j.electacta.2016.06.151.

[18] L. Demarconnay, E. Raymundo-Piñero, F. Béguin, A symmetric carbon/carbon supercapacitor operating at 1.6 V by using a neutral aqueous solution, Electrochem. Commun. 12 (2010) 1275–1278. doi:10.1016/j.elecom.2010.06.036.

[19] Long-term cycling behavior of asymmetric activated carbon/MnO2 aqueous electrochemical supercapacitor, J. Power Sources. 173 (2007) 633–641. doi:10.1016/J.JPOWSOUR.2007.04.074.

[20] M. Liang, L. Zhi, Graphene-based electrode materials for rechargeable lithium batteries, J. Mater. Chem. 19 (2009) 5871. doi:10.1039/b901551e.

[21] J.K. Gan, Y.S. Lim, A. Pandikumar, N.M. Huang, H.N. Lim, Graphene/polypyrrole-coated carbon nanofiber core–shell architecture electrode for electrochemical capacitors, RSC Adv. 5 (2015) 12692–12699. doi:10.1039/C4RA14922J.

[22] F. Zhang, T. Zhang, X. Yang, L. Zhang, K. Leng, Y. Huang, Y. Chen, A high-performance supercapacitor-battery hybrid energy storage device based on graphene-enhanced electrode materials with ultrahigh energy density, Energy Environ. Sci. 6 (2013) 1623. doi:10.1039/c3ee40509e.

[23] W. Gu, G. Yushin, Review of nanostructured carbon materials for electrochemical capacitor applications : advantages and limitations of activated carbon , carbide-derived carbon , aerogels , carbon nanotubes , onion-like carbon , and graphene, (2013). doi:10.1002/wene.102.

[24] X. Li, W. Xing, S. Zhuo, J. Zhou, F. Li, S.-Z. Qiao, G.-Q. Lu, Preparation of capacitor's electrode from sunflower seed shell, Bioresour. Technol. 102 (2011) 1118–1123. doi:10.1016/j.biortech.2010.08.110.

[25] K.S. Sulaiman, A. Mat, A.K. Arof, Activated carbon from coconut leaves for electrical double-layer capacitor, Ionics (Kiel). 22 (2016) 911–918. doi:10.1007/s11581-015-1594-9.

[26] A. Özhan, Ö. Şahin, M.M. Küçük, C. Saka, Preparation and characterization of activated carbon from pine cone by microwave-induced ZnCl2 activation and its effects on the

adsorption of methylene blue, Cellulose. 21 (2014) 2457–2467. doi:10.1007/s10570-014-0299-y.

[27] T.-C. Weng, H. Teng, Characterization of High Porosity Carbon Electrodes Derived from Mesophase Pitch for Electric Double-Layer Capacitors, J. Electrochem. Soc. 148 (2001) A368. doi:10.1149/1.1357171.

[28] A. Alonso, V. Ruiz, C. Blanco, R. Santamaría, M. Granda, R. Menéndez, S.G.E. de Jager, Activated carbon produced from Sasol-Lurgi gasifier pitch and its application as electrodes in supercapacitors, Carbon N. Y. 44 (2006) 441–446. doi:10.1016/J.CARBON.2005.09.008.

[29] F. Barzegar, A. Bello, D. Momodu, M.J. Madito, J. Dangbegnon, N. Manyala, Preparation and characterization of porous carbon from expanded graphite for high energy density supercapacitor in aqueous electrolyte, J. Power Sources. 309 (2016) 245–253. doi:10.1016/j.jpowsour.2016.01.097.

[30] D. Momodu, A. Bello, K. Oyedotun, F. Ochai-Ejeh, J. Dangbegnon, M. Madito, N. Manyala, Enhanced electrochemical response of activated carbon nanostructures from tree-bark biomass waste in polymer-gel active electrolytes, RSC Adv. 7 (2017) 37286–37295. doi:10.1039/C7RA05810A.

[31] A.A. Khaleed, F.U. Ugbo, K.O. Oyeniran, D.Y. Momodu, A. Bello, J.K. Dangbegnon, N. Manyala, Cycling and floating performance of symmetric supercapacitor derived from coconut shell biomass, (2016). doi:10.1063/1.4967348.

[32] J. Xu, Q. Gao, Y. Zhang, Y. Tan, W. Tian, L. Zhu, L. Jiang, Preparing two-dimensional microporous carbon from Pistachio nutshell with high areal capacitance as supercapacitor materials, Sci. Rep. 4 (2014) 845–854. doi:10.1038/srep05545.

[33] S.R. Sivakkumar, J.M. Ko, D.Y. Kim, B.C. Kim, G.G. Wallace, Performance evaluation of CNT/polypyrrole/MnO2 composite electrodes for electrochemical capacitors, Electrochim. Acta. 52 (2007) 7377–7385. doi:10.1016/j.electacta.2007.06.023.

[34] A. Bello, F. Barzegar, M.J. Madito, D.Y. Momodu, A.A. Khaleed, T.M. Masikhwa, J.K. Dangbegnon, N. Manyala, Electrochemical performance of polypyrrole derived porous activated carbon-based symmetric supercapacitors in various electrolytes, RSC Adv. 6 (2016) 68141–68149. doi:10.1039/C6RA12690A.

[35] K. Liang, T. Gu, Z. Cao, X. Tang, W. Hu, B. Wei, In situ synthesis of SWNTs@MnO2/polypyrrole hybrid film as binder-free supercapacitor electrode, Nano Energy. 9 (2014) 245–251. doi:10.1016/j.nanoen.2014.07.017.

[36] X. Cai, S. Hua, C. Kok, L. Lai, J. Lin, Z. Shen, High-performance asymmetric pseudocapacitor cell based on cobalt hydroxide / graphene and polypyrrole / graphene electrodes, J. Power Sources. 275 (2015) 298–304. doi:10.1016/j.jpowsour.2014.10.204.

[37] M. Huang, Y. Zhang, F. Li, L. Zhang, R.S. Ruoff, Z. Wen, Q. Liu, Self-assembly of mesoporous nanotubes assembled from interwoven ultrathin birnessite-type MnO2 nanosheets for asymmetric supercapacitors., Sci. Rep. 4 (2014) 3878. doi:10.1038/srep03878.

[38] Y. Jin, H. Chen, M. Chen, N. Liu, Q. Li, Graphene-Patched CNT/MnO $_2$ Nanocomposite Papers for the Electrode of High-Performance Flexible Asymmetric Supercapacitors, ACS Appl. Mater. Interfaces. 5 (2013) 3408–3416. doi:10.1021/am400457x.

[39] D. Gueon, J.H. Moon, MnO $_2$ Nanoflake-Shelled Carbon Nanotube Particles for High-Performance Supercapacitors, ACS Sustain. Chem. Eng. 5 (2017) 2445–2453. doi:10.1021/acssuschemeng.6b02803.

[40] B. Brown, I.A. Cordova, C.B. Parker, B.R. Stoner, J.T. Glass, Optimization of Active Manganese Oxide Electrodeposits Using Graphenated Carbon Nanotube Electrodes for Supercapacitors, Chem. Mater. 27 (2015) 2430–2438. doi:10.1021/cm504519m.

[41] J. Jiang, Y. Li, J. Liu, X. Huang, C. Yuan, X.W.D. Lou, Recent Advances in Metal Oxide-based Electrode Architecture Design for Electrochemical Energy Storage, Adv. Mater. 24 (2012) 5166–5180. doi:10.1002/adma.201202146.

[42] G. Lota, K. Fic, E. Frackowiak, Carbon nanotubes and their composites in electrochemical applications, Energy Environ. Sci. 4 (2011) 1592. doi:10.1039/c0ee00470g.

[43] H. Jiang, P.S. Lee, C. Li, 3D carbon based nanostructures for advanced supercapacitors, Energy Environ. Sci. 6 (2013) 41–53. doi:10.1039/C2EE23284G.

[44] S.C. Pang, S.F. Chin, C.Y. Ling, Controlled Synthesis of Manganese Dioxide Nanostructures via a Facile Hydrothermal Route, J. Nanomater. 2012 (2012) 1–7. doi:10.1155/2012/607870.

[45] G. Xiong, C. Meng, R.G. Reifenberger, P.P. Irazoqui, T.S. Fisher, Graphitic Petal Micro-

Supercapacitor Electrodes for Ultra-High Power Density, Energy Technol. 2 (2014) 897–905. doi:10.1002/ente.201402055.

[46] Ultrathin manganese dioxide nanosheets grown on partially unzipped nitrogen-doped carbon nanotubes for high-performance asymmetric supercapacitors, J. Alloys Compd. 702 (2017) 236–243. doi:10.1016/J.JALLCOM.2017.01.244.

[47] K. Makgopa, P.M. Ejikeme, C.J. Jafta, K. Raju, M. Zeiger, V. Presser, K.I. Ozoemena, A high-rate aqueous symmetric pseudocapacitor based on highly graphitized onion-like carbon/birnessite-type manganese oxide nanohybrids, J. Mater. Chem. A. 3 (2015) 3480–3490. doi:10.1039/C4TA06715K.

[48] T.K. Gupta, B.P. Singh, V.N. Singh, S. Teotia, A.P. Singh, I. Elizabeth, S.R. Dhakate, S.K. Dhawan, R.B. Mathur, MnO2 decorated graphene nanoribbons with superior permittivity and excellent microwave shielding properties, J. Mater. Chem. A. 2 (2014) 4256. doi:10.1039/c3ta14854h.

[49] Ultrathin manganese dioxide nanosheets grown on partially unzipped nitrogen-doped carbon nanotubes for high-performance asymmetric supercapacitors, J. Alloys Compd. 702 (2017) 236–243. doi:10.1016/J.JALLCOM.2017.01.244.

[50] Optimisation of an asymmetric manganese oxide/activated carbon capacitor working at 2 V in aqueous medium, J. Power Sources. 153 (2006) 183–190. doi:10.1016/J.JPOWSOUR.2005.03.210.

[51] I.I. Misnon, R. Jose, Synthesis and electrochemical evaluation of the PANI/δ-MnO

$_2$electrode for high performing asymmetric supercapacitors, New J. Chem. 41 (2017) 6574–6584. doi:10.1039/C7NJ00679A.

[52] Q. Gao, L. Demarconnay, E. Raymundo-Piñero, F. Béguin, Exploring the large voltage range of carbon/carbon supercapacitors in aqueous lithium sulfate electrolyte, Energy Environ. Sci. 5 (2012) 9611. doi:10.1039/c2ee22284a.

[53] A.N. Naveen, S. Selladurai, A 1-D/2-D hybrid nanostructured manganese cobaltite–graphene nanocomposite for electrochemical energy storage, RSC Adv. 5 (2015) 65139–65152. doi:10.1039/C5RA09288D.

[54] E. Frackowiak, Carbon materials for supercapacitor application, Phys. Chem. Chem. Phys. 9 (2007) 1774. doi:10.1039/b618139m.

[55] J.P. Cheng, L. Liu, J. Zhang, F. Liu, X.B. Zhang, Influences of anion exchange and phase transformation on the supercapacitive properties of α-Co(OH)2, J. Electroanal. Chem. 722–723 (2014) 23–31. doi:10.1016/j.jelechem.2014.03.019.

[56] L.-H.H. Su, X.-G.G. Zhang, Y. Liu, Electrochemical performance of Co-Al layered double hydroxide nanosheets mixed with multiwall carbon nanotubes, J. Solid State Electrochem. 12 (2008) 1129–1134. doi:10.1007/s10008-007-0455-5.

[57] X. Liu, R. Ma, Y. Bando, T. Sasaki, A General Strategy to Layered Transition-Metal Hydroxide Nanocones: Tuning the Composition for High Electrochemical Performance, Adv. Mater. 24 (2012) 2148–2153. doi:10.1002/adma.201104753.

[58] S.I. Cordoba, R.E. Carbonio, M.L. Teijelo, V.A. Macagno, The electrochemical response of

binary mixtures of hydrous transition metal hydroxides co-precipitated on conducting substrates with reference to the oxygen evolution reaction, Electrochim. Acta. 31 (1986) 1321–1332. doi:10.1016/0013-4686(86)80155-4.

[59] P.L. Taberna, P. Simon, J.F. Fauvarque, Electrochemical Characteristics and Impedance Spectroscopy Studies of Carbon-Carbon Supercapacitors, J. Electrochem. Soc. 150 (2003) A292. doi:10.1149/1.1543948.

4.4.3 Concluding remark

MnO_2-CNT nanocomposite and 3D microporous nanostructured activated carbon (AC) derived from cork (Quercus Suber) with good microstructural, morphological and electrochemical properties was successfully investigated. A hybrid EC device consisting of of MnO_2-CNT nanocomposite as positive electrode and AC as negative electrode was fabricated and tested for energy storage application. The device displayed a maximum working potential of up to 2 V owing to the excellent synergistic contribution from the MnO_2-CNT nanocomposite and AC material derived from cork (Quercus Suber). The fabricated device exhibited good electrochemical performance with an energy density of ~25 Wh Kg^{-1} and corresponding power density of 500 W Kg^{-1} at 0.5 A g^{-1} specific current in 1 M Li_2SO_4 aqueous neutral electrolyte. The device exhibited an excellent stability of ~100% coulombic efficiency after 10,000 charge-discharge cycles and excellent capacitance retention after potentiostatic floating test for 60 hours.

CHAPTER FIVE

GENERAL CONCLUSIONS AND FUTURE WORK

In this chapter, the results obtained from this work with respect to the stated objectives are summarized. 3D nanostructured biomass derived activated carbon (AC) from cork (Quercus Suber) for high performance supercapacitor application was synthesized. First, via direct activation with KOH in raw material: activating agent ratios, followed by carbonization in a CVD system and second, via hydrothermal pre-treatment, activation with $KHCO_3$ and carbonization in CVD system. Thin Co-Mn layered double hydroxide (LDH) nanoflakes, MnO_2-CNT nanocomposite, was also synthesized via solvothermal and facile hydrothermal reflux techniques respectively.

The electrode materials characterization were performed using scanning electron microscopy (SEM), energy dispersive X-ray spectroscopy (EDX), Raman spectroscopy, high resolution transmission electron microscopy (HR-TEM), X-ray diffraction (XRD), Fourier transform infra-red spectroscopy (FT-IR), X-ray photoelectron spectroscopy (XPS) and Brunauer-Emmett-Teller (BET) and Barrett-Joyner- Halenda (BJH) techniques. The electrochemical performance of the materials were investigated in three- and two-electrode configurations using cyclic voltammetry (CV), galvanostatic charge discharge (GCD), electrochemical impedance spectroscopy (EIS) and stability tests (GCD cycling for several thousand cycles and potentiostatic floating for several hours) techniques.

In section 4.1 the electrochemical performance of hierarchical porous activated carbon (AC) derived from cork (Quercus suber) synthesized by KOH activation was presented and discussed. The novel energy storage application study of the cork derived AC was succinctly elucidated.The morphology of the materials showed good 3D porous interconnected network structure and an evolution of the pores and structures of the materials studied at different raw material: KOH ratios, at the same carbonization temperature of 800 ^{o}C. A high surface area of 1081 m^{2} g^{-1} and a high pore volume of 0.66 cm^{3} g^{-1} was obtained when the raw material/KOH ratio was fixed at 1:2. A symmetric device was successfully fabricated and a specific capacitance of 166 F g^{-1} was obtained for the at 0.5 A g^{-1} in 1 M Na_2SO_4 with energy and power densities of 18.6 W h Kg^{-1} and 449.4 W Kg^{-1} respectively. The device displayed good cycling stability after potentiostatic floating test for 200 h at 1.8 V and a 99.8 % capacitance retention after cycling for 5000 cycles. The excellent electrochemical performance of the device demonstrates the potential of the material for energy storage application.

The result of the AC synthesized by $KHCO_3$activation was presented and discussed in section 4.3. $KHCO_3$was utilized as an activation agent because it is milder and less toxic as compared to KOH. The ACKHCO$_3$material synthesized at a carbonization temperature of 850 ^{o}C had a 3D granular porous network structure and well-defined microporous and mesoporous structures.A specific surface area of 1056.52 m^{2} g^{-1} and pore volume of 0.64 cm^{3} g^{-1} was obtained from the BET-BJH measurements. Three-electrode tests were performed in 6 M KOH alkaline, 1 M H_2SO_4acidic and 3 M KNO_3 neutral aqueous electrolytes. Specific capacitance values (C_s) of 133 F g^{-1} and 167 F g^{-1} at specific current of 1.0 A g^{-1} was recorded in 3 M KNO_3 in the positive and negative potential windows. Additional electrochemical study of the material was performed by constructing a symmetric devicein 3 M KNO_3 as a result of its reversible performance in this neutral aqueous medium. The device displayed a C_s valueof 122 F g^{-1}, energy ~14 W h kg^{-1} and corresponding power density of 450 W kg^{-1}at a specific current of 0.5 A g^{-1}.The device also exhibited an excellent cycling stability with~100% capacitance retention after 10,000 charge-discharge cycles and after potentiostatic floating for 120 h at a maximum voltage of 1.8 V. The excellent stability of the ACKHCO_3material makes it an excellent, inexpensive material for energy storage application.

Hybrid supercapacitor devices were fabricated and their electrochemical performance were evaluated. The hybrid cell configuration takes advantage of the individual working potentials of the electrode materials for enhanced supercapacitor performance. In section 4.2, Co-Mn layered double hydroxide (LDH)with thin nanoflake structure and ACderived from cork raw material (Quercus Suber) and $KHCO_3$activation with highly porous structure and good textural characteristics was presented and discussed. Co-Mn LDH wasused as the positive electrode and AC as negative electrode. The device Co-Mn LDH//ACKHCO_3 displayed a high energy density of 20.3 Wh kg^{-1} and corresponding power density of 435 W kg^{-1}at a specific current of 0.5 A g^{-1} in 1 M KOH aqueous electrolyte. The device also showed an excellent stability with 99.7% capacitance retention after 10,000 charge-discharge cycles and negligible degradation after subsequently subjecting it to potentiostatic floating test at 1.6 V maximum voltage for 70 h. These results shows the potential of this hybrid device as possible electrodes for high energy density energy storage application application.

Furthermore, MnO_2-CNT//ACKOH hybrid device was fabricated and tested in 1M Li_2SO_4 aqueous neutral electrolyte as presented and discussed in section 4.4. MnO_2-CNT nanocomposite was utilized as positive electrode and AC as negative electrode. The device displayed a maximum working voltage of up to 2V as a result of the excellent synergistic contribution from the MnO_2-CNT tubular nanocomposite and 3D porous ACKOH material derived from cork (Quercus Suber). The fabricated device showed good electrochemical performance with an energy density of ~25 Wh $Kg^{-1}$and corresponding power density of 500 W Kg^{-1} at a specific current of 0.5 A g^{-1}. The device displayed an excellent stability of ~100% coulombic efficiency after 10,000 charge-discharge cycles and excellent capacitance retention after60 hours of potentiostatic floating test.

In a nutshell, the materials and the supercapacitor devices investigated in this study have demonstrated excellent electrochemical performances with large operating voltage windows ranging from 1.6 – 2.0 V suggesting their potential use as electrode materials/devices for energy storage applications.

Future work can be done by testing the materials in other types of electrolyte media such as ionic liquid or organic electrolytes to investigate the possibility of increasing the operating potential windows and hence improve the energy and power densities performance of the materials. More work can also be done by working on improving the microstructure and morphology of the investigated materials in other to elicit better electrochemical performance from the materials.

REFERENCES

[1] C. Zhong, Y. Deng, W. Hu, J. Qiao, L. Zhang, J. Zhang, A review of electrolyte materials and compositions for electrochemical supercapacitors, Chem. Soc. Rev. 44 (2015) 7484–7539. doi:10.1039/C5CS00303B.

[2] A. Bello, N. Manyala, F. Barzegar, A.A. Khaleed, D.Y. Momodu, J.K. Dangbegnon, Renewable pine cone biomass derived carbon materials for supercapacitor application, RSC Adv. 6 (2016) 1800–1809. doi:10.1039/C5RA21708C.

[3] F.O. Ochai-Ejeh, A. Bello, J. Dangbegnon, A.A. Khaleed, M.J. Madito, F. Bazegar, N. Manyala, High electrochemical performance of hierarchical porous activated carbon derived from lightweight cork (Quercus suber), J. Mater. Sci. 52 (2017) 10600–10613. doi:10.1007/s10853-017-1205-4.

[4] R. Li, S. Wang, Z. Huang, F. Lu, T. He, NiCo2S4@Co(OH)2 core-shell nanotube arrays in situ grown on Ni foam for high performances asymmetric supercapacitors, J. Power Sources. 312 (2016) 156–164. doi:10.1016/j.jpowsour.2016.02.047.

[5] P. Simon, Y. Gogotsi, Capacitive Energy Storage in Nanostructured Carbon–Electrolyte Systems, Acc. Chem. Res. 46 (2013) 1094–1103. doi:10.1021/ar200306b.

[6] D.Y. Momodu, M.J. Madito, F. Barzegar, A. Bello, A.A. Khaleed, O. Olaniyan, J.K. Dangbegnon, N. Manyala, Activated carbon derived from tree bark biomass with promising material properties for supercapacitors, J. Solid State Electrochem. (2016) 1–

14. doi:10.1007/s10008-016-3432-z.

[7] Low voltage electrolytic capacitor, (1954). https://www.google.com/patents/US2800616 (accessed September 1, 2017).

[8] A. Davies, A. Yu, Material advancements in supercapacitors: From activated carbon to carbon nanotube and graphene, Can. J. Chem. Eng. 89 (2011) 1342–1357. doi:10.1002/cjce.20586.

[9] E. Raymundo-Piñero, K. Kierzek, J. Machnikowski, F. Béguin, Relationship between the nanoporous texture of activated carbons and their capacitance properties in different electrolytes, Carbon 44 (2006) 2498–2507. doi:10.1016/J.CARBON.2006.05.022.

[10] K. Kierzek, E. Frackowiak, G. Lota, G. Gryglewicz, J. Machnikowski, Electrochemical capacitors based on highly porous carbons prepared by KOH activation, Electrochim. Acta. 49 (2004) 515–523. doi:10.1016/J.ELECTACTA.2003.08.026.

[11] A. Bello, F. Barzegar, D. Momodu, J. Dangbegnon, F. Taghizadeh, N. Manyala, Symmetric supercapacitors based on porous 3D interconnected carbon framework, Electrochim. Acta. 151 (2015) 386–392. doi:10.1016/J.ELECTACTA.2014.11.051.

[12] M.D. Stoller, S. Park, Y. Zhu, J. An, R.S. Ruoff, Graphene-Based Ultracapacitors, Nano Lett. 8 (2008) 3498–3502. doi:10.1021/nl802558y.

[13] Z.-S. Wu, W. Ren, D.-W. Wang, F. Li, B. Liu, H.-M. Cheng, High-Energy MnO $_2$ Nanowire/Graphene and Graphene Asymmetric Electrochemical Capacitors, ACS Nano. 4 2010) 5835–5842. doi:10.1021/nn101754k.

[14] T. Brousse, B. Daniel, JES F OCUS I SSUE ON E LECTROCHEMICAL C APACITORS : F UNDAMENTALS TO A PPLICATIONS To Be or Not To Be Pseudocapacitive ?, 162 (2015) 5185–5189. doi:10.1149/2.0201505jes.

[15] M.D. Stoller, R.S. Ruoff, Best practice methods for determining an electrode material's performance for ultracapacitors, Energy Environ. Sci. 3 (2010) 1294. doi:10.1039/c0ee00074d.

[16] M. Zhou, J. Gomez, B. Li, Y.-B. Jiang, S. Deng, Oil tea shell derived porous carbon with an extremely large specific surface area and modification with MnO 2 for high-performance supercapacitor electrodes, Appl. Mater. Today. 7 (2017) 47–54. doi:10.1016/j.apmt.2017.01.008.

[17] Y.S. Yun, J.M. Kim, H.H. Park, J. Lee, Y.S. Huh, H.-J. Jin, Free-standing heterogeneous hybrid papers based on mesoporous γ-MnO2 particles and carbon nanotubes for lithium-ion battery anodes, J. Power Sources. 244 (2013) 747–751. doi:10.1016/J.JPOWSOUR.2012.11.056.

[18] K. Makgopa, P.M. Ejikeme, C.J. Jafta, K. Raju, M. Zeiger, V. Presser, K.I. Ozoemena, A high-rate aqueous symmetric pseudocapacitor based on highly graphitized onion-like carbon/birnessite-type manganese oxide nanohybrids, J. Mater. Chem. A. 3 (2015) 3480–3490. doi:10.1039/C4TA06715K.

[19] M. Min, K. Machida, J.H. Jang, K. Naoi, Hydrous RuO[sub 2]/Carbon Black Nanocomposites with 3D Porous Structure by Novel Incipient Wetness Method for Supercapacitors, J. Electrochem. Soc. 153 (2006) A334. doi:10.1149/1.2140677.

[20] H. Wang, Y. Liang, T. Mirfakhrai, Z. Chen, H. Sanchez Casalongue, H. Dai, Advanced Asymmetrical Supercapacitors Based on Graphene Hybrid Materials. https://arxiv.org/ftp/arxiv/papers/1104/1104.3379.pdf (accessed January 12, 2018).

[21] A.N. Naveen, S. Selladurai, A 1-D/2-D hybrid nanostructured manganese cobaltite–graphene nanocomposite for electrochemical energy storage, RSC Adv. 5 (2015) 65139–65152. doi:10.1039/C5RA09288D.

[22] D.-W. Wang, F. Li, H.-M. Cheng, Hierarchical porous nickel oxide and carbon as electrode materials for asymmetric supercapacitor, J. Power Sources. 185 (2008) 1563–1568. doi:10.1016/j.jpowsour.2008.08.032.

[23] J. Yan, Z. Fan, W. Sun, G. Ning, T. Wei, Q. Zhang, R. Zhang, L. Zhi, F. Wei, Advanced Asymmetric Supercapacitors Based on Ni(OH)2/Graphene and Porous Graphene Electrodes with High Energy Density, Adv. Funct. Mater. 22 (2012) 2632–2641. doi:10.1002/adfm.201102839.

[24] A. Saha, A. Mondal, S. Maiti, S.C. Ghosh, S. Mahanty, A.B. Panda, A facile method for the synthesis of a C@MoO $_2$ hollow yolk–shell structure and its electrochemical properties as a faradaic electrode, Mater. Chem. Front. 1 (2017) 1585–1593. doi:10.1039/C7QM00006E.

[25] P. Khiew, M. Ho, W. Chiu, R. Shamsudin, M. Azmi, Synthesis and Electrochemical Characterization of Iron Oxide / Activated Carbon Composite Electrode for Symmetrical Supercapacitor, 7 (2013) 615–619.

[26] K. Bhattacharya, P. Deb, Hybrid nanostructured C-dot decorated Fe_3O_4 electrode materials for superior electrochemical energy storage performance, Dalt. Trans. 44 (2015) 9221–9229. doi:10.1039/C5DT00296F.

[27] D. Momodu, A. Bello, J. Dangbegnon, F. Barzeger, F. Taghizadeh, M. Fabiane, A.T.C. Johnson, N. Manyala, Solvothermal synthesis of NiAl double hydroxide microspheres on a nickel foam-graphene as an electrode material for pseudo-capacitors, AIP Adv. 4 (2014) 97122. doi:10.1063/1.4896125.

[28] K. Zhang, L.L. Zhang, X.S. Zhao, J. Wu, Graphene/Polyaniline Nanofiber Composites as Supercapacitor Electrodes, Chem. Mater. 22 (2010) 1392–1401. doi:10.1021/cm902876u.

[29] F. Zhang, T. Zhang, X. Yang, L. Zhang, K. Leng, Y. Huang, Y. Chen, A high-performance supercapacitor-battery hybrid energy storage device based on graphene-enhanced electrode materials with ultrahigh energy density, Energy Environ. Sci. 6 (2013) 1623. doi:10.1039/c3ee40509e.

[30] K. Grupo Español del Carbón., W. Naoi, Boletin del Grupo Español del Carbón., Grupo Español del Carbón, 2005. https://digital.csic.es/handle/10261/81752?locale=en (accessed April 8, 2017).

[31] M. Armand, J.-M. Tarascon, Building better batteries, Nature. 451 (2008) 652–657. doi:10.1038/451652a.

[32] J.K. Gan, Y.S. Lim, A. Pandikumar, N.M. Huang, H.N. Lim, Graphene/polypyrrole-coated carbon nanofiber core–shell architecture electrode for electrochemical capacitors, RSC

Adv. 5 (2015) 12692–12699. doi:10.1039/C4RA14922J.

[33] J.H. Chae, G.Z. Chen, 1.9V aqueous carbon–carbon supercapacitors with unequal electrode capacitances, Electrochim. Acta. 86 (2012) 248–254. doi:10.1016/j.electacta.2012.07.033.

[34] C. Peng, S. Zhang, X. Zhou, G.Z. Chen, Unequalisation of electrode capacitances for enhanced energy capacity in asymmetrical supercapacitors, Energy Environ. Sci. 3 (2010) 1499. doi:10.1039/c0ee00228c.

[35] L. Demarconnay, E. Raymundo-Piñero, F. Béguin, A symmetric carbon/carbon supercapacitor operating at 1.6V by using a neutral aqueous solution, Electrochem. Commun. 12 (2010) 1275–1278. doi:10.1016/j.elecom.2010.06.036.

[36] L. Demarconnay, E. Raymundo-Piñero, F. Béguin, A symmetric carbon/carbon supercapacitor operating at 1.6 V by using a neutral aqueous solution, Electrochem. Commun. 12 (2010) 1275–1278. doi:10.1016/j.elecom.2010.06.036.

[37] S. Dörfler, I. Felhösi, T. Marek, S. Thieme, H. Althues, L. Nyikos, S. Kaskel, High power supercap electrodes based on vertical aligned carbon nanotubes on aluminum, J. Power Sources. 227 (2013) 218–228. doi:10.1016/j.jpowsour.2012.11.068.

[38] A. Bello, F. Barzegar, M.J. Madito, D.Y. Momodu, A.A. Khaleed, T.M. Masikhwa, J.K. Dangbegnon, N. Manyala, Stability studies of polypyrole- derived carbon based symmetric supercapacitor via potentiostatic floating test, Electrochim. Acta. 213 (2016) 107–114. doi:10.1016/j.electacta.2016.06.151.

[39] C. Portet, Z. Yang, Y. Korenblit, Y. Gogotsi, R. Mokaya, G. Yushin, Electrical Double-Layer Capacitance of Zeolite-Templated Carbon in Organic Electrolyte, J. Electrochem. Soc. 156 (2009) A1. doi:10.1149/1.3002375.

[40] V. Presser, M. Heon, Y. Gogotsi, Carbide-Derived Carbons - From Porous Networks to Nanotubes and Graphene, Adv. Funct. Mater. 21 (2011) 810–833. doi:10.1002/adfm.201002094.

[41] D. Pech, M. Brunet, H. Durou, P. Huang, V. Mochalin, Y. Gogotsi, P.-L. Taberna, P. Simon, Ultrahigh-power micrometre-sized supercapacitors based on onion-like carbon, Nat. Nanotechnol. 5 (2010) 651–654. doi:10.1038/nnano.2010.162.

[42] W. Gu, G. Yushin, Review of nanostructured carbon materials for electrochemical capacitor applications : advantages and limitations of activated carbon , carbide-derived carbon , aerogels , carbon nanotubes , onion-like carbon , and graphene, (2013). doi:10.1002/wene.102.

[43] M. Biswal, A. Banerjee, M. Deo, S. Ogale, From dead leaves to high energy density supercapacitors, Energy Environ. Sci. 6 (2013) 1249. doi:10.1039/c3ee22325f.

[44] M. Sevilla, A.B. Fuertes, A Green Approach to High-Performance Supercapacitor Electrodes: The Chemical Activation of Hydrochar with Potassium Bicarbonate, ChemSusChem. 9 (2016) 1880–1888. doi:10.1002/cssc.201600426.

[45] J. Wang, S. Kaskel, KOH activation of carbon-based materials for energy storage, J. Mater. Chem. 22 (2012) 23710. doi:10.1039/c2jm34066f.

[46] M. Sevilla, A.B. Fuertes, R. Mokaya, High density hydrogen storage in superactivated carbons from hydrothermally carbonized renewable organic materials, Energy Environ. Sci. 4 (2011) 1400. doi:10.1039/c0ee00347f.

[47] A. Jain, R. Balasubramanian, M.P. Srinivasan, Hydrothermal conversion of biomass waste to activated carbon with high porosity: A review, Chem. Eng. J. 283 (2016) 789–805. doi:10.1016/j.cej.2015.08.014.

[48] A. Jain, C. Xu, S. Jayaraman, R. Balasubramanian, J.Y.Y. Lee, M.P.P. Srinivasan, Mesoporous activated carbons with enhanced porosity by optimal hydrothermal pre-treatment of biomass for supercapacitor applications, Microporous Mesoporous Mater. 218 (2015) 55–61. doi:10.1016/j.micromeso.2015.06.041.

[49] X. Liu, R. Ma, Y. Bando, T. Sasaki, A General Strategy to Layered Transition-Metal Hydroxide Nanocones: Tuning the Composition for High Electrochemical Performance, Adv. Mater. 24 (2012) 2148–2153. doi:10.1002/adma.201104753.

[50] S.B. Kulkarni, U.M. Patil, I. Shackery, J.S. Sohn, S. Lee, B. Park, S. Jun, on a polyaniline nano fi bers / 3D graphene framework as an e ffi cient charge transporter †, (2014) 4989–4998. doi:10.1039/c3ta14959e.

[51] F. Barzegar, A. Bello, D.Y. Momodu, J.K. Dangbegnon, F. Taghizadeh, M.J. Madito, T. moureen Masikhwa, N. Manyala, J. Madito, T. moureen Masikhwa, N. Manyala, Asymmetric supercapacitor based on an α-MoO3 cathode and porous activated carbon anode materials, RSC Adv. 5 (2015) 37462–37468. doi:10.1039/C5RA03579A.

[52] D. Gueon, J.H. Moon, MnO $_2$ Nanoflake-Shelled Carbon Nanotube Particles for High-Performance Supercapacitors, ACS Sustain. Chem. Eng. 5 (2017) 2445–2453. doi:10.1021/acssuschemeng.6b02803.

[53] J. Jiang, Y. Li, J. Liu, X. Huang, C. Yuan, X.W.D. Lou, Recent Advances in Metal Oxide-based Electrode Architecture Design for Electrochemical Energy Storage, Adv. Mater. 24 (2012) 5166–5180. doi:10.1002/adma.201202146.

[54] G. Lota, K. Fic, E. Frackowiak, Carbon nanotubes and their composites in electrochemical applications, Energy Environ. Sci. 4 (2011) 1592. doi:10.1039/c0ee00470g.

[55] B. Brown, I.A. Cordova, C.B. Parker, B.R. Stoner, J.T. Glass, Optimization of Active Manganese Oxide Electrodeposits Using Graphenated Carbon Nanotube Electrodes for Supercapacitors, Chem. Mater. 27 (2015) 2430–2438. doi:10.1021/cm504519m.

[56] W. Yang, Z. Gao, J. Wang, J. Ma, M. Zhang, L. Liu, Solvothermal one-step synthesis of Ni-Al layered double hydroxide/carbon nanotube/reduced graphene oxide sheet ternary nanocomposite with ultrahigh capacitance for supercapacitors., ACS Appl. Mater. Interfaces. 5 (2013) 5443–5454.

[57] Zhaoping Liu, Renzhi Ma, Yasuo Ebina, Nobuo Iyi, and Kazunori Takada, T. Sasaki*, General Synthesis and Delamination of Highly Crystalline Transition-Metal-Bearing Layered Double Hydroxides, (2006). doi:10.1021/LA062345M.

[58] H. Chen, L. Hu, M. Chen, Y. Yan, L. Wu, Nickel-Cobalt Layered Double Hydroxide Nanosheets for High-performance Supercapacitor Electrode Materials, Adv. Funct.

Mater. 24 (2014) 934–942. doi:10.1002/adfm.201301747.

[59] L. Huang, D. Chen, Y. Ding, S. Feng, Z.L. Wang, M. Liu, Nickel–Cobalt Hydroxide Nanosheets Coated on $NiCo_2O_4$ Nanowires Grown on Carbon Fiber Paper for High-Performance Pseudocapacitors, Nano Lett. 13 (2013) 3135–3139. doi:10.1021/nl401086t.

[60] D. Wang, J. Li, D. Zhang, T. Liu, N. Zhang, Layered Co – Mn hydroxide nanoflakes grown on carbon cloth as binder-free flexible electrodes for supercapacitors, J. Mater. Sci. 51 (2016) 3784–3792. doi:10.1007/s10853-015-9696-3.

[61] A.D. Jagadale, G. Guan, X. Li, X. Du, X. Ma, X. Hao, A. Abudula, Ultrathin nanoflakes of cobalt–manganese layered double hydroxide with high reversibility for asymmetric supercapacitor, J. Power Sources. 306 (2016) 526–534. doi:10.1016/j.jpowsour.2015.12.097.

[62] A.G. Pandolfo, A.F. Hollenkamp, Carbon properties and their role in supercapacitors, J. Power Sources. 157 (2006) 11–27. doi:10.1016/j.jpowsour.2006.02.065.

[63] M. Guerrero, E. Romero, F. Barrero, M.I. Milanés, E. González, Supercapacitors: Alternative Energy Storage Systems, (2009). http://peandes.unex.es/archives%5CP126.pdf (accessed September 6, 2017).

[64] W. Yang, Z. Gao, J. Wang, J. Ma, M. Zhang, L. Liu, Solvothermal One-Step Synthesis of Ni–Al Layered Double Hydroxide/Carbon Nanotube/Reduced Graphene Oxide Sheet Ternary

Nanocomposite with Ultrahigh Capacitance for Supercapacitors, ACS Appl. Mater. Interfaces. 5 (2013) 5443–5454. doi:10.1021/am4003843.

[65] Electrochemical Supercapacitors: Scientific Fundamentals and Technological ... - B. E. Conway - Google Books (accessed September 7, 2017).

[66] E. Frackowiak, Carbon materials for supercapacitor application, Phys. Chem. Chem. Phys. 9 (2007) 1774. doi:10.1039/b618139m.

[67] M. Gidwani, A. Bhagwani, N. Rohra, Supercapacitors: the near Future of Batteries, Int. J. Eng. Invent. 4 (2014) 2278–7461. www.ijeijournal.com (accessed September 7, 2017).

[68] V.S. Marin Halper James C Ellenbogen, Supercapacitors: A Brief Overview MITRE MITRE MITRE MITRE, (2006). https://www.mitre.org/sites/default/files/pdf/06_0667.pdf (accessed September 7, 2017).

[69] R. Kötz, M. Carlen, Principles and applications of electrochemical capacitors, Electrochim. Acta. 45 (2000) 2483–2498. doi:10.1016/S0013-4686(00)00354-6.

[70] A.S. Aricò, P. Bruce, B. Scrosati, J.-M. Tarascon, W. van Schalkwijk, Nanostructured materials for advanced energy conversion and storage devices, Nat. Mater. 4 (2005) 366–377. doi:10.1038/nmat1368.

[71] Electrochemical Capacitor Applications, (2008). https://www.electrochem.org/dl/interface/spr/spr08/spr08_p53-57.pdf (accessed September 7, 2017).

[72] C. Meng, O.Z. Gall, P.P. Irazoqui, A flexible super-capacitive solid-state power supply for

miniature implantable medical devices, Biomed. Microdevices. 15 (2013) 973–983. doi:10.1007/s10544-013-9789-1.

[73] T. Brousse, D. Belanger, J.W. Long, templa, J. Electrochem. Soc. 162 (2015) A5185–A5189. doi:10.1149/2.0201505jes.

[74] F.O. Ochai-Ejeh, M.J. Madito, D.Y. Momodu, A.. Khaleed, O. Olaniyan, N. Manyala, High performance hybrid supercapacitor device based on cobalt manganese layered double hydroxide and activated carbon derived from cork (Quercus Suber), Electrochim. Acta. 252 (2017) 41–54. doi:10.1016/j.electacta.2017.08.163.

[75] Y. Bin Tan, J.-M. Lee, Graphene for supercapacitor applications, J. Mater. Chem. A. 1 (2013) 14814. doi:10.1039/c3ta12193c.

[76] F. Béguin, V. Presser, A. Balducci, E. Frackowiak, Carbons and Electrolytes for Advanced Supercapacitors, Adv. Mater. 26 (2014) 2219–2251. doi:10.1002/adma.201304137.

[77] E. Frackowiak, F. Béguin, Carbon materials for the electrochemical storage of energy in capacitors, Carbon 39 (2001) 937–950. doi:10.1016/S0008-6223(00)00183-4.

[78] L.L. Zhang, X.S. Zhao, Carbon-based materials as supercapacitor electrodes, Chem. Soc. Rev. 38 (2009) 2520. doi:10.1039/b813846j.

[79] A. Laheäär, P. Przygocki, Q. Abbas, F. Béguin, Appropriate methods for evaluating the efficiency and capacitive behavior of different types of supercapacitors, 2015. doi:10.1016/j.elecom.2015.07.022.

[80] X. Zhang, S. Wang, L. Xu, T. He, F. Lu, H. Li, J. Ye, Controllable synthesis of cross-linked CoAl-LDH/NiCo 2 S 4 sheets for high performance asymmetric supercapacitors, Ceram. Int. (2017). doi:10.1016/j.ceramint.2017.07.159.

[81] D. Chen, H. Chen, X. Chang, P. Liu, Z. Zhao, J. Zhou, G. Xu, H. Lin, S. Han, Hierarchical CoMn-layered double hydroxide nanowires on nickel foam as electrode material for high-capacitance supercapacitor, J. Alloys Compd. (2017). doi:10.1016/j.jallcom.2017.07.313.

[82] H. Zhang, G. Cao, Z. Wang, Y. Yang, Z. Shi, Z. Gu, Growth of Manganese Oxide Nanoflowers on Vertically-Aligned Carbon Nanotube Arrays for High-Rate Electrochemical Capacitive Energy Storage, Nano Lett. 8 (2008) 2664–2668. doi:10.1021/nl800925j.

[83] D. Choi, G.E. Blomgren, P.N. Kumta, Fast and Reversible Surface Redox Reaction in Nanocrystalline Vanadium Nitride Supercapacitors, Adv. Mater. 18 (2006) 1178–1182. doi:10.1002/adma.200502471.

[84] L.-Z. Fan, Y.-S. Hu, J. Maier, P. Adelhelm, B. Smarsly, M. Antonietti, High Electroactivity of Polyaniline in Supercapacitors by Using a Hierarchically Porous Carbon Monolith as a Support, Adv. Funct. Mater. 17 (2007) 3083–3087. doi:10.1002/adfm.200700518.

[85] M. Seredych, D. Hulicova-Jurcakova, G.Q. Lu, T.J. Bandosz, Surface functional groups of carbons and the effects of their chemical character, density and accessibility to ions on electrochemical performance, Carbon N. Y. 46 (2008) 1475–1488. doi:10.1016/J.CARBON.2008.06.027.

[86] Electrochemical Supercapacitors: Scientific Fundamentals and Technological ... - B. E. Conway - GoogleBooks).(accessed February 26, 2018).

[87] T.-C. Wen, C. Hu, Hydrogen and Oxygen Evolutions on Ru-Ir Binary Oxides, J. Electrochem. Soc. 139 (1992) 2158. doi:10.1149/1.2221195.

[88] L.-S. Zhong, J.-S. Hu, H.-P. Liang, A.-M. Cao, W.-G. Song, L.-J. Wan, Self-Assembled 3D Flowerlike Iron Oxide Nanostructures and Their Application in Water Treatment, Adv. Mater. 18 (2006) 2426–2431. doi:10.1002/adma.200600504.

[89] C. Xia, J. Guo, P. Li, X. Zhang, H.N. Alshareef, Highly Stable Aqueous Zinc-Ion Storage Using Layered Calcium Vanadium Oxide Bronze Cathode, Angew. Chemie. (2018). doi:10.1002/ange.201713291.

[90] P. He, G. Zhang, X. Liao, M. Yan, X. Xu, Q. An, J. Liu, L. Mai, Sodium Ion Stabilized Vanadium Oxide Nanowire Cathode for High-Performance Zinc-Ion Batteries, Adv. Energy Mater. (2018) 1702463. doi:10.1002/aenm.201702463.

[91] M. Salanne, B. Rotenberg, K. Naoi, K. Kaneko, P.-L. Taberna, C.P. Grey, B. Dunn, P. Simon, Efficient storage mechanisms for building better supercapacitors Efficient storage mechanisms for building better supercapacitors. Nature Energy Open Archive TOULOUSE Archive Ouverte (OATAO), Nat. Energy. 1 (2016) 1–10. doi:10.1038/NENERGY.2016.70.

[92] D.S. Patil, J.S. Shaikh, D.S. Dalavi, S.S. Kalagi, P.S. Patil, Chemical synthesis of highly stable PVA/PANI films for supercapacitor application, Mater. Chem. Phys. 128 (2011) 449–455. doi:10.1016/j.matchemphys.2011.03.029.

[93] J. Zhang, J.P. Cheng, M. Li, L. Liu, F. Liu, X.B. Zhang, Flower-like nickel–cobalt binary hydroxides with high specific capacitance: Tuning the composition and asymmetric capacitor application, J. Electroanal. Chem. 743 (2015) 38–45. doi:10.1016/j.jelechem.2015.02.021.

[94] H. Wang, Y. Liang, T. Mirfakhrai, Z. Chen, H. Sanchez Casalongue, H. Dai, Advanced Asymmetrical Supercapacitors Based on Graphene Hybrid Materials, Nano Res. 4 (2011) 729– 736. doi 10.1007/s12274-011-0129-6

[95] M. Li, J.P. Cheng, J. Wang, F. Liu, X.B. Zhang, The growth of nickel-manganese and cobalt-manganese layered double hydroxides on reduced graphene oxide for supercapacitor, Electrochim. Acta. 206 (2016) 108–115. doi:10.1016/j.electacta.2016.04.084.

[96] X. Li, W. Xing, S. Zhuo, J. Zhou, F. Li, S.-Z. Qiao, G.-Q. Lu, Preparation of capacitor's electrode from sunflower seed shell, Bioresour. Technol. 102 (2011) 1118–1123. doi:10.1016/j.biortech.2010.08.110.

[97] J. Xu, Q. Gao, Y. Zhang, Y. Tan, W. Tian, L. Zhu, L. Jiang,, Preparing two-dimensional microporous carbon from Pistachio nutshell with high areal capacitance as supercapacitor materials, Sci. Rep. 4 (2014) 845–854. doi:10.1038/srep05545.

[98] J. Hayashi, T. Horikawa, I. Takeda, K. Muroyama, F. Nasir Ani, Preparing activated carbon from various nutshells by chemical activation with K2CO3, Carbon N. Y. 40 (2002) 2381–2386. doi:10.1016/S0008-6223(02)00118-5.

[99] K.S. Sulaiman, A. Mat, A.K. Arof, Activated carbon from coconut leaves for electrical

double-layer capacitor, Ionics (Kiel). 22 (2016) 911–918. doi:10.1007/s11581-015-1594-9.

[100] F. Barzegar, A. Bello, D. Momodu, M.J. Madito, J. Dangbegnon, N. Manyala, Preparation and characterization of porous carbon from expanded graphite for high energy density supercapacitor in aqueous electrolyte, J. Power Sources. 309 (2016) 245–253. doi:10.1016/j.jpowsour.2016.01.097.

[101] K.-S. Kim, S.-J. Park, Easy synthesis of polyaniline-based mesoporous carbons and their high electrochemical performance, Microporous Mesoporous Mater. 163 (2012) 140–146. doi:10.1016/j.micromeso.2012.04.047.

[102] E.C.S. Transactions, T.E. Society, Floating of PPY Derived Carbon Based Symmetric Supercapacitor in Alkaline Electrolyte, ECS Trans. 6 (2017) 3–5.

[103] A. Özhan, Ö. Şahin, M.M. Küçük, C. Saka, Preparation and characterization of activated carbon from pine cone by microwave-induced ZnCl2 activation and its effects on the adsorption of methylene blue, Cellulose. 21 (2014) 2457–2467. doi:10.1007/s10570-014-0299-y.

[104] T.-C. Weng, H. Teng, Characterization of High Porosity Carbon Electrodes Derived from Mesophase Pitch for Electric Double-Layer Capacitors, J. Electrochem. Soc. 148 (2001) A368. doi:10.1149/1.1357171.

[105] A. Alonso, V. Ruiz, C. Blanco, R. Santamaría, M. Granda, R. Menéndez, S.G.E. de Jager, Activated carbon produced from Sasol-Lurgi gasifier pitch and its application as electrodes in supercapacitors, Carbon N. Y. 44 (2006) 441–446.

doi:10.1016/J.CARBON.2005.09.008.

[106] X. Xiang, E. Liu, Z. Huang, H. Shen, Y. Tian, C. Xiao, J. Yang, Z. Mao, Preparation of activated carbon from polyaniline by zinc chloride activation as supercapacitor electrodes, J. Solid State Electrochem. 15 (2011) 2667–2674. doi:10.1007/s10008-010-1258-7.

[107] R. Nandhini, P.A. Mini, B. Avinash, S.V. Nair, K.R.V. Subramanian, Supercapacitor electrodes using nanoscale activated carbon from graphite by ball milling, Mater. Lett. 87 (2012) 165–168. doi:10.1016/J.MATLET.2012.07.092.

[108] E. Frackowiak, Carbon materials for supercapacitor application, Phys. Chem. Chem. Phys. 9 (2007) 1774. doi:10.1039/b618139m.

[109] G. Salitra, A. Soffer, L. Eliad, Y. Cohen, D. Aurbach, Carbon Electrodes for Double-Layer Capacitors I. Relations Between Ion and Pore Dimensions, J. Electrochem. Soc. 147 (2000) 2486. doi:10.1149/1.1393557.

[110] Linoam Eliad, Gregory Salitra, and Abraham Soffer, D. Aurbach*, Ion Sieving Effects in the Electrical Double Layer of Porous Carbon Electrodes: Estimating Effective Ion Size in Electrolytic Solutions, (2001). doi:10.1021/JP010086Y.

[111] Linoam Eliad, Gregory Salitra, and Abraham Soffer, D. Aurbach*, Proton-Selective Environment in the Pores of Activated Molecular Sieving Carbon Electrodes, (2002). doi:10.1021/JP020336Q.

[112] Researches; Carbon Nanomaterials

http://laser.gist.ac.kr/board/bbs/board.php?bo_table=rese_04 (accessed February 25, 2018).

[113] Y. Zhang, Y. Bai, B. Yan, Functionalized carbon nanotubes for potential medicinal applications, Drug Discov. Today. 15 (2010) 428–435. doi:10.1016/J.DRUDIS.2010.04.005.

[114] L. Camilli, C. Pisani, E. Gautron, M. Scarselli, P. Castrucci, F. D'Orazio, M. Passacantando, D. Moscone, M. De Crescenzi, A three-dimensional carbon nanotube network for water treatment, Nanotechnology. 25 (2014) 65701. doi:10.1088/0957-4484/25/6/065701.

[115] L.L. Zhang, R. Zhou, X.S. Zhao, Graphene-based materials as supercapacitor electrodes, J. Mater. Chem. 20 (2010) 5983. doi:10.1039/c000417k.

[116] X. Guo, G. Lu, J. Chen, Graphene-Based Materials for Photoanodes in Dye-Sensitized Solar Cells, Front. Energy Res. 3 (2015) 50. doi:10.3389/fenrg.2015.00050.

[117] K.S. Novoselov, A.K. Geim, S. V. Morozov, D. Jiang, M.I. Katsnelson, I. V. Grigorieva, S. V. Dubonos, A.A. Firsov, Two-dimensional gas of massless Dirac fermions in graphene, Nature. 438 (2005) 197–200. doi:10.1038/nature04233.

[118] A. Yasmin, J.-J. Luo, I.M. Daniel, Processing of expanded graphite reinforced polymer nanocomposites, Compos. Sci. Technol. 66 (2006) 1182–1189. doi:10.1016/J.COMPSCITECH.2005.10.014.

[119] A.K. Geim, K.S. Novoselov, The rise of graphene, Nat. Mater. 6 (2007) 183–191. doi:10.1038/nmat1849.

[120] C.N.R. Rao, A.K. Sood, K.S. Subrahmanyam, A. Govindaraj, Graphene: The New Two-

Dimensional Nanomaterial, Angew. Chemie Int. Ed. 48 (2009) 7752–7777. doi:10.1002/anie.200901678.

[121] F. Schedin, A.K. Geim, S. V. Morozov, E.W. Hill, P. Blake, M.I. Katsnelson, K.S. Novoselov, Detection of individual gas molecules adsorbed on graphene, Nat. Mater. 6 (2007) 652–655. doi:10.1038/nmat1967.

[122] J.S. Bunch, A.M. van der Zande, S.S. Verbridge, I.W. Frank, D.M. Tanenbaum, J.M. Parpia, H.G. Craighead, P.L. McEuen, Electromechanical resonators from graphene sheets., Science. 315 (2007) 490–3. doi:10.1126/science.1136836.

[123] C.N.R. Rao, K.S. Subrahmanyam, H.S.S. Ramakrishna Matte, B. Abdulhakeem, A. Govindaraj, B. Das, P. Kumar, A. Ghosh, D.J. Late, A study of the synthetic methods and properties of graphenes, Sci. Technol. Adv. Mater. 11 (2010) 54502. doi:10.1088/1468-6996/11/5/054502.

[124] P.L. Chiu, D.D.T. Mastrogiovanni, D. Wei, C. Louis, M. Jeong, G. Yu, P. Saad, C.R. Flach, R. Mendelsohn, E. Garfunkel, H. He, Microwave- and Nitronium Ion-Enabled Rapid and Direct Production of Highly Conductive Low-Oxygen Graphene, J. Am. Chem. Soc. 134 (2012) 5850–5856. doi:10.1021/ja210725p.

[125] F. Bonaccorso, A. Lombardo, T. Hasan, Z. Sun, L. Colombo, A.C. Ferrari, Production and processing of graphene and 2d crystals, Mater. Today. 15 (2012) 564–589. doi:10.1016/S1369-7021(13)70014-2.

[126] Y. Wang, Z. Shi, Y. Huang, Y. Ma, C. Wang, M. Chen, Y. Chen, Supercapacitor Devices

Based on Graphene Materials, J. Phys. Chem. C. 113 (2009) 13103–13107. doi:10.1021/jp902214f.

[127] S.R.C. Vivekchand, C.S. Rout, K.S. Subrahmanyam, A. Govindaraj, C.N.R. Rao, Graphene-based electrochemical supercapacitors, J. Chem. Sci. 120 (2008) 9–13. doi:10.1007/s12039-008-0002-7.

[128] Y. Zhu, S. Murali, W. Cai, X. Li, J.W. Suk, J.R. Potts, R.S. Ruoff, Graphene and Graphene Oxide: Synthesis, Properties, and Applications, Adv. Mater. 22 (2010) 3906–3924. doi:10.1002/adma.201001068.

[129] L.L. Zhang, S. Zhao, X.N. Tian, X.S. Zhao, Layered Graphene Oxide Nanostructures with Sandwiched Conducting Polymers as Supercapacitor Electrodes, Langmuir. 26 (2010) 17624–17628. doi:10.1021/la103413s.

[130] H. Wang, L.-F. Cui, Y. Yang, H. Sanchez Casalongue, J.T. Robinson, Y. Liang, Y. Cui, H. Dai, Mn_3O_4 –Graphene Hybrid as a High-Capacity Anode Material for Lithium Ion Batteries, J. Am. Chem. Soc. 132 (2010) 13978–13980. doi:10.1021/ja105296a.

[131] Y. Wang, W. Lai, N. Wang, Z. Jiang, X. Wang, P. Zou, Z. Lin, H.J. Fan, F. Kang, C.-P. Wong, C. Yang, A reduced graphene oxide/mixed-valence manganese oxide composite electrode for tailorable and surface mountable supercapacitors with high capacitance and super-long life, Energy Environ. Sci. 10 (2017) 941–949. doi:10.1039/C6EE03773A.

[132] J.-K. Chang, C.-T. Lin, W.-T. Tsai, Manganese oxide/carbon composite electrodes for

electrochemical capacitors, Electrochem. Commun. 6 (2004) 666–671. doi:10.1016/j.elecom.2004.04.020.

[133] F. Shi, L. Li, X.-L. Wang, C.-D. Gu, J.-P. Tu, Metal oxide/hydroxide-based materials for supercapacitors, (n.d.). doi:10.1039/c4ra06136e.

[134] H.T. Tan, W. Sun, L. Wang, Q. Yan, 2D Transition Metal Oxides/Hydroxides for Energy-Storage Applications, ChemNanoMat. 2 (2016) 562–577. doi:10.1002/cnma.201500177.

[135] L. Deng, G. Zhu, J. Wang, L. Kang, Z.-H. Liu, Z. Yang, Z. Wang, Graphene–MnO2 and graphene asymmetrical electrochemical capacitor with a high energy density in aqueous electrolyte, J. Power Sources. 196 (2011) 10782–10787. doi:10.1016/J.JPOWSOUR.2011.09.005.

[136] J.M. Ko, K.M. Kim, Electrochemical properties of MnO2/activated carbon nanotube composite as an electrode material for supercapacitor, Mater. Chem. Phys. 114 (2009) 837–841. doi:10.1016/J.MATCHEMPHYS.2008.10.047.

[137] S.R. Sivakkumar, J.M. Ko, D.Y. Kim, B.C. Kim, G.G. Wallace, Performance evaluation of CNT/polypyrrole/MnO2 composite electrodes for electrochemical capacitors, Electrochim. Acta. 52 (2007) 7377–7385. doi:10.1016/j.electacta.2007.06.023.

[138] Z. Fan, J. Yan, T. Wei, L. Zhi, G. Ning, T. Li, F. Wei, Asymmetric Supercapacitors Based on Graphene/MnO2 and Activated Carbon Nanofiber Electrodes with High Power and

Energy Density, Adv. Funct. Mater. 21 (2011) 2366–2375. doi:10.1002/adfm.201100058.

[139] H. Chen, L. Hu, M. Chen, Y. Yan, L. Wu, Nickel-Cobalt Layered Double Hydroxide Nanosheets for High-performance Supercapacitor Electrode Materials, Adv. Funct. Mater. 24 (2014) 934–942. doi:10.1002/adfm.201301747.

[140] L. Li, Z.A. Hu, N. An, Y.Y. Yang, Z.M. Li, H.Y. Wu, Facile Synthesis of MnO_2 /CNTs Composite for Supercapacitor Electrodes with Long Cycle Stability, J. Phys. Chem. C. 118 (2014) 22865–22872. doi:10.1021/jp505744p.

[141] X. Zhang, X. Wang, L. Jiang, H. Wu, C. Wu, J. Su, Effect of aqueous electrolytes on the electrochemical behaviors of supercapacitors based on hierarchically porous carbons, J. Power Sources. 216 (2012) 290–296. doi:10.1016/j.jpowsour.2012.05.090.

[142] G. Lakshminarayana, M. Nogami, Inorganic–organic hybrid membranes with anhydrous proton conduction prepared from tetramethoxysilane/methyl-trimethoxysilane/trimethylphosphate and 1-ethyl-3-methylimidazolium-bis (trifluoromethanesulfonyl) imide for H2/O2 fuel cells, Electrochim. Acta. 55 (2010) 1160–1168. doi:10.1016/J.ELECTACTA.2009.10.020.

[143] A. Lewandowski, A. Olejniczak, M. Galinski, I. Stepniak, Performance of carbon–carbon supercapacitors based on organic, aqueous and ionic liquid electrolytes, J. Power Sources. 195 (2010) 5814–5819. doi:10.1016/j.jpowsour.2010.03.082.

[144] A. Brandt, S. Pohlmann, A. Varzi, A. Balducci, S. Passerini, Ionic liquids in supercapacitors, MRS Bull. 38 (2013) 554–559. doi:10.1557/mrs.2013.151.

[145] J.F. Wishart, Energy applications of ionic liquids, Energy Environ. Sci. 2 (2009) 956. doi:10.1039/b906273d.

[146] A. Bello, K. Makgopa, M. Fabiane, D. Dodoo-Ahrin, K.I. Ozoemena, N. Manyala, Chemical adsorption of NiO nanostructures on nickel foam-graphene for supercapacitor applications, J. Mater. Sci. 48 (2013) 6707–6712. doi:10.1007/s10853-013-7471-x.

[147] M. Inagaki, H. Konno, O. Tanaike, Carbon materials for electrochemical capacitors, J. Power Sources. 195 (2010) 7880–7903. doi:10.1016/J.JPOWSOUR.2010.06.036.

[148] D. Weingarth, A. Foelske-Schmitz, A. Wokaun, R. Kötz, PTFE bound activated carbon—A quasi-reference electrode for ionic liquids, Electrochem. Commun. 18 (2012) 116–118. doi:10.1016/J.ELECOM.2012.02.040.

[149] E. Frackowiak, F. Béguin, Electrochemical storage of energy in carbon nanotubes and nanostructured carbons, Carbon N. Y. 40 (2002) 1775–1787. doi:10.1016/S0008-6223(02)00045-3.

[150] D.Y. Momodu, Investigation of metal hydroxides graphene composites as electrode materials for supercapacitor applications, (2015). https://repository.up.ac.za/handle/2263/50281 (accessed March 19, 2018).

[151] J.R. Miller, A.F. Burke, Electric Vehicle Capacitor Test Procedures Manual Revision, (1994). https://avt.inl.gov/sites/default/files/pdf/battery/ultracap_test_procedures_manual_10_94.pdf (accessed March 19, 2018).

[152] F. Barzegar, Synthesis and characterization of activated carbon materials for supercapcitor applications, (2016). https://repository.up.ac.za/handle/2263/53524 (accessed March 20, 2018).

[153] T.-F. Hsieh, C.-C. Chuang, W.-J. Chen, J.-H. Huang, W.-T. Chen, C.-M. Shu, Hydrous ruthenium dioxide/multi-walled carbon-nanotube/titanium electrodes for supercapacitors, Carbon 50 (2012) 1740–1747. doi:10.1016/J.CARBON.2011.12.017.

[154] A. Bard, L.F.-E. Methods, undefined 2001, Fundamentals and applications, Researchgate.net. (n.d.). https://www.researchgate.net/profile/Asheesh_Kumar4/post/How_can_I_correlate_electrochemical_surface_area_and_double_layer_capacitance_in_a_PEM_fuel_cell/attachment/59d645b8c49f478072eae029/AS:273827819393024@1442297047554/download/R.+Faulkner.pdf (accessed March 20, 2018).

[155] L. Zhang, J. Wang, J. Zhu, X. Zhang, K. San Hui, K.N. Hui, 3D porous layered double hydroxides grown on graphene as advanced electrochemical pseudocapacitor materials, J. Mater. Chem. A. 1 (2013) 9046. doi:10.1039/c3ta11755c.

[156] J.W. Lee, A.S. Hall, J.-D. Kim, T.E. Mallouk, A Facile and Template-Free Hydrothermal Synthesis of Mn_3O_4 Nanorods on Graphene Sheets for Supercapacitor Electrodes with Long Cycle Stability, Chem. Mater. 24 (2012) 1158–1164. doi:10.1021/cm203697w.

[157] B. Akinwolemiwa, C. Peng, G.Z. Chen, Redox Electrolytes in Supercapacitors, J. Electrochem. Soc. 162 (2015) A5054–A5059. doi:10.1149/2.0111505jes.

[158] P.L. Taberna, P. Simon, J.F. Fauvarque, Electrochemical Characteristics and Impedance Spectroscopy Studies of Carbon-Carbon Supercapacitors, J. Electrochem. Soc. 150 (2003) A292. doi:10.1149/1.1543948.

[159] W. Sun, R. Zheng, X. Chen, Symmetric redox supercapacitor based on micro-fabrication with three-dimensional polypyrrole electrodes, J. Power Sources. 195 (2010) 7120–7125. doi:10.1016/J.JPOWSOUR.2010.05.012.

[160] F. Béguin, E. Frąckowiak, Supercapacitors : materials, systems, and applications, Wiley-VCH, 2013.

[161] D. Weingarth, H. Noh, A. Foelske-Schmitz, A. Wokaun, R. Kötz, A reliable determination method of stability limits for electrochemical double layer capacitors, Electrochim. Acta. 103 (2013) 119–124. doi:10.1016/J.ELECTACTA.2013.04.057.

[162] D. Weingarth, A. Foelske-Schmitz, R. Kötz, Cycle versus voltage hold – Which is the better stability test for electrochemical double layer capacitors?, J. Power Sources. 225 (2013) 84–88. doi:10.1016/J.JPOWSOUR.2012.10.019.

[163] B.W. Ricketts, C. Ton-That, Self-discharge of carbon-based supercapacitors with organic electrolytes, J. Power Sources. 89 (2000) 64–69. doi:10.1016/S0378-7753(00)00387-6.

[164] R. Holze, F. Béguin, E. Frąckowiak (eds): Supercapacitors – Materials, Systems, and Applications, J. Solid State Electrochem. 19 (2015) 1253–1253. doi:10.1007/s10008-014-2718-2.

[165] A.A. Mirghni, M.J. Madito, K.O. Oyedotun, T.M. Masikhwa, N.M. Ndiaye, S.J. Ray, N.

Manyala, A high energy density asymmetric supercapacitor utilizing a nickel phosphate/graphene foam composite as the cathode and carbonized iron cations adsorbed onto polyaniline as the anode, RSC Adv. 8 (2018) 11608–11621. doi:10.1039/C7RA12028A.

[166] K. Byrappa, M. Yoshimura, HANDBOOK OF HYDROTHERMAL TECHNOLOGY A Technology for Crystal Growth and Materials Processing,. http://citeseerx.ist.psu.edu/viewdoc/download?doi=10.1.1.473.5385&rep=rep1&type=pdf (accessed January 16, 2018).

[167] H. Hayashi, Y. Hakuta, Hydrothermal Synthesis of Metal Oxide Nanoparticles in Supercritical Water, Materials (Basel). 3 (2010) 3794–3817. doi:10.3390/ma3073794.

[168] Y. Song, J. Wang, Z. Li, D. Guan, T. Mann, Q. Liu, M. Zhang, L. Liu, Self-assembled hierarchical porous layered double hydroxides by solvothermal method and their application for capacitors, Microporous Mesoporous Mater. 148 (2012) 159–165. doi:10.1016/j.micromeso.2011.08.013.

[169] Z. Gao, J. Wang, Z. Li, W. Yang, B. Wang, M. Hou, Y. He, Q. Liu, T. Mann, P. Yang, M. Zhang, L. Liu, Graphene Nanosheet/Ni $^{2+}$ /Al $^{3+}$ Layered Double-Hydroxide Composite as a Novel Electrode for a Supercapacitor, Chem. Mater. 23 (2011) 3509–3516. doi:10.1021/cm200975x.

[170] Y. Tao, L. Ruiyi, L. Zaijun, L. Junkang, W. Guangli, G. Zhiquo, A free template strategy for the fabrication of nickel/cobalt double hydroxide microspheres with tunable nanostructure and morphology for high performance supercapacitors, RSC Adv. 3 (2013)

19416. doi:10.1039/c3ra42806k.

[171] E. Professor, Solvothermal Reactions: an original route for the synthesis of novel materials Gérard DEMAZEAU, (n.d.). https://hal.archives-ouvertes.fr/hal-00269253/document (accessed January 16, 2018).

[172] V. Subramanian, † Hongwei Zhu, ‡ Robert Vajtai, ‡ and P. M. Ajayan, † Bingqing Wei*, Hydrothermal Synthesis and Pseudocapacitance Properties of MnO2 Nanostructures, (2005). doi:10.1021/JP0543330.

[173] B. Gersten, Solvothermal Synthesis of Nanoparticles, https://www.sigmaaldrich.com/content/dam/sigma-aldrich/articles/chemfiles/volume5a13/Solvothermal_Synthesis_of_Nanoparticles.pdf (accessed January 16, 2018).

[174] O. Hugh Pierson, HANDBOOK OF CHEMICAL VAPOR DEPOSITION (CVD) Library of Congress Cataloging-in-Publication Data. http://www.chematscientific.com/UploadFiles/2016/11/Handbook-of-Chemical-Vapor-Deposition.pdf (accessed January 15, 2018).

[175] J.R. Creighton, P. Ho, Introduction to Chemical Vapor Deposition (CVD). https://www.asminternational.org/documents/10192/1849770/ACFAA6E.pdf (accessed January 17, 2018).

[176] SEM Scanning Electron Microscope A To Z Basic Knowledge For Using The SEM Construction of Instrument Electron Gun Construction of Lens Condenser Lens and

Objective Lens Specimen Stage Secondary Electron Detector Image Display and Recording Vacuum System. https://www.jeol.co.jp/en/applications/pdf/sm/sem_atoz_all.pdf (accessed January 18, 2018).

[177] W. Zhou, R.P. Apkarian, Z. Lin Wang, D. Joy, Fundamentals of Scanning Electron Microscopy, (n.d.). http://homes.ufam.edu.br/berti/nanomateriais/aulas pptx e livros/livro/Scanning Microscopy for Nanotechnology/Fundamentals of Scanning Electron Microscopy (SEM).pdf (accessed January 18, 2018).

[178] R.F. Egerton, Electron Optics, in: Phys. Princ. Electron Microsc., Springer US, Boston, MA, 2005: pp. 27–55. doi:10.1007/0-387-26016-1_2.

[179] A.A. Hilal, Microstructure of Concrete, in: High Perform. Concr. Technol. Appl., InTech, 2016. doi:10.5772/64574.

[180] Introduction to Energy Dispersive X-ray Spectrometry (EDS). https://cfamm.ucr.edu/documents/eds-intro.pdf (accessed January 18, 2018).

[181] D.B. Williams, C.B. Carter, The Transmission Electron Microscope, in: Transm. Electron Microsc., Springer US, Boston, MA, 2009: pp. 3–22. doi:10.1007/978-0-387-76501-3_1.

[182] P. Zinin, Transmission Electron Microscopy, (n.d.). www.soest.hawaii.edu%5C~zinin (accessed February 10, 2018).

[183] B.D. Cullity, S.R. Stock, Elements of X-ray Diffraction, Third Edition, (2001). https://www.scholars.northwestern.edu/en/publications/elements-of-x-ray-diffraction-

third-edition (accessed February 10, 2018).

[184] BASICS OF X-RAY DIFFRACTION INTRODUCTION TO POWDER/ POLYCRYSTALLINE DIFFRACTION Basics of X-ray Diffraction INTRODUCTION TO POWDER/POLYCRYSTALLINE DIFFRACTION. https://old.vscht.cz/clab/RTG/dokumenty/thermo/xrd/Introduction to powder diffraction.pdf (accessed February 10, 2018).

[185] B.E. (Bertram E. Warren, X-ray diffraction, Dover Publications, 1990.

[186] D.M. Moore, R.C. Reynolds, X-ray diffraction and the identification and analysis of clay minerals, Oxford University Press, 1997.

[187] A.C. Ferrari, J. Robertson, Raman spectroscopy of amorphous, nanostructured, diamond-like carbon, and nanodiamond., Philos. Trans. A. Math. Phys. Eng. Sci. 362 (2004) 2477–512. doi:10.1098/rsta.2004.1452.

[188] D. Masci UTAGRI, An introduction to Raman Spectroscopy. http://iaa.entecra.it/WS2015/9 Masci_ENEA_Raman.pdf (accessed February 15, 2018).

[189] W.A.P. Luck, D. J. Gardiner, P. R. Graves (Eds.): Practical Raman Spectroscopy, mit Beiträgen von H. J. Bowley, D. J. Gardiner, D. L. Gerrard, P. R. Graves, J. D. Louden, and G. Turrell, Springer-Verlag, Berlin, Heidelberg, New York 1989. 157 Seiten, brosch., Preis: D, Berichte Der Bunsengesellschaft Für Phys. Chemie. 94 (1990) 1047–1047. doi:10.1002/bbpc.19900940938.

[190] Introduction to Fourier Transform Infrared Spectrometry, (n.d.). https://www.niu.edu/analyticallab/_pdf/ftir/FTIRintro.pdf (accessed February 15, 2018).

[191] Reporting physisorption data for gas/solid systems — with special reference to the determination of surface area and porosity,. https://www.iupac.org/publications/pac-2007/1985/pdf/5704x0603.pdf (accessed February 17, 2018).

[192] K. Sing, The use of nitrogen adsorption for the characterisation of porous materials, Colloids Surfaces A Physicochem. Eng. Asp. 187 (2001) 3–9. www.elsevier.nl/locate/colsurfa (accessed February 15, 2018).

[193] S. Brunauer, L.S. Deming, W.E. Deming, E. Teller, On a Theory of the van der Waals Adsorption of Gases, J. Am. Chem. Soc. 62 (1940) 1723–1732. doi:10.1021/ja01864a025.

[194] A. V. Neimark, K.S.W. Sing, M. Thommes, A. V. Neimark, K.S.W. Sing, M. Thommes, Surface Area and Porosity, in: Handb. Heterog. Catal., Wiley-VCH Verlag GmbH & Co. KGaA, Weinheim, Germany, 2008. doi:10.1002/9783527610044.hetcat0037.

[195] Brundle CR and Baker AD, Electron Spectroscopy:Theory, Techniques and Applications, Volume 2 (1998). http://fadley.physics.ucdavis.edu/BasicConceptsofXPS.pdf (accessed February 17, 2018).

[196] L.R.F. A.J. Bard, Electrochemical methods: fundamentals and applications. http://glearning.tju.edu.cn/pluginfile.php/74331/mod_resource/content/0/参考书/Electrochemical_methods_2ed_2001_-_Bard_Faulkner.pdf (accessed February 13, 2018).

[197] C.G. Zoski, Handbook of electrochemistry, Elsevier, 2007.

[198] I.A. Sahito, K.C. Sun, A.A. Arbab, M.B. Qadir, S.H. Jeong, Graphene coated cotton fabric as textile structured counter electrode for DSSC, (2015).

doi:10.1016/j.electacta.2015.05.035.

[199] Wave Spring and Spacer for CR2032 (100 pairs/pck) - EQ-CR20-WS, (n.d.). http://www.mtixtl.com/WaveSpringandSpacerforCR2032100pairs/pck-EQ-CR20-WS.aspx (accessed February 15, 2018).

[200] F. Barzegar, Synthesis and characterization of activated carbon materials for supercapcitor applications, (2016). https://repository.up.ac.za/handle/2263/53524 (accessed February 19, 2018).

[201] Y. Korenblit, M. Rose, E. Kockrick, L. Borchardt, A. Kvit, S. Kaskel, G. Yushin, High-Rate Electrochemical Capacitors Based on Ordered Mesoporous Silicon Carbide-Derived Carbon, (n.d.). doi:10.1021/nn901825y.

[202] W. Guo, C. Yu, S. Li, J. Yang, Z. Liu, C. Zhao, H. Huang, M. Zhang, X. Han, Y. Niu, J. Qiu, High-Stacking-Density, Superior-Roughness LDH Bridged with Vertically Aligned Graphene for High-Performance Asymmetric Supercapacitors, Small. (2017) 1701288. doi:10.1002/smll.201701288.

[203] L. Demarconnay, E. Raymundo-Piñero, F. Béguin, Adjustment of electrodes potential window in an asymmetric carbon/MnO2 supercapacitor, J. Power Sources. 196 (2011) 580–586. doi:10.1016/j.jpowsour.2010.06.013.

[204] K.S. Sulaiman, A. Mat, A.K. Arof, Activated carbon from coconut leaves for electrical double-layer capacitor, Ionics (Kiel). 22 (2016) 911–918. doi:10.1007/s11581-015-1594-9.

[205] F. Barzegar, A.A. Khaleed, F.U. Ugbo, K.O. Oyeniran, D.Y. Momodu, A. Bello, J.K.

Dangbegnon, N. Manyala, Cycling and floating performance of symmetric supercapacitor derived from coconut shell biomass, (2016). doi:10.1063/1.4967348.

[206] H. Wang, Z. Xu, A. Kohandehghan, Z. Li, K. Cui, X. Tan, T.J. Stephenson, C.K. King'ondu, C.M.B. Holt, B.C. Olsen, J.K. Tak, D. Harfield, A.O. Anyia, D. Mitlin, Interconnected Carbon Nanosheets Derived from Hemp for Ultrafast Supercapacitors with High Energy, ACS Nano. 7 (2013) 5131–5141. doi:10.1021/nn400731g.

[207] H. Wang, Z. Xu, A. Kohandehghan, Z. Li, K. Cui, X. Tan, T.J. Stephenson, C.K. King'ondu, C.M.B. Holt, B.C. Olsen, J.K. Tak, D. Harfield, A.O. Anyia, D. Mitlin, Interconnected carbon nanosheets derived from hemp for ultrafast supercapacitors with high energy., ACS Nano. 7 (2013) 5131–41. doi:10.1021/nn400731g.

[208] L. Wei, M. Sevilla, A.B. Fuertes, R. Mokaya, G. Yushin, Hydrothermal Carbonization of Abundant Renewable Natural Organic Chemicals for High-Performance Supercapacitor Electrodes, Adv. Energy Mater. 1 (2011) 356–361. doi:10.1002/aenm.201100019.

[209] Quercus suber Cork Oak PFAF Plant Database. http://www.pfaf.org/USER/Plant.aspx?LatinName=Quercus+suber (accessed January 10, 2018).

[210] P.J.M. Carrott, M.M.L.R. Carrott, P.A.M. Mourão, R.P. Lima, Preparation of Activated Carbons from Cork by Physical Activation in Carbon Dioxide,. http://journals.sagepub.com/doi/pdf/10.1260/026361703772776457 (accessed January 10, 2018).

[211] B. Cardoso, A.S. Mestre, A.P. Carvalho, J. Pires, Activated Carbon Derived from Cork Powder Waste by KOH Activation: Preparation, Characterization, and VOCs Adsorption, Ind. Eng. Chem. Res. 47 (2008) 5841–5846. doi:10.1021/ie800338s.

[212] Y. Lv, F. Zhang, Y. Dou, Y. Zhai, J. Wang, H. Liu, Y. Xia, B. Tu, D. Zhao, A comprehensive study on KOH activation of ordered mesoporous carbons and their supercapacitor application, J. Mater. Chem. 22 (2012) 93. doi:10.1039/c1jm12742j.

[213] H. Kim, K.-Y. Park, M.-Y. Cho, M.-H. Kim, J. Hong, S.-K. Jung, K.C. Roh, K. Kang, High-Performance Hybrid Supercapacitor Based on Graphene-Wrapped $Li_4Ti_5O_{12}$ and Activated Carbon, ChemElectroChem. 1 (2014) 125–130. doi:10.1002/celc.201300186.

[214] A. Jain, C. Xu, S. Jayaraman, R. Balasubramanian, J.Y. Lee, M.P. Srinivasan, Mesoporous activated carbons with enhanced porosity by optimal hydrothermal pre-treatment of biomass for supercapacitor applications, Microporous Mesoporous Mater. 218 (2015) 55–61. doi:10.1016/j.micromeso.2015.06.041.

[215] X. Zheng, W. Lv, Y. Tao, J. Shao, C. Zhang, D. Liu, J. Luo, D.-W. Wang, Q.-H. Yang, Oriented and Interlinked Porous Carbon Nanosheets with an Extraordinary Capacitive Performance, Chem. Mater. 26 (2014) 6896–6903. doi:10.1021/cm503845q.

[216] Long-term cycling behavior of asymmetric activated carbon/MnO2 aqueous electrochemical supercapacitor, J. Power Sources. 173 (2007) 633–641. doi:10.1016/J.JPOWSOUR.2007.04.074.

[217] M. Huang, Y. Zhang, F. Li, L. Zhang, R.S. Ruoff, Z. Wen, Q. Liu, Self-assembly of

mesoporous nanotubes assembled from interwoven ultrathin birnessite-type MnO2 nanosheets for asymmetric supercapacitors., Sci. Rep. 4 (2014) 3878. doi:10.1038/srep03878.